UNIVERSITY OF SÃO PAULO
POLYTECHNIC SCHOOL

ALVARO DE FARIAS SOARES

Luminescence on HfO_2 crystals: synthesis, heat treatment effect, related defects, and their application in ionising radiation dosimetry

São Paulo
2023

ALVARO DE FARIAS SOARES

Luminescence on HfO_2 crystals: synthesis, heat treatment effect, related defects, and their application in ionising radiation dosimetry

Corrected Version

Doctoral thesis presented to the Polytechnic School of the University of São Paulo, Brazil, to obtain the degree of Doctor of Science.

Concentration Area: Electrical Engineering.

Supervisor: Prof. Dr. Sonia Hatsue Tatumi.

São Paulo
2023

Este exemplar foi revisado e corrigido em relação à versão original, sob responsabilidade única do autor e com a anuência de seu orientador.

São Paulo, de 15 de dezembro de 2023.

Assinatura do autor: Alvaro de Farias Soares

Assinatura do orientador: gov.br
Documento assinado digitalmente
SONIA HATSUE TATUMI
Data: 16/12/2023 11:31:50-0300
Verifique em https://validar.iti.gov.br

Catalogação-na-publicação

Soares, Alvaro de Farias
Luminescence on HfO_2 crystals: synthesis, heat treatment effect, related defects, and their application in ionising radiation dosimetry / A. F. Soares -- versão corr. -- São Paulo, 2023.
204 p.

Tese (Doutorado) - Escola Politécnica da Universidade de São Paulo. Departamento de Engenharia de Sistemas Eletrônicos.

1.Dosimetria 2.Luminescência 3.Óptica não linear I.Universidade de São Paulo. Escola Politécnica. Departamento de Engenharia de Sistemas Eletrônicos II.t.

To my family: my parents Ivanilda and Cicero, and my sister Soraia.
They are my steady support.

Acknowledgements

This thesis is without doubt a result of much work and support. Throughout the years of my doctorate, I was fortunate for having received lots of help from people who taught me something, gave me suggestions and advice, or opened their laboratories to me, and of course, people who are also friends and who made this journey easier. I hope I have not missed anyone here. As of now, thanks so much to you all.

Firstly, I want to thank God and my family (my parents Cicero and Ivanilda, and my sister Soraia) for the immeasurable support. The certainty I have of you being there is by itself a comfort. I was always encouraged that education is a powerful tool, and no one can take it from me.

My academic path would have been neither enjoyable nor successful if I did not have an advisor who is not just a scientific example, but also a friend. So, special thanks to Professor Dr Sonia Tatumi, whom I have known for more than eight years now, and who has an experience that she is always willing to pass on. Thank you for your endless patience, the wise advice, the incentive by saying "*vai dar certo!*" when I might have thought something would not work, and for pushing me forward to get the best.

Vielen Dank Dr Clemens Woda, for kindly hosting me at the Institute of Radiation Medicine of the Helmholtz Zentrum München for one year. Your expertise enriched this work. An extended acknowledgement to the other researchers of the group in Munich, Dr Markus, Dr Janine, and Dr Kaiser. Moreover, a special thanks to Alessia Mafodda and Elif Kara, for their friendship.

Thanks to Laurence Taylor, my partner, for your company and confidence in me, even in the harsh moments. Your support motivates me to seek the best.

To the people from the laboratory of dosimetry and dating (LDD) of the Federal University of São Paulo (UNIFESP), where I started to understand what it means to do research. Thanks to the professors Dr Marcio Yee, Dr Nilo Cano, Dr Juan Mittani and Dr Naghabushana. Further thanks to Dr René Rocca, for his patience in explaining and showing me the field of luminescence (beyond calculus). And to my friends and colleagues, Isadora (whom I was lucky for sharing part of my stay in Germany), Noemi Silva (always full of kindness and willingness to help), Diego Tudela, Joice Guilheiro, Ana Lícia, Meire Ogussuko, Vanessa Silva, Caroline Fernandes, and Carlos Salgueirosa.

This work was only possible due to collaborations with other laboratories. Therefore, thanks to Dr Lilia Courrol from the Institute of Environmental, Chemical and Pharmaceutical Sciences of UNIFESP (Campus Diadema), Dr Ana Regina Blak from the Institute of Physics of the University of São Paulo (USP), and Dr Regina Spadari from the Institute of Health and Society of UNIFESP (Campus Baixada Santista).

Thanks to my friends, Esther Cecília and Vitória Tassara, who like me, decided to follow in the sciences. Our conversations not only about academic life (not at all), helped me to feel at ease.

Special thanks for the funding given by the São Paulo Research Foundation, with grant #2019/20121-3, São Paulo Research Foundation (FAPESP) and grant #2020/15562-8. It allowed for the development of this study, and the one-year research period in Germany as well.

This study was financed in part by the Coordenação de Aperfeiçoamento de Pessoal de Nível Superior - Brasil (CAPES) - Finance Code 001.

“Crystals are like people: it is the defects in them which tend to make them interesting”.

C. J. Humphreys

Abstract

SOARES, A. F. **Luminescence on HfO_2 crystals:** synthesis, heat treatment effect, related defects, and their application in ionising radiation dosimetry. 2023. Tese (Doutorado em Engenharia Elétrica) – Escola Politécnica, Universidade de São Paulo, São Paulo, 2023.

As a consequence of using radiation, measurements of control and protection were established to avoid human beings and the environment from its harmful effects. In this instance, different kinds of materials are used to measure radiation doses, as is the case of dosimeters. Luminescent dosimeters based on thermoluminescence (TL) and optically stimulated luminescence (OSL) have been investigated since the middle of the 19th century, and nowadays, commercial detectors are available. Those techniques effectively allow for studying materials' properties, shedding light on the emission features and underlying mechanisms, and in the characterisation of them. In this regard, hafnium oxide (HfO_2), which has recently been widely studied in electronics, has poorly been studied regarding its luminescence, with few reports on its TL. Therefore, this study aimed to do a more in-depth investigation of the luminescence features of HfO_2, the influence of heat treatment on them, as well as the potential application of it as an ionising radiation dosimeter. For that, samples were synthesised by using the precipitation method followed by different heat treatments at 1000, 1200, 1400 and 1600 °C for 2 hours. Crystalline structure was evaluated by X-ray diffraction (XRD), whilst luminescent was approached by analysing the fluorescence, TL, and OSL emissions. Moreover, electron spin resonance (ESR) was carried out to understand the defects that play a role in those phenomena. Results demonstrated that the HfO_2 nanocrystals were successfully produced in a monoclinic arrangement, with crystallite sizes up to 41 nm which increased with the heat treatment temperature. The TL glow curves are composed of several peaks, indicating the presence of different levels of electron traps, with the most prominent peak at about 130 °C. T_M-T_{stop} and deconvolution analyses demonstrated that the peaks have activation energies of up to 1.6 eV, and that heat treatment at higher temperatures led to the improvement of the TL intensity and benefited the creation of deep traps. Similarly, the OSL signal was intensified by the heat treatment, showing the presence of two components in the continuous-wave (CW) mode and two peaks in the linear-modulated (LM) one, when using blue stimulation. Spectral measurements indicated that the material has a bright emission band in the blue region that can vary from 2.44 to 2.71 eV, depending on the technique. This characteristic blueish emission is mainly associated with oxygen vacancies of V^+ type, which was enhanced by the heat treatment and attested by the ESR signal (estimated g values of 1.898, 1.957 and 1.985). The mechanism in which the OSL takes place might be related to a non-linear optics process of two or three-photon absorption. The sample calcined at 1600 °C had the best luminescent response and the evaluation of its infrared-stimulated luminescence (IRSL) dosimetric properties confirmed the potential use as a radiation detector due to the good reproducibility (variation lower than 3 %), intense signal, and linear dose-response. Furthermore, to the best of the author's knowledge, this is the first report of IRSL for the material, as well as of the correlation of its luminescence to the ESR centres.

Keywords: Electron Spin Resonance. Hafnia. Infrared-Stimulated Luminescence. Non-linear Optics. Thermoluminescence.

Resumo

SOARES, A. F. **Luminescência em cristais de HfO_2:** síntese, efeito do tratamento térmico, defeitos relacionados, e sua aplicação em dosimetria de radiação ionizante. 2023. Tese (Doutorado em Engenharia Elétrica) – Escola Politécnica, Universidade de São Paulo, São Paulo, 2023.

Como uma consequência do uso da radiação, medidas de controle e proteção foram estabelecidas para evitar que humanos e o ambiente sofram com seus efeitos danosos. Nesse sentido, diferentes tipos de materiais são usados para mensurar doses de radiação, como é o caso dos dosímetros. Dosímetros luminescentes baseados em termoluminescência (TL) e luminescência opticamente estimulada (LOE) têm sido investigados desde a metade do século 19, e atualmente, detectores comerciais estão disponíveis. Essas técnicas permitem-nos efetivamente estudar propriedades de materiais, elucidando as características da emissão e os mecanismos relacionados, e fazendo parte na caracterização. Nesse escopo, o óxido de háfnio (HfO_2), que tem sido amplamente estudado em eletrônica, tem sido pouco estudado quanto à sua luminescência, com poucos relatos de sua emissão TL. Portanto, este estudo objetivou fazer uma investigação mais detalhada das características luminescentes do HfO_2, a influência do tratamento térmico, bem como o potencial de aplicação como um dosímetro de radiação ionizante. Para isso, amostras foram sintetizadas pelo método de precipitação seguido por diferentes tratamentos térmicos em 1000, 1200, 1400 e 1600 °C por 2 horas. A estrutura cristalina foi avaliada por difração de raio-X, enquanto a luminescência foi analisada pelas emissões fluorescente, TL e LOE. Além disso, ressonância de spin eletrônico (RSE) foi realizada para identificar quais defeitos pontuais cumprem papel nesses fenômenos. Resultados demonstraram que os nanocristais de HfO_2 foram produzidos com sucesso em fase monoclínica, com tamanhos de cristalito de até 41 nm os quais cresceram com a temperatura do tratamento térmico. As curvas TL são compostas de diversos picos, indicando a presença de diferentes armadilhas de elétrons, sendo o mais proeminente em aproximadamente 130 °C. Análises T_M-T_{stop} e deconvolução demonstraram que os picos têm energia de ativação de até 1,6 eV, que o tratamento térmico levou a uma melhor intensidade TL e beneficiou a criação de armadilhas profundas. Similarmente, o sinal LOE foi intensificado pelo tratamento térmico, tendo duas componentes quando usado estimulação contínua e dois picos para estimulação linearmente modulada, quando usada estimulação no azul. Medidas espectrais indicaram que o material tem uma intensa banda de emissão na região do azul que pode variar de 2,44 até 2,71 eV, dependendo da técnica. Essa característica emissão no azul é principalmente associada com vacâncias de oxigênio do tipo V^+, a qual foi aumentada devido ao tratamento térmico e atestada pelo sinal RSE (valores de g de 1,898, 1,957 e 1,985). O mecanismo no qual a LOE ocorre poderia estar relaciono com um processo de óptica não linear de absorção de dois ou três fótons. A amostra calcinada em 1600 °C teve a melhor resposta luminescente e a avaliação das suas propriedades dosimétricas para LOE com estimulação no infravermelho confirmaram o potencial de uso como um detector de radiações, devido a boa reprodutibilidade (variação menor que 3 %), sinal intenso e resposta linear à dose. Adicionalmente, para o melhor do conhecimento do autor, este é a primeira descrição de LOE com estímulo infravermelho para o material, assim como a correlação entre sua luminescência com os centros RSE.

Palavras-chave: Hafnia. Luminescência Opticamente Estimulada com Infravermelho. Óptica não linear. Ressonância de Spin Eletrônico. Termoluminescência.

List of Figures

List of Tables

List of Acronyms

ALD	Atomic Layer Deposition
BSL	Blue-Light Stimulated Luminescence
Cema	Converted energy per unit of mass
CB	Conduction Band
CCD	Charge-Coupled Device
CGCD	Computerised Glow Curve Deconvolution
CV	Coefficient of Variation
CW-OSL	Continuous-Wave Optically Stimulated Luminescence
DFT	Density Functional Theory
EDS	Electron Dispersive Spectroscopy
EMCCD	Electron Multiplying Charge-Coupled Device
EPR	Electron Paramagnetic Resonance
ESR	Electron Spin Resonance
FB	Forbidden Band
FOM	Figure of Merit
GOK	General-Order Kinetic
GSL	Green-Light Stimulated Luminescence
ICCD	International Centre for Diffraction Data
ICRP	International Commission on Radiological Protection
ICRU	International Commission on Radiation Units and Measurements
IE	Ionisation Energy
IMTS	Multi-Trap System
IP	Ionisation Potential
IR	Infrared
IRSL	Infrared-Stimulated Luminescence
Kerma	Kinetic energy released per unit of mass
LED	Light Emitting Diode
LET	Linear Energy Transfer
LM-OSL	Linear-Modulated Optically Stimulated Luminescence
MD	Minimum Detectable Dose
MOCVD	Metal-Organic Chemical Vapor Deposition
MOK	Mixed Order Kinetic
OSL	Optically Stimulated Luminescence
OTOR	One Trap One Recombination Centre
PET	Positron Emission Tomography
PL	Photoluminescence
PMT	Photomultiplier Tube
POSL	Pulsed-Optically Stimulated Luminescence
QS	Quasi-equilibrium
RF	Radiofluorescence
RPL	Radiophotoluminescence
RT	Room Temperature
SEM	Scanning Electron Microscopy
TA-OSL	Thermal-Assisted Optically Stimulated Luminescence
TL	Thermoluminescence
TLT	Tunnelling Localised Transitions
UV	Ultraviolet
VSL	Violet-Stimulated Luminescence

VB	Valence Band
XRD	X-ray Diffraction

List of Symbols

LiF	Lithium fluoride
Z_{eff}	Effective atomic number
BeO	Beryllium oxide
Al_2O_3	Aluminium oxide or alumina
CaF_2	Calcium fluoride
ZnO	Zinc oxide
HfO_2	Hafnium oxide
SiO_2	Silicon oxide
β	Beta particles irradiation; energy state in ESR
T_M-T_{stop}	Method for analysing thermoluminescence glow curves
g	Spectroscopic factor or g factor
eV	Electron Volt
nm	Nanometre
α	Alpha particles irradiation; energy state in ESR
He	Helium
A	Atomic mass; activity (in radioactivity); probability of retrapping in the GOK model for OSL; atom or plan in the X-ray diffraction scheme; intermediate level in PL process; atom; area below the curve in the FOM equation
Z	Atomic number
P	Parent nucleus
D	Daughter nucleus
MeV	Mega electron volts
μm	Micrometre
β^-	Beta minus decay
e^-	Electron
υ^*	Antineutrino
^{60}Co	Cobalt-60 isotope
$\tau_{1/2}$	Half-life
^{60}Ni*	Nickel-60 in an excited state
β^+	Beta plus decay
O	Oxygen
e^+	Positron
υ	Neutrino; frequency
^{18}Fe	Iron-18
γ	Gamma radiation; stimulation intensity increase
N	Mean number of transformations in the radionuclide
t	Time
Bq	Becquerel, a unit for activity in s^{-1}
Ci	Curie, a unit for activity. $1\ \text{Ci} = 3.7 \times 10^{10}$ Bq
^{226}Ra	Radium-226 isotope
λ	Decay constant; wavelength
K	Kerma, the quantity of ionising uncharged particles, in J/kg; level in the electronic distribution; Kelvin, a unit of temperature; Potassium
dE_{tr}	Initial energy of all charged particles
m	Mass; concentration of trapped holes (recombination centres); constant factor in the Z_{eff} equation
J	Joule, energy unit

kg	Kilogram
Gy	Gray, dosimetric quantity, in J/kg
$\dot{K}$	Kerma rate, in J.kg^{-1}.s^{-1} or Gy.s^{-1}
C	Cema, the quantity of ionising charged particles, in J/kg; constant in the OSL model
dE_{el}	Energy lost through electronic interactions
$\dot{C}$	Cema rate, in J.kg^{-1}.s^{-1} or Gy.s^{-1}
ε_i	Energy deposited in a medium due to radiation, in J
ε_{in}	Energy of the incident ionising radiation, in J
ε_{out}	Sum of energies from charged and uncharged ionising particles leaving an interaction, in J
Q	Change in the rest energy of the nucleus, in J; quality factor dependent on the radiation type and energy; distance in the X-ray diffraction scheme
ε	Energy imparted, is the sum of all energy deposited in a volume, in J or eV
D	Absorbed dose, in Gy or J/kg
$d\bar{\varepsilon}$	Average energy imparted, in J
rad	Former unit for absorbed dose, 100 rad = 1 Gy; unit radian
H	Dose equivalent, in J/kg or Sv
Sv	Sievert, unit for dose equivalent
keV	Kilo electron volts
w_R	Radiation weighting factor
H_T	Equivalent dose
$D_{T,R}$	Absorbed dose in a tissue or organ T
T	Tissue; temperature; unit Tesla
R	Radiation; ratio A/A_m; a distance in the X-ray diffraction scheme
E	Effective dose, in J/kg or Gy; energy
w_T	Tissue weighting factor
S/ρ	Mass stopping power
ρ	Density
l	Distance
L_Δ	Restricted linear electronic stopping power
b	Classical impact parameter; kinetic order in TL and OSL processes; unit cell parameter
r_a	Atomic radius
δ	Delta-ray
$h\nu$	Quantum energy; photon energy
h	Planck constant
E_B	Binding energy of an electron
θ	Scattering angle
E_k	Energy of the recoil electron
ϕ	Scattering angle in the Compton effect
E_{e-}	Kinetic energy of the photoelectron
L	Level in the electronic distribution
M	Level in the electronic distribution; metastable level in PL process; distance in the X-ray diffraction scheme; molar concentration
N	Level in the electronic distribution; concentration of electron traps in TL and OSL processes; ground level in PL process; distance in the X-ray diffraction scheme

c	Speed of the light; unit cell parameter
m_e	Mass of the electron
$E_{k(e^+)}$	Energy of the positron
$E_{k(e^-)}$	Energy of the electron in the pair production process
$E_{k(e^-_{orb})}$	Energy of the recoiling atomic electron in the pair production process
E_N	Energy of the ejected nucleon
E_{NB}	Nucleon's binding energy
n	Neutrons; concentration of trapped electrons
p	Protons; probability of release of an electron
V	Volt
NaI	Sodium iodide
Tl	Thallium
$\mathrm{CaF_2}$	Calcium Fluoride
Eu	Europium
CsI	Cesium iodide
Na	Sodium
$N(E)$	Density of occupied energy levels
$Z(E)$	Density of available energy states
$f(E)$	Fermi-Dirac distribution function
E_f	Energy at the Fermi level
k	Boltzmann constant; form factor
E_g	Energy of the gap
E_c	Energy at the bottom of the conduction band
E_v	Energy at the top of the valence band
T_R	Electron trap
R_C	Recombination centre
E_{TR}	Energy referred to a certain trap level
s	Attempt-to-escape factor, escape probability factor or frequency factor
T_I	Temperature during irradiation
I_{TL}	Intensity of the thermoluminescence signal
n_c	Concentration of free electrons in the conduction band
A_m	Probability of recombination
A_n	Probability of retrapping
n_0	Initial concentration of trapped electrons
t_0	Initial time
β_{T}	Heating rate
$I_{TL\,max}$	Maximum intensity of the thermoluminescence signal
T_{max}	Maximum temperature
s'	Pre-exponential factor constant in terms of s/N
s''	Pre-exponential factor in terms of $\mathrm{cm}^{3(b-1)}.\mathrm{s}^{-1}$
f	Rate of the release of electrons in OSL processes
$I_{CW\text{-}OSL}$	Intensity of the CW-OSL signal
Φ	Photon flux
σ	Cross-sectional area; standard deviation
I_0	Initial intensity
τ	Decay constant in OSL processes
k_1	Constant in the OSL process
K_1	Constant in the OSL process (derived from k_1)
$\alpha\text{-}\mathrm{Al_2O_3:C}$	Carbon doped alumina type alpha
$\mathrm{YAlO_3:Mn^{2+}}$	Manganese doped yttrium orthoaluminate

$CaSO_4$	Calcium sulphate
Al_2O_3:C	Carbon doped alumina
U	Uranium
Th	Thorium
K-40	Potassium-40
a_i	Fraction of a chemical element i in the Z_{eff} equation
i	Chemical element in the Z_{eff} equation
E_{xc}, E_{xc}'	Excited level
B	Intermediate level in PL process; atom or plan in the X-ray diffraction scheme; intensity of the magnetic field; peak width at half height
N'	Level state in PL process
$\mathring{A}$	Unit Angstrom
$\lambda_{c.\ x\text{-}ray}$	Wavelength of the characteristic X-ray
W	Tungsten
Cr	Chromium
Mo	Molybdenum
K_α, K_β	Transition in the shells of the electron
d	Distance between planes; crystallite size
1, 1a, 2, 1', 1a', 2'	Directions in the X-ray diffraction scheme
XX', ZZ'	Wavefront
d_{hkl}	Distance between planes
hkl	Miller indices
a	Unit cell parameter
S, S_x, S_y, S_z	Spin vector and its components
$\boldsymbol{S}$	Spin quantum number
$\hbar$	Planck constant divided by 2π
π	Mathematical proportion
μ_B	Bohr magneton
$HfCl_4$	Hafnium tetrachloride
KOH	Potassium hydroxide
NaOH	Sodium hydroxide
$Hf(OH)_4$	Hafnium hydroxide
rpm	Rotations per minute
^{90}Sr	Strontium-90
^{90}Y	Yttrium-90
mCi	Millicurie
mm	Millimetre
N_2	Nitrogen
mW	Milliwatt
T_m	Peak temperature
Y_{Exp}	Experimental curve data
Y_{Fit}	Fitted curve data
$I_{LM\text{-}OSL}$	Intensity of the LM-OSL signal
I_m	Intensity of the peak in the LM-OSL
t_m	Time of the peak maximum in LM-OSL
λ_{exc}	Wavelength of excitation
λ_{emi}	Wavelength of emission
kHz	Kilohertz
mT	Millitesla

mA	Milliampere
^{137}Cs	Caesium-137 isotope
T_M	Maximum temperature of the TL peak
T_{stop}	Temperature of the preheat
I	Intensity in TL and OSL
I_{max}	Maximum intensity of the peak in LM-OSL (in CGCD)
τ_{max}	Lifetime in LM-OSL (in CGCD)
$V_{O3}^{+}, V_{O3}^{++}, V_{O4}^{+}, V_{O4}^{+2}$	Oxygen vacancies: single and double charged in three or four coordination
V^+	Oxygen vacancy
ZrO_2	Zircon Oxide
g_e	*g* factor for the free electron
cGy	Centigray
Tb	Terbium
at%	Atomic concentration
$HfO_2:Dy^{3+}$	Dysprosium doped hafnium oxide
mol%	Molar concentration
Ti	Titanium
Gd	Gadolinium
D_{MDD}	Detection threshold
$s_{\bar{E}}$	Standard deviation of the TL or OSL signal for an unirradiated sample
Al	Aliquot
$\bar{x}$	Standard deviation
E_{opt}	Optical excitation energy
E_{the}	Thermal activation energy
B_G	Background

Contents

Chapter 1

1 Introduction

Luminescence is the phenomenon of the emission of light by a material as a response to energy absorption due to incident radiation, which leads atoms and/or molecules to move to a higher energy state. In order to return to the ground state, the absorbed energy is released in the form of photons of light (Sunta, 2015). A material's luminescence is a property of interest for society as it is present in several processes in everyday life, from the common case of lighting to more specific cases such as medical imaging, forensic investigations, dosimetry, and optical dating.

A certain name is given to the phenomenon depending on the mechanism by which the luminescent material is excited. For example, the emission of light from a material due to photon excitation is called photoluminescence, or by its acronym, PL. Because luminescence might be associated with different excitation processes and the materials' properties themselves, studying the emission mechanisms allows us to better understand the characteristics of the material and how they are involved in the process. In addition, this response can be evaluated and used for targeted applications.

Among the different luminescence phenomena, some of them are directly related to ionising radiation, as are the cases of thermoluminescence (TL) and optically stimulated luminescence (OSL). The incidence of ionising radiation in a material may produce pairs of electron-holes and induce the formation of metastable levels. Once this exposed material is stimulated with heat (in the case of TL) or light (for OSL), the rearrangement of charges may result in the emission of light (Bos, 2007; McKeever, 1985; Yukihara; McKeever, 2011). The TL and OSL emissions depend on the ionising radiation, however, the way in which the response takes place, and its features, say about the material's structure itself, as the type of defects which play the role of charge traps, for example. Therefore, the study of those phenomena is an important tool for deepening investigations into materials and might be applied for purposes of radiation detection.

As these mentioned processes of light emission are related to ionising radiation, it is straightforward to consider using them for detecting radiation, and not only detecting but also quantifying. It is possible to estimate an absorbed radiation dose because the signal obtained could be proportional to it. And how is that advantageous? Or even in a more primary point, what is the importance of that? Radiation is everywhere around us, due to cosmic rays, nuclear power plants, radioactive minerals, radioactive sources in hospitals and research institutes, or due to nuclear accidents. And the interaction of radiation with matter, and hence, with individuals, may have potentially harmful effects.

Concerns about radiation and its impacts arose after the studies which started throughout the final years of the 19th century, and the subsequent investigations, led to rapid developments in the field including: the discovery of X-rays by Röntgen in 1895 after his experience using Crooke's tube together with photographic plates and luminescent phosphors; the discovery of radioactivity in 1896 by Becquerel and further refinement by Marie S. Curie and her husband afterwards; and a basic radiation law brought by Planck in 1900 (Martin, 2006; Rühm *et al.*, 2020).

Because radiation became widely used, principles of radiation protection needed to be established to ensure that general people (public exposure), workers (occupational exposure), and exposed due to medical means were at safe levels. Although medical exposure accounts for most of the radiation exposure received by individuals (Bailey *et al.*, 2014), radiation due to natural sources (environmental) and accidents/disasters are also considered as they might unfold in the release of radioactive contaminants and radiation exposure. The nuclear accident involving the Fukushima Daiichi Nuclear Power Plant in 2011, caused by an earthquake followed by a tsunami, is an example of an emergency in which radiation doses needed to be assessed. Even years after the incident, studies have been performed for elucidating its consequences (Shuryak, 2023), as well as improvements in the measures of prevention and control adopted by different countries (Kong *et al.*, 2022).

How has luminescence and more specifically TL and OSL luminescent materials been applied in the scope of radiation protection? What types of material have been used for dosimetry? As regards ionising radiation, those luminescent materials, or phosphors, have been successfully studied and hence used as dosimeters. This application was pointed out already in the 1950s, when Daniels, Boyd and Saunders (1953), reported in their study the use of TL as a research tool, including for dosimetry.

Nowadays, decades after that first report, several different materials and their respective doped versions are used for TL and OSL dosimetry. For example, one might cite the doped lithium fluoride (LiF) variations depending on the doping element, which is well-known for having an effective atomic number (Z_{eff}) close to human tissue, and is therefore, interesting for personal dosimetry, as is also the case of beryllium oxide (BeO) and the lithium and magnesium borates. Despite the slightly higher values of Z_{eff} of alumina (Al_2O_3) and calcium fluoride (CaF_2) or sulphate-based materials, they are also widely used due to their sensitivity and linear dose-response to radiation (Sinclair; Pech-Canul, 2022; Yukihara *et al.*, 2022a).

Although these materials have long been used, it does not mean that their luminescence emission mechanisms are totally understood. Recent studies have been dedicated to deepening this knowledge. A good example is the case of BeO, in which the defects, dose-response and transfer of charges mechanisms are the focus of recent reports (Altunal; Guckan; Yegingil, 2023; Kara; Woda, 2023; Polymeris *et al.*, 2021; Yukihara, 2020).

Moreover, TL and OSL are powerful techniques for analysing materials beyond their application in dosimetry, hence, it has stimulated research in new materials, as well as a more in-depth comprehension of the underlying mechanisms. Just for a matter of exemplification, one might cite that the potential application of zinc oxide (ZnO) as a dosimeter has been reported (Cañes-Morales *et al.*, 2023; Soares *et al.*, 2017), as is also the case for strontium aluminate-based materials (Tatumi *et al.*, 2019; Zúñiga-Rivera *et al.*, 2014). Finally, investigations combining both microstructural and luminescence characterisation have been successfully reported for different materials, as is the case of magnesium aluminate and borates (Ozdemir *et al.*, 2021; Pan *et al.*, 2021).

In the scope of investigations on the luminescent properties of materials, studies regarding hafnium oxide (HfO_2), also named hafnia, are still unravelling the potential use of this material due to its luminescence. HfO_2-based materials have been used more intensively in the electronics area since the 2000s, arising as an important further step into the new generation of nano-electronics. A milestone moment being when it replaced silicon oxide (SiO_2) in a commercial device for the first time in 2007 (Gritsenko; Perevalov; Islamov, 2016; Matthews, 2008). This interest is due to the HfO_2 properties such as its high permittivity value, its large band gap, and thermal and chemical stabilities (Choi; Mao; Chang, 2011), as well as its ferroelectricity (Müller *et al.*, 2015). In the case of flash memory domain, for example, HfO_x-based matrixes have been used in different conformations, such as gate oxide and charge trapping layers (Banerjee; Kashir; Kamba, 2022).

The potential value of HfO_2 in microelectronics is already remarkable. However, its application in luminescence is still behind. Studies have demonstrated the potential for using it as a light-emitting diode (LED) phosphor (Ćirić; Stojadinović; Dramićanin, 2019) and in other optoelectronic devices (Manikantan *et al.*, 2017). When restricting to studies regarding TL and OSL emissions of HfO_2, and their use for radiation detection, the reports are much scarcer, but not discouraging at all. The material has shown to have a TL response when irradiated with ultraviolet (UV) radiation (Mendoza *et al.*, 2010; Pejaković, 2010), and gamma rays as well (Sekar *et al.*, 2020). Doped HfO_2 has been also investigated for those purposes (Fiaczyk *et al.*, 2016; Montes *et al.*, 2014). Furthermore, the presence of this material more often in different electronic devices may lead to an increase interest in its use for accidental dosimetry.

Not only are the luminescence findings of HfO_2 still not well explored, but also the defects and their relationship to luminescence, which have been the focus of investigations and discussions. However, many mechanisms to them related remain still unclear (Laganovska *et al.*, 2023; Wright; Barklie, 2009). These gaps in knowledge once filled might allow for a better comprehension of the underlying processes so far not known, and hence, their control, better tailoring of the material's properties, and advance on the application of it in areas that are not electronics. All of it justifies raising efforts on investigating HfO_2 luminescence.

Chapter 2

2 Thesis Overview and Objectives

This chapter gives information on the justification of this work, detailing the main and the specific objectives (which cover from the synthesis of the sample until the preliminary results of pulsed-OSL (POSL) measurements). It also explains how the thesis is structured.

2.1 Justification

There is still a lack of studies regarding the luminescence of HfO_2 and the role of the defects in the luminescence mechanisms is not well understood. In addition, the few reports that do exist have indicated a potential application in the area of radiation detection and that the conditions of synthesis and post-treatments of the material likely alter the properties. Therefore, it constitutes a gap of knowledge not addressed.

2.2 Objectives

Therefore, based on this justification, this work has as main objectives the synthesis of powder samples of HfO_2 by the precipitation method, the evaluation of their structural and luminescent properties and the influence of heat treatment on them. In addition, based on the luminescent response, the investigation of using the material in ionising radiation dosimetry.

2.2.1 Specific Objectives

To reach the main objectives, this work has a set of specific objectives, which can be grouped according to the general aim.

a) Synthesis and Structural Analysis

Samples of HfO_2 are synthesised using the precipitation method, followed by different heat treatment (or calcination) temperatures at 1000, 1200, 1400 and 1600 °C, to evaluate its effects on the properties of interest. The type of crystalline arrangement obtained is investigated by means of X-ray diffraction (XRD) measurements, as well as the crystallite size by using the Scherrer equation.

b) Luminescent Properties and the Influence of Heat Treatment

Evaluate the luminescent properties using different techniques, such as fluorescence, TL and OSL, always looking to analyse the heat treatment influence on them. Moreover, the selection of the best sample in terms of luminescent response to further analyses in dosimetry application.

Fluorescence measurements will give information regarding the emission and excitation spectra, indicating the main bands of absorption and emission, which are estimated by Gaussian fittings. The emission in the visible range is evaluated by plotting the Chromaticity Diagram.

The TL response will be evaluated regarding its dose-response curve for beta (β) irradiation over a wide range from low doses (< 2 Gy) up to doses of about 30 Gy. This curve is analysed to see whether it has a linear trend. The shape of the TL glow curve, that is, the number of peaks, their positions and the traps' (or kinetic) parameters are evaluated using two methods, T_M-T_{stop} and computerised deconvolution.

OSL signal is investigated by its dose-response curve using continuous-wave (CW) and linear-modulated (LM) modes, in which the linearity degree over a range of β irradiation doses is analysed. The number of components or peaks, for CW and LM modes, respectively, and their respective trapping parameters are studied by deconvolution using a general-order kinetic model. In addition, the signal dependence on the temperature is evaluated, to better understand the charge carriers' mechanisms.

The recombination centres are studied by spectral measurements for TL and OSL, as well as radiofluorescence. Spectral curves are fitted by using Gaussians, giving information on the main emission bands. The radiofluorescence spectrum is analysed for different readout temperatures to verify the presence or not of thermal quenching.

c) Defects in HfO_2

The possible paramagnetic defects existent in the samples are evaluated using electron spin resonance (ESR) by estimating the *g* value. The signal dependence on the heat treatment is studied to analyse likely changes in the defects. Moreover, the response is studied as a function of the irradiation dose and thermal bleaching.

d) Dosimetric Application

The sample with the best luminescent response is evaluated regarding its dosimetric properties of thermal stability, components of the curve, dose-response behaviour, lower limit of detection, reproducibility, repeatability, energy response, and unintentional decay (fading). Bleaching measurements are used to start understanding the correlation between the TL and OSL signals.

e) Relaxation Time in OSL Measurements

Measurements of POSL are used in order to define better parameters for recording the signal, and the fitting of the curves with exponential functions to determine the decay time (relaxation time) of the components in the POSL emission.

2.3 Thesis Structure

The thesis is structured in 7 chapters, in the following order: Introduction, Overview and Thesis Objectives, Literature Review, Methodology, Results and Discussion, Conclusions and Outlook. The first two chapters are dedicated to a brief overview of the scope of this work, giving details of the gaps of knowledge that are addressed, and how it is addressed by the objectives proposed.

Chapter 3 has a state-of-the-art review of the main topics covered by the work, which includes concepts in radiation physics, luminescence phenomena theory, techniques for material characterisation and hafnia properties. Chapter 4 deals with the methodology used to reach the objectives (process of synthesis of the samples, luminescence measurements protocols and equipment, characterisation methods and radiation sources used).

Results and discussion are approached in Chapter 5, which is subdivided in 5 parts. The first section (5.1) is dedicated to present the results obtained with the synthesis. Section 5.2 is more extensive and shows how the heat treatment influences the crystallite size and the luminescence properties (covering aspects of TL and OSL signal and spectral measurements, as well as correlations between theoretical models and experimental results). Sections 5.3 and 5.4

discuss the role of defects in the hafnia's luminescence and the investigations on the application as a radiation detector. The final section of the chapter (5.5) has the preliminary results of POSL.

Chapter 6 compiled the results of the work by the main conclusions obtained, and Chapter 7 is an outlook of the thesis, also giving suggestions of further studies that might be of interest.

Chapter 3

3 Literature Review

Chapter 3 is dedicated to the literature review of the subjects related to this thesis and is divided into four parts. The first part deals with radiation concepts, quantities, detectors, and interaction with matter. The second and third parts give information about luminescent processes, which are the aim of this study, and the techniques of characterisation used. Finally, the fourth subsection discusses the material that is the focus of the study.

3.1 Radiation Physics: Some Concepts

From the middle of the 19th century and over a period of a few decades, several concepts of atomic and nuclear physics were developed, which together constitute a wider field known as radiation physics. Physical laws were established, covering from electromagnetism described by Maxwell's equations, to the first and second laws of thermodynamics. During a period of twenty years, X-rays were first reported by Wilhelm C. Röntgen, Becquerel reported the discovery of radioactivity, Thomson stated the existence of the electron, Planck's radiation law was described, Einstein established his relativity theory, and alpha scattering experiments were carried out by Rutherford (Martin, 2006).

Those studies opened the door to a wider understanding of the matter and laws that rule the phenomena related to them. The comprehension of the atom's structure, its substructures and its energy states, the quantum emission of radiation and the processes made of a combination of them, required efforts in investigating and setting in place what was then an unknown field. Thereafter, an entire branch of physics was defined, dedicated to radiation science.

What is the nature of radiation? How does it affect humankind and the environment? How is it detected? How does one use it in their favour? Many questions like those moved several researchers and institutions in an attempt to elucidate the phenomena, allowing us to have a consolidated theoretical baseline.

This section aims to give sight of the main definitions of radiation, the quantities and units which have been used, a brief description of the interaction between radiation and matter, and how one might detect it, since an application of the material studied in this thesis is as an ionising radiation detector.

As above-mentioned, radiation physics covers a wide field of study. A reader seeking more detailed information is encouraged to start their search in the references presented here.

3.1.1 Radiation

Radiation is defined as the transport of energy by either electromagnetic waves or atomic particles, which are produced due to internal changes in the nucleus or at the electronic shell level, or as a result of the interaction of radiation or charged particles with the atom's structure (Bailey *et al.*, 2014). The ability of radiation to ionise matter classifies radiation into two main groups (Podgoršak, 2016):

- Non-ionising radiation: covers all the electromagnetic radiation types which do not carry enough energy per quantum to ionise atoms or molecules. The group includes radio and microwaves, infrared photons, and visible and near UV light.
- Ionising radiation: in this case, the quantum energy is enough to ionise atoms or molecules of the absorber in a direct or indirect mechanism. Examples of ionising radiation are X and gamma rays, energetic neutrons, protons, electrons, and heavy charged particles.

The minimum energy needed to ionise an atom is called ionisation energy (IE) or ionisation potential (IP), usually given in terms of electron volts (eV). Values of the IE may range from a few electron volts (of about 4 eV) for alkali metals up to 24.6 eV, which is the IE to ionise helium (Podgoršak, 2016).

Ionising radiation can still be subcategorised into two groups, typically named directly or indirectly ionising radiation (Bailey *et al.*, 2014; Podgoršak, 2005):

- Directly ionising radiation is the energy from charged particles and heavy ions that is directly deposited in the medium through Coulomb interactions with the orbital electrons from the absorbers' atoms.
- Indirectly ionising radiation is constituted of a two-step process in which first un-charged (neutral) particles induce the releasing or production of charged particles in the medium. Second, at least part of the kinetic energy is deposited in the absorber due to Coulomb interactions in the same way as it occurs in the directly ionising process.

Despite ionising radiation being classified into those two groups as mentioned, both of them can pass through human tissue. Consequently, it has been extensively used in medicine for both diagnosis and disease treatments. The use of ionising radiation in treating diseases is usually referred to as radiotherapy or radiation oncology, whilst the use in diagnosis is referred diagnostic radiology-based and nuclear medicine.

However, the use of ionising radiation is not restricted only to medicine. It has been applied for controlling insect pests (as insects can be made sterile due to exposure to high irradiation doses); for food processes (in order to extend the shelf life period, as it kills microorganisms such as bacteria, viruses and mould, it also slows the ripening process and reduces germination); in nuclear reactors to do research, produce radionuclides and electric power production; for waste management, such as sterilising hospital waste; for chemical processes (as is the case of polymers modification due to irradiation); among others (Podgoršak, 2016).

Figure 3.1 shows a spectrum for non-ionising and ionising radiation. As can be seen, the latter represents only a part of the electromagnetic spectrum, beginning with wavelengths shorter than the visible range (Kim *et al*., 2019).

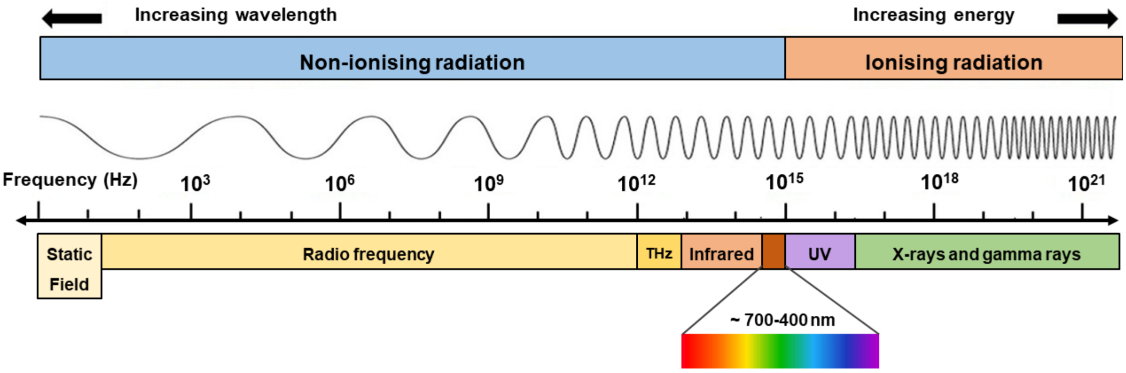

Figure 3.1 - Schematic illustration of the spectrum of electromagnetic field, and the classification into ionising and non-ionising radiation. Based on Kim *et al*. (2019).

The longer the wavelength the lower the frequency, meaning less energetic radiation. The interface between ionising and non-ionising radiation is given in the UV range (wavelengths from 300 up to 400 nm, approximately), in which the energy may already be enough to ionise atoms or molecules.

Despite UV radiation being in the boundary region, it plays an important role and can be found naturally due to sunlight, or from artificial artefacts. Hence, special attention has been given to its effects on human beings, since it is already known to increase the risk of developing certain kinds of cancer (Gallagher; Lee, 2006). Nevertheless, when it is used in a controlled manner, such as phototherapy, it has been shown to be an important tool in treating skin diseases (Ataş *et al.*, 2015). More recently, due to the coronavirus disease (COVID-19), studies focused on investigating the use of UV radiation as a method to inactivate virus replication (Biasin *et al.*, 2021).

3.1.1.1 Nuclear Radiation

Among the different sorts of ionising radiation, nuclear radiation covers the energy which is released in the form of particles or electromagnetic waves, due to internal rearrangements in the nucleus in order to reach a stable state. Because in the atomic nucleus there are strong bonding forces, nuclear radiation is quite energetic in comparison with the ones with electronic levels origin. Here there is a brief description of nuclear radiation types based on the works of Ahmed (2007), Bailey *et al.* (2014) and Obodovskiy (2019):

a) Alpha Decay or Alpha Radiation

When an atom has a high number of protons and neutrons, that is, a heavy nucleus, it makes the repulsion energy of the protons increase and the nucleus becomes unstable. Hence, the repulsion energy may be stronger than the attraction one, and there will be the release of particles to stabilise. This decay is known as alpha (α) decay, and it can be described by the nucleus emission of a helium (He) nucleus, that is, 2 protons and 2 neutrons:

$${}^{A}_{Z}P \rightarrow {}^{A-4}_{Z-2}D + {}^{4}_{2}He^{2+} = {}^{A-4}_{Z-2}D + \alpha$$

Where A is the atomic mass, Z is the atomic number, P is the parent nucleus, and D is the more stable daughter nucleus.

Alpha decay is a property observed in heavy atoms with a Z value higher than 82 and A higher than 200. Alpha particles have kinetic energies that can vary from 4 up to 9 MeV.

Alpha particles have a high mass and electric charge (+2), however, do not have a deep penetration power in human tissue (usually up to 100 μm). Despite the low penetration depth, those particles may strongly interact with other atoms in the medium due to their positive charges, they are abundantly emitted by natural radioisotopes and have been used in applications such as particle accelerators.

b) Beta Decay or Beta Radiation

The change in the nucleus' atomic number whilst keeping the same *A*, plus the emission of a positron or electron, or a capture of an electron, is known as beta (β) decay. This process is more common in nuclei of low or intermediate mass. A neutrino or antineutrino is also emitted as a result of the decay.

Beta decay is commonly classified into two types: beta minus (β^-) and beta plus (β^+) decay. β^- decay occurs when a parent nucleus *P* rich with neutrons transforms a neutron in a proton, accompanied by the ejection of an electron e^- and an antineutrino v^*:

$$ {}_{Z}^{A}P \rightarrow {}_{Z+1}^{\;\;A}D + e^- + \nu^* $$

A common example of β^- decay is ^{60}Co which has a half-life $\tau_{1/2}$ of about 5.26 years, when it transforms into an excited state of nickel, ^{60}Ni*:

$$ {}_{27}^{60}Co \rightarrow \xrightarrow[\tau_{1/2}\,=\,5.26\text{ years}]{} {}_{28}^{60}Ni^* + e^- + \nu^* $$

β^+ decay occurs when a parent nucleus *P* rich with protons transforms a proton into a neutron, accompanied by the emission of a positron e^+ and a neutrino v:

$$ {}_{Z}^{A}P \rightarrow {}_{Z-1}^{\;\;A}D + e^+ + \nu $$

An example of β^+ decay is in ^{18}F which is widely used in special imaging techniques, such as positron emission tomography (PET), where the targeted molecule is labelled with this specie, and has a $\tau_{1/2}$ of 110 minutes.

$$ {}_{9}^{18}F \rightarrow \xrightarrow[\tau_{1/2}\,=\,110\text{ minutes}]{} {}_{8}^{18}O + e^+ + \nu $$

c) Gamma Rays or Gamma Radiation

Gamma (γ) radiation is emitted as a result of the nucleus passing from an excited state to a ground state, which is usually associated with either alpha or beta decay, or another nuclear reaction. Since after an alpha or beta decay event, the daughter nucleus may be in an excited state, it is necessary to release the available excess energy, which can result in the emission of γ rays, X-rays, or Auger electrons.

An example of γ emission is after the β^- decay of ^{60}Co which results in the production of an excited Ni nucleus (${}_{28}^{60}$Ni*). This specie undergoes a transformation to reach the stable ${}_{28}^{60}$Ni by the emission of two γ photons, with energies values of 1.17 and 1.33 MeV.

Gamma radiation's emission has always a discrete energy spectrum, which is a valuable feature to use as a marker in a process. In addition, because it is not constituted of charged particles, γ radiation has a high power of penetration in human tissue.

3.1.1.2 Measuring Radiation: Some Quantities and Units

Ionising radiation can trigger several effects in human beings and the environment, consequently, it is of interest to quantify the radiation by using the radiation itself, or the effects and sub-products due to its interaction with matter.

There are two international commissions which work in the establishment of quantities and units in the radiation area. The International Commission on Radiation Units and Measurements (ICRU) founded in 1925 has as its main goal the development of international recommendations concerning quantities and units of radioactivity and radiation, procedures to measure those quantities, and the necessary physical data to apply the recommended procedures (ICRU, 2011). In addition, there is the International Commission on Radiological Protection (ICRP), which was founded in 1928, with similar scope.

The quantities of radiation may concern the measurement related to the radiation field, which includes for example, the activity of a radioactive material; the dosimetric quantities, which regard the effects of the interaction of radiation with a material (hence it is associated with the absorbed dose); the dosimetric quantities which are weighted according to the organ, for example; and the operational quantities which are used in practical applications, for example in monitoring situations regarding external exposure and radionuclides intake.

In this section there is a description of some of those quantities, based on publication numbers 60 (ICRP, 1991), 92 (ICRP, 2003) and 116 (ICRP, 2010) from the annals of ICRP, and in the ICRU report number 85 (2011). Here, the quantities described were sorted into radioactivity quantities, dosimetric ones and the interaction coefficient factors.

3.1.1.2.1 Radioactivity Quantities

Radioactivity covers the phenomena related to spontaneous transformations involving changes in the nucleus or the energy states of atoms. Energy from those transformations is released in radiation forms, such as nuclear particles and photons.

Nuclide is the term for a species of an atom with a specific number of protons and nucleons in its nucleus. Unstable nuclides are referred to as radionuclides, which may be a result of the transformations, that is, radioactivity (ICRU, 2011).

- Activity

Activity A is given by the mean number of changes of nuclei dN in an amount of radionuclide in a determined energy state, due to the spontaneous nuclear transformations per unit of time (ICRU, 2011), which can be described by Equation 3.1:

$$A = -\frac{dN}{dt} \tag{3.1}$$

Where N is the mean number of transformations in the radionuclide, and t is the time. The unit of A is s^{-1} and represents the total number of transformations per second. The special unit for activity is the Becquerel (Bq), which replaces the former unit of Curie (Ci), 1 Ci = 3.7 × 10^{10} Bq, which refers to the number of transformations per unit of time in 1 gram of ^{226}Ra.

- Decay Constant

The decay constant λ is described by the quotient dN/N per unit of time, due to spontaneous nuclear transformations (ICRU, 2011):

$$\lambda = \frac{\left(-\frac{dN}{N}\right)}{dt} \tag{3.2}$$

The unit of λ is s^{-1}.

Using the decay constant value, one can estimate the half-life of a radionuclide $\tau_{1/2}$, which is the mean time required for the radionuclide in a particulate energy state to decay to one half of its initial number:

$$\tau_{\frac{1}{2}} = \frac{\ln 2}{\lambda} \tag{3.3}$$

3.1.1.2.2 Dosimetric Quantities

Particle energies are converted and deposited into matter by different processes due to the interaction of radiation and matter. Therefore, dosimetric quantities describe those processes and are a product of the radiometry quantities and the interaction coefficients (ICRU, 2011).

- Kerma and Kerma Rate

The kerma K is a quantity for ionising uncharged particles, which is given by the quotient of the sum of the initial kinetic energies liberated from all charged particles dE_{tr} by an amount of mass dm due to uncharged particles incident in the material, that is (ICRP, 2010; ICRU, 2011):

$$K = \frac{dE_{tr}}{dm} \tag{3.4}$$

Kerma is given in terms of Joule per kilogram (J/kg), which has the special name Gray (Gy). Kerma is the acronym for kinetic energy released per unit mass.

And the kerma rate $\dot{K}$ is the quotient of K per unit of time:

$$\dot{K} = \frac{dK}{dt} \tag{3.5}$$

$\dot{K}$ is given in terms of Gy.s^{-1}.

- Cema and Cema Rate

The cema C is a quantity similar to kerma, but for ionising charged particles. It is given by the quotient of the average energy lost through electronic interactions dE_{el} in a dm by charged particles incident on the material, disregarding the secondary electrons (ICRU, 2011):

$$C = \frac{dE_{el}}{dm} \tag{3.6}$$

Cema is also given in terms of J/kg or Gy. It is the acronym for converted energy per unit of mass.

Similarly, the cema rate $\dot{C}$ is the quotient of C per unit of time:

$$\dot{C} = \frac{dC}{dt} \tag{3.7}$$

$\dot{C}$ is given in terms of J.kg^{-1}.s^{-1} or Gy.s^{-1}.

- Energy Deposit

Energy deposited ε_i is described by the energy deposited in the matter due to a single interaction i (ICRU, 2011):

$$\varepsilon_i = \varepsilon_{in} - \varepsilon_{out} + Q \tag{3.8}$$

Where ε_{in} is the energy of the incident ionising radiation (disregarding rest energy), ε_{out} is the sum of energies from charged and uncharged ionising particles that are leaving the interaction (also excluding the rest energy), and Q is the change in rest energy of the nucleus and is due to elementary particles present in the interaction. A $Q < 0$ means a decrease in rest energy.

The energy deposit is given in values of J. This quantity is stochastic.

- Energy Imparted

The sum of all energy deposited in a volume is called the energy imparted, or ε, which is the summation of all energy deposits (ICRU, 2011):

$$\varepsilon = \sum_i \varepsilon_i \tag{3.9}$$

The energy imparted is given in values of J and may also be expressed in eV. This quantity is also a stochastic one as the energy deposits in the summation can be related to one or more events of energy deposition.

- Absorbed Dose

The absorbed dose *D* is the average energy imparted *ε* due to the ionising radiation at a point of interest of a mass of matter dm, given by (ICRP, 1991; ICRU, 2011):

$$D = \frac{d\bar{\varepsilon}}{dm} \tag{3.10}$$

Where $d\bar{\varepsilon}$ is the average energy imparted at a point within dm. The unit for the absorbed dose is J/kg or Gy. The former unit of *D* was rad, and 100 rad = 1 Gy.

- Dose Equivalent

The dose equivalent *H* describes the absorbed dose at a point in the tissue, which is given by (ICRP, 2010):

$$H = DQ \tag{3.11}$$

Where *D* is the absorbed dose and *Q* is a quality factor. The unit for *H* is J/kg, specially named Sievert (Sv). For the avoidance of confusion, the term Gy is used for *D*, whilst the term Sv is applied in dose-equivalent quantities (ICRP, 2003). Because the probability of stochastic effects was found to have a dependence on the radiation quality, there was necessary to introduce a weighting factor to modify the *D* into *H* (ICRP, 1991). The quality factor *Q* is a dimensionless factor. Some values of *Q* are shown in Table 3.1.

Table 3.1 - Values of the quality factor Q, for different types of radiation.

Radiation type and energy range		**The quality factor, *Q***
Photons (all energies).		1
Electrons and muons (all energies, except Auger electrons emitted from nuclei bound to DNA).		1
Neutrons,	Energy < 10 keV	5
	For energy between 10-100 keV	10
	100 keV < energy < 2 MeV	20
	2 MeV < energy < 20 MeV	10
	Energy > 20 MeV	5
Protons, except recoil protons, and with energy > 2 MeV.		5
Alpha particles, heavy nuclei and fission fragments.		20

Reference: ICRP, 1991.

- Equivalent Dose

When it comes to radiological protection, the absorbed dose due to the ionising radiation needs to consider the radiation quality. For this purpose, the radiation weighting factor w_R is used, which shares similar values as Q, and the dose is termed equivalent dose H_T (ICRP, 1991):

$$H_T = \sum_R w_R . D_{T,R} \tag{3.12}$$

Where $D_{T,R}$ is the average absorbed dose in a tissue or organ T, due to the radiation R. The unit for dose equivalent is J/kg, or Sv.

- Effective Dose

The effective dose E is the sum of all equivalent doses weighted by the specified tissue or organ of the body, and is given by (ICRP, 1991; ICRP, 2010):

$$E = \sum_T w_T . H_T \tag{3.13}$$

Where H_T is the equivalent dose for a tissue or organ T, and w_T is the weighting factor for a certain tissue T. The unit for dose equivalent is J/kg or Sv. Some values of w_T are shown in Table 3.2.

Table 3.2 - Values of the weighting factor, w_T, depending on the human body tissue.

Tissue/organ	**Tissue weighting factor, w_T**	**Tissue/organ**	**Tissue weighting factor, w_T**
Gonads	0.2	Liver	0.05
Bone marrow (red)	0.12	Oesophagus	0.05
Colon	0.12	Thyroid	0.05
Lung	0.12	Skin	0.01
Stomach	0.12	Bone surface	0.01
Bladder	0.05	Remainder	0.05
Breast	0.05		

Reference: ICRP, 1991.

The classification "remainder" in Table 3.2 refers to additional tissues and organs including for example adrenals, brain, kidney, muscle, pancreas, spleen, uterus, etc. Additional details are in the ICRP report number 60 (1991).

3.1.1.2.3 Interaction Coefficient and Related Quantities

The interaction between radiation and matter triggers different processes which may result in changes in the direction and energy of the incident radiation, as well as absorption by the medium. The probability of those interactions happening is characterised by the interaction coefficients. Two of those coefficients are described in this section, the mass stopping power and the linear energy transfer, based on report number 85 of ICRU (ICRU, 2011), which may be useful for more detailed information on other coefficients.

- Mass Stopping Power

The mass stopping power *S/ρ* is a quantity that describes the loss of energy by charged particles when crossing a material, and is given by (ICRU, 2011):

$$\frac{S}{\rho} = \frac{1}{\rho}\frac{dE}{dl} \tag{3.14}$$

Where *dE* is the energy, *ρ* is the density of the material, and *dl* is the distance. The unit for dose equivalent is $J.m^2.kg^{-1}$. The linear stopping power is described by $S = dE/dl$.

- Linear Energy Transfer

The linear energy transfer (LET) also named restricted linear electronic stopping power (L_Δ), is the mean loss of energy by charged particles dE_Δ due to the interaction through the material along a traversal distance *dl*, not considering the sum of kinetic energies in excess due to the released electrons by the charged particles (ICRU, 2011):

$$L_\Delta = \frac{dE_\Delta}{dl} \tag{3.15}$$

The linear stopping transfer is given in terms of $J.m^{-1}$. The quantity dE_Δ may be expressed in eV, hence L_Δ is given in $eV.m^{-1}$.

3.1.1.3 Interaction Between Radiation and Matter

Measuring radiation relies on the interaction of the radiation with the medium, therefore, it is of primary importance to understand the mechanisms on which those interactions are based.

The interaction of radiation with matter is an extensive subject, hence this section intends to give a brief introduction to the main sort of interactions one may find. Because of similarities, they are usually divided into two groups: charged particles and photons.

3.1.1.3.1 Interaction of Charged Particles with Matter

When charged particles, which are surrounded by their electric field, go through a material, they may interact with one or more electrons, and/or with the nucleus. This results in interactions – the probability of a charged particle going through a layer of matter without having any interaction is meant to be nil. As a matter of example, a charged particle of 1 MeV going through a material may undergo about 10^5 interactions before all of its kinetic energy is lost (Attix, 1986).

The passage of the charged particles produces a change in their direction of motion and loss of energy to the medium. The medium in turn, by being traversed by the particles, undergoes changes too, such as atoms getting ionised or moving to an excited state (Andreo *et al.*, 2017; Attix, 1986).

The interaction of charged particles that occurs due to the Coulomb force is usually characterised according to the relative size of the classical impact parameter b in comparison with the atomic radius r_a of the absorber, as follows (Attix, 1986; Podgoršak, 2016):

1. For $b \gg r_a$, the interaction is termed a soft collision.
2. For $b \approx r_a$, the interaction is termed a hard collision.
3. For $b \ll r_a$, the interaction is termed a radiative collision.

Those collisions may trigger processes of ionisation and excitation, and because of that, they are referred to as inelastic collisions (Tsoulfanidis; Landsberger, 2015).

- Soft Collisions

Soft collision (also named distant interaction) is the phenomenon in which the charged particle's trajectory lies at a significant distance from the atom with which it is interacting, consequently, the Coulomb force field interacts with the atom as an entire unit, resulting in distortions. The electron of the medium may be either excited and go to a higher energy level or be ejected from the valence band due to the ionisation process (Attix, 1986), as shown in the scheme of Figure 3.2a.

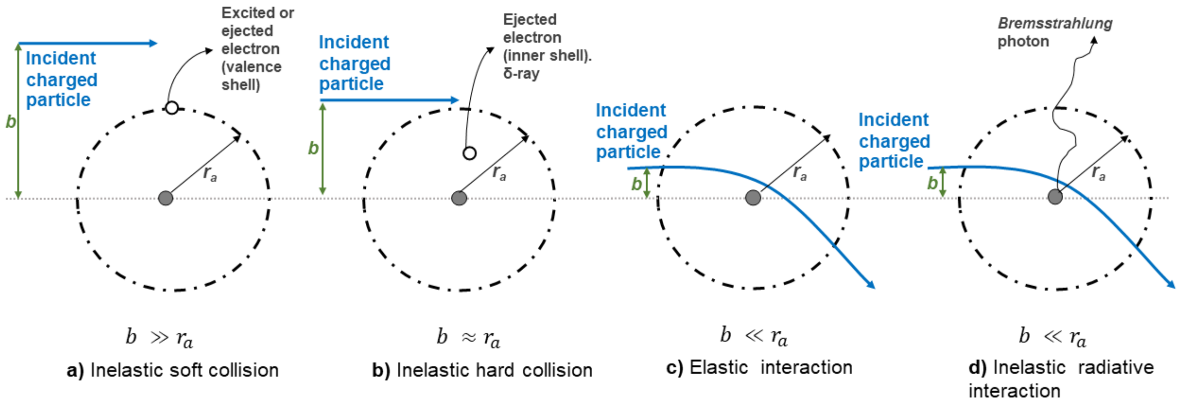

$b \gg r_a$ **a)** Inelastic soft collision

$b \approx r_a$ **b)** Inelastic hard collision

$b \ll r_a$ **c)** Elastic interaction

$b \ll r_a$ **d)** Inelastic radiative interaction

Figure 3.2 - Illustrative scheme for different types of collision of a charged particle with an atom, according to the impact parameter b and the atomic radius r_a. Case (a) stands for the inelastic soft collision ($b \gg r_a$), (b) is the inelastic hard collision ($b \approx r_a$), (c) the elastic case for $b \ll r_a$, and (d) inelastic interaction with $b \ll r_a$.

The probability of having large values of *b* is higher than the occurrence of near hits on individual atoms, which makes soft collisions the most common type of charged particles interaction (Attix, 1986). Although the energy transfer due to this kind of collision is around a few tens of eV, approximately half of total the energy loss occurs via these interactions (Attix, 1986; Podgoršak, 2016).

A very small part of the energy spent during the soft collisions, under certain conditions, can be emitted by the absorber as visible light (bluish-white range), due to the phenomenon of Cherenkov radiation. In this case, a high energy charged particle with non-zero rest mass (for example, an electron) travels faster than the speed of light in that medium resulting in the emission of a photon of light. Cherenkov radiation represents less than 0.1 % of soft collisions, and it is normally not used for radiological purposes, but it is helpful in high-energy nuclear physics analyses (Ahmed, 2007; Attix, 1986).

- Hard Collisions

When the charged particle has a trajectory closer to the atom, that is, when the impact parameter is of the atom's dimensions order, the interaction will first occur with a single atomic electron (usually from an inner shell level) and is referred to as a hard collision or close interaction (Fig. 3.2b). Consequently, the electron is ejected with significant kinetic energy, called a delta (δ) ray and this feature results in the phenomenon also being termed a knock-on collision. Thus, the ejected electron may also be called a knock-on electron (Andreo *et al.*, 2017).

The δ-ray has enough energy to undergo additional Coulomb interactions, which dissipate its kinetic energy along a separate track from the primary charged particle, and this track is named spur or impulse (Attix, 1986). The number of hard collisions is fewer than soft ones, however, the energy spent by the primary particle in both processes is comparable (Andreo *et al.*, 2017; Attix, 1986).

It is worthwhile mentioning that when an inner-shell electron is ejected from an atom due to a hard collision, it also leads to other emission processes, such as the emission of characteristic X-rays and Auger electrons (Attix, 1986).

- Radiative collisions

What occurs when the impact parameter of the charged particles is much smaller than the atom's radius? In this case, the interaction under the Coulomb force takes place mostly with the nucleus, and either inelastic or elastic scattering is possible, and they are accompanied by a change in the direction of motion (Podgoršak, 2016).

In most of the interactions in which $b \ll r_a$, elastic scattering occurs, and there is no emission of X-ray photons or excitation of the nucleus. The loss of kinetic energy is insignificant and just enough to meet the conservation of momentum for the collision (Fig. 3.2c). Therefore, even this though phenomenon is not a representative way of absorbing energy by the material, it represents an important mechanism for deflecting electrons (Attix, 1986).

As elastic scattering is the dominant mechanism for deflecting electrons, it explains their characteristic random paths, which is more accentuated with high Z-media, as electron backscattering increases with the atomic number (Tsoulfanidis; Landsberger, 2015).

And what about the minority of the cases? In about 2-3 % of the cases, an inelastic radiative interaction takes place, which results in the emission of X-ray photons (Fig. 3.2d). The electron is deflected as in the elastic interaction case, but it gives up 100 % of its kinetic energy to the photon, hence, slowing down the process. The specific X-ray photon is referred to as *bremsstrahlung* which is the German word used for “braking radiation” (Attix, 1986).

The *bremsstrahlung* production is proportional to the atomic number *Z*, therefore, it represents an important mechanism of energy dissipation in high-*Z* materials. However, the dissipation of energy is also inversely proportional to the square of the charged particle’s mass, for a given particle velocity. The consequence of it being that the *bremsstrahlung* production by charged particles is not significant in comparison with electrons. In practical terms, it is an advantage for X-ray analysis seeking trace elements analyses, because the generated X-ray spectrum will be composed by the characteristic X-ray lines from the knock-on collision, and no *bremsstrahlung* contribution (Andreo *et al.*, 2017; Attix, 1986).

3.1.1.3.2 Interaction of Photons with Matter

Photons are electromagnetic radiation, and the definition includes both X-rays and γ-radiation. The usual distinction between them is given according to the photon energy *E*. For *E* > *1 MeV*, the photon is classified as γ-rays, and for lower values of *E*, as X-rays (X-rays range starts at energies above the UV radiation). The atomic transitions due to excitation and ionisation processes are responsible for producing X-rays, whilst γ-rays are a result of nuclear transitions (Tsoulfanidis; Landsberger, 2015). Photons are also produced by *bremsstrahlung*, which has a continuous spectrum, different from X-rays characteristic and γ-rays emitted by atoms and nuclei, which are monoenergetic.

There are five main types of interactions of X-rays or γ-rays with mater, which are the Compton effect, photoelectric effect, pair production, Rayleigh scattering and photonuclear ones. Considering the aim of radiation detection, the three first interactions are the most important because they transfer energy to electrons, which leads to the imparting of the energy to matter by Coulomb-force interactions along their tracks (Attix, 1986; Tsoulfanidis; Landsberger, 2015).

The predominance of the Compton effect, photoelectric effect or pair production depends on the quantum energy (hv), where h is the Planck constant and v the frequency, and on the atomic number of the absorber. Here, there is a description of those processes. Since they are extensive subjects, the reader is encouraged to search in the cited references for additional information.

- The Compton Effect

The Compton effect, also named incoherent scattering, is of primary importance in scattering phenomena regarding physics applied to radiology and health areas, as a significant part of this radiation is used in those areas (Andreo *et al.*, 2017; Knoll, 2010).

It is defined as the interaction of a photon with a free (or unbound) and stationary electron. The electron is said to be free, but it is bound to the absorber's atomic nucleus, or it is said to be bound (Bailey *et al.*, 2014; Johns; Cunningham, 1983). Therefore, the electron in this process is usually refers to the one at a more external shell level.

Therefore, the Compton effect occurs when an incident photon of energy ($E = hv$) higher than the binding energy (E_B) loses its energy to the electron (considered to be initially at rest) and is consequently scattered as a photon with new energy hv' at an angle θ, as shown in Figure 3.3a. In addition, there is a recoil electron which has an energy E_k, given by the difference between the initial energy of the incident photon and the scattered one ($E_k = hv - hv'$) and departs at an angle ϕ (Bailey *et al.*, 2014). Therefore, part of the energy is scattered, and part is transferred to kinetic energy, which is the most important mechanism in tissue-like materials. This happens because in soft tissues, Compton scattering is much more significant than either pair process or photoelectric, considering photons in the range from 100 keV to 10 MeV (Johns; Cunningham, 1983).

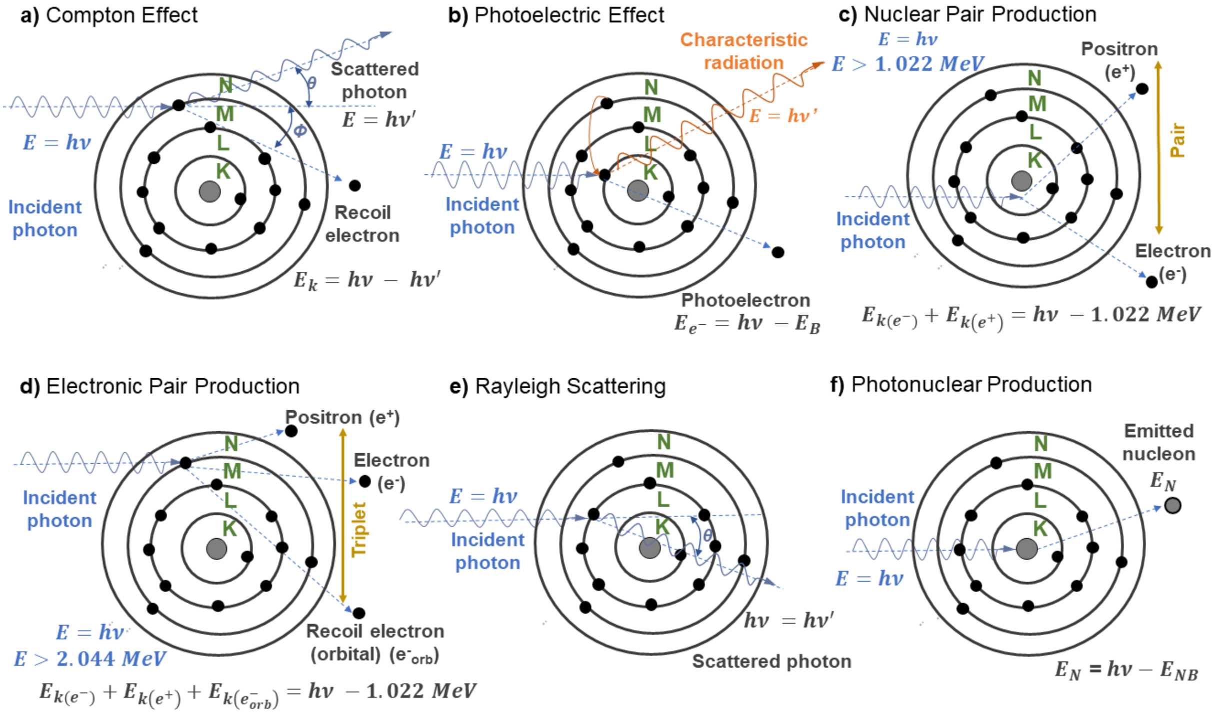

Figure 3.3 - Illustrative schemes for the interaction of an incident photon with an atom, by different effects. (a) Compton photon, in which a recoil electron is produced due to the interaction, (b) Photoelectric effect, (c) nuclear pair production, with positron and electron emission, (d) electronic pair production, (e) Rayleigh scattering and (f) photonuclear production, in which there is interaction with the nucleus. The distribution of electrons in the shells was considered for an atom of aluminium, which has an electron distribution of $1s^2\ 2s^2\ 2p^6\ 3s^2\ 3p^1$.

- Photoelectric Effect

The photoelectric effect is the most common interaction with matter for low energy photons (< 0.5 MeV), and the occurrence is more probable in high atomic number media (Attix, 1986; Knoll, 2010). In this process, the incident photon interacts with a tightly bound electron at the orbital level in the absorber atom. The photon loses its energy in the process and disappears, whilst the electron is ejected from the atom (so-called photoelectron), as shown in the scheme (Fig. 3.3b) (Bailey *et al.*, 2014).

The kinetic energy of the photoelectron E_{e-}, is given by the energy of the photon ($E = hv$) minus the binding energy (E_B): $E_{e-} = E - E_B$. In 1905, Einstein gave the explanation of the photoelectric effect, considering that it would occur when a single electron in a metal completely absorbs a single photon. This work led to him being awarded the Nobel Prize some years later.

Due to this interaction, in addition to the photoelectron produced, the absorber atom gets ionised, and a vacancy is left as an electron was ejected. In order to get an energetic neutrality/equilibrium, this vacancy is promptly filled by another electron, which can occur by capturing a free electron from the medium or by arrangement from other shell levels of the same atom (Turner, 2007).

The photon collision leads to the ejection of the electron from one of the shells (K, L, M, or N, for example). When the vacancy is filled by an electron from a more energetic shell, the excess of energy is released in the form of characteristic radiation, such as an X-ray photon or Auger electron. This radiation is called characteristic because it is discrete and it is related to the energy difference between the levels, that is, the shell levels (Johns; Cunningham, 1983).

- Pair Production

Pair production is described as the absorption process in which a photon disappears, since when passing near the nucleus of the atom, the photon is subjected to the strong field of the nucleus of the atom. As a result, the energy loss gives rise to an electron-positron pair as shown in Figure 3.3c (Johns; Cunningham, 1983). This phenomenon only occurs in a Coulomb force field, usually near an atomic nucleus, even if it does not undergo any change due to the interaction (Attix, 1986; Tsoulfanidis; Landsberger, 2015).

Due to the conversion of the photon into an electron-positron pair, it needs to have energy at least twice that of the electron rest: $h\nu \geq 2m_ec^2$, where m_e is the electron mass and c the speed of light. Therefore, a minimum energy of 1.022 MeV is required for pair production (Attix, 1986; Johns; Cunningham, 1983). Hence, the sum of the energy of the positron $E_{k(e^+)}$ and the electron $E_{k(e^-)}$ is given by the energy of the incident photon minus 1.022 MeV.

Pair production may also occur in the field of an atomic electron (Fig. 3.3d), however, the probability is smaller as the energy threshold is $4m_ec^2$. This process is also referred to as triplet production due to the presence of a recoiling atomic electron from the orbital beyond the pair created, which has an energy $E_{k(e^-_{orb})}$ (Turner, 2007).

- Rayleigh Scattering

Another type of scattering which occurs due to γ-ray photons' interactions with matter is Rayleigh scattering, also known as coherent scattering. This phenomenon is said to be "coherent" because scattering takes place due to a combined action with the whole atom. It is an elastic interaction as the photon fundamentally loses none of its energy in the process and only moves the necessary amount to conserve momentum (Attix, 1986). The photon interacts with the bound atomic electrons in the orbital of the absorber, and the slight movement is given by the small scattering angle θ (Fig. 3.3e).

Since in Rayleigh scattering there is neither excitation nor ionisation of atoms, the γ-ray photon keeps its original energy, and virtually there is no transfer of energy. Therefore, it does not have relevance in radiation dosimetry (Bailey *et al.*, 2014). Furthermore, the probability of Rayleigh scattering is noticeable only for low photon energies, usually lower than a few hundred keV (for most common materials) and is more prominent in high-Z materials (Knoll, 2010).

- Photonuclear Reactions

The process of photonuclear reaction takes place when a photon is absorbed by an atomic nucleus and triggers the emission of a proton or neutron (Fig. 3.3f). For it to happen, the photon needs to exceed an energy of a few MeV in order to excite the nucleus. Thus, the energy of the ejected nucleon (E_N) is given by the photon energy minus the nucleon's binding energy (E_{NB}): $E_N = E - E_{NB}$ (Attix, 1986; Turner, 2007).

The events in which protons are produced due to photonuclear reaction (γ, p) may contribute directly to the kerma, but the relative amount remains less than 5 % when compared with pair production, and as such, is not significant for dosimetry. Whilst the neutrons produced due to the photonuclear reactions (γ, n) may require special attention in radiation protection when dealing with shielding (Attix, 1986). Moreover, the threshold for (γ, p) reactions is usually higher than the ones for (γ, n) as the proton must overcome the repulsive Coulomb energy barrier to escape from the nucleus, which is more probable for heavy elements (Turner, 2007).

3.1.1.4 Radiation Detectors

Previous sections have approached the different types of radiation, covering some of the quantities and units used when dealing with radiation, along with some aspects regarding the interaction of radiation with matter. Once it is known how radiation behaves and the mechanisms of its interaction with a medium, it is possible to use systems to measure the amount of radiation emitted by a source, and the absorbed dose by a material.

A radiation detector is a sensor that produces a signal due to interaction with radiation, and is usually converted and processed electronically, giving the information of interest. As above-mentioned, the processes of Compton scattering, the photoelectric effect, and pair production are the main contributors to photon radiation, while charged particles usually transfer their energies directly by excitation and ionisation (Bailey *et al.*, 2014).

Independent of those mechanisms, the ionising radiation may induce changes in the medium, such as charged carriers in a gas and electron-hole pairs in semiconductors. The responses to radiation are used for detection. Based on that, a short overview of the main groups of radiation detectors is presented ahead, including gas-filled detectors, semiconductor detectors, scintillators, and luminescent dosimeters.

3.1.1.4.1 Gas-filled Detectors

The most common and even oldest type of radiation detectors are based on the effect of charged particles passing through a gas. As primary interaction, the incident radiation excites and ionises the gas molecules, and from that, an appropriate signal can be collected (Knoll, 2010).

Gas-filled detectors consist usually of a system of two electrodes to which a determined electrical potential is applied, and the space between the electrodes is filled with a gas or a noble liquid. When ionising radiation passes through the gas, it dissipates part of its energy and produces pairs of ions. Both the electrons and positive ions move under the influence of the electrical field, which induces an electric current on the electrodes. The electric current can be measured and correlated with the irradiation dose (Tsoulfanidis; Landsberger, 2015). All the gas-filled detectors use this mechanism to get an electronic output signal. The mode of operation depends on the applied voltage and defines the classification of the detector as an ionisation chamber, a proportional counter, or a Geiger-Müller counter.

Ionising chambers operate in the ionisation region, in which the voltage is not so low, consequently, the electrons and ions created move fast enough to reduce the recombination rate to an insignificant value, even zero, and all the charges created by the ionising radiation are collected (Tsoulfanidis; Landsberger, 2015). However, as the signal is not that large, only strongly ionising particles such as protons, alpha particles and heavy ions are detected. In addition, ionising chambers are usually found in either a cylindrical design (in which the electrode is centre-positioned) or in a parallel-plate arrangement (Martin, 2006).

By increasing the voltage, enough energy can be given to the primarily ionised electrons to produce additional ionisation by collisions in the chamber. Thus, the number of pairs of electrons and positive ions increases proportionally to the initial ionisation. The devices operating in this region are called proportional counters. An advantage of the proportional counter is the discrimination of the radiation quality. Because alpha and beta particles have different ionisation effectiveness, the resulting pulses due to a beta particle irradiation might be different from the alpha ones (Martin, 2006).

At a higher voltage range, the electric field gets so strong that a single electron-positive ion pair can trigger an avalanche of similar pairs. As a result, a strong signal is generated whose shape and height are independent of the primary ionisation, as well as is independent of the type of particle, therefore, providing information about the number of particles only. The detector operating in this region are called Geiger-Müller counters (Tsoulfanidis; Landsberger, 2015).

3.1.1.4.2 Semiconductors Detectors

Semiconductors are materials which have an energetic distance separating the conduction band from the valence band. At absolute temperature, there is no conductivity in a semiconductor material since the electrons cannot move under any voltage. However, similar to the gas-filled detectors, when a semiconductor is exposed to ionising radiation, it may produce electron-hole pairs in the material, and this charge creation can be measured and the output signal related to the radiation dose (Tsoulfanidis; Landsberger, 2015).

Applying an electric field in the active volume semiconductor, which is being exposed to ionising radiation, makes both charge carriers drift in opposite directions, and the motion of those charges persists until they are collected at the boundaries (Knoll, 2010).

One of the most common semiconductors used for radiation detection are diodes, which use the p-n junction configuration. In a p-n junction semiconductor, the material has two regions, one with an excess of electron carriers (type n) and another with an excess of holes (type p). Once they are joined together in the system, electrons and holes can move from areas of low to high concentrations, in a process of diffusion, and under the effect of an electric field, they move in opposite directions due to their charges. When ionising radiation passes through the p-n junction, it will produce electron-hole pairs, that diffuse into the depleted region and are swept away due to the electric field, generating a current in the reverse direction (reverse bias), which is collected and recorded (Podgoršak, 2005; Tsoulfanidis; Landsberger, 2015).

3.1.1.4.3 Scintillation Detectors

Scintillators are materials that when exposed to ionising irradiation emit photons. When the incident radiation interacts with the atoms of the scintillator material, it transfers part of its energy, making the atoms of the absorber reach an excited state for a short while. When the atom returns to its ground state, the excess energy is released in the form of photons, usually in the visible and UV range of the spectrum. The photons are collected by a proper device, such as a photodetector, and the signal is electronically processed. However, the number of photons produced by scintillators is not high, and the efficiency of typical scintillators is about 10 to 15 % (Ahmed, 2007). To get a feasible signal, the signal is amplified or multiplied before the electronic processing, by using a well-known device, the photomultiplier tube (PMT).

The PMT usually consists of a photocathode which converts the photons into electrons. The photocathode is normally made of a thin alkaline material layer. The first electrons generated in the photocathode are focused into a series of dynodes, which are under a voltage of about 200-500 V, to help bring forward the electrons. The signal is then collected from the last series' dynode at an anode. The gain in signal may reach values of 10^7 (Bailey *et al*., 2014).

Therefore, the scintillator is part of the detection process which interacts with radiation, giving a response to it. However, to obtain a measurable and feasible signal, it is incorporated in a system that has an amplifier, such as the PMT. Scintillators are usually classified according to the nature of the material into inorganic, organic or gaseous scintillators.

In the case of inorganic scintillations, the mechanism behind the phenomenon is based on the energy states determined by the crystal lattice in insulators or semiconductors. Electrons in a pure material have available only discrete levels of energy in the lattice and are usually bound in the lower band, known as the valence band. If the electron receives enough energy, it can surpass the forbidden band and reach the conduction band. The forbidden band is said to not allow energetic levels for electrons. However, the presence of impurities in the material, which are called activators, creates metastable levels of energy in the forbidden band, for example, due to doping processes.

When an inorganic scintillator is exposed to radiation, it creates pairs of electron-holes. The electron created is then raised from the valence to the conduction band, and the hole can drift to an activator site, forming a recombination centre within the forbidden band. The excited electron migrates through the crystal, and, at a certain time, it can drop in the recombination centre, and a neutral configuration is reached. Since this excited configuration of an electron in the recombination centre can allow a transition to the ground state, there is a quick de-excitation which has a high probability of emitting a photon. This is the main process related to scintillation (Knoll, 2010). The photon is then detected, and the output signal is correlated with the radiation dose. Some examples of inorganic scintillators are the NaI(Tl), CaF_2(Eu), and CsI(Na), in which the element between parentheses is the activator (Tsoulfanidis; Landsberger, 2015).

As regards organic scintillators, they are based on the molecular transitions that happen in the molecule due to exposure to ionising radiation. The incident ionising radiation transfers energy to the atoms, which go through transitions from the ground level to different vibrational levels, transitions which depend on the energy of the radiation. Because of the instability of the system, it induces the electrons to go back to the ground levels through non-radiative transitions, which are very fast in comparison with the scintillation in inorganic materials (Tsoulfanidis;

Landsberger, 2015). The excess energy is emitted as photons, in which the energy is related to the energetic levels' transitions. It is usually observed that the emission band is shifted to a higher wavelength, in a phenomenon called Stokes shift, and it is explained by the fact the electron does not de-excite to the ground level but goes via intermediate levels.

The gaseous scintillators are based on the efficient scintillation properties mainly observed in noble gases. The drawback of using this method is that the gas might need to be condensed, hence there would be changes in the efficiency due to optical scattering induced by the different densities (Knoll, 2010).

3.1.1.4.4 Luminescent Dosimeters: Storage Phosphors

A storage phosphor is a material which shares a similar mechanism of interaction with radiation as semiconductors. However, the main difference is that part of the absorbed energy from the incident radiation is stored in deep (or long-living) traps. Hence, one of the advantages is being able to measure the absorbed dose over a period (Bailey *et al.*, 2014). The incident ionising radiation can create electron-hole pairs in semiconductors or insulators, which can move through the crystalline lattice. After the radiation exposure is ceased, some of the charges will be placed at metastable levels, due to the presence of impurities or defects in the material which act as traps. The concentration of the trapped charges is proportional to the absorbed dose. By stimulating the material with heating or light, there is emission of photons, which are detected. If the stimulation is by heating, the emission is called thermoluminescence (or TL), and when is by light, it is named optically stimulated luminescence (OSL). Those techniques are the main ones used to do the luminescent characterisation in this study. Therefore, a more in-depth approach regarding them is covered in Section 3.2.

Another technique which has this property of "storing" the radiation is radiophotoluminescence (RPL). In this case, a material has a precursor material introduced, such as silver, which acts as a charge-trapping centre in the forbidden band. When it is exposed to ionising radiation, the electrons and holes created due to the ionisation interact with the charge-trapping centres. The centre which captures a charge undergoes a transition and becomes a luminescent centre, which is stable, and the concentration of luminescent centres is related to the absorbed dose. When stimulated with UV light of a certain wavelength, the centre may be excited and emit photons. A remarkable feature of RPL dosimeters is that the signal is not lost due to the light stimulation, hence, the information about the absorbed dose is maintained, unless a proper cleaning procedure is adopted (Yanagida *et al.*, 2022).

3.1.1.4.5 Other Examples

In addition to the radiation detector types already mentioned, which are the most widely used, there are many others which have different mechanisms of interaction. The choice of a detector needs to consider several aspects, such as the range of irradiation dose, type of radiation, conditions of operation, necessity of an *in-vivo* measurement or passive characteristic, and so on. Other examples one might cite are (Obodovskiy, 2019; Podgoršak, 2016; Turner, 2007):

- Chemical dosimeters, such as Fricke dosimeters, which are based on the characteristic of ferrous ions in sulphate solutions. The chemical compound used is oxidised due to the interaction with radiation, changing the colour.
- Calorimetry detectors, which are based on the mechanism in which part of the absorbed energy from the incident radiation is converted into heat. The heat would be proportional to the dose.
- Bubble detectors, which are an effective way of detecting alpha radiation. It is constituted of a polymer with tens of thousands of dispersed microscopic droplets of a superheated liquid. The interaction with radiation makes the droplets transform into small bubbles in which the concentration is associated with the irradiation dose.
- Film badge dosimeters, which, despite being an old method of detection, are still in use. The mechanism is based on the image projected on the film, and different photon energies are attenuated differently by the same material.
- Diamond dosimeters, which work analogous to a gas-filled ionisation chamber but instead of air as a cavity radiation-sensitive medium, use diamond. Diamond is less prone to mechanical damage and to be affected by radiation history, as well as it has a closer tissue and water equivalence than silicon.

In any case, this section does not have the intention either of being exhaustive or giving such detailed description about the radiation detectors above-mentioned. See the references for a good theoretical background.

3.2 Luminescence Phenomena

The phenomenon of luminescence in a cursory way may be defined by the light emission from a material after it has been exposed to incident radiation. The energy may be absorbed, which leads the atom or the molecule to an excited state, that is, a higher energy state. When it returns to the ground state, the energy is released in the form of light (Sunta, 2015). Considering Stokes' law, the energy is re-emitted as longer wavelength photons. The spectral characteristic of the emission is related to the material/substance and not to the incident radiation. Most studies investigate the emission in the visible light range, however, emissions in shorter and longer wavelengths are also possible, such as in the UV and infrared ranges (Mckeever, 1985).

Luminescence in comparison with incandescence is a much more efficient way of light emission, and it is related to the selective excitation of atomic or molecular energy levels (Sunta, 2015).

There are several types of luminescence phenomena which are observed in nature or artificial devices, and their classification is given according to the related method of excitation, as is summarised in Table 3.3.

Table 3.3 - Classification of the light emission according to the excitation mechanism.

Luminescence phenomenon	**Excitation mechanism**	**Comments**
Fluorescence	Photons	A modality of photoluminescence.
Phosphorescence	Photons	A modality of photoluminescence. Different from fluorescence, there is a delay between the process of radiation absorption and the emission of light, and it is strongly dependent on temperature.
Cathodoluminescence	Electrons	-
Radioluminescence	X-rays or nuclear radiation	Nuclear irradiation might be by beta or alpha particles, or gamma rays.
Electroluminescence	Electric field	-
Chemiluminescence	Chemical reactions	For example, the light emitted due to the oxidation of white phosphors when in air.
Bioluminescence	Biochemical reactions	Due to the electronic excited states which can be observed in biomolecules.
Triboluminescence	Mechanical stress	Also called mechano-luminescence.
Sonoluminescence	Sound waves	-
Thermoluminescence	Ionising radiation followed by heat	In these cases, the primary excitation is due to ionising radiation, which induces the creation of charges trapped at metastable levels in the material. Afterwards, a stimulation process (heat or light) is responsible for the release of the stored energy. Thermoluminescence may be also referred thermally stimulated luminescence.
Optically stimulated luminescence	Ionising radiation followed by optical stimulation	

References: McKeever (1985) and Sunta (2015).

Luminescence phenomena constitute an important way of evaluating the properties of materials and even living organisms, as by analysing the emission one might understand the underlying mechanisms behind it. Therefore, each of those techniques is by itself a branch of study.

This section does not have the intention either of citing all the possible luminescence phenomena or giving an in-depth approach regarding them, however, the references here cited might be a good start.

In this work, the luminescence properties of the hafnium oxide were investigated mainly as regards its thermoluminescence and optically stimulated luminescence, but additionally the fluorescence and radioluminescence emissions as well, these techniques are detailed in the following subsections.

3.2.1 Thermoluminescence

As briefly mentioned before, the phenomenon of TL is defined as the light emission supplied by a material when it is heated. However, previous to heating, the material must have absorbed radiation energy from an ionising irradiation source, otherwise, it would be just a spontaneous emission of light due to the heating, which is called incandescence (McKeever, 1985).

The phenomenon of TL is known since the 17th century. The first report of it is associated with Robert Boyle, who in 1663 described to the Royal Society an event in which he observed a sort of glimmering light when taking a diamond into bed with him, and holding it for a while, making it warmer with his body (Chen; Pagonis, 2011; Harvey, 1957; Heckelsberg, 1980). However, it was only in the 19th century that the studies approaching TL were performed, at first it was mainly investigated for mineral materials, such as fluorite and calcite (Chen; Pagonis, 2011). Since then, this emission has been explored in different applications, for example, in 1981, Wintle reported the first study of using the technique for dating purposes.

Nevertheless, it is worth emphasising that not any material can supply a TL emission, there are some minimum requirements to fulfil for it to supply TL emission, which are (Bos, 2007; McKeever, 1985):

- To be an insulator or semiconductor: the TL phenomenon is based on the presence of metastable levels in the forbidden band (FB), which separates the conduction band (CB) from the valence band (VB). In the case of conductors, this region is not considered, and the electrons can move freely. Glasses may also display TL emission, however, the band energy model proposed would not cover this case.
- Energy absorption: the material must have absorbed some energy during the ionising radiation exposure. The ionising radiation is responsible to promote the trapping of electrons and holes, which are strongly related to the TL phenomenon.
- The TL emission occurs when the energy stored is released in the way of photons of light. An important note here is that the TL is related to the thermal stimulation of luminescence in a sample that was excited in a different way (ionising irradiation), hence, TL is not related to thermal excitation. This characteristic also points out that after the

TL emission, if the material goes into a cooling process, and then is re-heated, any signal would not be observed. Therefore, exposing again to ionising radiation would be necessary, which explains the interest in using the material for dosimetric purposes.

The reason for these requirements will be clarified in the next sections where the models used to explain the TL are presented.

3.2.1.1 Theoretical Model for Thermoluminescence: Band Energy Levels

To explain the TL phenomenon, the theory of band energy levels for solid-state is usually applied. The solution of the Schrödinger Equation for electrons under different potentials has demonstrated that the electrons can occupy 'allowed regions', but also pointed out the existence of other possible regions, which are commonly named 'forbidden zones' or 'forbidden bands' (McKeever, 1985). The classification of a material as an insulator, semiconductor or conductor lies in the presence of those forbidden bands.

The occupancy of the bands in the crystal is described by Equation 3.16 (or also called density states function):

$$N(E) = Z(E)f(E) \tag{3.16}$$

Where the density of occupied energy levels $N(E)$ is a function of the density of available energy states $Z(E)$, and the Fermi-Dirac distribution function $f(E)$, given by:

$$f(E) = \frac{1}{\exp\left[\left(\frac{E - E_f}{kT}\right)\right] + 1} \tag{3.17}$$

Where E is energy, E_f is the Fermi level (or chemical potential), k is the Boltzmann constant, and T is the temperature.

At a temperature of absolute zero, all the energy levels below E_f are full, whilst those above this level are empty. In the case of the insulators and semiconductors, at 0 K, E_f is above the higher energy level of the VB, it is therefore, totally full. Consequently, there is no charge transport in the net of the material, making them non-conductors at this temperature. To obtain electronic conduction, it is necessary for the electrons to have sufficient energy to overcome the energy gap E_g, allowing them to reach the next empty band, which is the CB (McKeever, 1985). Figure 3.4 shows a scheme for the three categories of materials: (a) insulators, (b) semiconductors, and (c) conductors. Theoretically, for an ideal crystalline semiconductor or insulator, when $E_c > E > E_v$, then $Z(E) = 0$, where E_c is the energy at the bottom of the conduction band and E_v is the energy at the top of the valence band.

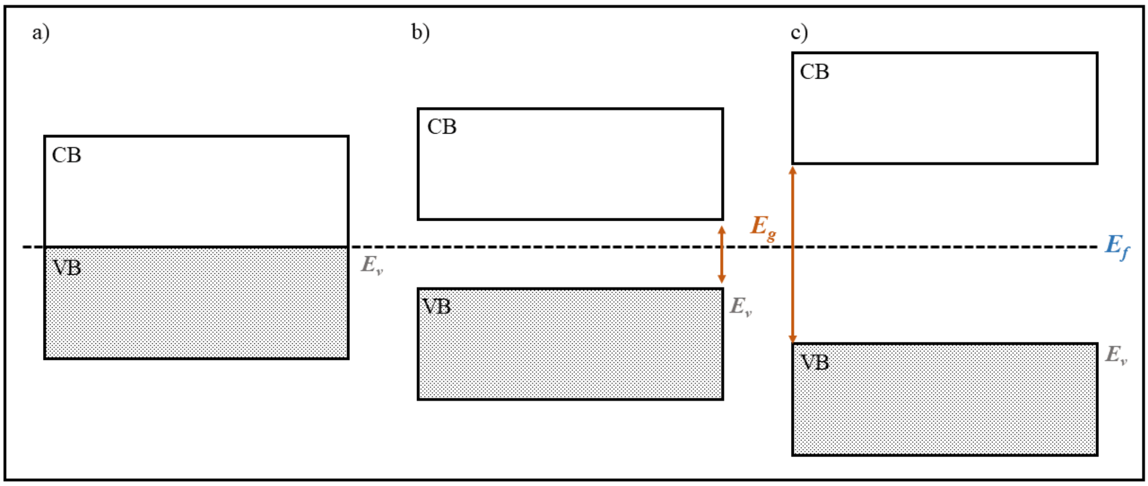

Figure 3.4 - Illustrative schemes for the energy bands' diagram for (a) a conductor, (b) a semiconductor and (c) an insulator. CB stands for conduction band whilst VB stands for valence band.

This structure is a theoretical model and assumes a crystalline material with no defects. However, in natural materials, and even synthesised ones, structural defects and impurities are present. This leads to an interruption in the crystalline periodicity, creating new levels in the FB, meaning the electrons can have energy levels in this region (McKeever, 1985). In this sense, the presence of these defects allows levels in the FB which carry out an essential role in the TL mechanism.

Therefore, in crystals, it is the presence of impurities or imperfections that gives rise to the colour centres and luminescence. Among the point defects, one might cite the lattice vacancy, in which there is a missing atom or ion (Fig. 3.5) also named Schottky defect (the Schottky defect may be also known as Schottky pair, and in this case, there are two vacancies related to a cation and an anion, in a pair); the interstitial position, which can be the introduction of an intrinsic or extrinsic atom or ion; the substitutional when an atom or ion of the crystal is replaced by a different one; and the Frenkel defect, in which an atom or ion is transferred from the previous lattice site to an interstitial arrangement (Kittel, 2005).

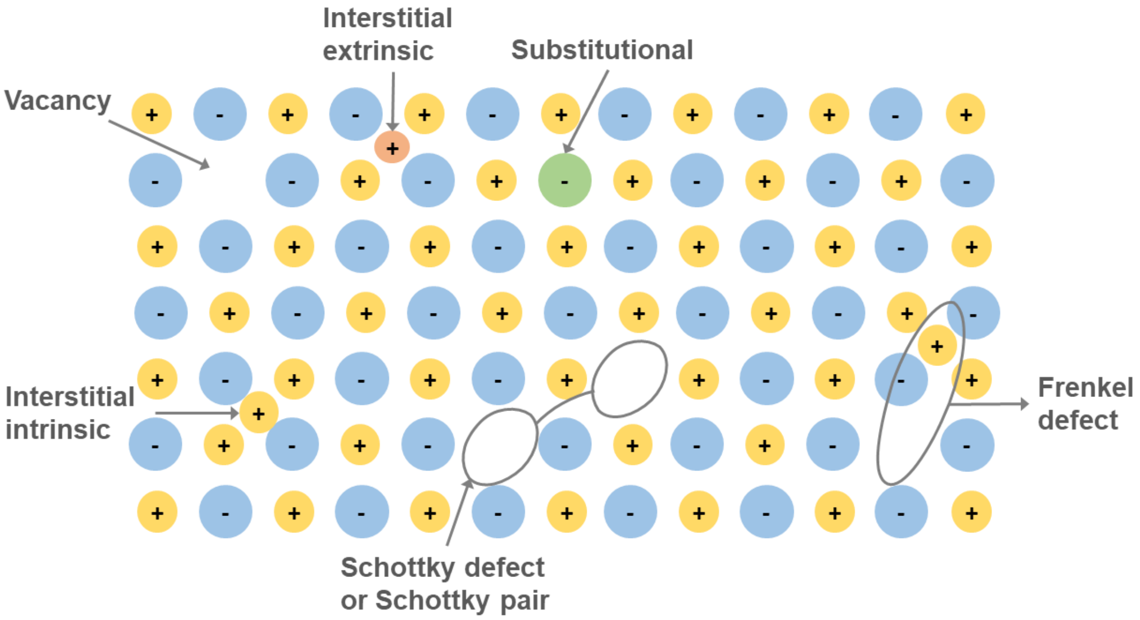

Figure 3.5 - Illustrative scheme of a two-dimensional crystalline arrangement, in which the presence or absence of ions that are not predicted for an ideal crystal (no impurities) are shown.

It is not only the point defects which play a role in the luminescence but also the line and planar defects, such as grain boundaries and dislocations. Whilst the CB and VB are extended throughout the crystal, the influence of the defect is related to its position in the lattice. For this reason, the levels created by the presence of defects are named localised energy levels (McKeever, 1985).

By using the energy band levels diagram, the TL phenomenon can be explained in a simplified way, as shown in Figure 3.6. In this scheme, it is represented by a crystalline material (insulator or semiconductor), which has an energy difference between the VB and CB (due to the FB) divided by the E_f. The FB region has different traps, which are metastable levels due to the presence of defects in the material net. The traps above E_f are called electron traps (T_R), whilst the ones below E_f are hole traps and can perform the role of a recombination centre (R_C). The T_R trap types are empty in the equilibrium, that is before the electron-hole pair is created by the ionising radiation exposure.

When the material is exposed to ionising irradiation, pairs of electron-holes are created, and free electrons and holes can move in the crystalline net, being the electrons moving more easily than holes. Due to this ionising process, the free electron located on the VB receives an energy $E > E_f$, which allows it to reach the CB (transition 1). Once the electron is in the CB, it can be trapped in metastable levels (T_R), which are due to defects in the crystalline net (transition 2) or even recombine directly in a R_C, releasing the energy in the form of photons (in this case, the phenomenon is called radioluminescence, and it happens in $< 10^{-8}$ s). In turn, the hole created might also be trapped in a hole trap (transition 3), which performs a role as a R_C (Bos, 2007).

After irradiation, the material has absorbed the energy, and holes and electrons are trapped in the FB. When a thermal stimulus is applied to the material (heat), the electron trapped in the metastable level receives enough energy to reach the CB again (transition 4). Then, the electron can recombine in a R_C (transition 5), and the energy is released in the form of photons, what is called thermoluminescence, or TL (Bos, 2007). Another possibility is for the electron to be retrapped in a T_R (transitions 6 and 7). In the continuation of heating, the retrapped electron might reach the CB again (transitions 8 and 9).

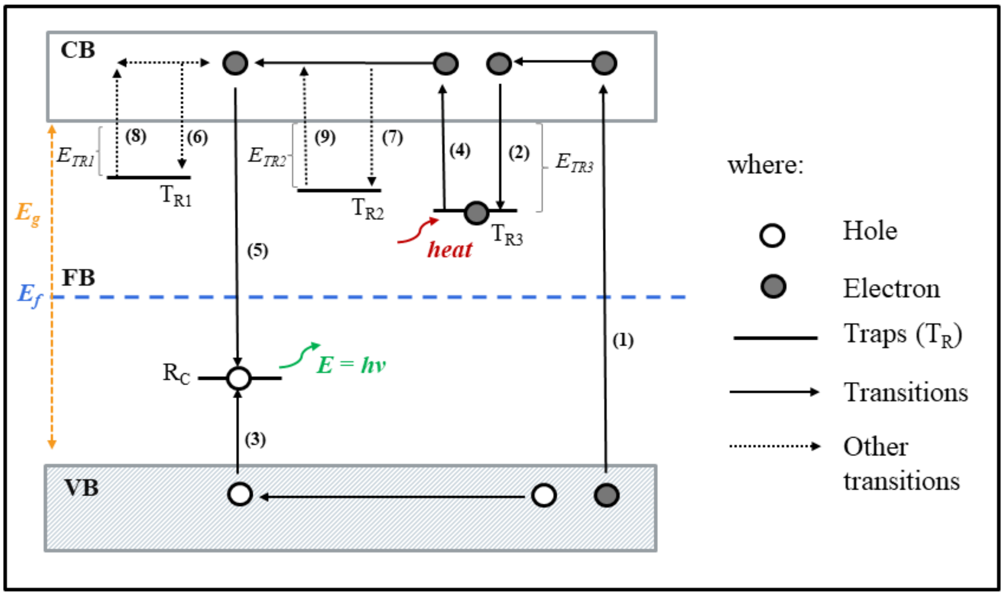

Figure 3.6 - Illustrative energy bands' diagram for TL phenomenon.

It is worth mentioning that there are different levels of traps, which depends on the material's properties, such as the defect types. Depending on the trap, more energy may be necessary for releasing the trapped electron, for example, an electron trapped in a deeper trap will require more energy than one in a shallower trap: $E_{TR1} < E_{TR2} < E_{TR3}$. The existence of different trap levels is easily observed in the TL glow curve because each peak is associated with a stimulus temperature, consequently, to a trap level. As a result, several peaks might be observed, alone or overlapped, according to the materials' properties.

Another aspect that needs to be explained is that this scheme represents only a simple model, wherein there is only an electron and some illustrative trap levels. In a real material, this process occurs with several electrons and holes at the same time, and with different trap levels. Moreover, retrapping of electrons may occur more than once.

If the free electron in the CB does not recombine directly but is trapped in a metastable level, it is possible to calculate the probability of the electron releasing per unit of time, by using the energy band theory and the Arrhenius Equation (Bos, 2007):

$$p = s\exp\left(-\frac{E}{kT}\right) \tag{3.18}$$

Where the probability of release of an electron p is dependent on the attempt-to-escape factor (or escape probability factor, also known as frequency factor) s, the energy E (also called activation energy or trap depth, which in Figure 3.6 is represented by E_{TR}), the Boltzmann constant k and the absolute temperature T.

Due to the normal equilibrium, the Fermi level is located between the trapped electrons level (T_R) and the trapped holes (R_C). These populations of electrons and holes that are trapped constitute a non-equilibrium state, which is metastable and will last for an indefinite period, depending on the rate parameters E and s. The way back to equilibrium is always open, however, because of the disturbance to the system, that is, the process of irradiation was made at a low temperature (T_I), usually, room temperature (RT) or at a lower temperature in comparison with E/k, the time for relaxing is slow since the material is usually kept in RT (Bos, 2007).

When the thermal stimulus is applied to the material, with temperatures higher than T_I, the return to the equilibrium is quicker, which in turn increases the probability of the electron being released and recombining in a R_C. The energy is released as an emission of light, the TL signal (McKeever; Chen, 1997).

The TL intensity I_{TL} is given as a function of time (t) and can be described by Equation 3.19 (Bos, 2007; Furetta, 2003):

$$I_{TL}(t) = -\frac{dm}{dt} = n_c m A_m \tag{3.19}$$

The signal is negative because it is considered that with time, the concentration of trapped holes will decrease as a consequence of the recombination process. The signal is then dependent on the concentration of free electrons in the CB n_c (cm^{-3}), on the concentration of holes (recombination centres) m (cm^{-3}) and on the probability of recombination A_m (cm^{-3}.s^{-1}) in which A_m is considered independent of the temperature. This previous equation describes the phenomenon with relation to the concentration of free electrons n_c and holes m.

However, it is also necessary to take into account another concentration of electrons, which is the trapped electrons n (cm^{-3}). The following equation considers it, and the probability of retrapping as well (Furetta, 2003; Bos, 2007):

$$-\frac{dn}{dt} = np - n_c(N-n)A_n \tag{3.20}$$

Therefore, the rate of the concentration is dependent on the concentration of electrons traps N (cm^{-3}) and of the probability of the electron being retrapped A_n (cm^{-3}.s^{-1}).

Replacing p by the Equation 3.18, one can obtain:

$$\frac{dn}{dt} = -ns\exp\left(-\frac{E}{kT}\right) + n_c(N-n)A_n \tag{3.21}$$

Using Equations 3.19-3.22, one can describe the concentration of free electrons n_c based on the charge neutrality (Furetta, 2003):

$$\frac{dn_c}{dt} = \frac{dm}{dt} - \frac{dn}{dt} \tag{3.22}$$

From this, the concentration of free electrons is assumed to be the concentration of trapped holes minus the trapped electrons with respect to time. Replacing the terms in Equation 3.22 by Equations 3.19 and 3.20, it becomes:

$$\frac{dn_c}{dt} = ns\exp\left(-\frac{E}{kT}\right) - n_c m A_m - n_c(N-n)A_n \tag{3.23}$$

Those equations cited so far explain the carried charge traffic in a material, for a simplified situation where there is a single electron releasing, in a system with one trap and one recombination centre, and they are the basis for many analyses approaching TL. Nevertheless, in order to get an analytical expression, some assumptions need to be adopted. One is the quasi-equilibrium (QE) condition, as defined by McKeever and Chen (1997):

$$\left|\frac{dn_c}{dt}\right| \ll \left|\frac{dn}{dt}\right|, \left|\frac{dm}{dt}\right| \tag{3.24}$$

It introduces the notion that the concentration of free electrons in the conduction band is quasi-stationary at any time. Consequently, it means there is no concentration of carriers in the CB, which leads to:

$$dn_c = 0 \tag{3.25}$$

In addition, from charge neutrality:

$$n_c + n = m \tag{3.26}$$

Then

$$n \approx m \tag{3.27}$$

Considering $dn_c \approx 0$, using Equations 3.23 and 3.24, Equation 3.19 becomes:

$$I_{TL}^{GOT}(T) = \frac{mA_m ns \exp\left(-\frac{E}{kT}\right)}{(N-n)A_n + mA_m} \tag{3.28}$$

Equation 3.28 is also called the general one-trap (GOT) equation (Furetta, 2003).

3.2.1.1.1 Model for First-order, Second-Order and General-Order Kinetic

To solve Equation 3.28 analytically, some assumptions to simplify are necessary. Throughout the development of the theory for the TL phenomenon, studies have used different approaches to reach a more feasible equation for describing TL. One of the aspects focused on the probability of retrapping of electrons or not.

Based on negligible retrapping during the measurement, that is, during heating, Randall and Wilkins (1945a, 1945b) developed the model of first-order kinetics. This started from the below assumption (Bos, 2007):

$$mA_m \gg (N-n)A_n \tag{3.29}$$

It states that the probability of recombination A_m is much higher than the probability of retrapping A_n. Hence, the first-order kinetic model is known for not having retrapping. In this case, the Equation 3.19 becomes:

$$I_{TL}(t) = -\frac{dn}{dt} = ns \exp\left(-\frac{E}{kT}\right) \tag{3.30}$$

Assuming constant temperature, the probability of the release of an electron p is also constant, one has:

$$\text{For } T = \text{constant} \rightarrow \; p = s \exp\left(-\frac{E}{kT}\right) = \text{constant} \tag{3.31}$$

From Equation 3.30, and considering the assumption on 3.31, the number of trapped electrons n can be described by (Furetta, 2003):

$$\frac{dn}{dt} = -\,np \tag{3.32}$$

Integrating the equation on both sides, from an initial concentration of trapped electrons n_o to a concentration n, and from an initial time t_0 to a time t, one has:

$$\int_{n_0}^{n} \frac{dn}{n} = -\int_{t_0}^{t} p\, dt \tag{3.33}$$

Obtaining:

$$n = n_0 \exp\left[-s \exp\left(-\frac{E}{kT}\right) t\right] \tag{3.34}$$

Consequently, Equation 3.30 becomes:

$$I_{TL}(t) = -\frac{dn}{dt} = n_0 s \exp\left[-st \exp\left(-\frac{E}{kt}\right)\right] \exp\left(-\frac{E}{kT}\right) \tag{3.35}$$

However, if one only considers this equation as a function of time at a constant temperature, it describes a phosphorescence phenomenon instead of a TL, which has a decay shape. In the case of TL, the increase in temperature leads to the release of trapped electrons, which can recombine in a recombination centre and emit light. The light emission reaches a maximum, which is related to the concentration of trapped electrons, and then, it decreases, since the number of charges carriers gets depleted: the trapped electrons were released and recombined since retrapping is not considered in the first-order kinetic (Bos, 2007).

Usually, the TL is measured with a constant heating rate β_T:

$$\beta_T = \frac{dT}{dt} \tag{3.36}$$

Adopting the heating rate, Equation 3.33 becomes:

$$\int_{n_0}^{n} \frac{dn}{n} = -\int_{T_0}^{T} \frac{s}{\beta_T} \exp\left(-\frac{E}{kT'}\right) dT' \tag{3.37}$$

Resulting in:

$$n = n_0 \exp\left[-\frac{s}{\beta_T} \int_{T_0}^{T} \exp\left(-\frac{E}{kT'}\right) dT'\right] \tag{3.38}$$

Finally:

$$I_{TL}^{RW}(T) = -\frac{dn}{dt} = n_0 s \exp\left(-\frac{E}{kT}\right) \exp\left[-\frac{s}{\beta_T} \int_{T_0}^{T} \exp\left(-\frac{E}{kT'}\right) dT'\right] \tag{3.39}$$

Expression 3.39 is called the peak shape for first-order kinetic. The term RW refers to Randall and Wilkins (it was here adopted to better distinguish from the next TL equations). The TL glow peak according to this equation has a peak shape as shown in Figure 3.7 (blue curve). It can be noticed firstly that there is an exponential behaviour which increases with temperature due to the trapped electrons being released and recombining in the recombination centres. It reaches a maximum intensity ($I_{TL\ max}$) for a maximum temperature T_{max}, and is followed by a second exponential, which decreases faster than the first, as the traps are getting emptied, and the signal is erased (Furetta, 2003).

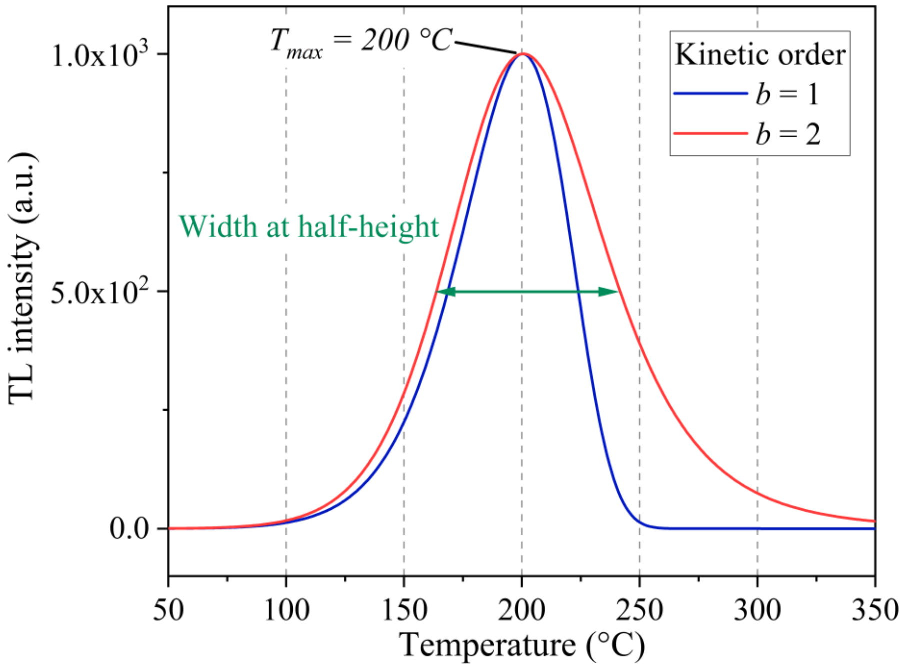

Figure 3.7 - Computerised Glow Curve Deconvolution for two theoretical TL glow curve cases using general-order kinetic (GOK) equation. The red curve represents a second-order kinetic TL glow curve, and the blue one, a first-order kinetic curve. Apart from the kinetic order, the other parameters were the same: T_{max} = 200 °C, $I_{TL\ max}$ = 1000 a.u., activation energy = 0.8 eV, and β_T = 5 °C/s. The letter b indicates the kinetic order.

A few years later, Garlick and Gibson (1948), who like Randall and Wilkins were from University of Birmingham, proposed a model in which the retrapping is considered (Equation 3.40) (Bos, 2007):

$$mA_m \ll (N-n)A_n \tag{3.40}$$

Moreover, it was assumed that the concentration of traps is far from saturation, that is:

$$N \ll n \tag{3.41}$$

And that the neutrality from Equation 3.26 still applies.

Considering the escape probability of the trapped electron and its recombination in a centre as:

$$\frac{m}{(N-n)+m} = \frac{n}{N} \tag{3.42}$$

Equation 3.30 can be rewritten as:

$$I_{TL}(t) = -\frac{dn}{dt} = \frac{n^2}{N} s \exp\left(-\frac{E}{kT}\right) \tag{3.43}$$

Introducing the pre-exponential factor constant s' = s/N (in cm^3.s^{-1}), it becomes:

$$\frac{dn}{dt} = -n^2 s' \exp\left(-\frac{E}{kT}\right) \tag{3.44}$$

Then, doing the same procedure as before, and integrating from an initial concentration of trapped electrons n_o to a concentration n, from initial time t_0 to time t, and considering constant temperature T, one has:

$$\int_{n_0}^{n} \frac{dn}{n^2} = -s' \exp\left(-\frac{E}{kT}\right) \int_{t_0}^{t} dt \tag{3.45}$$

From Equation 3.44, it is obtained:

$$n = n_0 \left[1 + s' n_0 t \exp\left(-\frac{E}{kT}\right)\right]^{-1} \tag{3.46}$$

Consequently, the intensity can be rewritten as:

$$I_{TL}(t) = -\frac{dn}{dt} = n^2 s' \exp\left(-\frac{E}{kT}\right) = \frac{n_0^2 s' \exp\left(-\frac{E}{kT}\right)}{\left[1 + s' n_0 t \ \exp\left(-\frac{E}{kT}\right)\right]^2} \tag{3.47}$$

As the TL is dependent on the temperature, adopting the heating rate, Equation 3.45 becomes:

$$\int_{n_0}^{n} \frac{dn}{n^2} = -\frac{s'}{\beta_T} \int_{T_0}^{T} \exp\left(-\frac{E}{kT}\right) dT \tag{3.48}$$

Resulting in:

$$n = n_0 \left[1 + \left(\frac{s' n_0}{\beta_T}\right) \int_{T_0}^{T} \exp\left(-\frac{E}{kT'}\right) dT'\right]^{-1} \tag{3.49}$$

Finally, the intensity is given by Equation 3.50:

$$I_{TL}^{GG}(T) = -\frac{dn}{dt} = n^2 s' \exp\left(-\frac{E}{kT'}\right) = \frac{n_0^2 s' \exp\left(-\frac{E}{kT}\right)}{\left[1 + \frac{s' n_0}{\beta_T} \int_{T_0}^{T} \exp\left(-\frac{E}{kT'}\right) dT'\right]^2} \tag{3.50}$$

The expression 3.50 is denominated as the second-order kinetic equation for TL. The term GG refers to Garlick and Gibson. As shown in Figure 3.7 (red curve), the second-order peak is almost symmetric, with the half side at higher temperatures a bit broader than the lower one. The reason is that due to the retrapping process occurring during the TL measurement, a considerable part of the released electrons in the CB is retrapped before recombining in the recombination centre. Thus, there is a delay in the emission (Bos, 2007).

Later, May and Partridge (1964) approached a model in which intermediate kinetic orders are possible between 1 and 2 (first and second orders), and wrote an empirical expression considering measurement conditions that indicated the existence of intermediate orders:

$$I_{TL}(t) = -\frac{dn}{dt} = n^b s'' \exp\left(-\frac{E}{kT}\right) \tag{3.51}$$

Where the TL intensity takes into account the kinetic order b that can vary between 1 and 2, and the pre-exponential factor s'' which is expressed in terms of $\mathrm{cm}^{3(b-1)}.\mathrm{s}^{-1}$ (Furetta, 2003; Bos, 2007). Integrating that, one has:

$$\int_{n_0}^{n} \frac{dn}{n^b} = -\int_0^t s'' \exp\left(-\frac{E}{kT}\right) dT \tag{3.52}$$

Which becomes:

$$n = n_0 \left[1 + \mathrm{s}(b-1)t \exp\left(-\frac{E}{kT}\right)\right]^{\frac{1}{1-b}} \tag{3.53}$$

Where $s = s''n_0^{b-1}$ (units of s^{-1}). Thus:

$$I_{TL}(t) = -\frac{dn}{dt} = sn_0 \exp\left(-\frac{E}{kT}\right)\left[1 + \mathrm{s}(b-1)t \exp\left(-\frac{E}{kT}\right)\right]^{\frac{b}{1-b}} \tag{3.54}$$

Assuming the linear heating rate β_T, integrating and rearranging, the intensity can be written as (Furetta, 2003):

$$I_{TL}^{MP}(T) = sn_0 \exp\left(-\frac{E}{kT}\right)\left[1 + \frac{\mathrm{s}(b-1)}{\beta_T} \exp \int_{T_0}^{T} \exp\left(-\frac{E}{kT'}\right) dT'\right]^{-\frac{b}{b-1}} \tag{3.55}$$

Equation 3.55 represents a model of general-order kinetics (MP refers to May and Partridge). Later studies have derived a function that takes into account the experimental parameters of maximum peak intensity $I_{TL\,max}$ at a maximum temperature T_{max} (Bos, 2007).

3.2.2 Optically Stimulated Luminescence

Another phenomenon which shares similarities and has been used together with TL measurements to better understand the luminescence mechanisms in crystalline materials is optically stimulated luminescence, or OSL. The technique was first used by Huntley, Godfrey-Smith and Thewalt (1985) when their work proposed the use of light stimulation from an argon-ion laser in order to excite electrons located at light-sensitive traps in the materials, and hence, measure the luminescence. The luminescence intensity was proportional to the radiation dose absorbed by the sediment and gave information about the sedimentation process. Since then, due to practical aspects of OSL, which usually does not require the use of heating (or heating at high temperatures as it is common for TL), together with advances in LEDs and experimental set-up technologies, it has spread to other areas beyond dating, such as dosimetry (Bøtter-Jensen; McKeever; Wintle, 2003).

OSL is the transient luminescence which occurs during the light stimulation (or illumination) of insulators or semiconductors that were previously excited, usually by ionising radiation (Yukihara; McKeever, 2011). The process can be represented with an energy band levels diagram, as was used for TL in the previous section (Fig. 3.8).

When the semiconductor or insulator material, which has defects in its crystalline net is exposed to ionising radiation, it generates pairs of electron-holes. As is the case for TL, the created electron can move freely through the lattice, and reach the CB, the hole can also move freely in the VB. After the irradiation process, the material is in a latency period, in which there are metastable concentrations of trapped electrons (from transition 2) and holes (transition 3), which are possible due to the presence of defects in the material, here identified in the FB (Yukihara; McKeever, 2011).

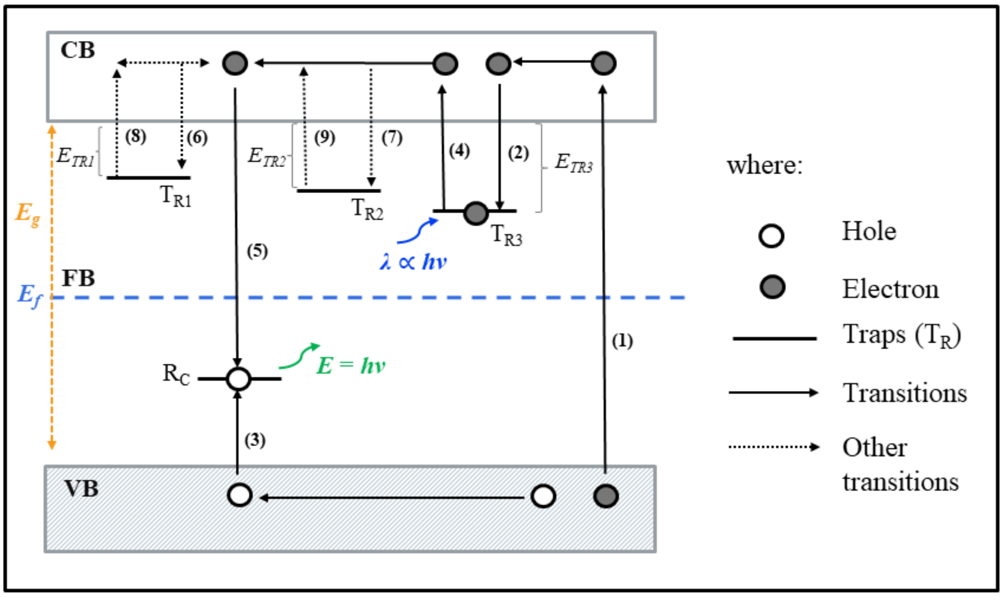

Figure 3.8 - Illustrative energy bands' diagram for OSL phenomenon.

Once the electrons are trapped in metastable levels, an optical stimulation can be applied to the material. If the energy supplied by this stimulation (usually with wavelengths between the infrared (IR) and UV range depending on the material's characteristics) is enough to release the trapped electrons, they can again reach the CB (transition 4), recombine into a R_C (transition 5) and emit light that is denominated OSL. As above-mentioned, the electron can follow different paths that do not involve direct recombination, such as a new retrapping process (here illustrated by the transitions 6 and 7) and be further released (transitions 8 and 9).

As is also observed for TL, an electron trapped in a shallow trap is more easily released, since lower temperatures (as RT) might supply enough energy to it. The signal associated with the shallow traps (that is, temperatures below or near RT), is often neglected due to its natural instability (Yukihara; McKeever, 2011).

In the TL measurement, the signal is often recorded while applying an increasing temperature with a constant heating rate. Hence, the curve is peak-shaped, as the trapped electrons are released progressively according to the E_{TR}, which allows for an easier identification of the trap levels in the material than in OSL. In the case of OSL, the most common procedure uses continuous stimulation, in the so-called continuous-wave OSL (CW-OSL). As a result, the curve has an exponential decay because most of the trapped electrons are released at the beginning of the stimulation, and a tail is related to other factors, such as recombination probability and transfer process, until the traps are empty (McKeever; Chen, 1997).

Further, with the use of the CW-OSL, different approaches regarding the stimulation were studied and are currently widespread, including the linear-modulated OSL (LM-OSL), and more recently, the pulsed-OSL (POSL) (Yukihara; McKeever, 2011). These different stimulation methods will be briefly commented on Section 3.2.2.2.

3.2.2.1 Theoretical Models for Optically Stimulated Luminescence

As has been studied for TL, the theoretical models for OSL are varied, and they change according to the assumptions made. The simplest model, for example, will consider only one type of trap for electrons and one recombination centre and will disregard the possible effects of recombination. Attempts to perform a more realistic model need to consider the competing effects, non-radiative centres, and different levels of traps, for example.

This section approaches four examples from the work of McKeever and Chen (1997), in order to illustrate the parameters that could affect the models, and those which are taken into account when modelling OSL curves. It should be pointed out that these models apply to CW-OSL.

In this study, the computerised deconvolution of TL and OSL curves is used to analyse the experimental data, based on general-order kinetic equations. The equations for it are presented later in this thesis, in the Methodology section.

The first and simplest model considers only the presence of one electron trap (T_{R1}) and a hole trap (acting as a R_{C1}), as shown in Figure 3.9a. The ionising radiation creates an electron-hole pair, which are trapped in their respective traps. When light stimulation is applied to the material, the trapped electrons in a concentration n are released and get to the conduction band at a rate f. In this model, the assumption is the electron has only one path from it, which is the recombination with a trapped hole (presented in a concentration *m*), resulting in the emission of light, called OSL.

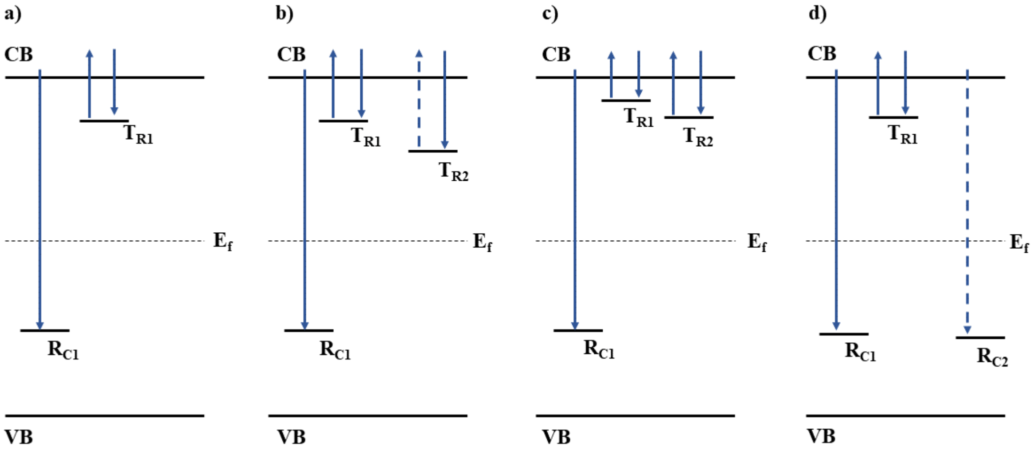

Figure 3.9 - Energy bands' diagram models for OSL considering the (a) simplest model with one electron trap and hole trap, (b) an additional and deep competing trap, (c) competition due to shallow traps, and (d) two recombination centres (R_c), one being radiative and another non-radiative. Based on the work of McKeever and Chen (1997).

To get the equation, two main assumptions need to be considered. One is the charge neutrality, which was also introduced in the TL models (see Equation 3.26) and the non-retrapping probability, resulting in (McKeever; Chen, 1997):

$$I_{CW-OSL} = -\frac{dm}{dt} = -\frac{dn}{dt} = nf \tag{3.56}$$

The rate f can be rewritten in terms of the photon flux Φ and the cross-section σ, as (Bøtter-Jensen; McKeever; Wintle, 2003):

$$f = \Phi\sigma \tag{3.57}$$

Solving Equation 3.56:

$$I_{CW-OSL} = n_0 f \exp(-tf) = I_0 \exp\left(-\frac{t}{\tau}\right) \tag{3.58}$$

Where the n_o is the initial concentration (at $t = 0$) of trapped electrons, I_0 is the initial intensity, and τ is the decay constant, given as $\tau = 1/f$.

The OSL curve shape according to Equation 3.58 is an exponential one, with a fast decay, representing that the electrons are quickly released due to the light stimulation, and recombining in a C_R with no retrapping.

In the next model, another factor is added, which is the presence of a second, and deeper electron trap (T_{R2}), acting in a competing scheme (Fig. 3.9b). If both traps are optically active/sensitive then both will contribute with the OSL signal as described in Equation 3.59 (McKeever; Chen, 1997):

$$I_{CW-OSL} = -\frac{dm}{dt} = -\frac{dn_1}{dt} - \frac{dn_2}{dt} \tag{3.59}$$

The charge neutrality still needs to be considered, in this case:

$$n_1 + n_2 = m \tag{3.60}$$

Where the concentration of trapped electrons *n* is given according to the trap type (1 and 2). Assuming it, the intensity OSL is described as:

$$I_{CW-OSL} = n_{10} f_1 \exp(-t f_1) + n_{20} f_2 \exp(-t f_2) \tag{3.61}$$

Which becomes:

$$I_{CW-OSL} = I_{10} \exp\left(-\frac{t}{\tau_1}\right) + I_{20} \exp\left(-\frac{t}{\tau_2}\right) \tag{3.62}$$

This equation represents an OSL curve composed of two components related to two different trap levels decaying at different times. The curve still has an exponential decay shape, however, it might be not that sharp as in the previous case.

If the second trap is not thermally or optical sensitive, that is, the trapped electron in it could not be released by light stimulation or heating, then it would function as a capturing of electrons and decrease the recombination (in comparison with a sensitive one). This is represented in Figure 3.9b by the dashed arrow. In this case, the concentration of trapped electrons in the second traps type is described by Equation 3.63 (McKeever; Chen, 1997):

$$\frac{d_{n2}}{dt} = n_c (N_2 - n_2) A_2 \tag{3.63}$$

Considering that the concentration of trap of electrons N_2 is much higher than the concentration of trapped electrons n_2 ($N_2 \gg n_2$), then $n_c N_2 A_2 \approx C$, where *C* is a constant. *A* is the probability of trapping. Hence, Equation 3.62 becomes:

$$I_{CW-OSL} = I_{10} \exp\left(-\frac{t}{\tau_1}\right) - C \tag{3.64}$$

The constant *C* will give information about the signal reduction due to the trapping of electrons in the non-light-sensitive traps.

A third approach takes into account the existence of competition of shallow traps, as shown in Figure 3.9c. In this case, there is a probability of the electron being released due to thermal excitation, as the shallow traps are more unstable at RT, which is determined by a rate *p* (as used in the TL models). Consequently, the OSL intensity is described as (McKeever; Chen, 1997):

$$\frac{d_{n2}}{dt} = n_c(N_2 - n_2)A_2 - n_2p \tag{3.65}$$

Hence, the OSL intensity for this case is given by:

$$I_{CW-OSL} = n_{10}f_1 \exp(-tf_1) - n_c(N_2 - n_2)A_2 + n_2p \tag{3.66}$$

The dependence on temperature and probability of retrapping might lead to a long tail represented by the second component, which initially drops and then gets steadier. The temperature dependence in this case could be more noticeable for low values of f.

A fourth approach considers the existence of a radiative recombination centre with a concentration of trapped holes m_1 and non-radiative recombination centre, with concentration m_2, shown in Figure 3.9d. With these conditions one has the equation 3.67 (Bøtter-Jensen; McKeever; Wintle, 2003; McKeever; Chen, 1997):

$$I_{CW-OSL} = n_{10}f_1 \exp(-tf_1) - \frac{dm_2}{dt} \tag{3.67}$$

In this case, the charge neutrality condition is maintained, thus the concentration of trapped electrons n is equal to the sum of the trapped holes: $n = m_1 + m_2$ and $n = n_0 f \exp(-tf)$.

As one of the centres is non-radiative, it will not contribute to the OSL emission, consequently, there will be a reduction in the signal intensity. The concentration of trapped holes can be described by Equations 3.68 and 3.69:

$$-\frac{dm_1}{dt} = -n_c m_1 A_{m1} \tag{3.68}$$

$$-\frac{dm_2}{dt} = -n_c m_2 A_{m2} \tag{3.69}$$

Where the concentration of trapped holes m is dependent on the concentration of free electrons in the CB n_c and the probability of recombination A_m.

Once in the quasi-equilibrium condition $-\frac{dn_c}{dt} \approx 0$, the Equations 3.68 and 3.69 become:

$$m_1 \approx m_{10} \exp(-tn_c A_{m1}) \tag{3.70}$$

And

$$m_2 \approx m_{20} \exp(-tn_c A_{m2}) \tag{3.71}$$

Combining Equations 3.70 and 3.71, one gets:

$$\frac{m_1}{m_2} \approx \frac{m_{10}}{m_{20}} \exp[-tn_c(A_{m1} - A_{m2})] \tag{3.72}$$

McKeever and Chen (1997) assumed that the ratio m_1/m_2 is dependent on time, but if the probabilities of recombination are the same $A_{m1} = A_{m2}$, the ratio m_1/m_2 is a constant k_1. The charge neutrality then can be then rewritten as:

$$n \approx m_1 + \frac{m_1}{k_1} \tag{3.73}$$

Considering $K_1 = 1 + 1/k_1$, one gets:

$$-\frac{dm_1}{dt} = \frac{1}{K_1}\frac{dn}{dt} = -\frac{nf}{K_1} \tag{3.74}$$

Finally, the OSL intensity has a less intense signal which is reduced by the factor $1/K_1$, as given by:

$$I_{CW-OSL} = \frac{1}{K_1} n_0 f \exp(-tf) = I_0' \exp\left(-\frac{t}{\tau}\right) \tag{3.75}$$

If the probability of retrapping is considered for the optically active trap from the fourth case, the OSL intensity is given by:

$$I_{CW-OSL} = \frac{dm}{dt} = -\frac{dn}{dt} = nf - n_c(N-n)A \tag{3.76}$$

Assuming the concentration of trap of electrons N being much higher than the trapped electrons one ($N \gg n$) and $R = A/A_m$. Then $R \gg n/(N-n)$. Equation 3.76 becomes:

$$I_{CW-OSL} = \frac{n^2 f}{NR} = \frac{dm}{dt} = -\frac{dn}{dt} \tag{3.77}$$

Which after integration becomes:

$$I_{CW-OSL} = I_0\left(1 - \frac{n_0 f t}{NR}\right)^{-2} \tag{3.78}$$

In this case, $I_0 = n_0^2 f/NR$. For $I = n^b f/NR$ (general case), Equation 3.78 can be rewritten as:

$$I_{CW-OSL} = I_0\left(1 - \frac{n_0 f t}{NR}\right)^{-\frac{b}{1-b}} \tag{3.79}$$

3.2.2.2 Modes of Operation: Continuous-Wave, Linear-Modulated and Pulsed

When analysing the OSL emission of a material in more detail, there are many parameters which can influence the obtained signal. Among them, one might mention the wavelength of stimulation, the readout temperature, the set of filters used, the detector unit (e.g., the photomultiplier tube), and the stimulation intensity. However, the OSL measurement is usually categorised in different modalities according to the kind of stimulation which has been used in the recording.

The most common approach considers stimulating the sample with a constant wavelength intensity, in a modality called continuous-wave OSL, or CW-OSL. Due to the advance in LEDs properties and the readers' set-up, new arrangements started to be introduced in the

1990s, allowing control of the light intensity. As a result of this, different features of the OSL mechanisms can be more easily assessed.

In this section, the three most approached OSL modalities will be summarised, which were also used in the experimental development of this study.

a) Continuous-Wave OSL

In CW-OSL, the sample is light-stimulated with a constant intensity, commonly used at 90 % (power), from an initial time, t_0, up to the end of the measurement (Fig. 3.10a). The signal is recorded over all the stimulation. Because the light stimulation is done whilst the OSL emission is detected, a set of filters are required to block the stimulation and collect only the OSL signal plus the background from the instrument.

A CW-OSL curve has an exponential decay shape. When the sample is stimulated with light after an irradiation exposure, most of the trapped electrons which are in light-sensitive traps are released at the beginning, and then it progressively releases all of them. In the case of a first-order kinetic, in which retrapping is not assumed, they will recombine directly in a recombination centre and the energy will be emitted in the form of photons, the OSL. Even if there is retrapping occurring in the process, it will delay the recombination and consequently, there will be a long tail, however, the OSL curve will still have a decay shape.

Different levels of traps can be light-sensitive in the material, each one related to a component, which in the CW-OSL are overlapped. Therefore, some studies have approached the deconvolution of the curves, in order to identify those components.

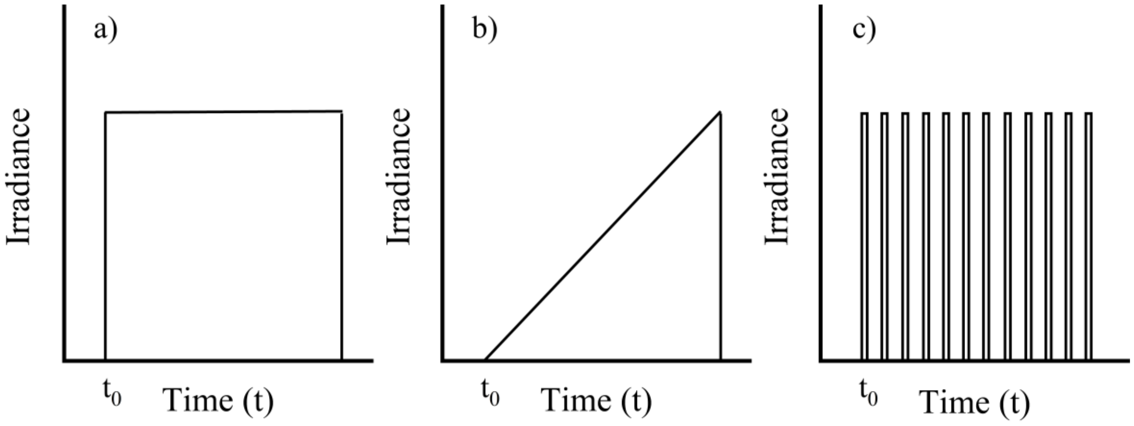

Figure 3.10 - Illustrative schemes for the operation modes for OSL. (a) CW-OSL, (b) LM-OSL and (c) pulsed-OSL. Based on the work of Akselrod, Bøtter-Jensen and McKeever (2007).

It is worth mentioning that usually the OSL emission occurs at a longer wavelength (less energetic) than the stimulation one. Nevertheless, an anti-Stokes shift is possible once the electron traps and the recombination centres are different (Yukihara *et al*., 2022b).

The CW-OSL modality is the most common and widely approach used in both dating and dosimetry since there is no significant variation in the light stimulation and the signal is a decay curve, for example (Yukihara; McKeever, 2011).

b) Linear-Modulated OSL

As advances in LED technology have allowed better control of the stimulation intensity, other variations in the stimulation during OSL have been studied (Yukihara; McKeever, 2011). Bulur (1996) proposed an alternative method in which the stimulation light intensity would increase from zero up to a maximum value during the measurement (Fig. 3.10b), a method which is known as linear-modulated OSL, or LM-OSL.

The LM-OSL curve has a peak-shape. It occurs because an increase in the stimulation intensity leads to a progressive release of trapped electrons. In the beginning, the lower intensity stimulation starts to promote the releasing of trapped electrons, which once they recombine in a radiative recombination centre, emit photons. However, the intensity is usually not enough to promote the release of electrons trapped in different traps' levels. When the intensity increases, more light-sensitive traps are affected, and the output signal is higher. It grows until reaching a peak, followed by a decrease.

And what would be the advantages of the modulated stimulation instead of a constant one? As the recorded curve has a peak shape, it is easier to identify the OSL parameters which are used in dating and dosimetry, in addition, the separation of the easy and hard-to-bleach centres might be facilitated (Bulur, 1996).

Another aspect that might be considered is that because the OSL intensity, in this case, is distributed over a peak area instead of an exponential decay curve, the maximum intensity value will be lower in the LM mode. Thus, if a sample has a high response to a dose when measuring CW-OSL, it could be a limitation due to the overexposure of the photomultiplier tube, which could be solved by changing to LM.

Bulur (2000) introduced a mathematical transformation in order to convert the CW-OSL decay curves data to an LM-OSL curve (then, called pseudo LM-OSL), considering a linear increase in the intensity of stimulation, using experimental data from infrared stimulated luminescence of feldspar, and OSL using green stimulation of K and Na feldspars. Although there is some loss in resolution when doing the conversion, this allows for an LM-OSL curve to be acquired in situation in which there is no proper equipment.

c) Pulsed-OSL

In the 1990s, researchers started to investigate the use of pulses instead of constant stimulation to obtain the OSL emission, in order to better understand the underlying mechanisms associated with the phenomenon (see scheme in Figure 3.10c). In the conventional OSL measurement the signal is recorded during the stimulation and the processes of charge carrier depletion and recombination are overlapped within a single output, which makes it difficult to obtain a physical interpretation. Later, Markey, Colyott and McKeever (1995) studied the application of the same technique applied to α-Al_2O_3:C, recording the signal during and after pulses, and pointed out the possibility of re-reading the OSL signal from a sample, since a short pulse would not be able to deplete all the trapped charges. Further work analysing the same material approached the dosimetric properties by using the same technique (Mckeever; Akselrod; Markey, 1996).

POSL has become more popular because it allows for a more in-depth analysis of the signal and its interpretation, among other advantages. As the signal detection can be made either in a continuous counting operation or a gated one, it extends the approaching possibilities. The utilisation in the gated mode, when the PMT operates in-between pulses, reduces the background contribution as the scattered light from the stimulation is avoided (Yukihara *et al.,* 2022b).

Because the pulse width used in the stimulation is short, the signal depletion per each readout cycle is low. Hence, one might read the signal again, and obtain information about the absorbed dose. A study analysed the depletion in In-Light nanoDots^{TM} OSLD systems and found a reduction of only 0.03 % per readout (Dunn *et al.,* 2013).

Additionally, the possibility of doing temporal discrimination of the OSL, that is, the time-resolved OSL, is a remarkable advantage of this technique. When the measurement is carried out in the CW mode, the contribution of both the time for the charge carrier depletion and the lifetimes of the luminescence centres, are overlapped. However, the depletion step occurs when the sample is being stimulated. If the signal between stimulations is recorded, it is possible to get the contribution only from the relaxation time when the excited centres go to the ground state due to the recombination process (radiative decay time or lifetime of the luminescent centre). Therefore, using a stimulation pulse sufficiently shorter than the centre lifetime, and measuring the centre decay after the pulse is over, one might estimate their lifetime values (Yukihara; McKeever, 2011).

Theoretical considerations, simulations, and practical aspects of the POSL technique and the time-resolved OSL analysis approach were already reported (Chithambo, 2007a, 2007b). The use of it also has been applied to different materials such as quartz (Kim; Choi; Hong, 2011), BeO (Bulur; Saraç, 2013), natural zircon mineral (Bulur; Kartal; Saraç, 2014), and $YAlO_3:Mn^{2+}$ crystals (Zhydachevskii *et al.,* 2016).

3.2.3 Applications of Thermoluminescence and Optically Stimulated Luminescence

The phenomenon of TL was first described in 1663 by Robert Boyle. As of that point in time, several reports regarding this emission had been made, but the focus and diversification of fields of application were observed much later, posteriorly to the pioneering works of Randall and Wilkins (1945a, b), and Garlick and Gibson (1948). The work of Daniels, Boyd and Saunders (1953) proposed the TL as a research tool. It summarised some applications of the technique, which could be used in dosimetry (as the signal intensity might be proportional to the amount of absorbed radiation); identification of the crystal impurities (as the impurities would lead to a specific emission and TL glow curve shape) in spectroscopy; to investigate radiation damage, because radiation can induce defect production, which is related to the luminescent emission; ancient pottery dating and stratigraphy (since the local environment at the time the rock was formed influences its chemical conditions and hence a correlation with the TL might be done); as well for age determination, considering that a sample is continuously exposed to environmental radiation.

Despite all the potential applications above-mentioned, some of them showed to be more successful, and set a base for further investigations. These are nowadays widespread and well consolidated, such as dosimetry, dating and geo-archaeological studies.

Once it was established that the TL emission was related to the absorbed dose, it was easier to correlate the TL signal with the age of a rock or other material, and in the 1950s studies started to approach the technique as a tool for dating. The base to estimate the age is in the fact that the sample accumulates an amount of dose per year, which results in an amount of TL per unit of dose. By measuring the accumulated TL signal, the age is conveniently estimated (McKeever, 1985).

However, dating did not get restricted only to rocks. In the 1970s, studies used the TL to date archaeological pottery, tiles, and bricks. In the case of ceramics, the technique can estimate the last time when the signal was erased thermally, that is when the material was burnt during its manufacture, and thus, when it was produced. Moreover, tests were performed with art ceramics to confirm their authenticity, which made the technique application even more popular (Aitken, 1985; Chen; Pagonis, 2019). Since then, TL has been widespread and successfully applied to estimate the age of excavated objects (Polikreti; Michael; Maniatis, 2003), coastal aeolianites (Murray-Wallace *et al.*, 2010), bricks (Sabtu, *et al.*, 2015), stalactites (Yee; Mo, 2018), freshwater fossil shells (Vichaidid; Saeingjaew, 2022), volcanic glasses (Rodrigues; Huot; Keen-Zebert, 2022), among others.

In geology, most of the studies which make use of TL, have an interest in either dating/thermochronology or investigating the properties of minerals, which are commonly said to be naturally doped (Brown; Rhodes; Harrison, 2017; Qiu *et al.*, 2019). Some minerals exhibit a natural TL intensity, which is so intense that it could be easily measured or even observed by the naked eye (McKeever, 1985). For example, one might cite studies dedicated to investigating the potential of using minerals for dating and retrospective dosimetry (Mahmood *et al.*, 2022; Ogundare *et al.*, 2016) and the understanding of the defects and lattice parameters (Kalita; Wary, 2016; Sawakuchi; Dewitt; Faleiros, 2011). Furthermore, TL has also been applied in the research of meteorites because their TL signal might be used to deduce the orbital temperatures and ageing (from the fall), in addition, the metamorphism degree might be inferred due to the change in the TL sensitivity (Biswas *et al.*, 2011; Bossin *et al.*, 2017; Bull, 1986).

TL has also been approached to analyse irradiated foods since the late 1980s, albeit of a lesser extent than the previously mentioned branches (Göksu-Ögelman; Regulla, 1989). The technique was applied to identify irradiated samples on different food types (Kiyak, 1995; Shin; Kim; Lim, 2012), and also using food as a possible fortuitous dosimeter for retrospective and accidental dosimetry (Karampiperi, Theologitis; Kazakis, 2022; Monaca; Fattibene; Bortolin, 2013).

As regards the OSL, as it has a similar theoretical base to TL, the applications are found to be quite the same. However, OSL dosimetry started to be a steadfast application after its successful use in geological dating (Yukihara; McKeever, 2011). Dating using OSL shares the same principles, with the more noticeable difference being the way in which the sample signal was erased. Whilst the burning/exposure to high temperature dictates the zero-age of the sample in TL dating, for OSL it is due to the light erasing, which is usually adopted as sunlight exposure. It showed to be useful for sediments dating, consequently, the method quickly gained importance and was spread in geology.

The method of OSL as a tool to age sediments was proposed in the 1980s, by the work of Huntley, Godfrey-Smith and Thewalt (1985), and in about a decade, protocols and procedures were established (Wintle, 1997), and an entire branch in OSL was opened by what started to be called of optical dating after the publication of the book “An Introduction to Optical Dating” by Aitken (1998), a breakthrough. Since then, the studies have advanced and improved the methodology, which has been used for dating samples originating from different environments (Galbraith; Roberts, 2012; Murray; Olley, 2002; Tatumi; Rossetti; Soares, 2020; Tsodoulos *et al*., 2016). Recent studies have tried to extend the upper limit of the optical dating by using violet-stimulated luminescence (VSL), and findings so far are encouraging and indicate this to be a reasonable approach (Ankjærgaard; Jain; Wallinga, 2013; Colarossi *et al*., 2018).

OSL has an advantage over TL, which is there being no need to heat the sample, hence the thermal quenching effect is removed, and a simpler apparatus is required (Yukihara; McKeever, 2011). Since the 1990s, studies have pointed out the impressive TL, and later, OSL signal and dosimetric properties of Al_2O_3:C (Akselrod *et al*., 1990; Marvey; Colyott; McKeever, 1995). Those works started a boom in the development of OSL dosimeters, and nowadays there are well-established materials in use as well as several studies looking for new ones (Yukihara *et al*., 2022a).

Because TL and OSL luminescent signals are proportional to the absorbed dose (limited to a range which can vary depending on the material’s properties), it enables the use of the material as a radiation detector. This is one of the most explored branches when considering TL and OSL, therefore, it is detailed separately in the next section.

3.2.3.1 Thermoluminescence and Optically Stimulated Luminescence Dosimetry

Measuring radiation exposure in hospitals, human beings, and the environment is important to ensure that organisms are not exposed to high levels of radiation, which might lead to harmful effects. Based on this, by dosimetry, the measurement or calculation of radiation doses is done, and luminescent dosimeters based on TL and OSL emission have been extensively used.

Depending on the application, the dosimetry can be named differently. The following classification was taken considering the works of McKeever (1985) and Bøtter-Jensen, Mckeever and Wintle (2003):

a) Personal Dosimetry

In personal dosimetry, the aim is to assess and limit the radiation dose delivered to individuals, to avoid an absorbed dose by a person being above the limits determined by

International Commission on Radiological Protection (ICRP). The limit values are related to the maximum equivalent dose values which are set to not cause injuries to a person while working.

In this case, the dosimeter needs to be worn by the user, according to its design, which can be a ring, a badge, or another accessory. Rigorous control of the manufacturing of those dosimeters is necessary to obtain good reproducibility.

There are already several options of TL commercial dosimeters available, based on different matrixes such as lithium fluoride (LiF), alumina (Al_2O_3), calcium fluoride (CaF_2), and calcium sulphate ($CaSO_4$), among others, which are found in different combinations of doping (Duragkar *et al.*, 2019). Regarding OSL, the main detectors used in personal dosimetry are made of carbon doped alumina (Al_2O_3:C), and beryllium oxide (BeO) (Yukihara; McKeever, 2011). Most of them have an effective atomic number close to the human body, which is an advantage for using in personal dosimetry.

b) Environmental Dosimetry

There is natural radiation exposure in the environment due to the presence of natural radioisotope elements (U, Th, K-40) in the surroundings and from cosmic rays. Moreover, the irradiation from man-made sources needs to be considered, including nuclear waste disposal, and emissions from nuclear plants and industries. Environmental dosimetry encompasses the monitoring of all of them.

Different from personal dosimetry, it is not necessary to seek tissue equivalence in phosphors, hence, the dose is measured in terms of absorbed dose. In addition, as the dosimeters used for environmental measurements are exposed to more drastic conditions, they need to be stable to the changes in the weather, such as light and temperature variations.

Some of the same dosimeters used in personal dosimetry are also used in environmental dosimetry, such as Al_2O_3:C, CaF_2, and $CaSO_4$ since they usually display a high TL and/or OSL emission, that is, a good sensitivity (Bøtter-Jensen; McKeever; Wintle, 2003; Yukihara; McKeever, 2011).

c) Medical Dosimetry

In medicine, radiation is used as a method of treatment, for example in radiotherapy, as well as it is used in diagnosis. Therefore, to ensure that the treatment is delivering the specific dose of irradiation which was calculated to be a compromise of successful treatment and avoiding side effects, or that the patient under a medical exam is not receiving a dose above the determined limits, radiation doses in those environments are measured. Medical dosimetry aims to support this.

As in personal dosimetry, the radiation dose is measured in terms of tissue equivalence. Moreover, it can be either measured *in vivo* or not. In the first case, it is also called real-time dosimetry and can give information about the dose or the rate at which it is being delivered.

The same TL and OSL detectors used in personal dosimetry are also used for medical dosimetry, as the focus is on the absorbed dose by the person.

d) Retrospective Dosimetry

Retrospective dosimetry concerns the determination of the absorbed radiation dose in situations where there were no conventional dosimeters at the time of the exposure. From that, one might still subcategorise into dating and accident dosimetry. As regards dating, the aim is mostly to determine the absorbed dose by materials exposed to natural background radiation, whilst in accident dosimetry, the aim is to determine the absorbed dose after an event, such as a radiation event. In the latter case, the materials available at the incident place are used, which might be bricks, porcelain, etc.

Studies have investigated the use of different fortuitous materials and showed that materials such as clothing, jewellery, and electronic devices have the potential for being used as luminescent detectors of radiation (Bailiff; Sholom; McKeever, 2016; Discher; Bassinet; Woda, 2023), as well as porcelain (Oks *et al.*, 2011), common salt (Spooner *et al.*, 2012), and building materials (Yasmin *et al.*, 2022).

3.2.3.1.1 Thermoluminescence and Optically Stimulated Luminescence Dosimeters: Properties of Interest

Nowadays there are widespread TL and OSL dosimeters available commercially and for which the properties have now been long studied. However, the ideal properties will vary from dosimeter to dosimeter depending on the application. For example, the sensibility range might depend on the usual radiation dose used in the place or the limits determined by the legislation. The tissue equivalence will be an advantage if the focus is to determine the absorbed dose in an individual. Choosing the TL or OSL signal to be detected might depend on the apparatus available and the exposure conditions. The photon energy response should be considered according to the radiation qualities as well.

Because one material would not fulfil all the ideal features for use in a wide range of applications and exposure conditions, research on new materials for ionising radiation dosimetry using TL and OSL brings forth other options. Furthermore, the luminescent mechanisms and related phenomena might be elucidated.

Therefore, what would be the main properties one should address when investigating materials for TL and OSL dosimetry applications? Evidently, there are several aspects to be considered which depend on the final application. However, some of them are more common.

Table 3.4 summarises the main aspects regarding dosimetry application to be considered when investigating a material. It does not intend to be exhaustive, but the references cited are excellent studies to be based on.

Table 3.4 - General and more common requirements for analysing materials for TL and OSL dosimetry.

	General Requirements	**References**
Linearity (in dose-response)	The dose-response curve relates the absorbed dose by the material with the signal intensity. The higher the irradiation dose, the higher the concentration of trapped electrons, hence, the TL and OSL intensities. However, due to the material's characteristics, this response might have a non-linear behaviour, some hypotheses rely on the presence of deep traps which are involved in capturing electrons and changing the sensibility of the material, which might induce a supralinear trend; or the saturation of the traps, which establish an upper limit of absorbed dose in the material, that is, a sublinearity. Ideally, the dose-response curve should have a linear behaviour in the range of interest, which would avoid the necessity of doing corrections.	1, 2, 3, 4, 5
Sensitivity	The sensitivity is related to the intensity of the signal per unit of absorbed dose and mass. In general, one desires to get a response which is detectable over a wide range of absorbed doses. Thus, a high sensitivity might be required in the application as environmental and individual monitoring, as the absorbed doses are usually low in comparison to accidental dosimetry. Sensitivity is evaluated regarding the whole dosimetry system instead of only the material though. Moreover, as the physical form and annealing might influence the signal, they also would influence the sensitivity.	2, 3
Reproducibility	TL and OSL signals are dependent on both the material and experimental conditions. By being reproducible, the dosimetry system should not show a significant variation when estimating the absorbed dose. If the material has no dependence on the thermal and/or dosimetry history, then it will contribute to obtaining better reproducibility.	2
Photon energy response	Personal and medical dosimetry concern the measurement of the absorbed dose in the individual's body. Therefore, it is desirable for the material to have a photon energy response similar or proportional to the absorbed dose in the medium of interest, hence, to be tissue equivalent. The targeted behaviour is to have a flat relative response in the range of use. Relative values higher than one mean an overresponse to the photon field, and lower values represent an under response. The effective atomic number (Z_{eff}) was introduced to get a value in characterising the energy response and to facilitate the interpretation, which is given by the following equation: $Z_{eff} = \sqrt[m]{\sum_i a_i Z_i^m}$ Where a_i is the fraction of the electron content for an element i, with respective atomic number Z_i, m is a factor that may vary between 3 and 4 (usually adopted 3.5). The tissue is calculated to have a $Z_{eff} = 7.35$, therefore a material with a close value should present a similar response.	1, 2, 3, 4, 5

Table continues in the next page.

	General Requirements	References
Angle dependence	The TL and OSL signal response might be influenced by the angle of the incident irradiation. In some cases, it is related to planar geometry. A dosimetry system with little angular dependence is desirable.	1, 4
Dose-rate dependence	The dosimeter should get a response proportional to the absorbed dose, independent of the rate at which it was delivered. However, due to the use of high dose rates (more than 10^6 Gy per second) in radiotherapy, for example, a discriminated response according to the dose-rate would be valuable.	1, 2, 5
Possibility of reusing	The possibility of reusing the material is important because of its practical and economical aspects. However, special attention needs to be given to the process of erasing the residual signal, either by heating or bleaching once the previous irradiation dose or even the erasing method chosen may affect the material sensibility.	1, 5
Stability	Dosimetry systems may be exposed to different conditions of temperature and lighting, which perform the role of stimulation in TL and OSL, respectively. Therefore, more stable signals would be addressed. For example, in the case of TL, peaks in temperatures higher than 150 °C are meant to be more stable; and for OSL, a previous heat treatment might be done to remove the influence of shallow traps, or a longer elapsed time considered between the irradiation and the measurement (hence, the fast decay component would not influence the detected signal).	2, 5
Annealing	In the case of TL, an annealing procedure aims to erase the TL signal to zero, that is, a resetting mechanism. Annealing also re-establishes the thermodynamic defect equilibrium which is disturbed due to the irradiation. Therefore, having a well-established annealing protocol allows reaching higher reproducibility.	3, 5
Limit of detection	The limit of detection regards the lowest and highest values of dose which would lead to a detectable signal. In the case of the highest one, determining a single value is more difficult due to the non-linear behaviours found when getting close to the saturation part of the curve. Hence, it is usually taken as the endpoint within the linear range. Concerning the lowest limit, the standard determines it to be three times the standard deviation of the signal at a zero-dose recording.	3, 5
Fading	The unintentional loss of the signal is called fading. This is a tricky issue because it may lead to the underestimation of the absorbed dose. Thermal fading is related to signal loss even at room temperature due to the trapped charges escaping. In addition, other mechanisms such as quantum mechanical tunnelling and localised transitions may lead to fading.	3, 5
Physical form	The signal may be influenced by the physical form of the detector material. For example, for powder materials, granulometry may induce changes in sensitivity.	3
Simple curve shape	In the case of TL, a curve composed of single isolated peaks are easier to analyse, consequently, the dose-response curve would be more conveniently obtained.	5

Table's end.

References: [1]Yukihara, McKeever and Akselrod (2014); [2]Yukihara *et al.* (2022a), [3]Bos (2001), [4]Olko (2010), [5]McKeever (1985).

3.2.4 Considerations on the Models for TL and OSL

The models concerning TL and OSL mechanisms have been developed for some decades since the pioneering works in the middle of the 1950s (Garlick; Gibson, 1948; Randall; Wilkins, 1945a, 1945b). Predicting the behaviour of those phenomena involves complex numerical calculations to assess the non-linear features, which have been better understood due to advances in computing and its use in such calculations (McKeever; Chen, 1997).

The models of the phenomenological energy band to explain TL and OSL range from the simplest one, which is known as one trap one recombination centre (OTOR), which can consider (second order kinetic) or not (first order kinetic) the probability of retrapping, to models considering a multi-trap system (IMTS), tunnelling localised transitions (TLT), as well as the mixed order kinetics (MOK) and general-order kinetics (GOK) (Bos, 2001; Kitis; Polymeris; Pagonis, 2019; Peng *et al*., 2021). The search for deepening the understanding of the phenomena in materials widely used in dating, such as quartz and feldspar, has shed light on the models, and improvements and discussions arose from that (Jain; Guralnik; Andersen, 2012; Wintle; Adamiec, 2017).

As there is a variety of models which have been studied in this area when dealing with experimental data obtained in TL and OSL measurements, it is necessary to do a thorough analysis of the application of those models because the parameters might vary within physical acceptable ranges (Pagonis; Kitis, 2006), and one wants them to be physically meaningful.

Pagonis and Kitis (2012) stated the prevalence of first-order kinetic peaks in dosimetric materials by analysing the TL signal. According to their work, there is a correlation between the strength in which the competition occurs and the kinetic order. The stronger the competition, the lower the retrapping probability and the b value. Furthermore, it explains why some materials do not show a shift in the peak temperature with different doses, which is a feature of the first-order kinetic. However, the authors highlight in their conclusions that the general-order kinetic model is not an excluded possibility, even if it seems to be more rarely observed in experimental data. Therefore, it shows the importance in having demonstrations supporting the model adopted.

Yukihara (2022), addressing the tools used to analyse the TL and OSL, also argued that the first-order kinetic has been the prevailing behaviour found in materials due to the competition between trapping pathways and the retrapping, or even because of the monomolecular recombination, in which trapping and recombination centres are strongly related.

Therefore, what would be a compromise approach when fitting TL and OSL curves? Should the first-order kinetic be favoured instead of a general-order one? Based on those recent discussions, one needs to consider that first-order kinetic behaviours would be prevalent, but not solely that.

Different methods of analysis may be used to try to identify the characteristic of the traps related to the TL phenomenon such as various heating rates, initial rise, step annealing, T_M-T_{stop}, peak shape, and curve fitting, among others. The latter is also applicable to OSL. Moreover, the recombination process may be clarified using spectral measurements, and for the OSL case, the pulsed mode as well (or POSL) (Chen; Kirsh, 1981; McKeever, 1985; Pagonis; Kitis; Furetta, 2006; Yukihara; McKeever, 2011; Yukihara, 2022).

In this study, the deconvolution of the TL glow and OSL decay curves was performed, to try to identify the parameters related to the traps in the material. When feasible, those supplementary methods were used to base the deconvolution, to seek a more accurate fitting,

3.2.5 Photoluminescence

Photoluminescence, or PL, is the phenomenon of light emission as a result of optical excitation. When excited with light, a material may absorb the energy which allows an atom or molecule to go from the ground state to an excited one, or in the case of semiconductor crystals, from the VB to the CB due to the electron-hole pair created. The system goes in a non-radiative relaxation process in which interactions within the crystalline structure or molecular vibrational modes (and rotational ones), and results in the excited electron going to a more stable excited level. After the lifetime related to the excited state, which may span from picoseconds to seconds, the system returns to the ground state, and in this final transition, energy is released in the form of photons, which occurs in a radiative way. This light emission is called photoluminescence, or PL (Brundle; Evans; Wilson, 1992).

PL may be subcategorised into two processes, fluorescence and phosphorescence. Fluorescence emission takes place whilst there is the absorption of radiation and stops as soon as the radiation ceases, whilst the phosphorescence shows a delay between the absorption and the time when a full emission intensity is reached. Due to this difference in time, the processes might be distinguished by considering the delay time. Nevertheless, the more proper and practical way to distinguish them is by changing the temperature in which the process is carried out. Fluorescence is fundamentally not dependent on temperature, whilst the decay emission of phosphorescence is strongly influenced by temperature (McKeever, 1985; Sunta, 2015).

Figure 3.11a depicts some schematic mechanisms that may happen during the fluorescence phenomenon according to the theory presented in the book by Sunta (2015). The simplest mechanism of fluorescence emissions occurs when the atom returns from the excited level E_{xc} to its respective ground state N and re-emits photons with energy equal to the absorbed (case 1, Figure 3.11a), which is termed resonance fluorescence. There may exist intermediate levels between the ground state and the excited one, such as the levels here named A and B. The transition from the excited level to those intermediate levels leads to the emission of photons of longer wavelengths than the absorbed wavelength (case 2, Figure 3.11a). This energetic difference is known as Stokes shift and is the most common case of fluorescence. There are also cases in which thermal energy may be absorbed from atoms in the surrounding area after the light excitation, which allows the raising from excited level E_{xc} to a more energetic one E_{xc}', which results in an emission wavelength shorter than the absorbed one (case 3, Figure 3.11a). Similarly, if the thermal energy is absorbed before the light excitation, a raising from a ground state *N* to a more energetic one *N'* may occur, resulting in an emitted fluorescence with energy higher than the absorbed photon (case 4, Figure 3.11a). In those cases, in which the absorption is with a longer wavelength than the emission, the process can be said to follow an anti-Stokes shift.

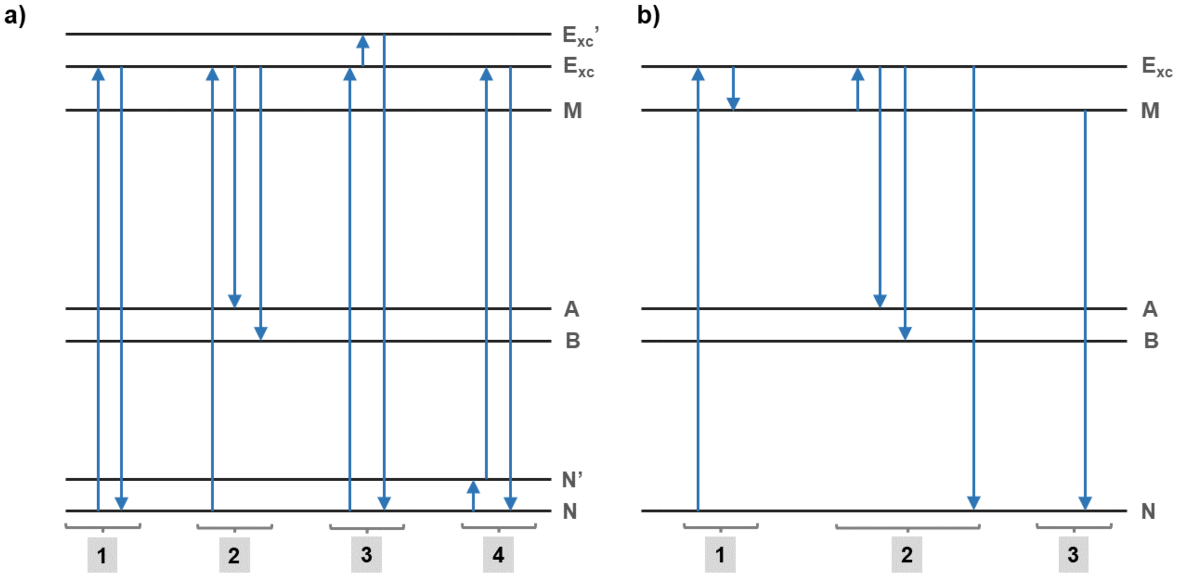

Figure 3.11 - Illustrative scheme for (a) fluorescence and (b) phosphorescence emissions by using energy level diagrams. Based on the work of Sunta (2015). In part a, case 1 represents the resonance fluorescence, 2 represents the fluorescence with a Stokes shift, whilst 3 and 4 stand for anti-Stokes shift fluorescence. In part b, the first case shows an excitation transition, 2 stands for a temperature sensitive case, and 3 for a long-lived case.

Different from fluorescence, in phosphorescence the electron is brought into a metastable level *M* after the excitation process. The transition from the ground state *N* to *M* is not allowed, therefore it might occur indirectly (transition 1, Figure 3.11b). If the energy difference between *M* and E_{xc} is small, and considering thermal equilibrium with the surrounding, the electron may gain energy to reach E_{xc} again. Once the electron is at E_{xc}, the same transitions observed in fluorescence may take place (transition 2, Figure 3.11b). The thermal excitation from *M* to E_{xc} is responsible for speeding up the depopulation of the state *M* (Sunta, 2015). Transition 3 in Figure 3.11b represents the case of a long-lived phosphorescence.

PL is a widely used and well-established technique which can be used to assess material properties in the scope of surface and microanalyses, allowing for a (semi-)qualitative study to correlate structure and material composition with their electronic states. The results might also shed light on the presence of impurities and defects in the material, the band gap characteristics, and the homogeneity by doing spatial distribution of the PL intensity (Brundle; Evans; Wilson, 1992; Perkowitz, 1993).

3.2.6 Radiofluorescence

The luminescence emitted by a material during exposure to X-rays or nuclear radiations such as β and α particles, or gamma rays, that is, ionising radiation, is called radioluminescence also known as radiofluorescence, or RF. This phenomenon can be easily differentiated from other delayed luminescence techniques such as TL and OSL, as the light is emitted while the exposure occurs (Schmidt *et al.*, 2015; Sunta, 2015).

The mechanism behind the emission is related to the excitation of the luminescent species in the targeted material. The irradiation of either incident electrons or the production of secondary electrons due to the X-ray photons or nuclear particles is responsible for triggering the excitation (Sunta, 2015). Because different elements may present a characteristic emission behaviour, this technique is important in the elemental analysis of trace impurities.

Radiofluorescence has been extensively used for investigating some materials, with the aim of performing dosimetry and dating on, for example, quartz. Moreover, it is considered a valuable approach to reveal the underlying mechanism of charge trafficking in crystals of quartz (Krbetschek; Trautmann, 2000; Schmidt *et al.*, 2015).

3.3 Materials Characterisation

The analysis and characterisation of a material allow us to figure out its properties, hence, investigate its potential application. The number of techniques used for materials characterisation is wide, and the decision about which one to use will depend mainly on the type of material, the property of interest, and the degree of specificity.

Most of the methods rely on the idea of the interaction of a beam such as a beam of photons, electrons, or ions, with the material being analysed. As a result of the interaction, one may monitor the changes in the beam or the signals which come from the sample, for example, ejected electrons or X-rays. As different processes occur at the same time, some techniques may be coupled in a single device. For example, there is scanning electron microscopy (SEM) that gives the image of the material, from which the morphology and homogeneity may be evaluated, moreover, it can be coupled with electron dispersive spectroscopy (EDS), giving information about the composition, as the signal required for both comes from the interaction of electrons with the matter.

Among the information which one might assess by using techniques of characterisation, the main ones are the elemental composition, chemical state, phase identification, type of structure and its features, morphology, and homogeneity.

In this work, two techniques other than the luminescent ones were used. X-ray diffraction (XRD) to evaluate the crystalline structure of the synthesised crystal, the presence of secondary phases, and to estimate the crystallite size. Second, electron spin resonance (ESR), gives information about the presence of defects in the material, as well as its identification. Therefore, the next two sections give a brief overview of these techniques.

3.3.1 X-ray Diffraction

The study of crystal structure is made through diffraction, it may be by photons, neutrons or electrons. Diffraction depends on the crystal structure and the incident wavelength. When the incident wavelength is in the order of thousands of Å, the superposition of the elastically scattered wave by single atoms of a crystal will result in ordinary optical refraction. However, when the incident wavelength is similar to or smaller than the lattice constant, the result of the interaction will be diffracted beams in directions quite different from the incident one (Kittel, 2005). This property is the interest because this difference can be related to the structure of the material.

X-rays are electromagnetic radiation constituted of wavelengths, which can vary between 0.1-100 Å. Since these wavelengths fall in the condition mentioned before, in which they are of the order of the lattice constant, X-rays are suitable to be used as a tool in structure characterisation by XRD. In XRD, the wavelength range used is about 0.6-3.0 Å (Ladd; Palmer, 2003).

The X-rays are produced by the rapid deceleration of charged particles with sufficient kinetic energy. For XRD, electrons are the charged particles most commonly used. The common method of generation consists of applying a high voltage (of some tens of thousands of Volts) between two electrodes. Due to this high voltage, electrons with very high velocity are drawn out from the X-ray tube, or cathode, and collide with the anode, which is a metallic target, such as cobalt, molybdenum and copper. The result of this strike is the production of X-rays at the point of impact which radiate in all directions (Cullity; Stock, 2014; Waseda; Matsubara; Shinoda, 2011).

The X-rays produced consist of various wavelengths, and the curve behaviour depends on the target material (as shown in Figure 3.12), as well as on the applied voltage. Those X-rays are called continuous, polychromatic or white radiation as they constitute a mixture of wavelengths. Another common name given to them is *bremsstrahlung* as they are produced by deceleration (Cullity; Stock, 2014). However, most of the kinetic energy from the striking electrons is converted into heat with about less than 1% being converted into X-rays (Waseda; Matsubara; Shinoda, 2011).

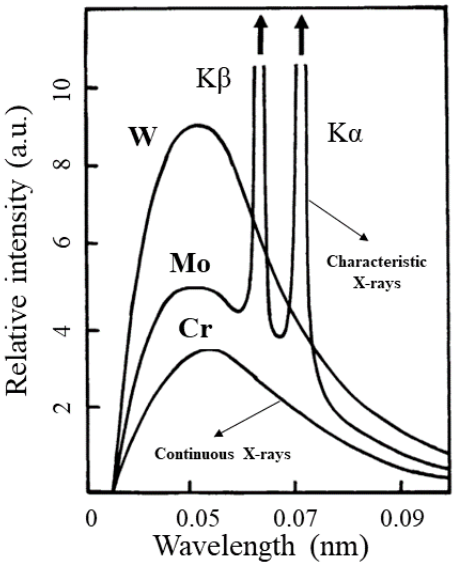

Figure 3.12 - Schematic X-ray spectrum of tungsten (W), molybdenum (Mo) and chromium (Cr), showing characteristic and continuous X-rays. Reference: adapted from Waseda, Matsubara and Shinoda (2011)*.

Nevertheless, the X-ray spectrum generated from this decelerating process is not only constituted by the continuous X-rays' contribution. For a certain and higher value of voltage, called the critical value, which is characteristic of the target material, a maximum sharp intensity appears. This occurs because the impinging electrons give sufficient energy to inner electrons in the target atoms, exciting them, and inducing the photoelectric effect. Hence, electrons from higher energy levels fall back to those inner levels (holes). The transition is followed by the emission of X-ray radiation, with a specific energy, the characteristic X-rays ($\lambda_{c.\ x\text{-}ray}$). The emission in the spectrum is discrete (Fig. 3.12) because the wavelength of the X-ray is related to the difference of energy between the two levels, E_1 and E_2 (Ladd; Palmer, 2003):

$$\lambda_{c.\ x-ray} = \frac{hc}{|E_2 - E_1|} \tag{3.80}$$

The characteristic X-rays are also named characteristic lines. They are of great interest for use in X-ray diffraction because most of the experiments require monochromatic or nearly

---

* Permission given by Springer Nature. Reconstructed from the the book: Waseda, Matsubara and Shinoda, X-ray Diffraction Crystallography: Introduction, Examples and Solved Problems. 1st ed. Heidelberg: Springer-Verlag Berlin Heidelberg, in Chapter 1 – Fundamental Properties of X-rays, 2011. Copyright Springer Nature (2011).

monochromatic radiation (Cullity; Stock, 2014). In commercial equipment, as both continuous and characteristic are produced, a filter or monochromator is used.

In Figure 3.12, the characteristic radiation begins to appear for a voltage higher than 20.01 kV, which is the critical value for molybdenum (Mo). The increase in the voltage will induce an increase in the lines' intensities, but the wavelength stays the same. The nomenclature is related to the inner transition between the electronic shells in the material, thus the letter *K* represents that the electron came from a higher energetic level to level/shell *K*, and the Greek letter in subscript gives the original shell. In the example of Figure 3.12, K_α and K_β represent transitions from an electron of *L* and *M* shells into a vacancy in *K*, respectively (Cullity; Stock, 2014).

But when was the association of the result of the interaction of X-rays and matter (that results in diffraction patterns) made?

In 1913, W.L. Bragg gave the first mathematical explanation for the position of X-ray diffraction spots. When a train of parallel waves falls upon a specular reflecting surface, the reflection from any two points on the surface will produce waves which are in phase with the reflected beam. However, experimentally it is observed that this condition is true only for some angles of incidence θ. This situation is solved when the distance between two parallel reflecting planes is taken into account. Therefore, it is only necessary to point out that reflection from any point on a plane is in phase, as well as being in phase with any point on another plane, resulting in total reflection which is a sum of both, that is, constructive interference (Woolfson, 1997).

Figure 3.13 shows the waves in phase for the same plane and different planes with a distance d, in between. When two incident rays 1 and 1a from the beam strike respectively two atoms of the same plane, A_3 and A_4, they are scattered in all directions, however only directions 1' and 1a' are completely in phase (constructive). This is because of the difference in the pathway between the wavefronts XX' and ZZ' is null (Cullity; Stock, 2014):

$$QA_4 - A_3R = A_3A_4 \cos\theta - A_3A_4 \cos\theta = 0 \tag{3.81}$$

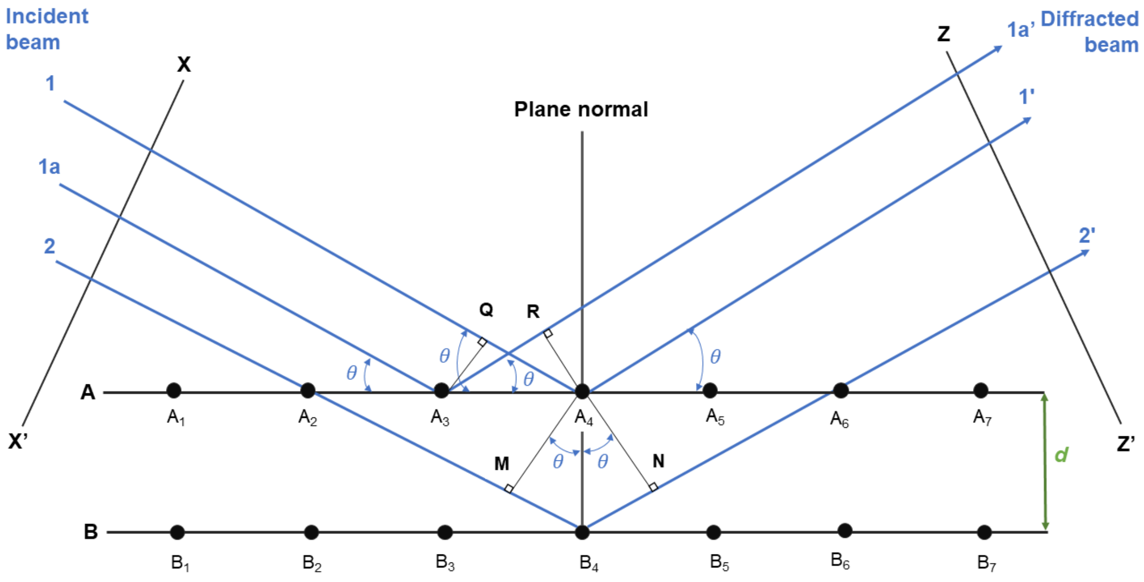

Figure 3.13 - Illustrative scheme for diffraction of X-rays by a crystal. A and B stand for plans, blue lines stand for the beams, and the dots for the atoms. Based on Cullity and Stock (2014).

This will be valid for all atoms in the same plane, as well as for all the planes separately. The path difference of rays 1 and 2, where 2 is striking an atom in a different plane, is given by:

$$MB_4 + B_4N = d\sin\theta + d\sin\theta \tag{3.82}$$

The scattered rays 1' and 2' will be totally in phase if the difference in the pathway is equal to an integer n of wavelength λ, which results in:

$$n\lambda = 2d\sin\theta \tag{3.83}$$

Relation 3.83 is called Bragg's law and is the essential condition that must be met for diffraction to occur, that is, constructive interference. The integer n is also called the order of diffraction. The distance between the planes d is also named d_{hkl}, where hkl represents the plane intercepts the crystallographic axes, that is: a/h, b/k and c/l, and a, b and c mean unitary cell parameters.

Scattering may occur in three different modes (Cullity; Stock, 2014):

a) If scattered by atoms arranged randomly in space, it occurs in all directions and the signal is weak.

b) If scattered by atoms periodically arranged in space, such as in a perfect crystal, there will be two cases: (i) scattering will occur in most directions, but the scattered rays will cancel each other (destructive interference), or (ii) in few directions which meet with Bragg's law, the scattering will be strong, and amplitude summed due to the constructive interference.

Crystalline materials are constituted of regularly spaced atoms, with a distance d in between. The arrangement of the atoms is a feature of each material. Hence, when exposed to the characteristic wavelength, there will be diffraction for the angles which meet with the Bragg condition. The resulting diffractogram of the crystalline structure is constituted of peaks in different Bragg's angles of diffraction. The number of the peaks, their positions and intensity ratios with the most intense peak (called 100 % intensity peak), give information about the structure and the material. For non-crystalline materials, because there is no long-distance periodic arrangement of the atoms, the curve has no sharp peaks of diffraction. Therefore, X-ray diffraction is based on this property of constructive interference.

The basic setup of a diffractometer is designed using a Hull/Debye-Scherrer camera. A source of monochromatic radiation is used to produce the incident characteristic X-rays (the monochromatic radiation may be obtained by filtering the spectrum and removing the continuous radiation mentioned before either coupled to the tube or the detector), which strikes the sample to be analysed. The sample is positioned in the middle of a circle (the diffractometer circle) on a flat plate. The X-rays are diffracted by the specimen, and the constructive waves which follow Bragg's Law are collected in the detector (Cullity; Stock, 2014). In the Bragg-Brentano configuration, the specimen is usually kept fixed in the centre position. The tube (source) may either be fixed, and the receiving slit varied or both tube and receiving slit varied. The rotation is based on the diffraction angle θ or its multiple 2θ (Jenkins; Snyder, 1996).

XRD is a powerful technique for characterising materials and is useful not only for identifying the crystalline phase(s), despite it being a notable property of interest. Other information that may be obtained from the technique includes the determination of strain and crystallite size, as the width of the diffractogram peaks is related to the crystallinity degree; the thickness of a crystalline film; the evaluation of defects on the surface by doing an X-ray topography; preferred orientation, which is observed by the ratio between the diffracted peaks; and even the atomic arrangements in amorphous materials (Brundle; Evans; Wilson, 1992).

3.3.2 Electron Spin Resonance

Electron spin resonance (ESR) also known as electron paramagnetic resonance (EPR) is a technique based on the property of absorption of electromagnetic radiation usually in the microwave frequency region, by a paramagnetic sample which is exposed to an external magnetic field. Paramagnetism in materials is a consequence of unpaired electrons in atoms or molecules. This absorption is meant to occur for definite frequency values and magnetic field combinations, which depend on the characteristics of the sample. Therefore, this principle is quite useful for characterising such materials (Brustolon; Giamello, 2009; Rowlands; Murphy, 2017).

Elementary particles such as electrons are characterised by having spin, which is an intrinsic mechanical angular momentum. The angular momentum is a vector quantity and is defined by its magnitude and the direction in space. The electron spin, in a simplified description, can be found in two states, α and β, which share the same magnitude of angular momentum but differ in orientation. The spin vector is defined as $\boldsymbol{S}$, and it comes together with components related to the Cartesian frame, S_x, S_y, S_z (Brustolon; Giamello, 2009).

The magnitude of magnetic momentum is given by (Rowlands; Murphy, 2017):

$$|\boldsymbol{S}| = \hbar\sqrt{S(S+1)} \tag{3.84}$$

Where S is the spin quantum number, of value 1/2, and $\hbar$ is the Planck constant divided by 2π.

Conventionally, it is considered that the spins α and β have definitive components S_z, with units of $\hbar$ of either 1/2 or -1/2, α and β states, respectively.

Related to the electron spin angular momentum is the magnetic moment μ_e, which is proportional to S (Brustolon; Giamello, 2009):

$$\boldsymbol{\mu_e} = g\mu_B\mathbf{S} \tag{3.85}$$

Where g is the spectroscopic factor, also known as g factor, and $\mu_B = -\frac{|e|h}{4\pi m_e}$ (m_e is the electron mass, and e is the electron charge), μ_B is called Bohr magneton and has a value of -9.2740×10^{-24} J.T^{-1}. The g factor for a free electron is 2.0023.

In the absence of an external magnetic field, the spins of states α and β are said to be degenerate, however, by applying an external magnetic field, it is lifted and results in a difference of energy (Rowlands; Murphy, 2017). The difference in energy between the electrons of α and β states is explained by the existence of this magnetic moment associated with the electron spin when the electron is under the influence of a magnetic field.

The energy E associated with the interaction of the electron magnetic moment μ_e with the magnetic field B, with z axis along the direction of B is described by (Brustolon; Giamello, 2009):

$$E = g|\mu_B|BS_z \tag{3.86}$$

Where B is the intensity of the magnetic field.

As it was assumed that the electron spin can be in two states with z components of spin 1/2 and -1/2, the presence of the magnetic field may induce the spin electron to assume the values:

$$E = \frac{1}{2} g|\mu_B|B \text{ (for an } \alpha \text{ state)} \tag{3.87}$$

$$E = -\frac{1}{2} g|\mu_B|B \text{ (for a } \beta \text{ state)} \tag{3.88}$$

This splitting of the electron into two energy levels is well-known as the *Zeeman effect* and the interaction of the external magnetic field with the electron magnetic moment is called *Zeeman interaction*, which is described in Figure 3.14a.

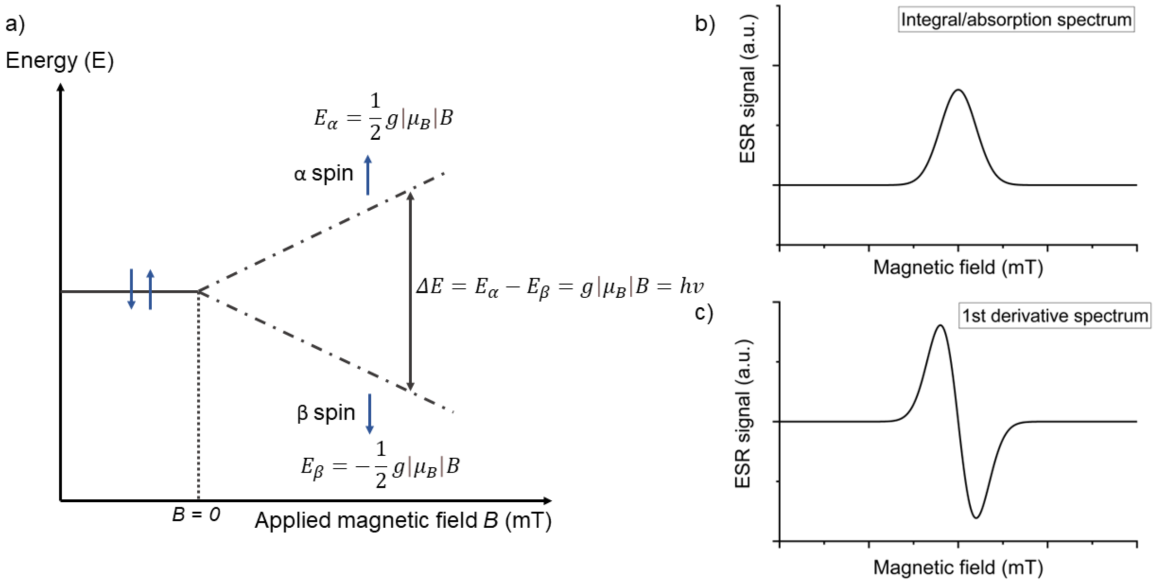

Figure 3.14 - (a) Illustrative scheme for the Zeeman effect observed in ESR measurements on the left side. And examples of curves for an ESR signal considering the (b) absorption and (c) derivative spectra.

This difference in energy ΔE between the two levels is proportional to the magnetic field and linearly dependent on the g factor. An electron spin in β state, that is, in the low energy state, can go through a transition to the higher energy state by absorbing a photon of energy hv, which is equal to ΔE (Brustolon; Giamello, 2009):

$$\Delta E = g|\mu_B|B = hv \tag{3.89}$$

When a paramagnetic material is under a certain magnetic field magnitude and frequency of radiation, the electron spin in β state moves to a higher level, resulting in an absorption peak (Fig. 3.14b), which has a specific value of a magnetic field in T, and its respective g value. Analyses of the ESR spectrum are usually done by considering the first derivative of the spectrum (Fig. 3.14c).

ESR spectroscopy is a useful technique for detecting paramagnetic species. The shape of the curve, the position of the signal (hence its *g* value), the number of signals, and so on, gives information about the nature of the paramagnetism. Examples of an application include the detection of organic and inorganic materials, as well as the coordination complexes and biological macromolecules which have paramagnetic centres (Rieger, 2007; Schweiger; Jeschke, 2001). Therefore, ESR covers a wide range of applications, such as detecting irradiation in food (Aleksieva; Yordanov, 2018), the presence of different radicals in food (Krakowian *et al.*, 2014), dosimetry (Fattibene; Callens, 2010), and the determination of paramagnetic defects in luminescent materials (Zhou *et al.*, 2021)

In the case of investigating luminescent materials, ESR may be a powerful technique for identifying the defects in the lattice which are associated with the luminescence. Considering TL emission, ESR is useful to evaluate the influence of radiation on the luminescent centres and may be used to associate the TL peaks with a certain kind of defect.

3.4 Hafnium Oxide

Hafnium Oxide (HfO_2), also known as hafnia, is a metal oxide from the IV-B family of the periodic table, which has been extensively used, mainly in electronics. The chemical element hafnium has similar properties as other elements from the same family (being previously named as the “little brother” of zirconium and titanium) and so the derived metal oxide forms share similarities too. The use of those metals, as well as their respective oxide forms, dates back only to the 1950s when they started being more explored together with the advances in aerospace, chemical and nuclear engineering (Alper, 1970; Tricot, 1992).

The interest in hafnium-based materials was first based on the high neutron cross-section absorption coefficient, which is a valuable property to the nuclear industry, where it can be used as a control rod material in reactors, moreover, the ceramics of HfO_2 have a high melting temperature of about 2800 °C, which makes the material a useful high-temperature refractory material (Wang; Li; Stevens, 1992).

However, the application of hafnium-based material has not been centred only on nuclear applications. For example, when compared with the other transition metal oxides from the IV-B family, HfO_2 is thought of to be the most promising in electronics due to its properties such as a large bandgap (values can vary between 5.5-6 eV), high dielectric constant (22-25), high thermal stability, among others (Choi; Mao; Chang, 2011). More cases of applications are described in Section 3.4.3.

3.4.1 Hafnia Polymorphism

According to the stoichiometry, and conditions of temperature and pressure, HfO_2 may be found in different crystalline phases and their polymorphic arrangements, which brings about changes in the properties.

The most common structure which HfO_2 possesses is the monoclinic baddeleyite $P2_{1/C}$, or m-HfO_2, found for ambient temperature and pressure conditions, and that has the lowest formation energy (Choi; Mao; Chang, 2011). Increasing the temperature to higher than about 1700 °C under atmospheric pressure sees the monoclinic phase transforms into tetragonal (t-HfO_2) of space group $P4_2nmc$, and further heating to higher than 2600 °C results in a cubic structure (c-HfO_2) with a fluorite arrangement Fm3m. The temperature threshold for a given phase transition may vary slightly depending on the reference. Here it was adopted the description by Gritsenko, Perevalov and Islamov (2016). Figure 3.15 shows a phase diagram of Hf-O. Note in this case this slight variation is observed in the data from the book "Ferroelectricity in Doped Hafnium Oxide: Materials, Properties and Devices" by Schroeder, Hwang and Funakubo (2019).

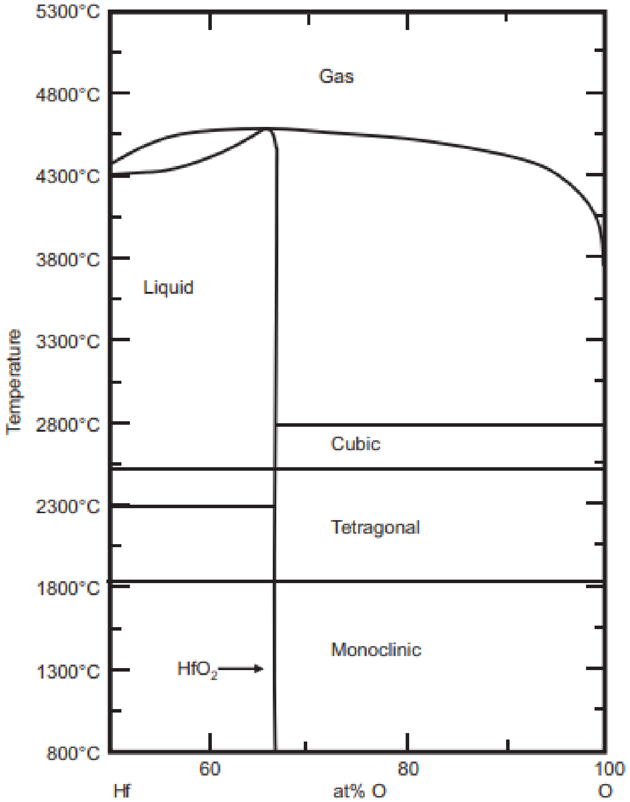

Figure 3.15 - Phase diagram for HfO_2 material. Reference: reprinted from Schroeder, Hwang and Funakubo (2019)[†].

[†] Permission given by Elsevier. This figure was published in the book: Schroeder, Hwang and Funakubo, Ferroelectricity in Doped Hafnium Oxide: Materials, Properties and Devices, Woodhead Publishing Series in Electronic and Optical Materials, in Chapter 2 - Structures, Phase Equilibria, and Properties of HfO_2, p. 26. Copyright Elsevier (2019).

The transformation from monoclinic to tetragonal phase has been described as martensitic and occurs over a finite temperature range. This transition happens without diffusion, and the atoms retain their neighbours with less than one interatomic distance of displacement. As a result, the density increases by about 3.4 %. There is no consensus about the nucleation induction in the material, with models suggesting either a homogeneous or heterogeneous process, although this transformation is known to be controlled by nucleation and growth (Schroeder; Hwang; Funakubo, 2019). Regarding the cubic phase, experiments seeking to validate the temperature values for the transition to a cubic phase are more challenging due to the ultrahigh temperature required.

HfO_2 also undergoes a phase transition when high pressure is applied. Monoclinic transforms into an orthorhombic phase (o-HfO_2) of space group Pbca. Further increase in pressure leads to an orthorhombic of space group Pnma (Gritsenko; Perevalov; Islamov, 2016). Figure 3.16 shows the unit cells for HfO_2 in different phases.

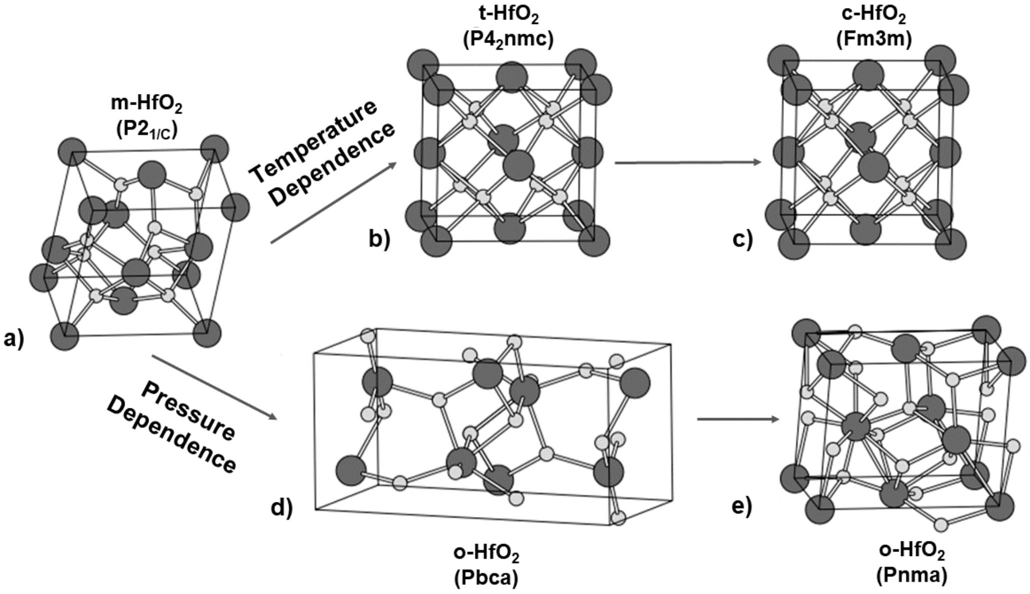

Figure 3.16 - Different unit cells for HfO_2. (a) monoclinic phase, (b) tetragonal, (c) cubic, (d) and (e) represent orthorhombic arrangments. Reference: reconstructed from Caravaca and Calisi (2005)[‡].

Pure tetragonal and cubic phases are not possible to obtain at RT under standard conditions, even considering an ultrafast quenching (Gritsenko; Perevalov; Islamov, 2016). However, some studies have found stabilised polymorph HfO_2 with a tetragonal phase when doping the material. This was found by Borges *et al*. (2022) who successfully produced HfO_2 nanoparticles

---

[‡] Reconstructed from Caravaca and Casali, Ab initio localized basis set study of structural parameters and elastic properties of HfO_2 polymorphs. Journal of Physics: Condensed Matter, v. 17, n. 37, p. 5795-5811, 2005. DOI: 10.1088/0953-8984/17/37/015. © IOP Publishing. Reproduced with permission. All rights reserved.

in a t-HfO_2 phase when doping with 20 mol% of europium ions. Similarly, it was observed by Montes *et al*. (2014) when doping HfO_2 with concentrations higher than 15 at% of terbium.

3.4.2 Synthesis Routes

Hafnia can be synthesised by different routes depending on the final conformation desired, such as nanoparticles, powder, deposited film, composite, and so on. However, as beforementioned, the monoclinic phase is the most common at RT under atmospheric pressure, thus additional steps would be required to reach a different result.

Regarding the deposition of HfO_2 in thin film form, some methods may be used (Choi; Mao; Chang, 2011):

- *Sol-Gel* method is a wet chemical method which uses as main precursors the hafnium tetrachloride ($HfCl_4$) and Hf-ethoxide. The method has advantages which include good control of the composition, a high level of purity, and low operational cost. Usually, a firing temperature higher than 500 °C is required to crystallise in a monoclinic structure.
- *Pulsed laser deposition* is a physical method in which a high-intensity laser hits a HfO_2 ceramic target. It is a well-known method for growing films, it has a simple and flexible operation, a large deposition rate and control of stoichiometry. Also, a heat treatment at 500 °C is needed to crystallise the material.
- *Sputtering* is also a physical method, which uses a hafnium-based material as a target. It is widely used due to the low level of contamination, simplicity and the deposition does not require high temperatures. The film when deposited is in an amorphous condition and annealing at temperatures higher than 500 °C is necessary to get a crystalline phase.
- *Metal-organic chemical vapor deposition*, or MOCVD, is a chemical deposition method which allows the production of films with good control of composition, uniformity, and a large area of growth. However, it may have a high cost. Typical hafnium precursors are metal halides and alkoxides. The same temperature of crystallisation as in the previous methods is required.
- *Atomic layer deposition*, or ALD, is another well-known chemical method. Compared with MOCVD, ALD usually uses a slower growth rate, but shows an atomic level control of the thickness, hence ultrathin films are possible to be produced. Some of the precursors may be the same as the ones used in MOCVD processes, as well as the temperature of crystallisation.

If the interest is to obtain powder and/or nanoparticles of HfO_2 the main methods successfully used so far include:

- *Sol-Gel*, the same method used for deposition may be used for synthesising nanoparticles, but without depositing on a substrate. This is a low-cost method that uses ethylene glycol and citric acid to polymerise, and $HfCl_4$ (Chattopadhyay; Nayak, 2022).
- *Precipitation method*, in which only two precursors are necessary, which are $HfCl_4$ and potassium hydroxide (KOH). This is a simple method that is based on the mixing of two starting solutions, followed by centrifugation and drying. Moreover, there is no use of organic solvents or a high temperature, except for the final heat treatment at 500 °C. A variation of that includes an additional sonification step, which converts the method from precipitation to sonification. As a base solution, sodium hydroxide (NaOH) may be used instead of KOH (Ramadoss; Kim, 2012; Ramadoss; Krishnamoorthy; Kim, 2012).

In this work, the material was synthesised using the precipitation method. A detailed description of it is in the methodology section.

3.4.3 Applications: Some Examples

HfO_2 as well as other high dielectric materials with high dielectric permittivity has been used more and more in electronic devices to replace SiO_2 which is a traditional dielectric. For example, in 2007, Intel Corporation ® implemented hafnium oxide as one of the dielectric gates in its device (Gritsenko; Perevalov; Islamov, 2016; Matthews, 2008).

Regarding electronics, HfO_2-based materials are the interest for memristive devices due to the good control of ferroelectricity by modifying the concentration of oxygen vacancies and impurities, which allows linear and low-power operation (Das *et* al., 2021; Lee *et al.*, 2023; Silva *et al.*, 2023). There is also potential for using it in non-volatile memory due to its resistive switching properties (García *et al.*, 2021; Lata *et al.*, 2020).

The use of HfO_2 in memory devices has been extensively studied and as a result, it is already implemented in different devices. Nowadays, what has been observed is a sharp increase in the number of publications approaching the ferroelectricity in HfO_2 as it shows remarkable potential in the area, and it may miniaturise memory devices and obtain better properties in comparison with the already established materials (Banerjee; Kashir; Kamba, 2022; Liao *et al.*, 2023).

However, the applications are not restricted to electronics but extend to other fields. HfO_2 has been shown to display interesting luminescent properties, which cover a wide range of applications. For example, HfO_2 was used in the production of nanocomposites, and it performed an important role in the generation of photocurrent under visible light photoexcitation (Rauwel *et al.*, 2019).

HfO_2 has been successfully used in medical applications, and it is already approved for medical injections as an effective method of treatment of tumours which are radiosensitive and radioresistant. Recently, studies have been dedicated to investigating the rare-earth elements doped versions of the material for *in vivo* diagnostics and therapy, as well as their biocompatibility (Chen, Y. *et al.*, 2022; Furasova *et al.*, 2017; Kaszewski *et al.*, 2019).

The intense blue emission of polycrystalline HfO_2 has also been reported when the sample is stimulated with ultraviolet light, which is associated with oxygen vacancies presented in the material (Pejaković, 2010). As the concentration of defects may be controlled by the synthesis conditions and post-treatments, it widens the range of applications, which is even more extended by doping. Hence, the material is promising for use in LED devices (Ćirić; Stojadinović; Dramićanin, 2019).

Despite being less explored and thus, scarcer, studies regarding the thermoluminescence properties of HfO_2 after exposure to ionising radiation, such as ultraviolet photons and X-rays, showed that the material displays an intense emission glow curve (Fiaczyk *et al.*, 2016; Mendoza *et al.*, 2010; Sekar *et al.*, 2021). And even the results being encouraging and showing that the material might be suitable for use in radiation detection, its use in dosimetry have only been reported in a few reports and restricted to medical dosimetry (Sekar *et al.*, 2020, 2021).

Chapter 4

4 Methodology

This section is divided into four parts which together describe all the methodologies used in this work. The first section (4.1) is dedicated to explaining the method of synthesis to obtain the crystals of HfO_2. Section 4.2 describes the characteristics of the equipment used to investigate the luminescent properties, including fluorescence, TL and OSL. Section 4.3 specifies the setup used to investigate the structural properties of the HfO_2 by using XRD and its defects by ESR spectroscopy. The last section, 4.4, talks about the radiation sources used to irradiate the samples, which was needed before carrying out subsequent measurements.

4.1 Synthesis Route

Samples of HfO_2 crystals were synthesised by the precipitation method, by adapting the work of Ramadoss, Krishnamoorthy and Kim (2012). The hafnium tetrachloride ($HfCl_4$) of 98 % purity and potassium hydroxide (KOH) at 8 M, both from Sigma-Aldrich, were used as precursors.

The synthesis started with two solutions of KOH and $HfCl_4$ in concentrations of 0.4 and 0.1 M, respectively. The $HfCl_4$ solution was placed in an Erlenmeyer flask under a stirred plate at RT plus a magnetic stir bar (the room humidity was not a controlled aspect). Then, KOH solution was added to that by dropping, and the mixture was kept in agitation for 3 hours. The mixing allows the dissolved ions to form hafnium hydroxide ($Hf(OH)_4$) at the end, which has a suspension characteristic.

The precipitate material from the mixture was placed in Falcon conical centrifuge tubes, and centrifuged at 3500 rpm for 10 minutes at RT, with a Kasvi bench centrifuge model K14-5000M. The process of centrifugation was repeated 3 times, with the exchange of distilled water in order to remove impurities that were separated from the precipitate.

Subsequently, the precipitate part was separated and had a gel aspect. This gel was placed on glass Petri dishes and dried in an oven at 80 °C for 24 hours (oven Ethik Technology model 420-TD with air-circulation), and crystals were obtained as a result. The crystals were ground on an agate pestle and mortar to get the powder form.

Finally, the powder sample underwent two heat treatments. The first heat treatment was performed at 500 °C for 2 hours in a Novus N480 oven, with a heating rate of 15 °C/s to remove any organic residue and to improve crystallisation in the material. The second one was performed at different, higher temperatures of 1000, 1200, 1400 and 1600 °C for 2 hours with a heating rate of about 15 °C/min, to evaluate the influence of the temperature on the crystallisation, concentration of defects and luminescent properties. The latter heat treatment here is also called calcination and was carried out in an oven. Figure 4.1 shows a scheme of the synthesis process.

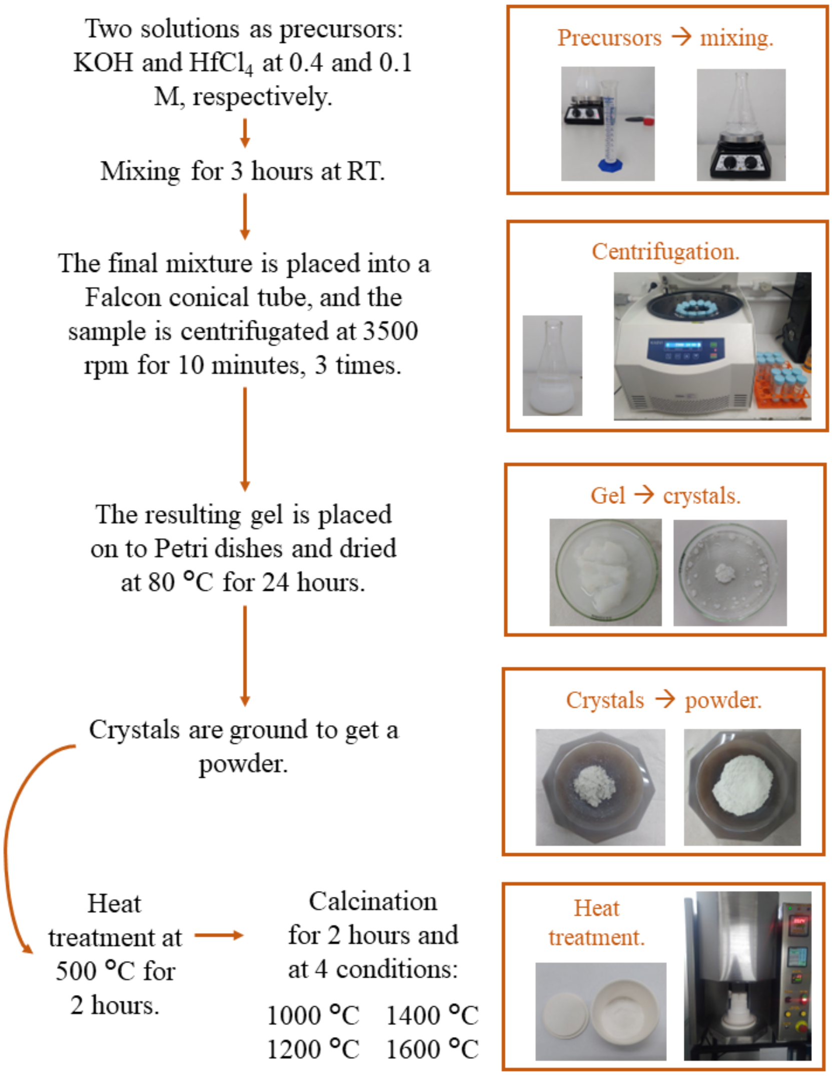

Figure 4.1 - Scheme for the precipitation method synthesis used in this work. Photos on the right show steps of the process.

The use of a heat treatment at 500 °C is a known step that allows for the crystallisation of the material, which is commonly adopted in hafnia film deposition and production of powder samples (Choi; Mao; Chang, 2011; Ramadoss; Krishnamoorthy; Kim, 2012). The choice of the calcination conditions was made by the expertise of the author in previous works, in addition, most of the studies that evaluated the TL signal have not used temperatures above 1000 °C (; Laganovska *et al.*, 2023; Sekar *et al.*, 2020). Moreover, the increase of oxygen vacancies concentration due to higher temperature of calcination is expected (Chuang; Lin; Cheng, 2012).

Therefore, for this study, 4 different kinds of samples were synthesised by the precipitation method, which are different due to the temperature of the final heat treatment, that is calcination. Throughout this work, the samples are named as per Table 4.1.

Table 4.1 - Names for the samples used in this study.

Sample name	Conditions of synthesis
HfO_2 – 1000 °C 2h or HfO_2 – 1000 °C	Precipitation method with final heat treatment at 1000 °C for 2 hours.
HfO_2 – 1200 °C 2h or HfO_2 – 1200 °C	Precipitation method with final heat treatment at 1200 °C for 2 hours.
HfO_2 – 1400 °C 2h or HfO_2 – 1400 °C	Precipitation method with final heat treatment at 1400 °C for 2 hours.
HfO_2 – 1600 °C 2h or HfO_2 – 1600 °C	Precipitation method with final heat treatment at 1600 °C for 2 hours.

This method of precipitation, which is sometimes referred to as co-precipitation, is a process in which the processes of nucleation, growth, and agglomeration occur simultaneously (Bhagyaraj *et al*., 2018). It was chosen because of its simple and rapid preparation, good control of particle size (usually obtaining particles in the nanoscale), non-use of organic solvents, and high levels of purity that can be obtained depending on the precursors' purity.

4.2 Luminescence Characterisation

Luminescence characterisation of the HfO_2 crystals was carried out for the TL, OSL and PL (here named fluorescence) techniques. For each of the techniques, a set of configurations and protocols were adopted. This section covers the standard parameters used for all measurements unless otherwise stated.

4.2.1 Thermoluminescence and Optically Stimulated Luminescence

TL and OSL measurements were carried out using two different brands of reader, Risø from DTU Nutech and Lexsyg from Freiberg Instruments. Due to practical aspects, this section is divided into four parts, one for each brand (plus one for comparing them readers), and one for dealing with the theoretical models used to fit the TL and OSL curves and the T_M-T_{stop} method.

4.2.1.1 Risø TL/OSL Reader Models DA15 and DA20

The Risø TL/OSL reader is an automated equipment for measuring TL and OSL emissions. Two models were used in this work, model DA15 and DA20, the latter one being more recent.

The Risø TL/OSL reader is basically composed of a vacuum-tight measurement chamber, a blue/UV sensitive photomultiplier tube which is responsible for detecting the photons and amplifying the signal (model PDM9107Q-AP-TTL-03 with quartz window, and maximum efficiency between 200-400 nm), detection filters, an optical system which may have different LEDs for light stimulation (blue centred at 470 nm, green centred at 525 nm and infrared centred at 850 nm), and 48-position platforms in a carrousel designed for cups. The system also has an in-built β source ($^{90}Sr/^{90}Y$). For TL measurements, there is a heating and lifting unit which allows for the heating of individual samples up to 700 °C, using linear heating rates that can vary between 0.1 to 10 °C/s (DTU Nutech, 2023). Figure 4.2 shows a scheme of the reader.

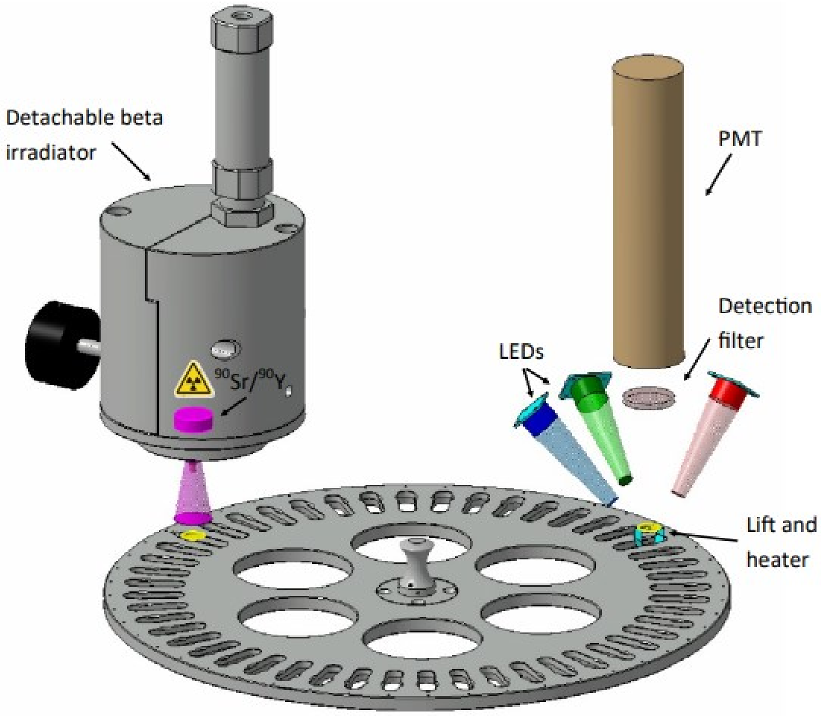

Figure 4.2 - Illustrative scheme for the RISØ TL/OSL reader, showing the main components, such as PMT tube, irradiation source, LEDs, heating unit and samples carrousel. Reference: Available on https://www.fysik.dtu.dk/english/research/radphys/research/radiation-instruments/tl_osl_reader, and accessed on 12.05.23.

There are four main optical filters which may be used while measuring TL and OSL measurements according to the required specifications, with different transmittance characteristics as shown in Figure 4.3:

- Filter Hoya U-340 with a thickness of 2.5 or 5 mm, which has a narrower transmittance band in comparison to the others, located between 200-400 nm, with maximum transmittance of 80 % (for 2.5 mm thickness). There is also a smaller band in the infrared region at about 710 nm. Due to those characteristics, this filter is widely used for analysing samples that emit in the UV region, and when low signal-to-noise is desired. In addition, it is useful when doing OSL with blue and green stimulation, as it blocks these stimulation wavelengths.

- Filter Schott UG11 has 1 mm of thickness and a transmittance curve similar to the Hoya U-340, however with higher values of transmittance, mainly in the infrared region.
- Filter Schott BG 39, of 2 mm of thickness, with a large single transmittance band in the visible region between 300-700 nm, with transmittance reaching values close to 90 % (for 1 mm thickness). This filter is interesting for measuring TL in the visible range, however special attention needs to be given to measurements at high temperatures (> 300 °C) when the emission due to black-body radiation gets more significant. For OSL, it cannot be used alone because the transmittance band covers the most common stimulation wavelengths, such as blue and green.
- Filter Schott BG3, which has high transmittance in the UV and visible region (between 200-500 nm) as well as in the infrared region. As it has a large area of transmittance, its use might be limited.

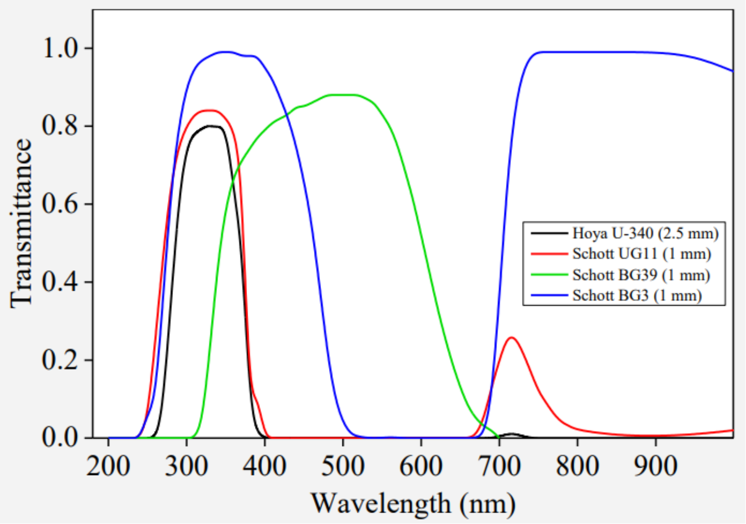

Figure 4.3 - Transmittance curves for different filters and their respective thicknesses, which are usually used in the TL/OSL reader from DTU Nutech. Reference: DTU Nutech, product catalogue. Reference: Available on https://www.fysik.dtu.dk/english/research/radphys/research/radiation-instruments, and accessed on 12.05.23.

TL measurements were carried out in a Risø TL/OSL reader model DA20, which has an in-built β source (^{90}Sr/^{90}Y) with a dose rate of 0.081 Gy/s (40 mCi activity). Irradiations were performed in a large dose range (0.2-30 Gy). TL glow curves were measured between 0-500 °C, using a heating rate of 5 °C/s, in an N_2 atmosphere (to avoid spurious signal), subtracting the background signal. Schott BG39 (2 mm thickness) and Hoya U-340 (2 mm thickness) filters were used to get the visible and UV emissions, respectively.

CW decay curves and LM-OSL curves with blue stimulation (centred at 470 nm) were also carried out in the DA20 model, at 30 °C and using the Hoya U-340 filter. In the CW mode, the LED power was 90 % and recording time was 60 s, whilst for LM-OSL the power range was 0-100 % with 100 seconds of duration.

Measurements of infrared OSL, or here called infrared-stimulated luminescence (IRSL), were carried out in a Risø TL/OSL reader model DA15 with an in-built β source (^{90}Sr/^{90}Y) with a dose rate of 0.02 Gy/s. IRSL decay curves were obtained using a stimulation centred at 870 nm with an optical power of 90 % and a recording time of 120 seconds. A readout temperature of 100 °C (heating rate of 5 °C/s) was adopted to remove the contribution from shallower traps, and after each measurement, a preheat up to 500 °C for 10 seconds (heating rate of 5 °C/s) was used in order to ensure there was no residual signal, since the IR stimulation might not deplete all of it. The Schott BG-39 (2 mm thick) filter was used for detecting emission in the visible range.

4.2.1.2 Lexsyg Research Reader

The Lexsyg reader is a flexible modular system for measuring TL, OSL, IRSL (infrared-stimulated luminescence) and fluorescence emissions. The novelty of the system is based on the ability to easily modify any of the predefined configurations, such as the luminescence excitation and detection units, which may also be done automatically (Richter; Richter; Dornich, 2013).

The equipment is composed of storage, detector and measurement chambers, which allow for the separation of the aliquot that is being measured from the sample storage section. Figure 4.4 shows a scheme of the chambers which compose the equipment and the different configurations that one can obtain. Due to this versatility, each part of the equipment may be individually configured. Further in this section, there is a detailed description of the equipment used for the measurements in the framework of this study.

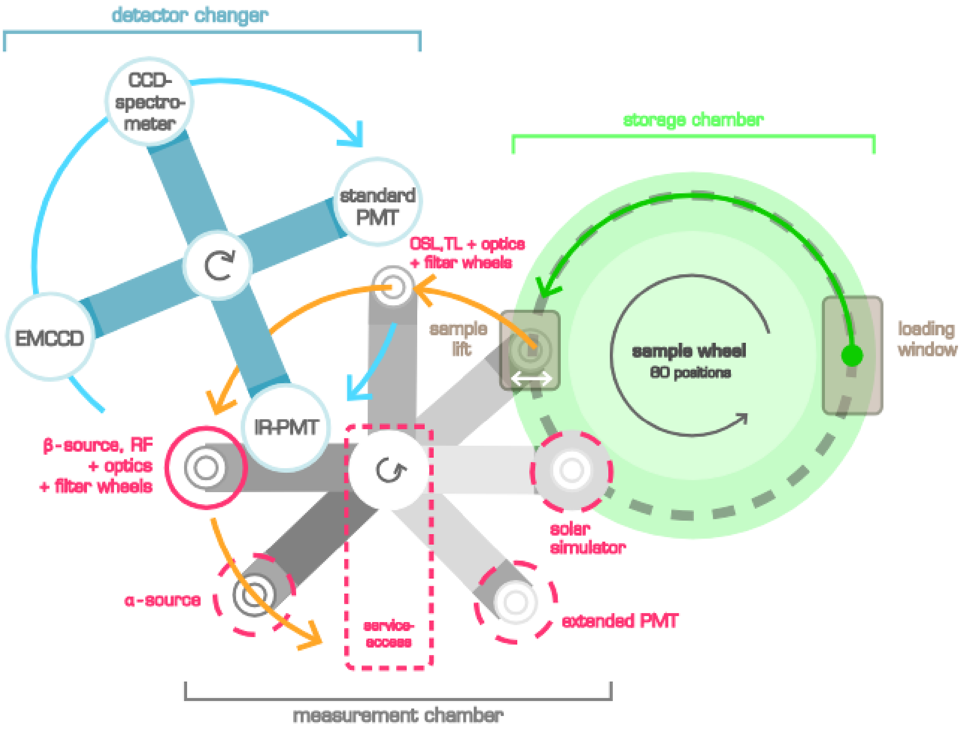

Figure 4.4 - Illustrative scheme of the Lexsyg Research reader, showing the three main parts of the equipment: detector, measurement and storage chambers. Reference: reprinted from Richter, Richter and Dornich (2013).

The storage chamber has a sample wheel with 80 positions and a loading window. An advantage of having the units separated from the loading window is the possibility of removing/changing samples' positions whilst a measurement is carried out (Richter *et al.*, 2012).

Separated by a rubber seal from the storage chamber, the measurement chamber is mechanically opened and closed for transferring the aliquot, which is lifted up by a piston from the wheel, held in a place under vacuum, picked by a grabber and then transferred to the heater plate, for example. The chamber may be operated with different atmospheres, such as air, He or N_2. This unit can hold up to two irradiation sources (α and β particles), plus three positions which can hold filter wheels, optical devices, a detector (such as a PMT) or a solar bleaching unit (to simulate the effect of sunlight).

The heating place can operate at rates between 0.1-20 °C/s for temperatures up to 400 °C and at rates between 0.1-10 °C/s for temperatures up to 700 °C. The temperature calibration is done by pyrometer measurements. Using a closed-loop gas flow system, both heating and cooling can be performed at specified rates, including non-linear heating. It allows for the measuring of TL, OSL and IRSL at elevated temperatures of up to 700 °C (Richter; Richter; Dornich, 2013).

Still regarding the measurement chamber, it may hold different optical stimulations for OSL measurements (a set of three different wavelengths), such as in the IR, green, blue and violet regions. In addition, either LEDs or laser diodes can be used, in which the latter is interesting for measuring POSL because of their fast rise. Because the interest is in the emitted light, a set of filters are used to narrow the detection window to avoid collecting the stimulation light. In Lexsyg, there may be up to two filter wheels with 6 positions each, which allows good versatility and is automatically controlled (Richter; Richter; Dornich, 2013).

Finally, the detector chamber, which can in principle hold up to six luminescence detectors. Those detectors can include PMT tubes with different wavelength bands and quantum efficiencies, which are used according to the sample spectral emission features; an electron multiplying charge-coupled device (EMCCD) camera, which is useful for doing spatially resolved measurements either of grains or solid samples; and a CCD-spectrometer (CCD stands for charge-coupled device), which allows performing TL and OSL spectral measurements.

Figure 4.5 shows the Lexsyg research equipment used in this work, which was operated in the laboratory of luminescence at the Institute of Radiation Medicine in Helmholtz Zentrum München.

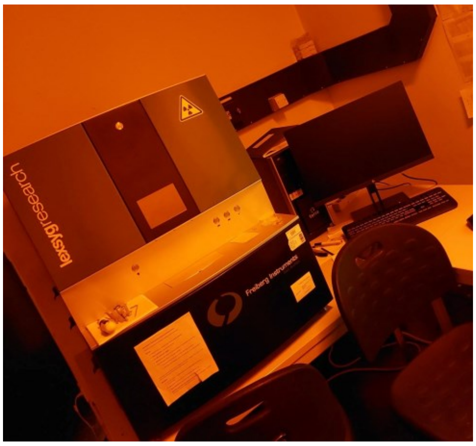

Figure 4.5 - Photo of the Lexsyg Research equipment from the Institute of Radiation Medicine at Helmholtz Zentrum München in Germany.

The Lexsyg Research used here has an in-built β source (^{90}Sr/^{90}Y) with a dose rate of 0.02 Gy/s, and three detectors: an Andor Technology iDus 420 Series CCD camera coupled to a Shamrock 163 spectrometer (used for spectral measurements), and two PMT tubes.

The first of these is a PMT model H7421-40 from Hamamatsu, with a spectral response between 300-720 nm at temperatures above 25 °C, and high effectiveness in the red and IR region (Hamamatsu, 2019), which is useful for measuring signals in this region of the spectrum. The second is a PMT model 9235QB from ET Enterprises electron tubes, which is a blue-green sensitive bialkali photocathode due to its spectral range covering between 160-630 nm (ET Enterprises, 2010), which is interesting for measuring UV and visible signals from TL and OSL emissions.

Light stimulation includes IR (emission centred at 850 nm and a maximum intensity of 300 mW/cm^2) and blue laser diodes (emission centred at 458 nm and a maximum intensity of 100 mW/cm^2) and green (emission centred at 525 nm and a maximum intensity of 100 mW/cm^2). Different filters can be used in combination to delimit the detection window, such as glass filters (Schott series, models BG39, BG25, KG3, OG 570 and Hoya U340, with respective thicknesses of 3, 3, 2 or 3, 3 and 7.5 mm) and interference ones (AHF Bright Line models HC 340/26 of 5 mm thickness, HC 414/46 of 3.5 mm thickness, HC 475/50 of 5 mm thickness, HC 575/25 of 5 mm thickness. Also, a delta BP 365/50, an AHF-ET Bandpass 620/60, and an Edmund Optics 525 nm OD4 short pass of 5, 3.5 and 3 mm thickness, respectively).

OSL spectral measurements were carried out using the Andor Technology iDus 420 Series CCD camera coupled to a Shamrock 163 spectrometer. For narrowing the detection window, the IRSL spectrum was measured with the filter Schott BG-39 of 3 mm thick. A combination of the Schott BG-39 and Edmund Optics 525 nm OD4 (both of 3 mm thickness) was utilised for measuring the green OSL spectrum. For RF spectral measurements, the same detector was used, but without filters (as there is no stimulation light).

OSL decay curves were recorded after different doses of β particles for a comparative study of the OSL signal according to the different stimulation wavelengths of blue, green stimulation, and IR. For IR, a 3 mm thick Schott BG-39 filter was used, a 7.5 mm thick Hoya U-340 for blue OSL, and three combinations for green OSL, with the set of filters made of a Schott BG-3 and an Edmund Optics 525 nm OD4 (both 3 mm thick) plus an interference filter (AHF Bright Line HC340, Delta BP365 or HC414, to obtain the OSL signal when the detection window is restricted to the region around 340, 365 and 410 nm, respectively). A comparison among the types of equipment used is presented in the next section.

4.2.1.3 Summary: Risø and Lexsyg readers

This work used three different types of TL and OSL readers, of which the configurations are detailed in the previous two sections. Table 4.2 has a summary of the main features and uses of them to facilitate the reader’s understanding.

Table 4.2 - Main characteristics and measurements performed according to the type of TL and OSL reader.

Characteristics and usages	Risø TL/OSL reader model DA15	Risø TL/OSL reader model DA20	Lexsyg Research
Dose rate of the in-built β source	0.02 Gy/s	0.08 Gy/s	0.02 Gy/s
Light stimulation wavelengths used	Infrared (850 nm), power density of 300 mW/cm^2.	Blue (470 nm), power density of 80 mW/cm^2.	Infrared (850 nm), green (525 nm) and blue (458 nm), with maximum power densities of 300, 100 and 100 mW/cm^2, respectively.
TL measurements performed?	Yes.	Yes.	No.
Filters used	Schott BG-39 2mm.	Schott BG-39 4.5 mm and Hoya U-340 7.5 mm.	Schott BG-39 3 mm, Edmund Optics OD4 3 mm, Hoya U-340 7.5 mm, AHF HC 340 5 mm, Delta BP 365 5 mm and HC 414 3.5 mm.
Detectors	PMT Blue/UV sensitive (160-630 nm).	PMT Blue/UV sensitive (160-630 nm).	Blue-green sensitive (160-630 nm) and CCD camera coupled to the spectrometer.
Measurements	IRSL.	CW and LM-OSL with blue stimulation, and TL spectral measurements.	CW-OSL with IR, green and blue stimulations, OSL spectral measurements, POSL with blue stimulation, and radiofluorescence.

4.2.1.4 T_M-T_{stop} and Computerised Deconvolution for Thermoluminescence and Optically Stimulated Luminescence

The deconvolution of TL and OSL curves is a method to fit the experimental curves by using theoretical models. From that, one can obtain an estimation of parameters related to those emissions. As mentioned before in Section 3.2, the mechanism of TL and OSL phenomena is associated with the presence of defects in the materials, their concentration, and energy levels.

Different models have sought to describe those processes. Most of them are based on the possibility (or not) of retrapping, which is represented by the parameter b, known as kinetic order (see Section 3.2). In this study, a method known as CGCD (for computerised glow curves deconvolution) is used.

The TL and OSL curves in this work were fitted with a general-order kinetic (GOK) model, in which b can assume values between 1-2, that is, from a condition of non-retrapping to a significative retrapping condition. The models used for fitting TL glow curves, CW-OSL decay curves and LM-OSL curves are described here. In addition, the T_M-T_{stop} is also described, which is an important experimental protocol for analysing TL peaks.

4.2.1.4.1 T_M-T_{stop} for TL glow peaks analysis

The analysis of the TL emission can be detailed by investigating the number of peaks present in the glow curve and their respective traps' parameters. To investigate those properties, the T_M-T_{stop} method was used to estimate the number of peaks, their position and the likely kinetic order associated with them. Subsequently, the data obtained from T_M-T_{stop} were used for the input values in the deconvolution study with the GOK equation (described in the next section, 4.2.1.4.2).

T_M-T_{stop} protocol consists of irradiating an aliquot with a constant dose followed by preheating until a temperature called T_{stop}. After the preheating, the sample is quickly cooled until it reaches RT. Once RT is reached, the TL glow curve is recorded. From the recorded TL, the maximum peak position closest to the T_{stop} is taken, which is called TM. The analysis results in a graph of T_M versus T_{stop}, in which one can obtain information about the number of peaks, the position and possible kinetic order (McKeever, 1980, 1985). The protocol is composed of a cycle which is repeated until covering the region of interest. In this study, as there were observed TL peaks even at high temperatures, the method was carried out from a T_{stop} of 20 to 500 °C, with a step of 5 °C/cycle. The irradiation dose was 20 Gy, and the preheating duration was 10 seconds. Figure 4.6 summarises the procedure adopted here.

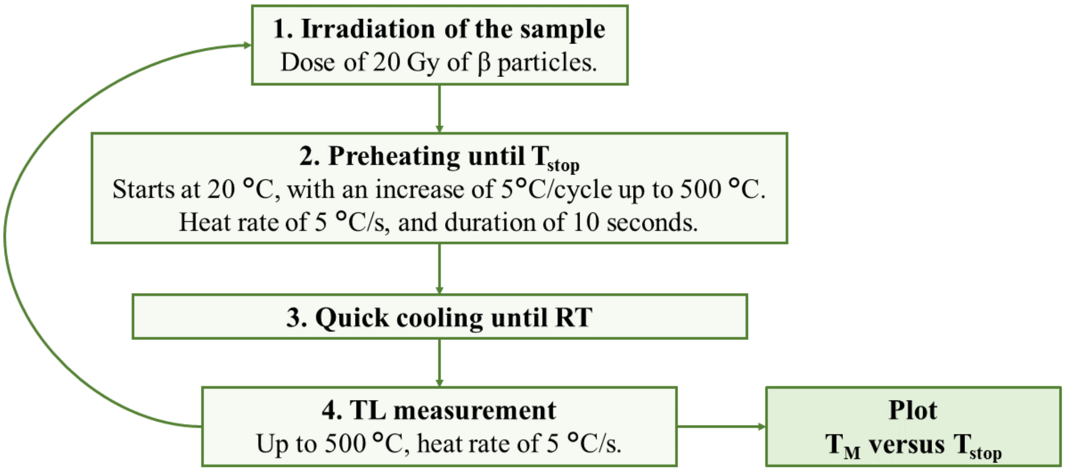

Figure 4.6 - Illustrative scheme for the T_M-T_{stop} method showing the parameters used.

Depending on the shape of the T_M-T_{stop} curve, it is possible to infer for example, if: the peak is an isolated peak (plateau region in the graph); there is a region of discrete peaks overlapped (plateaus connected, following a "staircase" pattern); there is a continuous distribution of peaks (characterised by a positive slope in the graph). The kinetic order can be associated with the presence (second-order kinetic) or not (first-order kinetic) of a tail at the end of a plateau (McKeever, 1985).

4.2.1.4.2 Computerised Deconvolution for TL

TL glow curves were fitted according to the general-order kinetic model proposed by Kitis, Gomez-Ros and Tuyn (1998) for individual peaks, and using the programme developed by Afouxenidis *et al.* (2012). This model uses parameters which can be obtained experimentally, and is given by:

$$I_{TL}(T) = I_m b^{\frac{b}{b-1}} \exp\left(\frac{e}{kT}\frac{T-T_m}{T_m}\right)\left[(b-1)(1-\Delta)\frac{T^2}{T_m^2}\exp\left(\frac{E}{kT}\frac{T-T_m}{T_m}\right)+Z_m\right]^{-\frac{b}{b-1}} \quad (4.1)$$

where:

$$\Delta = \frac{2kt}{E}, \Delta_m = \frac{2kT_m}{E} \text{ and } Z_m = 1 + (b-1)\Delta_m \quad (4.2)$$

The TL intensity I_{TL} as a function of the temperature T, depends on the activation energy E or the trap depth (in eV), the kinetic order b, the Boltzmann constant k and the peak temperature T_m. The fitting was performed using Microsoft Excel software with Solver supplement.

The performance of the fitting by deconvolution was measured according to the figure of merit (FOM), which compares the experimental data with the fitted ones and is given by (Balian; Eddy, 1997):

$$FOM = \sum_i \frac{|Y_{Exp} - Y_{Fit}|}{A} \times 100\ \% \quad (4.3)$$

Where A is the area below the fitted TL glow curve, Y_{Exp} is the experimental curve data and Y_{Fit} is the fitted curve data. The lower the value the better the fitting. Usually, the fitting is considered good when values of FOM lower than 5 % are obtained (Afouxenidis *et al.*, 2012; Soni *et al.*, 2014).

Derived from the TL intensity equation, the frequency factor s (s^{-1}) is given by:

$$s = \frac{\beta_T E}{kT_m^2}\exp\left(\frac{E}{kT_m}\right) \quad (4.4)$$

Where β_T is the heating rate ($K.s^{-1}$) used in the experiment.

4.2.1.4.3 Computerised Deconvolution for OSL

OSL curves were also fitted using general-order kinetic models based on values that can be experimentally obtained. CW-OSL has an exponential decay behaviour, which can be fitted with one or more components, and is given by:

$$I_{CW-OSL}(t) = I_0\left[1 + (b-1)\frac{t}{\tau}\right]^{\frac{b}{b-1}} \tag{4.5}$$

Where the CW-OSL intensity $I_{CW\text{-}OSL}$ is a function of time t, and dependent on the kinetic order b, the time t and the component lifetime τ.

LM-OSL curves have a peak-shape behaviour, and were also fitted using a general-order kinetic model, given by (Kitis; Pagonis, 2008):

$$I_{LM-OSL}(t) = I_m\frac{t}{t_m}\left[\frac{b-1}{2b}\frac{t^2}{t_m^2} + \frac{b+1}{2b}\right]^{\frac{b}{1-b}} \tag{4.6}$$

Where the LM-OSL intensity $I_{LM\text{-}OSL}$ is a function of time t, and dependent on the maximum intensity of the peak I_m at a time t_m, and on the kinetic order b.

The photoionisation cross-section σ of each component in the OSL fitted curve can be calculated by (McKeever, 2001):

$$\sigma = \frac{1}{\tau\Phi} \tag{4.7}$$

Where the σ depends on the lifetime τ in the case of CW-OSL (or t_m for LM-OSL), and on the incident flux Φ. In the case of LM-OSL, because the stimulation intensity is not constant but depends on the rate of stimulation intensity increase (γ) and on the time t, Φ is given by $\Phi = \gamma t$.

4.2.2 Fluorescence

The fluorescence emission of HfO_2 was assessed regarding its emission and excitation spectra. Moreover, the influence of the heat treatment and correlations between the fluorescence emission with the other luminescent properties and the defects in the material were investigated.

The spectra were obtained with a Jobin Fluorolog FL3-11 fluorometer (maker: Horiba) which constitutes a xenon arc lamp of 450 W power, a photomultiplier tube, and emission and excitation monochromators. The fluorometer has a bifurcated fibre-optic probe composed of collection and illumination fibres with numerical apertures of 0.22. Measurements were carried out in darkroom conditions to avoid disturbance during the procedure. Figure 4.7 shows the scheme for the Jobin Fluorolog FL3-11 fluorometer.

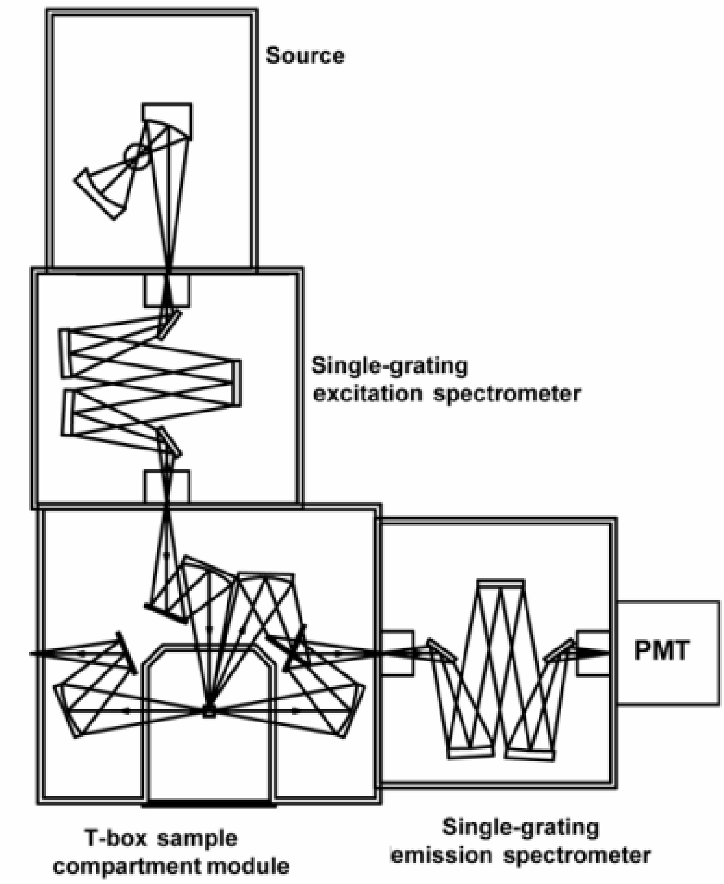

Figure 4.7 - Illustrative scheme for the Jobin Fluorolog FL3-11 fluorometer. Reference: reprinted from Horiba (2008).

The equipment has a radiation source that produces photons (xenon lamp). The beam of light is then filtered using an excitation monochromator in order to reduce the emission to a single wavelength, which reaches the sample in the sample-compartment module. The response of the sample to the incident radiation is detected and filtered by the emission monochromator, which delivers the signal to a photomultiplier tube. The signal is further sent to a controller and digitally converted. Setting either emission or excitation monochromators, or even both, allows us to obtain spectral measurements (Horiba, 2008).

The emission spectrum was obtained by excitation of the samples with a wavelength in the UV region at 300 nm (λ_{exc} = 300 nm), and the excitation spectrum was detected at an emission wavelength (λ_{emi}) defined according to the main emission band. The results were also plotted in a Chromaticity diagram, which allows us to more easily understand the emission in the visible region.

4.3 Structure Characterisation

The structure of the synthesised samples was investigated as regards its crystalline phase and average crystallite size according to XRD data, and the identification of defects in the lattice by ESR technique, as described here.

4.3.1 X-ray Diffraction

XRD was carried out using a benchtop MiniFlex diffractometer from Rigaku, which has a CuK$_{\alpha}$ radiation (1.54059 Å), as shown in Figure 4.8. Samples in powder form were placed on acrylic plates and compacted to obtain a smooth surface. The measurements were carried out at RT, in the range between 10-75° (2θ degree), in steps of 0.01° and 2 s of time per step.

Figure 4.8 - Rigaku D'Max 2500 PC diffractometer. Reference: available on https://www.rigaku.com/products/xrd/miniflex?index=0, accessed on 12.05.23.

The experimental curves were compared and analysed using the X'PertHighScore Plus software and with the standard database PDF2 (2003 version) from the International Centre for Diffraction Data (ICCD), to remove the background signal, mark the peak positions, and correlate with the database.

4.3.2 Electron Spin Resonance

ESR analyses were performed to identify the presence of defects in the material, correlate them with the luminescence signal and evaluate their dependence on irradiation. For those measurements, the ESR signal was detected using a benchtop MiniScope MS5000 spectrometer from Bruker (before, from Freiberg Instruments), as shown in Figure 4.9.

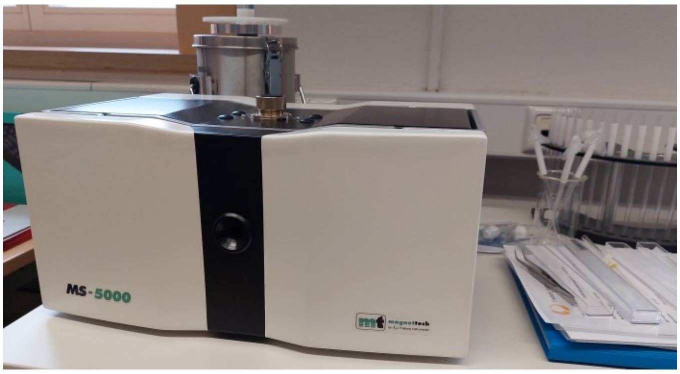

Figure 4.9 - Photo of the MS5000 spectrometer from Bruker used in this study.

The MS5000 spectrometer operates with frequency in the X-band, microwave power in the range between 1 μW-100 mW, magnetic field range from 0 to 650 mT, and modulation frequency of 10 kHz. This equipment is useful for several applications, covering environmental toxicology, alanine dosimetry, petrochemistry, pharmacy, food chemistry, and so on.

To analyse the ESR signal of HfO_2, the powder samples were irradiated by means of X-rays with a dose of 50 Gy within a black plastic bag to shield them against the light. Firstly, the signal was evaluated by varying the parameters of measurement, such as the amplitude of modulation (in mT), microwave power (in mW), sweep time (in s) and the number of accumulations.

Once the best parameters were defined regarding the signal-to-noise proportion, the signal was evaluated for different irradiation doses, and the effect of preheating treatment in between the irradiation and the measurement.

The elapsed time between the end of the irradiation and the beginning of the measurement was always kept the same. Moreover, for comparisons among different aliquots, the signal was normalised by the mass.

The study about the type of defect in the sample was made by analysing the position of the ESR signals, calculating the *g* values and comparing them with reports in the literature.

4.4 Radiation Sources

In addition to the irradiation with β particles from the in-built sources available in the luminescent readers, irradiation was also performed with gamma and X-ray sources available in the radiation facilities at Helmholtz Zentrum München. It was necessary to either use a higher dose rate (used for irradiating with high doses) or different photon energies (to analyse photon energy response). Another practicality was to irradiate more than one aliquot per cycle, which is not possible in the previously mentioned readers.

4.4.1 X-ray Sources

Two different X-ray sources were used, an Xstrahl RS225 cabinet and a PTW irradiator with a 320 kV X-ray tube. Xstrahl RS225 cabinet (Fig. 4.10a) is a lead-shielded irradiation chamber with a movable operator control panel and different beam hardening filters, such as Cu or Al filters, which allow for choosing the best configuration of the irradiation. The X-ray tube operates with voltages up to 220 kV and currents from 1 to 30 mA.

In this study, this source was used to irradiate samples before doing spectral measurements (OSL spectra) and ESR analyses, as more than one aliquot may be irradiated at the same time, and due to its higher dose rate than in the TL/OSL readers. Irradiation was carried out with a voltage of 195 kV, a current of 10 mA and a dose rate of about 6.67 Gy/minute, for a focal spot distance of 20 cm, field size of 12.5 cm diameter and using a 3 mm thick filter of aluminium.

Figure 4.10 – Photos of (a) a Xstrahl RS225 cabinet and (b) a PTW Freiburg irradiator available at the Institute of Radiation Medicine of the Helmholtz Zentrum München.

The PTW Freiburg irradiator (Fig. 4.10b) available at Helmholtz is comprised of two X-ray tubes: a 160 kV Yxlon and a 320 kV Philips, placed one in front of the other, however only the latter one was used in the framework of this study. The tubes are separated by a seven-metre bench. X-ray irradiation is narrowed and attenuated by metal filters, providing a specified photon energy. This selection is made in a dedicated software, which controls the set of filters (filters wheel) and the shutter system.

The PTW source was used for the analysis of energy dependence, in which samples were irradiated at RT with X-rays of ISO narrow spectrum qualities from N30 to N300, which corresponds to photon energies of 24 to 250 keV. The dose rate varied depending on the radiation quality and the distance from the tube and ranged between 14 and 200 mGy.h^{-1} (Greiter; Denk; Hoedlmoser, 2016).

4.4.2 Gamma Source

An Amersham Buchler OB20 gamma irradiator (Fig. 4.11) was used in this study as the calibrated source for studying energy dependence. The irradiator has seven ^{137}Cs and five ^{60}Co sources in an eight-metre calibration band. The calibrated air kerma rates can vary from 4 µGy.h^{-1} up to 20 mGy.h^{-1} and up to 2 Gy.h^{-1} for ^{60}Co and ^{137}Cs, respectively, at 1 metre of distance (Greiter; Denk; Hoedlmoser, 2016).

Figure 4.11 - Amersham Buchler OB20 gamma irradiator available at the Institute of Radiation Medicine of the Helmholtz Zentrum München.

Aliquots of HfO_2 were irradiated with a ^{137}Cs gamma source at a photon energy of 662 eV in order to normalise the photon energy response curve.

Chapter 5

5 Results and Discussion

This section covers the results of the characterisation of the synthesised material, and it is divided into five subsections, from the synthesis of the material and its structure identification to the studies regarding its application in ionising radiation dosimetry.

The first subsection is dedicated to the synthesis of the material and the XRD analysis, which allowed us to investigate the crystalline arrangement obtained. The subsequent subsection is focused on how the heat treatment influences the luminescent properties of HfO_2.

The third subsection approaches a short review of the main defect types reported to be found in HfO_2 samples and the ESR findings, which shed light on the possible defects involved in the HfO_2 luminescence studied here. The fourth subsection is dedicated to the investigation of the application in IRSL dosimetry, considering the best sample in terms of luminescence intensity. Finally, the fifth section has a preliminary analysis of the pulsed-OSL for HfO_2.

5.1 The Synthesis of Hafnium Oxide Nanoparticles

Powder samples of HfO_2 were successfully synthesised using the precipitation method. After the heat treatment at 500 °C for 2 hours, the sample conformation was found to be a whitish-thin powder, which stays the same after the subsequent heat treatment at higher temperature, as is shown in Figure 5.1.

Figure 5.1 - Photo of the powder sample of HfO_2 after the calcination at 1600 °C for 2 hours.

The subsequent heat treatment, that is calcination, at high temperatures of up to 1600 °C did not change the appearance of the samples, which kept the whitish-powder characteristic. This result was expected as the melting point of HfO_2 is above 2500 °C. For the calcination, the samples were placed in a high-purity alumina crucible which supports working temperatures of up to about 1800 °C.

5.1.1 X-ray Diffraction: Structure Identification

To confirm that the material synthesised was indeed HfO_2, XRD measurements were carried out. Figure 5.2 shows the diffractogram for samples obtained by the precipitation method and calcined at different temperatures of 1000, 1200, 1400 and 1600 °C for 2 hours. Results indicate that the material has a crystalline structure independent of the heat treatment, which is proven by the presence of sharp and defined peaks and no wide bands, the latter ones are characteristic of amorphous materials.

The analysis comparing the experimental curves with the database from ICCD confirmed that all the samples were associated with a HfO_2 crystalline structure in a monoclinic arrangement (m-HfO_2), so-called Baddeleyite, of space group $P2_1/c$ number 14, with PDF2/2003 reference code number 01-078-0050. The most intense peaks were associated with their respective Miller indices, in which the 100 % peak is at about 28.3°, and is associated with the *hkl* plane $(\bar{1}11)$.

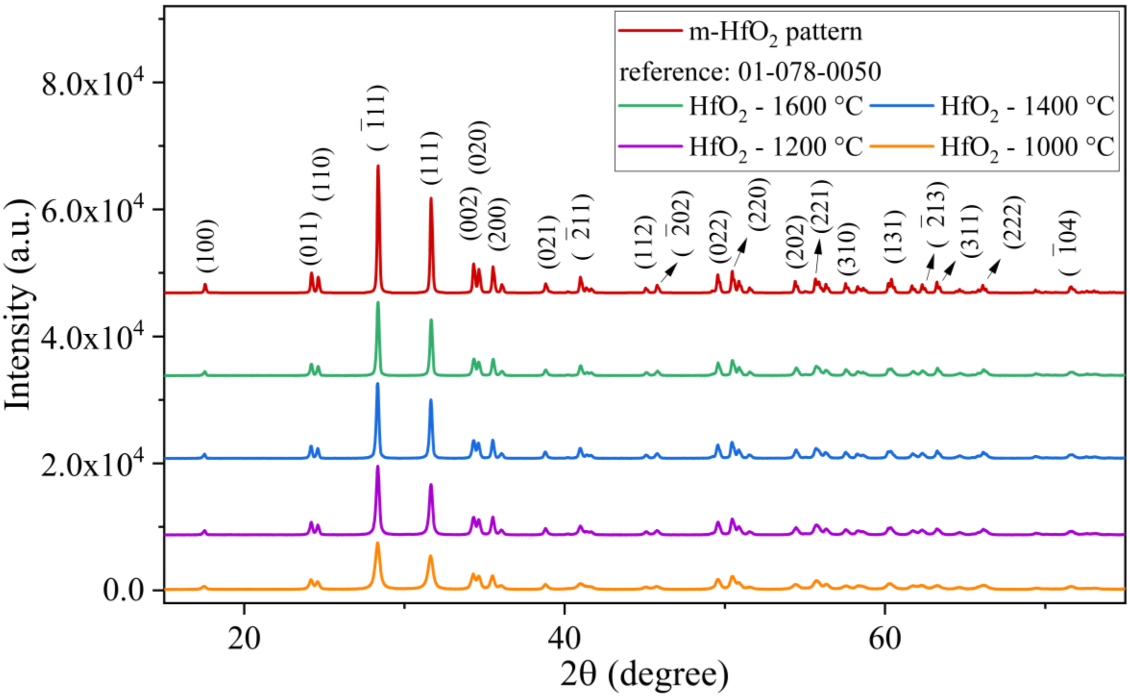

Figure 5.2 - XRD powder patterns of HfO$_2$ synthesised by the precipitation method and calcined at 1000, 1200, 1400 and 1600 °C for 2 h. The red curve indicates the pattern of the monoclinic phase. The most intense peaks are related to their respective Miller index values.

This arrangement in a monoclinic phase was expected as the phase diagram and previous studies already reported that at normal conditions of pressure and temperature, that this is the favoured phase (Choi; Mao; Chang, 2011), and is independent of the synthesis route. Kiisk *et al*. (2010) for example, reported a m-HfO$_2$ by using the sol-gel route, as well as Ramadoss and Kim (2012) by using the sonochemical method and Manikantan *et al*. (2017) with a variation of the co-precipitation method.

5.2 Heat Treatment Influence on Hafnium Oxide Crystallite Size and Luminescence Properties

One of the main aims of this study is to evaluate how heat treatment influences the properties of the material, more specifically regarding its crystalline structure and luminescence. The next subsections discuss this.

5.2.1 Average Crystallite Size

XRD findings showed that the increase of the heat treatment temperature did not induce changes in the crystalline phase as all the samples have a monoclinic arrangement. However, differences are noticeable when looking at the peaks' height and width. Figure 5.3 shows a zoom of the 100 % peak related to the plane *hkl* $(\bar{1}11)$. It shows that the increase in temperature led to more intense and thinner peaks, which reflects changes in the interatomic distances, despite there being no changes in the crystalline phase (as mentioned in Section 3.4.1, a higher temperature is usually necessary for the phase transition).

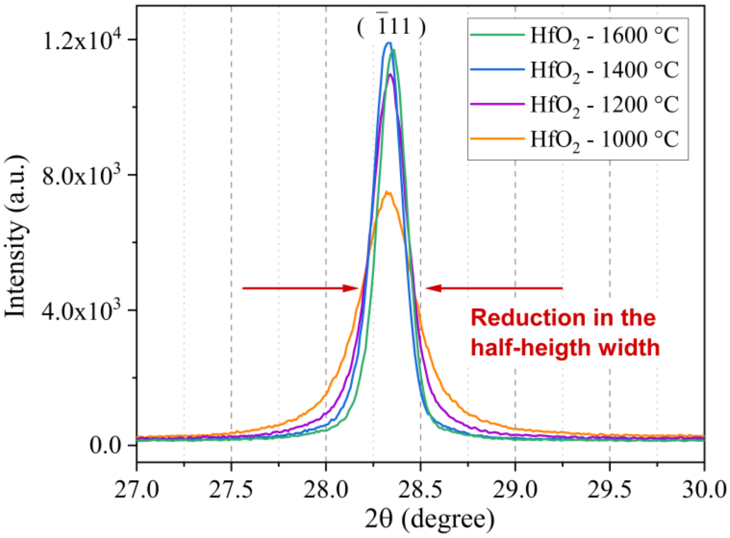

Figure 5.3 - 100 % peak of the XRD powder patterns of HfO_2 synthesised by the precipitation method and calcined at 1000, 1200, 1400 and 1600 °C for 2 h.

The line broadening in polycrystalline materials can be an effect of the finite size of crystallites, due to its participation in coherent X-ray scattering, also because of micro-strains due to the interatomic-spacing fluctuation that may be defect-mediated, and even related to instrumental broadening (Zolotoyabko, 2014).

To evaluate the influence of the heat treatment in the crystallite size *d*, the Scherrer equation can be used to estimate the average value of *d*, given by (Langford; Wilson, 1978):

$$d = \frac{k\lambda}{B\cos\theta} \tag{5.1}$$

Where *d* depends on the form factor *k*, here adopted as 0.9 (based on the work of Ramadoss; Krishnamoorthy; Kim, 2012), the wavelength of the incident X-ray λ (1.54059 Å), the peak half-height width *B* (rad) and the peak position θ. The average crystallite size was calculated considering the three most intense peaks associated with the planes $(\bar{1}11)$, (111) and (200).

The results of *d* indicated that the heat treatment temperature induced an increase in the crystallite size (Table 5.1). HfO_2 calcined at 1000 °C has an average *d* value of 22.8 ± 2.7 nm (average ± standard deviation). When the sample undergoes a heat treatment at 1200 °C for 2 hours, the crystallite size increases to 34.3 ± 1.2 nm. Further increases were observed for higher temperatures, reaching *d* values of 41.6 ± 0.6 nm and 41.6 ± 2.6 nm for HfO_2 calcined at 1400 and 1600 °C for 2 hours, respectively. It is noted that for temperatures higher than 1400 °C, the material seems to find a more stable crystalline conformation since the estimated values of *d* remained similar.

Table 5.1 - Average Crystallite Size for HfO_2 synthesised by precipitation method and calcined at different temperatures.

Sample	**Average Crystallite Size (average ± standard deviation) in nm**
HfO_2 – 1000 °C 2h	22.8 ± 2.7
HfO_2 – 1200 °C 2h	34.3 ± 1.2
HfO_2 – 1400 °C 2h	41.6 ± 0.6
HfO_2 – 1600 °C 2h	41.6 ± 2.6

Those results confirmed that the material is arranged in a nano scale. Previous studies have shown results in agreement with the ones found here. Ramadoss, Krishnamoorthy and Kim (2012) synthesised the material using the same method of precipitation and calculated a *d* value of 18 nm. The smaller size could be attributed to the fact they did not perform the heat treatment at high temperatures. Chuang, Lin and Chen (2012) obtained HfO_2 powders using the sol-gel method subjected to conventional heat treatment and microwave treatment, and by using the same equation, they found grain sizes of 96, 147 and 161 nm for the conventional heat treatment at 450, 550 and 650 °C, respectively.

This tendency of increased crystallite size due to high-temperature heat treatments is observed in other materials, as already reported for ZnO (Soares *et al.*, 2017), BeO (Altunal *et al.*, 2020) and TiO_2 (Lukong; Ukoba; Jen, 2022). One feasible reason for this is that more energy is being supplied to the system, which results in rearrangements in the lattice, either by getting longer interatomic distances or the creation of defects.

5.2.2 Fluorescence Spectra

The HfO_2 crystals synthesised by the precipitation method display an intense broad emission band in the blue region when stimulated with UV light at 300 nm (λ_{exc}), independent of the heat treatment, as shown in the emission spectra (Fig. 5.4). There is also a smaller band in shorter wavelengths which is centred at around 345 nm.

Analysing the excitation spectra for a detection wavelength at 469 nm (λ_{emi}), it is observed that the emission is associated with a broad absorption band centred at about 300 nm.

The comparison of the signal for samples with different heat treatment temperatures shows that higher treatment temperatures led to an improvement in the fluorescence signal. The calcination at 1600 °C induced a maximum intensity of the emission band about seven times higher than the one observed for the sample calcined at 1000 °C. Thus, even though a higher temperature did not change the crystalline phase of the material, it was responsible for increasing the crystallite size and the fluorescent emission as well.

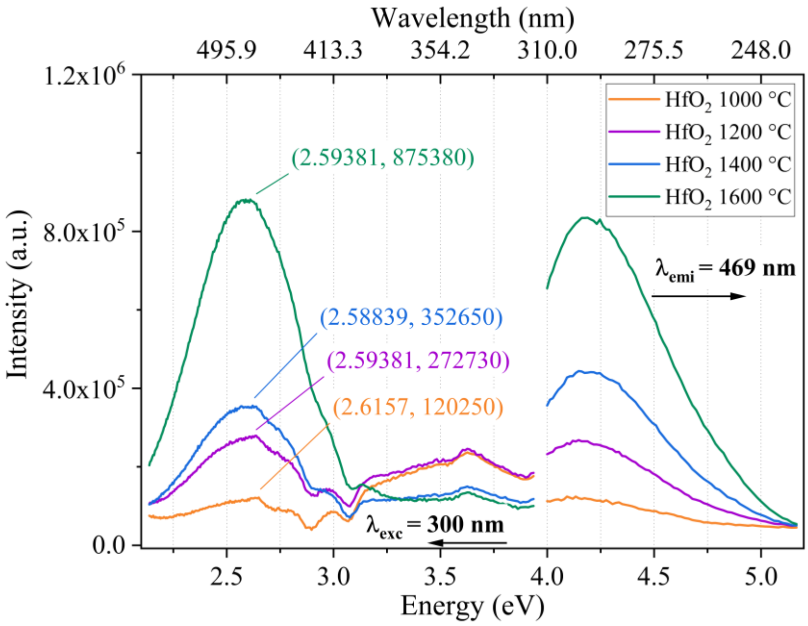

Figure 5.4 - Fluorescence spectra of HfO_2 calcined at 1000, 1200, 1400 and 1600 °C. Curves on the left refer to the emission spectrum (λ_{exc} = 300 nm), and curves on the left refer to the excitation spectrum (λ_{emi} = 469 nm).

A hypothesis for this result is that the creation of defects was facilitated by the high temperatures of calcination, and these defects may be related to the blue emission. The main emission band from the emission spectrum for each sample was fitted with a Gaussian curve, and it was found that the band is centred at 2.56, 2.58, 2.58 and 2.59 eV for HfO_2 calcined at 1000, 1200, 1400 and 1600 °C for 2 hours, respectively. The fitted curves are in Appendix A.

Reports in the literature indicated that the significant emission at 2.7 eV of HfO_2 is related to oxygen vacancies as they lead to the existence of electron-hole pairs in the lattice, hence to the charge carriers (Kiisk *et al.*, 2010). Chuang, Lin and Chen (2012) investigated the photoluminescence of HfO_2 powder samples, synthesised by two variations of the sol-gel method, and found that higher heat treatment temperatures were responsible for diminishing the stoichiometric ratio O/Hf, which agrees with the increase in the concentration of oxygen vacancies. Their photoluminescence spectral results showed that the sample treated at 650 °C had a much more intense signal than the one treated at 400 °C, considering either conventional heat treatment or the microwave one. It reaffirms the role of temperature calcination in creating defects and its importance in luminescence.

As regards the absorption region related to this emission, previous studies have found it to be at around 5.2 eV (Gritsenko; Perevalov; Islamov, 2016), which is in a more energetic region than used here. The excitation at 4.2 eV was found in the work of Kiisk *et al.* (2010) which analysed sol-gel prepared hafnia thermally treated up to 1000 °C. The work reported that the excitation band would be a result of the charge transfer transitions from the valence band to either singly or doubly ionised oxygen vacancies. Therefore, it is reasonable to infer that oxygen vacancies also play an important role in the sample studied here.

Figure 5.5 depicts the Chromaticity diagram for all the samples. It is observed that there is a slight change in the emission from blue-greenish to blueish, which may indicate a different contribution of defects.

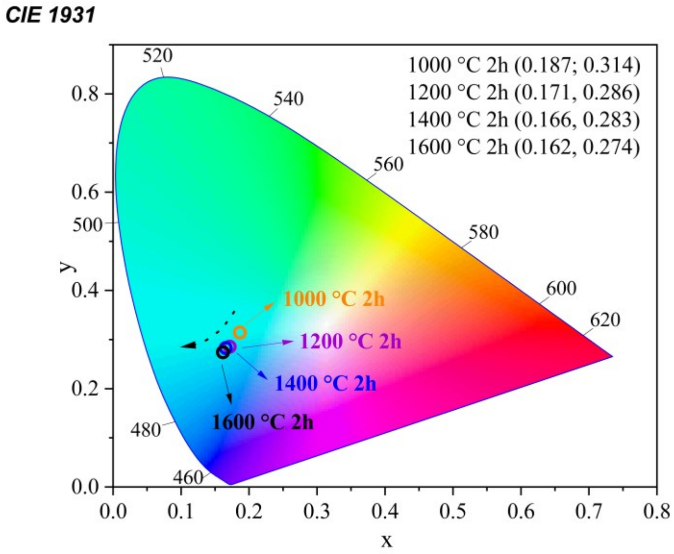

Figure 5.5 - Chromaticity diagram plot for HfO_2 calcined at 1000, 1200, 1400 and 1600 °C.

Plotting on a chromaticity diagram is interesting when studying the application in LED devices and other light sources, as it clearly displays the main emission in the visible range. So far and to the best of the author's knowledge, no other studies have analysed the HfO_2 emission regarding its chromaticity diagram.

5.2.3 Thermoluminescence in the Visible Range

The TL glow curves of HfO_2 after beta irradiation doses were recorded for all the samples concerning the emission in the visible range, by using the optical filter Schott BG-39. For means of comparison, the samples were weighed to all have the same mass (4 mg for each aliquot).

Figure 5.6a shows the TL glow curves for HfO_2 calcined at 1000 °C for 2 hours and irradiated with doses lower than 2 Gy. It is possible to notice that the sample has a signal which increases with dose. The curve is composed of at least two peaks at temperatures lower than 200 °C, indicating the presence of shallow traps. The first and most prominent peak is also the shallower one, located at a temperature below 100 °C. As it is at a low temperature, the trapped electrons related to this peak may be easily released at room temperature with time, making this a less stable peak.

Figure 5.6b shows the same measurement but for the sample calcined at 1200 °C. This result shows the influence of the heat treatment temperature on the TL properties. The TL glow curve has a higher intensity (one order of magnitude more). In addition, not only has the intensity increased but the curve shape has also changed. Therefore, the higher temperature of heat treatment may have not only enhanced the signal by creating more traps, but also changed the proportion of the concentrations for each trap's levels. The TL of HfO_2 calcined at 1200 °C has a set of overlapped peaks between 50 and 250 °C, the most prominent of which is at about 125 °C.

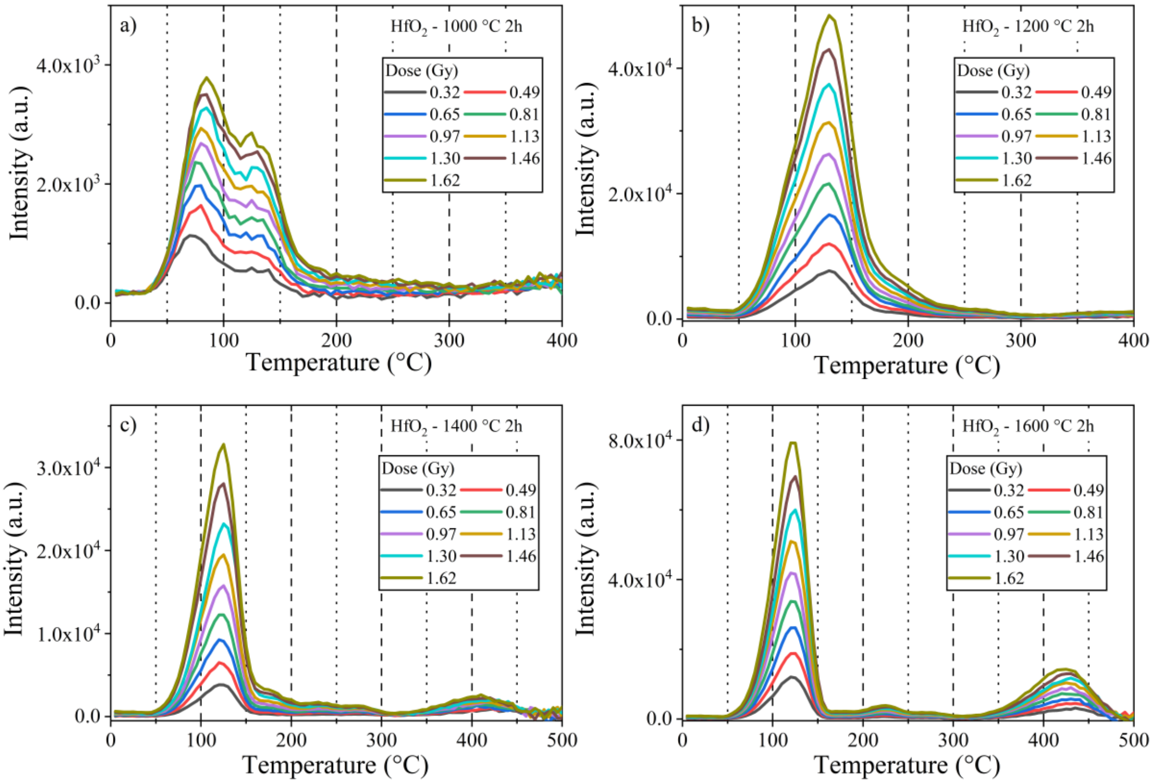

Figure 5.6 - TL glow curves after different beta doses between 0.32 and 1.62 Gy for HfO_2 powder calcined at (a) 1000, (b) 1200, (c) 1400 and (d) 1600 °C for 2h.

Whilst the sample calcined at 1000 °C does not have any TL peaks at temperatures above 250 °C, the presence of peaks in this region starts to appear for the sample treated at 1200 °C. Thus, it indicates that traps of higher activation energies were created in the material, which may or not be associated with different defect types.

By calcinating the sample at 1400 °C, the intensity magnitude remains the same as the magnitude of the sample calcined at 1200 °C (Fig. 5.6c), however, some changes are observed in the peaks' distribution. The first set of peaks at around 125 °C is still the most intense, therefore the shallow traps are meant to be representative. It is worthwhile to mention that thermal quenching may occur significantly for temperatures above 200 °C, hence the shallow traps would not be that affected by it.

An interesting aspect of the TL curve for the sample calcined at 1400 °C, is the presence of deeper peaks, with one of them in the region around 400 °C. It shows that calcinating the sample at 1400 °C allows for the creation of deeper trap levels. The signal is proportionally dependent on the irradiation dose.

When the sample is calcined at 1600 °C, a further increase in intensity is observed (Fig. 5.6d), thus the increase in the temperature of heat temperature proved to be an important mechanism for enhancing the TL emission. The most intense set of peaks is found in the same temperature range that was observed for the sample calcined in lower temperatures. However, in this case, the deeper peak at about 400 °C is more remarkable in scale, when compared with the most intense part of the curve.

Those findings highlight that the heat treatment influenced the concentration of defects in the material, which are directly related to the TL emission. Moreover, the changes in the shape of the curve indicates that the ratio of traps' concentration may have changed as well.

The TL emission was further investigated for higher doses, up to 30 Gy, to verify if the irradiation dose might influence the glow curve and if the TL intensity would saturate or not at a particular dose. In this section, the term "high doses" is used for irradiation doses above 5 Gy.

Figure 5.7 shows the TL glow curves for all the samples irradiated with β particles with doses ranging between 5 and 30 Gy. Results show that the TL intensity increases with dose in this analysed range as well. Figure 5.7a shows that for doses higher than 10 Gy, the TL glow curve for the sample calcined at 1000 °C starts to present a change in shape. Whereas the most intense peak is located below 100 °C for low doses, there is a second, more intense peak located at a higher temperature of about 125 °C for doses above 10 Gy. Some hypotheses for this behaviour may include either the saturation of the traps related to this peak or the signal decay while the irradiation is being performed. Since the irradiation was made with the same dose rate, and getting a high dose requires a longer irradiation time, there is more time for the unstable signal (< 100 °C) to decay.

The TL glow curve for HfO_2 calcined at 1200 °C at high doses has similar behaviour to the one observed for low doses (Fig. 5.7b). In addition, the intensity of the here so-called “second” peak is accentuated. The reasons why may be the same as for the results from the sample calcined at 1000 °C.

TL intensity growth due to the heat treatment temperature is also observed for high temperatures. Figures 5.7c and 5.7d depict the emission for the samples calcined at 1400 and 1600 °C, respectively. The most noticeable peak remains at about 125 °C, and their curve characteristics are similar to the low dose ones. It means that the same set of traps is responsible for the emission either at low or high irradiation doses.

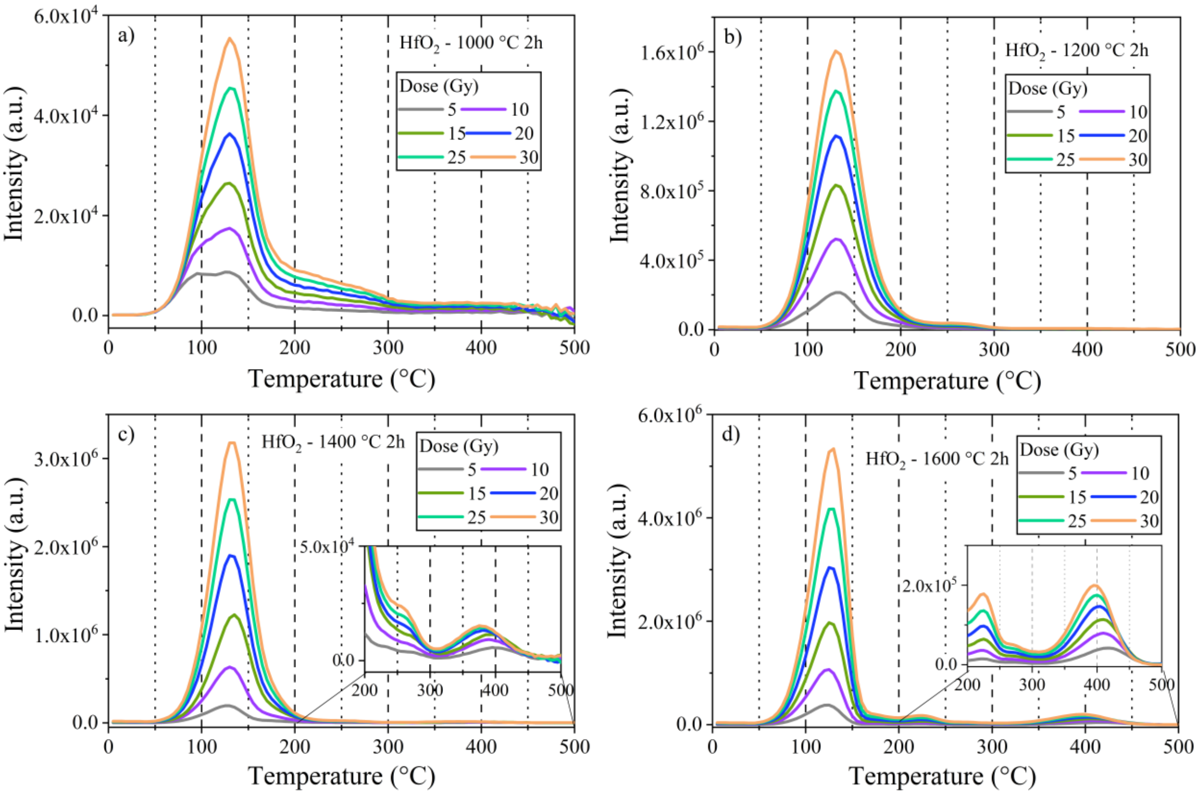

Figure 5.7 - TL glow curves after different beta doses between 5 and 30 Gy for HfO_2 calcined at (a) 1000, (b) 1200, (c) 1400 and (d) 1600 °C for 2h.

To better understand the tendency of the signal growth, the TL intensity as a function of the absorbed dose was plotted, considering both the intensity over a range by the integrated area and at the peak maximum temperature. As the area below the TL glow curve represents the concentration of trapped electrons and the peak intensity is meant to be proportional to this concentration, both of them can be used for analysing the dose-response behaviour.

The dose-response curve for the sample calcined at 1000 °C has a linear behaviour over the entire range of doses studied (Fig. 5.8a), either considering the peak intensity at 125 °C or the integrated area between 50 and 200 °C, with no indication of saturation. When the same analysis is done for HfO_2 treated at 1200 °C, a linear tendency is observed in the range of low doses, however, a non-linear trend is observed in the first part of the curve (probably due to the higher uncertainty level associated with the experimental setup), but also for doses above 5 Gy, being a supralinear followed by a like-saturation tendency (Fig. 5.8b). A case of supralinearity is usually associated with the presence of deep trapping centres. In the presence of the deep trapping centres, at low doses, the deep traps will compete with the shallow ones (or dosimetric traps). The signal arises mostly (if not totally) from the shallow traps. With high doses, the deep traps may be filled (saturation), and more charges will be available for the shallow ones, resulting in more emission of light than expected (Yukihara; McKeever, 2011).

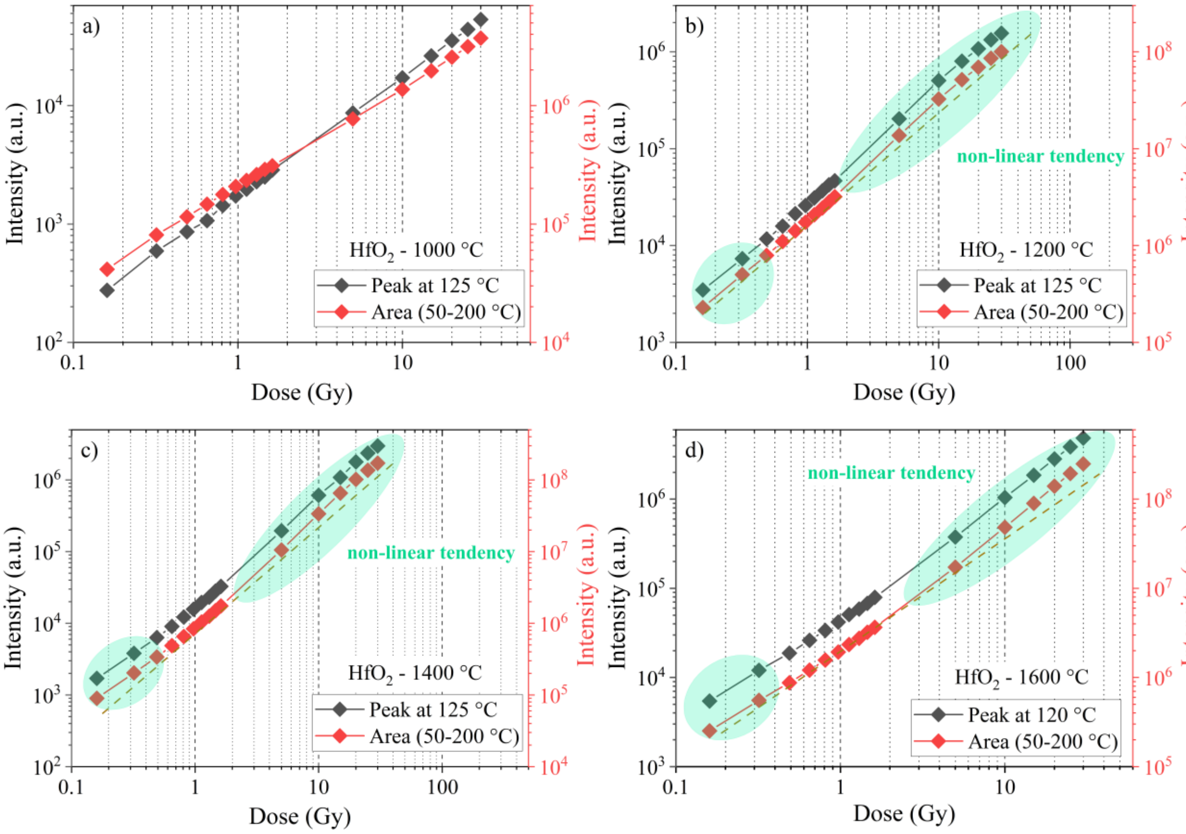

Figure 5.8 - TL dose-response curves for beta doses between 0.32 and 30 Gy for HfO_2 calcined at (a) 1000, (b) 1200, (c) 1400 and (d) 1600 °C for 2h. The curves in black refer to the intensity at the peak maximum temperature, whilst the red curves refer to the intensity over an integrated region between 50 and 200 °C. The brown dashed line refers to the linear tendency. Green areas indicate a non-linear region in the dose-response curve.

Figures 5.8c and 5.8d show that the TL intensity for HfO_2 calcined at 1400 and 1600 °C also present a linear trend in the dose-response curve, limited to a range of low doses, and a supralinear behaviour for doses above 5 Gy. In the curves in which the intensity was integrated over an area between 50 and 200 °C the supralinearity is evident.

Few studies have reported the TL emission for pure HfO_2. Pejaković (2010) investigated the TL of polycrystalline HfO_2 pellets sintered at different temperatures and in atmospheric air and reported a TL curve composed of three peaks in the region between -50 and 150 °C after irradiation with UV at 254 nm, at -10, 30 and 100 °C. The most intense peak was found to be located at -10 °C for the sample not sintered, becoming the one at 30 °C after sintering at 1300 or 1500 °C. Mendoza *et al.* (2010) studied the TL emission for HfO_2 films deposited by ultrasonic spray pyrolysis and reported a broad TL peak between 100 and 300 °C, of low intensity, after UV radiation at 240 nm.

Nanoparticles synthesised by precipitation method were evaluated regarding their TL after ^{60}Co irradiation by Sekar *et al.* (2020), which resulted in an emission curve with a set of peaks between 200 and 350 °C, in which the most intense peak was at about 325 °C. And more recently, Laganovska *et al.* (2023) obtained HfO_2 nanoparticles following different routes of synthesis, including the precipitation method, and evaluated the TL emission and its possible associated defects. The sample synthesised by the precipitation method was calcined at 800 °C for 2 hours, and its TL glow curve after X-ray irradiation was shown to be composed of three peaks at about 63, 95 and 172 °C.

Those reports in the literature illustrate that the synthesis route and quality of irradiation, among other aspects, influence the TL properties. Moreover, they are quite different from the ones described here. Therefore, the results reported here are outstanding by themselves as no similar studies have been found.

In this section, the influence of heat treatment on the TL emission was demonstrated through intensity and dose-response curve behaviour. The next section approaches the deconvolution of the glow curves, which gives more information about the traps' parameters related to the phenomenon.

5.2.3.1 T_M-T_{stop} Method and Computerised Glow Curve Deconvolution Study

TL emission can be detailed by using two methods, the T_M-T_{stop} and CGCD, both detailed in Section 4.2.1.4. T_M-T_{stop} method allow for estimating the number of peaks, their position and likely kinetic order (McKeever, 1980, 1985). Based on the values obtained with T_M-

T_{stop}, they can be used as input for fitting the curves with a GOK model, using the CGCD (Afouxenidis *et al*., 2012; Soni *et al*., 2014).

Figure 5.9 depicts the T_M-T_{stop} analysis for all the samples, with different heat treatment temperatures. According to the T_M-T_{stop} analysis for HfO_2 calcined at 1000 °C for 2 hours, its TL emission curve is estimated to have at least four peaks, which are indicated by the presence of four plateaus in the graph at T_M values of 95, 130, 230 and 260 °C (Fig. 5.9a). The plateau at 95 °C suggests that the peak at this temperature should have a kinetic order close to 1, as the slope of it is close to zero and there is no tail at the end. This is characteristic of first-order peaks because there is no shift in T_M whilst the initial population of trapped charges decreases (McKeever, 1985). The other plateaus have tails, therefore, their kinetic order is likely closer to 2 than 1 ($b \approx 2$). Moreover, there is a sloping line between T_M values of 130 and 230 °C, which is a characteristic of a region of overlapped peaks in the TL glow curve (McKeever, 1980).

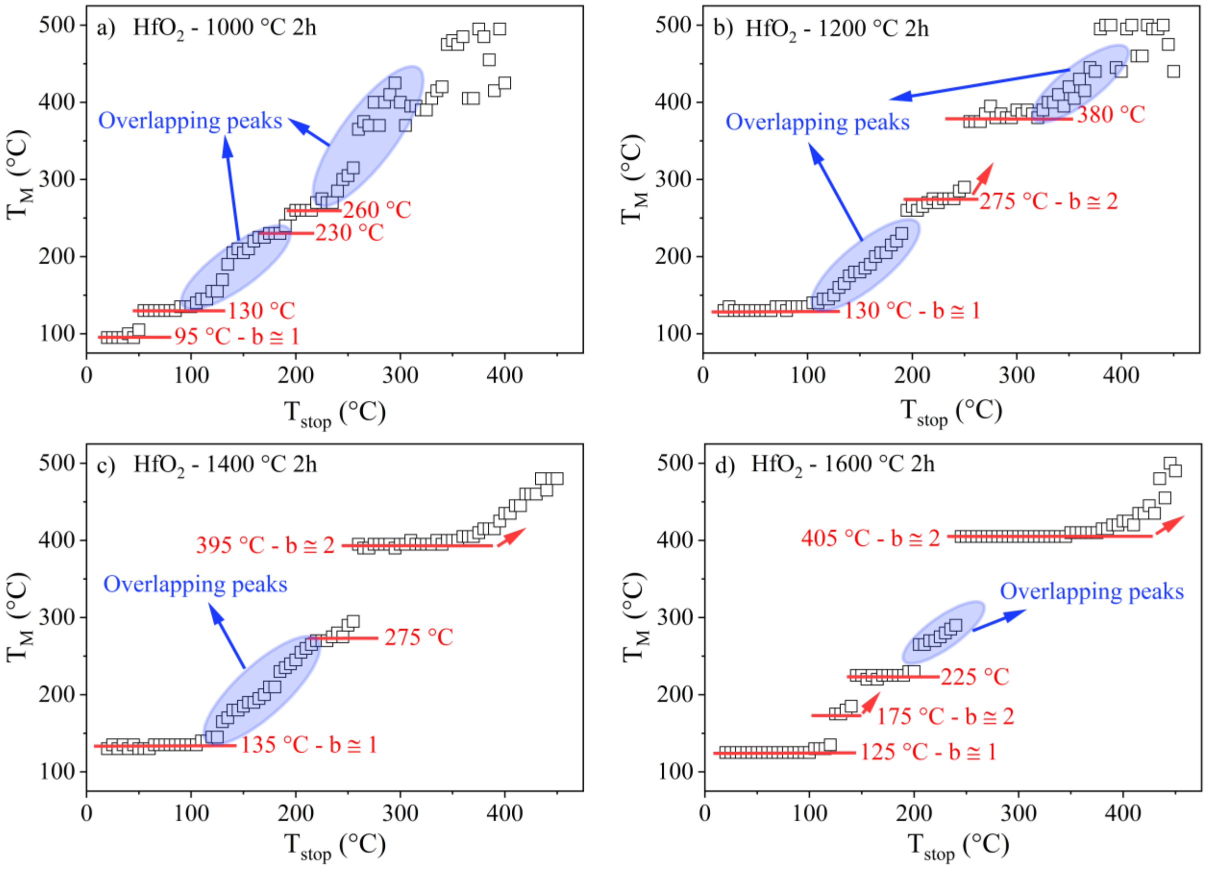

Figure 5.9 - Analysis of T_M-T_{stop} for HfO_2 powder samples calcined at (a) 1000, (b) 1200, (c) 1400 and (d) 1600 °C for 2 h. The red lines indicate plateau patterns, and the blue areas indicate a region with overlapped peaks.

A different pattern is observed for the sample calcined at 1200 °C (Fig. 5.9b). There are no plateaus at temperatures below 100 °C, as was obtained for the sample calcined at 1000 °C.

The T_M-T_{stop} plot has a well-defined plateau at a T_M of 130 °C, which seems to be related to a peak of kinetic order close to 1 ($b \approx 1$). Overlapped to the first peak, there is probably a set of peaks between 150 and 250 °C, which is characterised by the slopping line trend. Two other plateaus are found at 275 and 380 °C, which may indicate peaks at those temperatures. Above a T_M = 380 °C, another region of overlapped peaks is identified. A further feature of this graph is the presence of a gap between 300 and 375 °C, indicating that this region may correspond to an absence of peaks in the TL glow curve.

The T_M-T_{stop} plot for the sample calcined at 1400 °C is shown in Figure 5.9c. It has a remarkable plateau at 135 °C, which has no tail at its end, hence a kinetic order close to 1 ($b \approx 1$). Another plateau is at about 395 °C, which presents an increasing value of T_M at its end, indicating to be associated with a second-order kinetic peak ($b \approx 2$). A more discrete plateau is located at 275 °C and due to its characteristic, the associated peak may have a kinetic order close to 1 ($b \approx 1$). Furthermore, a large region of overlapped peaks is estimated to be between 150 and 300 °C.

It is worthwhile mentioning that the results of the T_M-T_{stop} agree with the experimental TL glow curve. For the sample calcined at 1400 °C, as was mentioned before, the high temperature of heat treatment allowed for the creation of deeper traps. It is seen here by the clear plateau at T_M of 395 °C (Fig. 5.9c).

The analysis of the sample calcined at 1600 °C shows the existence of four plateaus at 125, 175, 225 and 405 °C (Fig. 5.9d). The first and third plateaus do not have significant tails, which leads to estimating their kinetic orders as being close to 1 ($b \approx 1$). Whilst the ones at 175 and 405 °C have a more second-order kinetic ($b \approx 2$) characteristics. There is also a region of overlapped peaks between 250-300 °C.

Based on the approximate number of peaks identified by the T_M-T_{stop}, as well as their T_M positions, and probable values of b (if closer to 1 or 2), the data were used as input for the CGCD study. Table 5.2 shows the parameters obtained with the CGCD study for all the samples, by fitting TL glow curves after an irradiation dose of 25 Gy, such as the intensity I, the temperature of the peak T_m, the activation energy E, the kinetic order b and the frequency factor s.

In all the cases the value of FOM was found to be lower or close to 5%, which is a good indicator of the fitting (Afouxenidis *et al.*, 2012; Soni *et al.*, 2014). In addition, it can be observed that the energy of activation increases with T_m, which is an expected result because electrons trapped in deeper levels will need more energy to be released. Values of E varied between 0.68 to 1.6 eV, for the shallower peak of the sample calcined at 1000 °C to the deeper one for the sample calcined at 1600 °C, respectively.

Table 5.2 - Parameters used in the CGCD study of TL glow curves of HfO_2 samples calcined at different temperatures, for a beta irradiation dose of 25 Gy.

Peak number	**Parameter**				
	I (a.u.)	**T_m (°C)**	**E (eV)**	**b**	**s (s^{-1})**
Sample: HfO_2 – 1000 °C. FOM: 3.82 %					
1	7000	99	0.68	1.15	4.59×10^{8}
2	38000	129	0.70	1.34	1.45×10^{8}
3	7450	140	1.05	1.7	2.25×10^{12}
4	6590	188	1.11	1.52	3.99×10^{11}
5	4300	228	1.20	1.34	3.19×10^{11}
6	4100	269	1.30	1.57	3.02×10^{11}
7	1900	331	1.35	2	3.66×10^{10}
8	2000	411	1.4	2	3.31×10^{9}
Sample: HfO_2 – 1200 °C. FOM: 3.99 %					
1	1370000	132	0.68	1.4	6.70×10^{7}
2	67000	194	1	1.7	1.56×10^{10}
3	25500	268	1.15	1.4	1.09×10^{10}
4	4000	345	1.5	2	3.64×10^{11}
5	4900	403	1.51	2	3.11×10^{10}
Sample: HfO_2 – 1400 °C. FOM: 6.05 %					
1	2370000	132	0.69	1.001	9.42×10^{7}
2	360000	163	0.97	1.8	4.55×10^{10}
3	2000	203	1	1.4	9.53×10^{9}
4	7000	240	1.15	1.5	4.85×10^{10}
5	12000	281	1.3	1.6	1.58×10^{11}
6	13000	399	1.5	2	3.18×10^{10}
Sample: HfO_2 – 1600 °C. FOM: 3.30 %					
1	4160000	127	0.76	1.001	1.04×10^{9}
2	99000	167	0.97	1.9	3.51×10^{10}
3	99000	221	1	1.4	3.60×10^{9}
4	7600	237	1.14	1.6	4.48×10^{10}
5	24000	284	1.2	2	1.50×10^{10}
6	168000	397	1.6	1.8	2.12×10^{11}

The CGCD analysis estimated that the TL glow curve for HfO_2 calcined at 1000 °C and for a dose of 25 Gy is composed of eight peaks. The first two peaks are at 99 and 129 °C and have respective kinetic order values of 1.15 and 1.34. These results corroborate the finding from T_M-T_{stop}, in which two plateaus were found at 95 and 130 °C. This small variation in the T_m is predicted by the T_M-T_{stop} protocol, which may be of ± 5 °C (McKeever, 1985). The other two plateaus from the T_M-T_{stop} which are at 230 and 260 °C, are the ones found at 228 and 269 °C in the CGCD, both do not have a second-order characteristic, as estimated before. As regards the other four peaks, two of them are between 130 and 230 °C, and the other two are at temperatures above 260 °C. These sets of peaks correspond to the two areas of overlapping peaks indicated by the T_M-T_{stop}.

The combined use of T_M-T_{stop} and CGCD proved to be an effective mechanism for characterising the TL emission of the material. The fitted TL glow curve for HfO_2 calcined at 1000 °C is shown in Figure 5.10a.

Figure 5.10b depicts the fitted TL glow curve after the CGCD study for HfO_2 calcined at 1200 °C. The CGCD analyses found the TL curve to be composed of five peaks. The most intense peak is also the shallowest one at 132 °C and has a *b* value of 1.001, agreeing with the result from T_M-T_{stop}, which had previously shown a plateau at 130 °C. The peak at 194 °C corresponds to the slopping line tendency obtained in the T_M-T_{stop}, while the peak at 268 °C relates to the plateau at 275 °C. Two other deeper peaks of lower intensities were determined at 345 and 403 °C, both following a second-order kinetic.

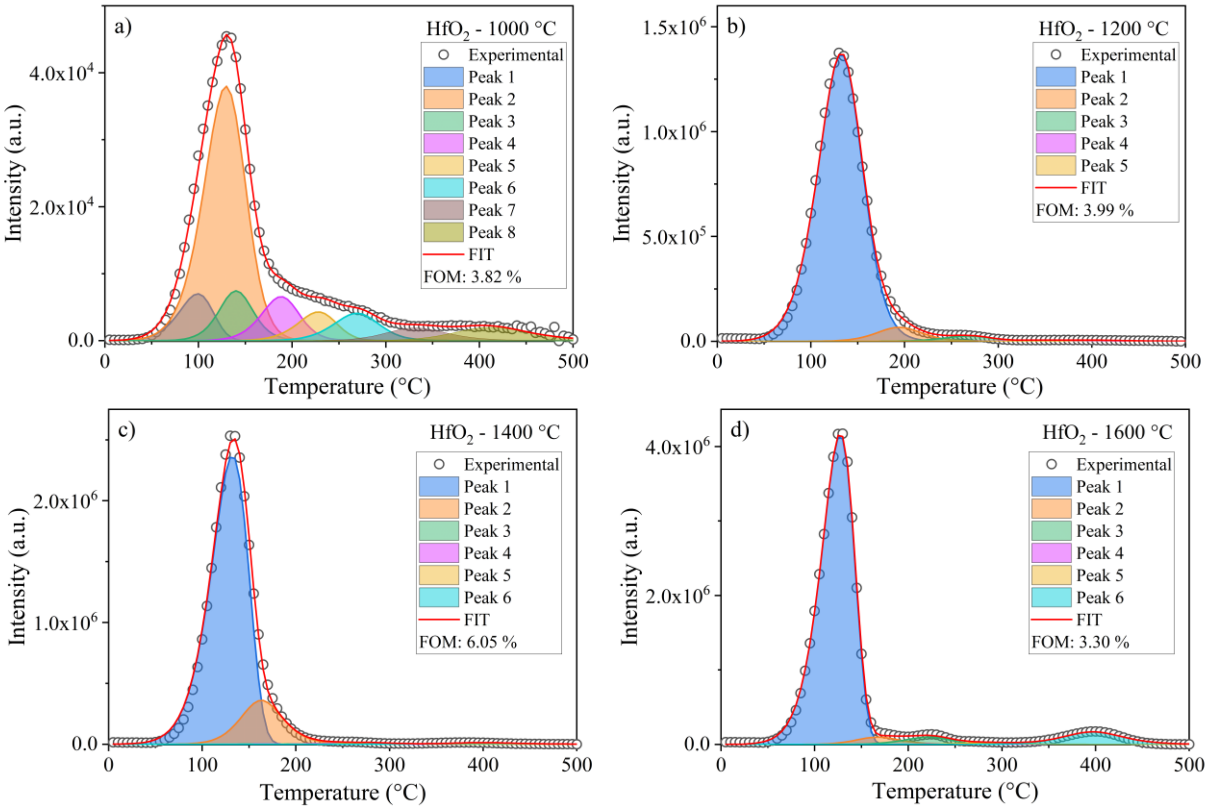

Figure 5.10 - CGCD analyses of TL glow curves for HfO_2 synthesised by the precipitation method and calcined at (a) 1000, (b) 1200, (c) 1400 and (d) 1600 °C for 2 h, after a beta irradiation dose of 25 Gy.

When analysing the CGCD for the TL emitted by the aliquot of HfO_2 calcined at 1400 °C, it shows the presence of six peaks (Fig. 5.10c). The first and most prominent peak is at 132 °C with a kinetic order of 1.001, values which agree well with the T_M-T_{stop}, which has a flat and well-defined plateau at 135 °C. The peaks at 163, 203 and 240 °C with *b* values spanning between 1.4-1.8 may be associated with the long slope observed in the T_M-T_{stop} plot. The fitted peaks at 281 and 399 °C are related to the plateaus at 275 and 395 °C. The sixth peak follows a second-order kinetic, as was also found by the T_M-T_{stop} analysis.

In the case of HfO_2 calcined at 1600 °C, six peaks were also used to fit the TL glow curve (Fig. 5.10d). The first peak is at 127 °C and has a kinetic value close to 1 (as found for the respective plateau in T_M-T_{stop} analysis at 125 °C). The other plateaus identified by T_M-T_{stop} are represented in the fitted peaks at 167, 221, and 397 °C. The second peak has a *b* value of 2, corroborating the previous result. A small peak was adjusted at 237 °C and together with the one at 284 °C, they may be associated with the observed slope. Finally, the deeper peak was fitted at 397 °C and $b = 1.8$, which agrees with the plateau at 405 °C with features of second-order kinetic.

The results of both the T_M-T_{stop} and CGCD analyses verified that the heat treatment played an important role in the concentration and distribution of traps in the material. Moreover, the values estimated for the traps' parameters, such as *E* and *s*, are important for characterising the luminescence. Those results are the first ones reported for this material and are part of an international peer-reviewed publication (Soares; Tatumi; Rocca, 2021). Moreover, in Appendix B, there are the parameters used for deconvoluting the TL glow curves for irradiation doses of 5 and 30 Gy, for matter of comparison, which showed to agree well independent of the dose, for example, the same number of peaks and their values of *E* and *b*.

5.2.4 Optically Stimulated Luminescence

Nanocrystals of HfO_2 were also evaluated regarding their OSL emission in both continuous-wave (CW) and linear-modulated (LM) modes, using blue stimulation (at 470 nm), and after beta irradiation doses up to 30 Gy. The detection was mainly in the UV region, as the Hoya U-340 filter was used.

Figure 5.11a shows the CW-OSL shine-down curves for HfO_2 calcined at different temperatures, for a dose of 25 Gy of beta particles. As is shown, all the samples supply a significant emission, indicating that the traps are not only thermal-sensitive but light-sensitive too.

Independent of the heat treatment temperature, most of the signal decays within 10 s of light stimulation, which demonstrated that trapped electrons are quickly released due to the stimulation. Moreover, it is possible to notice that the signal does not decay abruptly (more noticeable for the HfO_2 – 1600 °C case), there is a prominence at the beginning. It might indicate the occurrence of retrapping, that is, non-first-order kinetic.

Comparing the curves for different heat treatment temperatures, a similar behaviour observed with the TL signal is obtained: higher temperatures led to an improvement in the CW-OSL intensity. The most noticeable increase is when comparing the signal from the sample calcined at 1000 °C and the one calcined at 1200 °C. The latter has a seven times more intense emission. Further increase of about 1.5 times is observed when comparing the OSL intensity for HfO_2 calcined at 1200 °C with the one calcined at 1400 °C. Comparing the signal for the samples calcined at 1400 and 1600 °C, the latter one has a 2.7 times higher intensity.

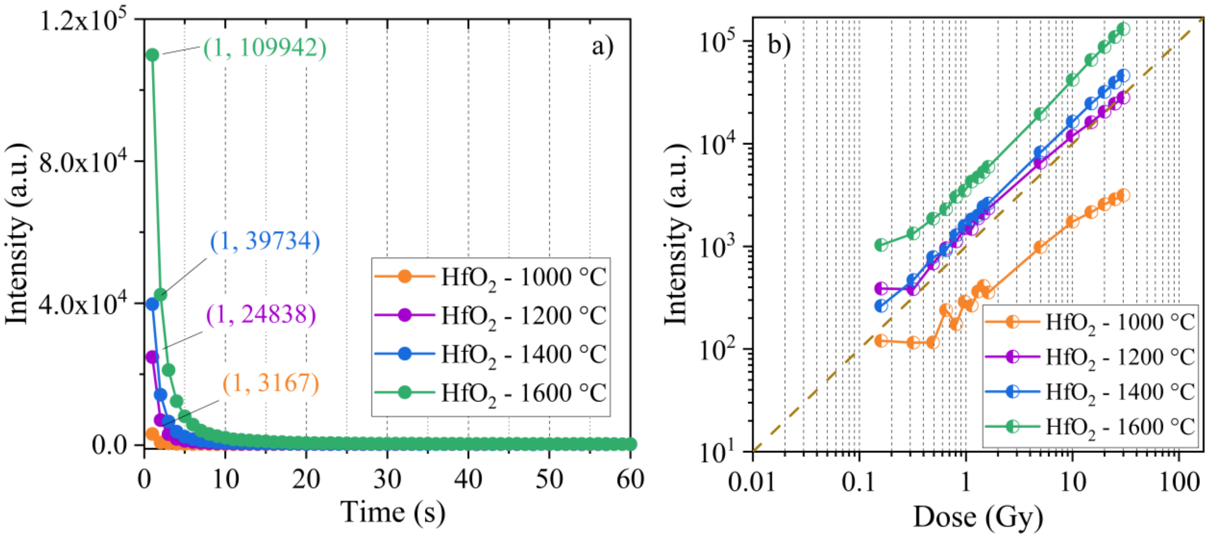

Figure 5.11 - (a) OSL shine-down curves for HfO_2 calcined at different temperatures of 1000, 1200, 1400 and 1600 °C for 2 h, after a dose of 25 Gy of beta particles, and (b) respective dose-response curves. For the dose-response curves, the intensity was taken from the first point minus the background. The background was calculated as the average of the intensity at the latest five points. The doses in the dose-response curve varied from 0.16 up to 30 Gy. The brown dashed line refers to the linear tendency in (b).

The dose-response curve analysis for each sample is shown in Figure 5.11b. The signal was taken from the first point and subtracted by the background, where the background was calculated as the average of the final 5 points of the curve. HfO_2 calcined at 1000 °C does not show a signal for doses below 0.5 Gy, as indicated by the flat region in the graph. Thus, one might assume that the irradiation dose was not enough to populate the traps. For doses above 1 Gy, the signal increases with dose and seems to have a sublinear trend at the end of the curve, for this range of doses.

HfO_2 calcined at 1200 °C shows an increasing CW-OSL intensity due to doses higher than 0.3 Gy. The curve has a linear tendency, followed by a like-saturation (sublinear) region. The same pattern is obtained in the dose-response curve of HfO_2 calcined at 1400 °C, there is an initial linear growth and then, a saturation region. Whilst the one calcined at 1600 °C has an exponential behaviour at the beginning followed by a linear tendency over a wide range of doses. From those results, it may be inferred that the heat treatment influenced the traps' concentrations and/or energy levels somehow.

To try to better identify if there is more than one component in the OSL emission, LM-OSL measurements were carried out with the same stimulation wavelength used in the CW mode, with varying illumination power from 0 to 100 %. The idea being that it might be possible to notice the presence of peaks which would be associated with different components.

Figure 5.12a presents the LM-OSL curves for HfO_2 calcined at different temperatures after a beta irradiation dose of 25 Gy. All curves have a single-peak shape which is centred at a time between 5-8 s, indicating the predominance of one kind of trap's level in the role of luminescence. This main component may be associated with the most intense peak at the TL glow curve, which is located at a low temperature.

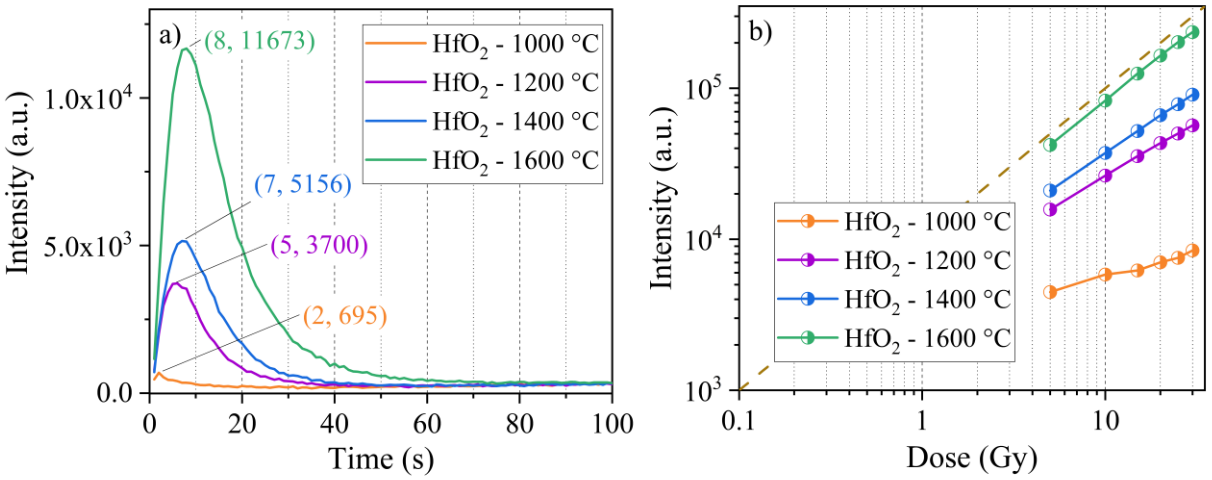

Figure 5.12 - LM-OSL curves for HfO_2 calcined at different temperatures of 1000, 1200, 1400 and 1600 °C for 2 h, after a dose of 25 Gy of beta particles, and the (b) respective dose-response curves. For the dose-response curves, the intensity was taken as the area over an integrated region between 0 and 40 s, and doses varied between 5 and 30 Gy. The brown dashed line refers to the linear tendency in (b).

It is worth drawing attention to the fact that the sample calcined at 1000 °C does not have a significant LM-OSL signal. It is even lower than in the CW mode because the electrons are progressively released, which splits the signal along the recording time (more details on the models were given in Section 3.2.2.2).

Analyses of the dose-response curve show that the LM-OSL intensity increases with dose, as shown in Figure 5.12b, in which the integrated area from 0-40 s was used to plot the intensity.

All curves have a linear trend over the range of doses used here (from 5 up to 30 Gy), apart from the sample calcined at 1600 °C, as a slight sublinear feature might be observed for doses above 25 Gy.

To the best of the author's knowledge, there are no other reports regarding the OSL emission of HfO_2, except for the publications so far derived from this study (Soares *et al.*, 2020; Soares; Tatumi; Rocca, 2021; Soares *et al.*, 2022).

5.2.4.1 Computerised Glow Curve Deconvolution Study

CW-OSL shine-down curves and LM-OSL curves were fitted using the CGCD method with GOK equations, as described in Section 4.2.1.3, apart from the LM-OSL of HfO_2 calcined at 1000 °C because the signal was too low to perform a good fitting.

Table 5.3 shows the parameters used for fitting the CW-OSL shine-down curves by CGCD after a dose of 25 Gy. All the curves (for different heat treatment temperatures) are composed of two components, named fast and medium due to their lifetime values (τ). Apart from the fitting of the CW-OSL of HfO_2 calcined at 1000 °C, all fitted curves resulted in FOM values lower or around 5 %, which is said to be a good indicator.

Table 5.3 - Parameters used in the CGCD study of CW-OSL curves of HfO_2 samples calcined at different temperatures, for a beta irradiation dose of 25 Gy.

		Parameter		
Component	**I_0 (a.u.)**	**b**	**τ (s)**	**σ (cm^2)**
		Sample: HfO_2 - 1000 °C		
C1 (fast)	51500	1.8	0.28	2.10×10^{-17}
C2 (medium)	1850	1.8	0.81	7.25×10^{-18}
Background (a.u.): 294.6			**FOM:** 6.99 %	
		Sample: HfO_2 - 1200 °C		
C1 (fast)	507000	1.7	0.28	2.10×10^{-17}
C2 (medium)	1500	1.7	0.85	7.25×10^{-18}
Background (a.u.): 293.6			**FOM:** 1.98 %	
		Sample: HfO_2 - 1400 °C		
C1 (fast)	982000	2	0.23	2.55×10^{-17}
C2 (medium)	9800	1.3	1.84	3.19×10^{-18}
Background (a.u.): 275			**FOM:** 5.65 %	
		Sample: HfO_2 - 1600 °C		
C1 (fast)	2800000	2	0.22	2.66×10^{-17}
C2 (medium)	38000	1.3	1.76	3.34×10^{-18}
Background (a.u.): 310			**FOM:** 3.40 %	

Figure 5.13a presents the CW-OSL deconvoluted curve for the sample calcined at 1000 °C, in which it is possible to identify both components and the background area. The background was calculated to be the average of the last five points of the curve (Table 5.3). The fast component has a lifetime of 0.28 s, while it is 0.81 s for the medium, with both having a kinetic order *b* of 1.8, indicating a significant retrapping process. The fast component is the most intense, which means that most of the trapped electrons are quickly released due to light stimulation. It is also explained because the (σ) of 2.10×10^{-17} cm^2 is larger that of the photoionisation cross-section related to the medium component. The high FOM value might be justified by the lower signal-to-noise value.

When the same analysis is done for HfO_2 calcined at 1200 °C, the parameter values are quite close to those found for HfO_2 calcined at 1000 °C, however, the FOM value is significantly smaller. The two components have the same value of *b* and τ (0.28 and 0.85 s). However, the contribution of the fast component is much more noticeable than the medium one (Fig. 5.13b).

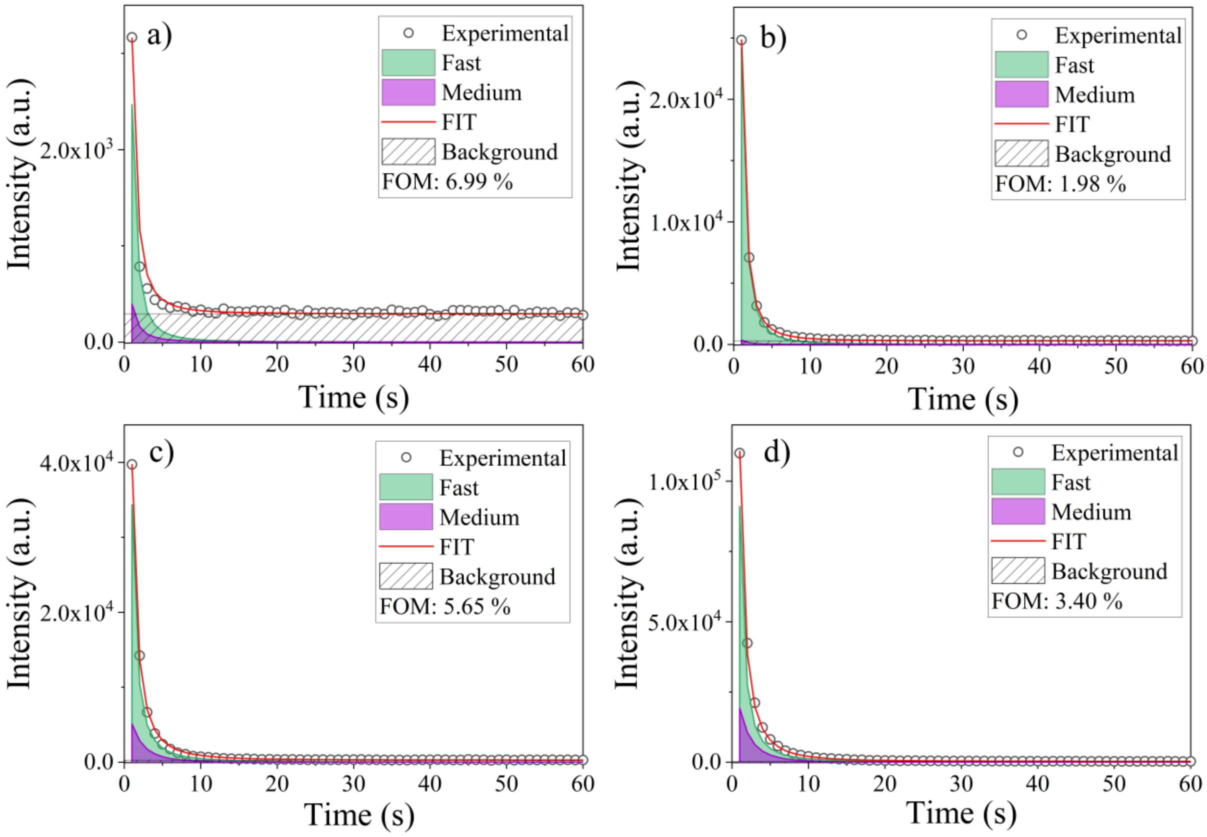

Figure 5.13 - CGCD study for the CW-OSL curves of HfO_2 powder samples calcined at (a) 1000, (b) 1200, (c) 1400 and (d) 1600 °C for 2 h, for a beta irradiation dose of 25 Gy.

Despite the analyses of CGCD for the samples calcined at 1000 and 1200 °C showing similar parameter values, when it comes to the samples calcined at higher temperatures, some differences are noticed. The CW-OSL shine-down curve for the sample calcined at 1400 °C, as shown in Figure 5.13c, was deconvoluted and has a fast component following a second-order kinetic and decaying at 0.23 s, whilst the medium component has a kinetic order closer to 1 (*b* = 1.3). The photoionisation cross-section result of 2.55×10^{-17} cm^2 is higher than the ones mentioned before.

For HfO_2 calcined at 1600 °C, the fitted curve gives parameter values close to the one calcined at 1400 °C, including the same values of *b* (Fig. 5.13d). However, the lifetimes are slightly shorter, with values of 0.22 and 1.76 s, for the fast and medium components, respectively. Photoionisation cross-sections were found to be larger, which may be contributing to the improved luminescence.

The study of CGCD for the LM-OSL found that the emission is constituted of 2 peaks in all the cases analysed, which might roughly be related to the two components estimated by the same analysis for CW-OSL (Table 5.4). Fitted curves show a good agreement with the experimental ones based on the low values of FOM obtained.

Table 5.4 - Parameters used in the CGCD study of LM-OSL curves of HfO_2 samples calcined at different temperatures, for a beta irradiation dose of 25 Gy.

		Parameter		
Peak No.	**I_{max} (a.u.)**	**b**	**τ_{max} (s)**	**σ (cm^2)**
		Sample: HfO_2 - 1200 °C - FOM: 4.08 %		
Peak 1	3650	1.81	5.8	1.57×10^{-17}
Peak 2	355	1.53	149	2.38×10^{-20}
		Sample: HfO_2 - 1400 °C - FOM: 5.46 %		
Peak 1	5210	1.62	6.8	1.14×10^{-17}
Peak 2	343	1.10	131	3.08×10^{-20}
		Sample: HfO_2 - 1600 °C - FOM: 4.75 %		
Peak 1	12000	1.76	7.6	9.15×10^{-18}
Peak 2	350	1.28	132	3.03×10^{-20}

The LM-OSL curve of HfO_2 calcined at 1200 °C after 25 Gy of beta irradiation has two peaks (Fig. 5.14a) with lifetimes values of 5.8 and 149 s and respective kinetic order values of 1.81 and 1.53, therefore, both peaks are likely influenced by retrapping. The first peak is more intense and with a larger photoionisation cross-section area.

In comparison with the sample calcined at 1200 °C, LM-OSL of HfO_2 calcined at 1400 °C has a second peak with shorter decay and a bigger photoionisation cross-section area. Moreover, the intensity of the first peak is more significant (Fig. 5.14b). Finally, HfO_2 - 1600 °C has the most intense first peak with an I_{max} of 12000 counts and a kinetic value of 1.76 (Fig. 5.14c).

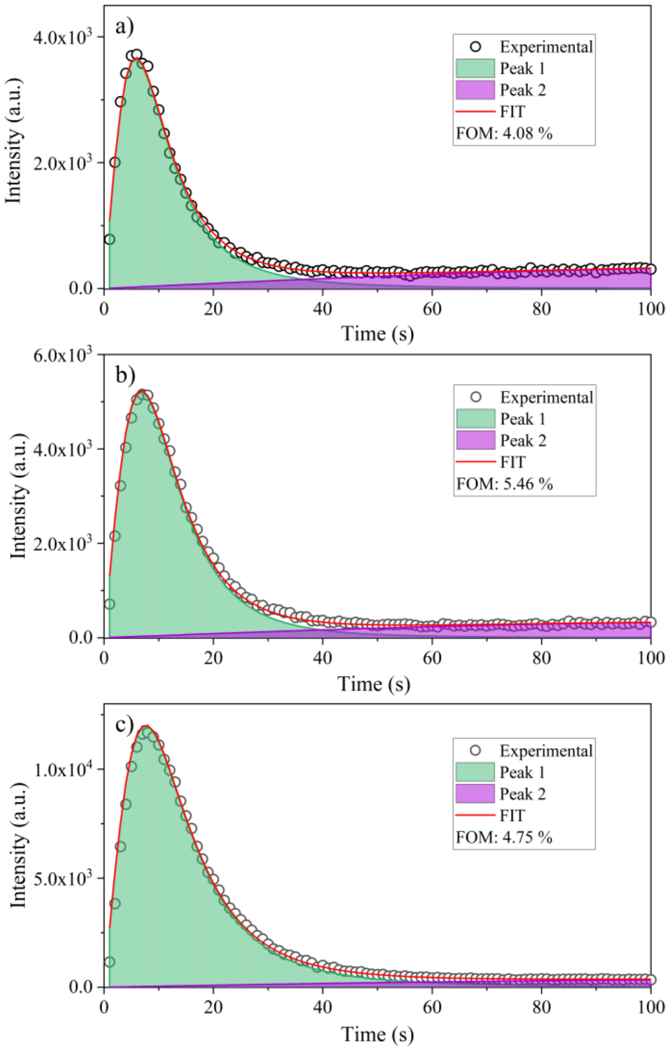

Figure 5.14 - CGCD study for the LM-OSL curves of HfO_2 powder samples calcined at (a) 1200, (b) 1400 and (c) 1600 °C for 2 h, for a beta irradiation dose of 25 Gy.

CGCD studies are helpful in trying to clarify the underlying mechanisms related to the TL and OSL emissions, allowing for the estimating of the traps' characteristics involved in the charge carriers. Those studies on the OSL deconvoluted curves of HfO_2 have not been reported before, which gives emphasis to the findings presented here.

5.2.4.2 Optically Stimulated Luminescence as Function of Readout Temperature

TL glow curves presented in the previous sections show that HfO_2 has peaks at low temperatures (above 150 °C), indicating the presence of shallow traps. The presence of those kinds of traps might induce competition by shallow traps. In order to analyse this phenomenon, a study on the CW-OSL intensity as a function of the readout temperature was carried out. The OSL signal as a function of readout temperature is taken by measuring the thermal-assisted OSL, or TA-OSL.

Figure 5.15a shows a TL emission in the UV region of the sample calcined at 1000 °C after an irradiation dose of 20 Gy (the detection was made by using a Hoya U-340 filter, in which the main transmittance is in the UV region). The curve has a main peak at about 100 °C, and a smaller one at a higher temperature. The shape of the curve has a similarity with the one recorded in the visible region, indicating that the same traps might be playing the role of luminescence in both cases. However, the signal is quite a bit lower in comparison.

The CW-OSL integrated signal over the area from 0 to 20 s, measured at different readout temperatures up to 300 °C, shows that the intensity increases up to a readout temperature of 60 °C, and then, sharply decreases. The final part of the curve has a second increasing trend. The optimum temperature of measurement regarding the highest intensity is at 60 °C, just after the main peak, therefore, before the first traps' energy level.

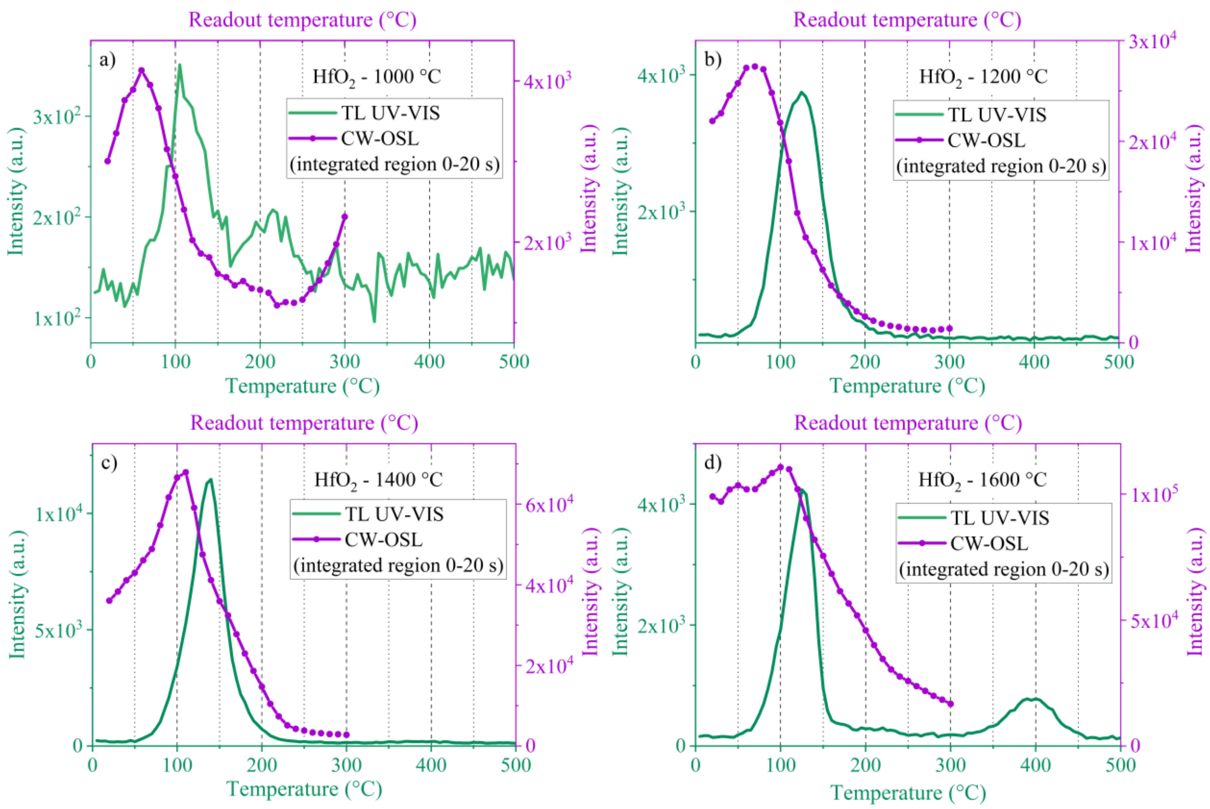

Figure 5.15 - TL glow curves measured with the Hoya U-340 filter (green curves) and CW-OSL intensity as a function of the readout temperature (purple curves) for HfO_2 powder samples calcined at (a) 1000, (b) 1200, (c) 1400 and (d) 1600 °C for 2 h, after a beta irradiation dose of 20 Gy. The CW-OSL intensity was taken from the integrated area between 0 and 20s.

When the OSL is measured at RT, instead of the electrons recombining directly in a recombination centre, they may be retrapped in shallow traps, and as a result, the recombination process and the emission of photons is delayed. Therefore, to avoid competition from shallow traps, they need to be filled (with trapped electrons).

This first raising in the CW-OSL intensity with the readout temperature is explained due to the reduction in the competition of shallow traps. At temperatures higher than RT, the electrons trapped at these shallow levels can easily be released to the conduction band, due to the thermal stimulation, and then recombine in a centre. Even in the case of the electron retrapped, it may be released again by thermal stimulation. Therefore, a direct result of this competition is the apparent increase in the OSL intensity (Yukihara; McKeever, 2011).

The same effect was observed for the other samples. HfO_2 calcined at 1200 °C after 20 Gy of irradiation dose shows a TL glow curve in the UV-Visible region composed of a main peak at about 120 °C, which is similar to the one found for the visible region (Fig. 5.15b). The CW-OSL intensity increases with readout temperature up to a maximum of 70 °C. It shows that by removing the contribution of shallow traps, the signal increased. When the readout temperature gets close to the main peak temperature, the CW-OSL is reduced, indicating that the light-sensitive traps are mostly related to traps of the first TL peak.

HfO_2 calcined at 1400 °C supplies a TL emission in the UV-Visible region with the most prominent peak at approximately 140 °C, and a small one at about 350 °C (Fig. 5.15c). As observed in the previous cases, the analysis of CW-OSL intensity regarding the readout temperature indicates competition of shallow traps taking place. This is similar for the sample calcined at 1600 °C (Fig. 5.15d): the TL glow curve presents a behaviour less intense but with a similar set of peaks as the TL in the visible region. However, the CW-OSL intensity does not decrease that sharply. A possible hypothesis for it is that the light stimulation plus the elevated temperature (e.g., 300 °C) may promote the transfer of electrons from deeper traps, such as the ones related to the peak at about 400 °C.

Those results help in elucidating the underlying processes occurring in the OSL emission and may allow us to develop better strategies of measurement and obtaining the parameters associated with it.

5.2.5 TL, OSL and Radiofluorescence Emissions: Spectral Measurements

In the previous section, the heat treatment effects in TL and OSL emission for nanocrystals of HfO_2 after irradiation with β particles were shown. In addition, a study of CGCD was performed to estimate the traps' parameters associated with the TL glow curves, and CW and LM-OSL curves.

By analysing the TL and OSL curves one might obtain information regarding the traps associated with the emission, those traps are the ones in which electrons get into a metastable level. In TL glow curves, it will reflect in the peak position, whilst in the CW-OSL, the decay time of the component is a parameter that changes due to the traps' level.

But how could one obtain information about the recombination centres? In this case, it is useful to carry out spectral measurements as they relate to the energy of the emitted photon. Just remembering then, that the energy of the emitted photon is related to the charges recombining in a centre. This energy is given by the energetic difference from the excited electron to the centre level, hence it is related to the centre.

Therefore, the next subsections are dedicated to studying the spectral measurements of HfO_2 considering its TL and OSL spectra. Radiofluorescence is also covered as a spectral measurement.

5.2.5.1 TL Spectra

TL spectra measurements were carried out using a Risø TL/OSL reader model DA/20 after beta irradiation dose. No filters were used as all emitted wavelengths are of interest. For separating the signal by wavelength, a monochromator was added in-between the sample and the PMT, and the detection was made between 200-700 nm, with steps of 20 nm. Because a longer distance is used between the sample and the PMT in comparison with the normal setup and considering that the detected signal is far more reduced (just a narrow detection window due to the monochromator), a higher dose was required.

Figure 5.16a shows the TL spectrum for HfO_2 calcined at 1000 °C after a dose of 24.3 Gy. It is possible to notice that the main peak is at about 120 °C, as already analysed previously. When plotted in a contour plot, it is easier to identify that the emission occurs in a wide range between 350 and 550 nm, however, it is centred at about 450 nm (Fig. 5.16b). This result corroborates with findings from fluorescence, in which a band at approximately 480 nm was found by Gaussian fitting, which may indicate that similar centres are playing a role in TL.

At high temperatures (> 450 °C), a signal in the infrared region, between 550 and 700 nm is observed. Nevertheless, this emission is not related to the irradiation or TL phenomenon, it is actually due to black-body emission (remember that no filters were used for trying to prevent this emission from being detected).

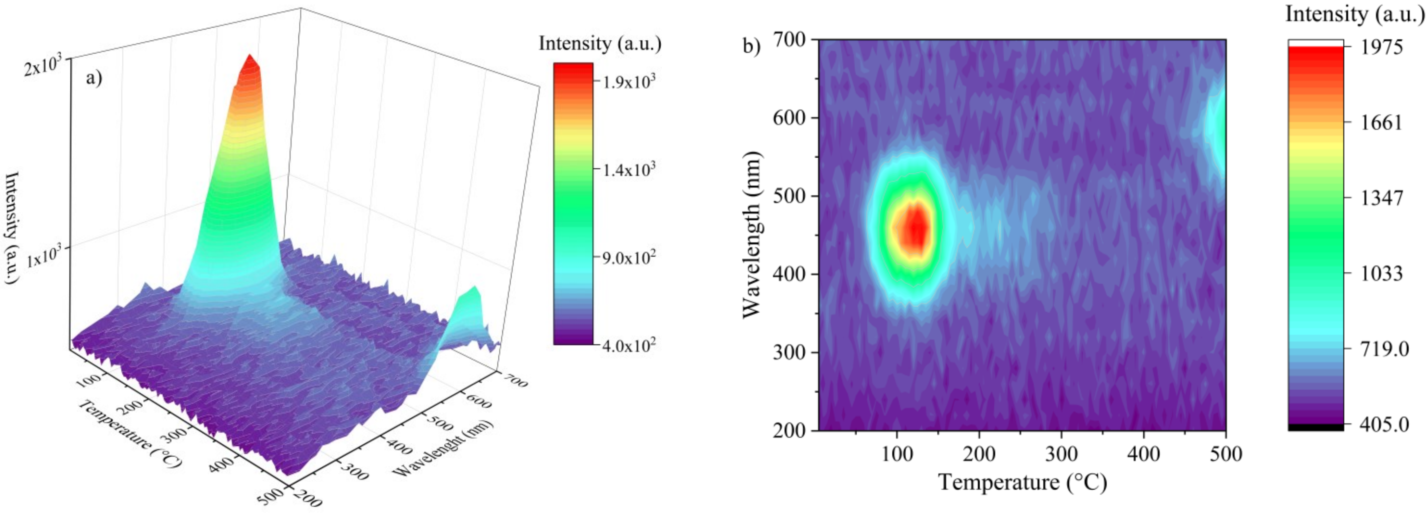

Figure 5.16 - TL spectrum for HfO_2 powder sample calcined at 1000 °C after a dose of 24.3 Gy, considering (a) 3D plot and (b) the contour map.

Figure 5.17a depicts the same analysis but for the sample calcined at 1200 °C. Once more, a remarkable emission related to the first and shallow peak at about 125 °C is obtained. Looking at the contour plot, it is observed that all the TL peaks (the most prominent plus the set of peaks between 150-300 °C) have an emission centred at 450 nm (Fig. 17b), which is the same as the sample calcined at 1000 °C, as well as from fluorescence. It suggests that the increase in the heat treatment temperature would have favoured the raising of concentration of the same defects in the material. Because the signal of the sample is much higher than the background (black-body emission), of one order of magnitude in comparison with the calcined at 1000 °C, it does not appear to be significant in the graph.

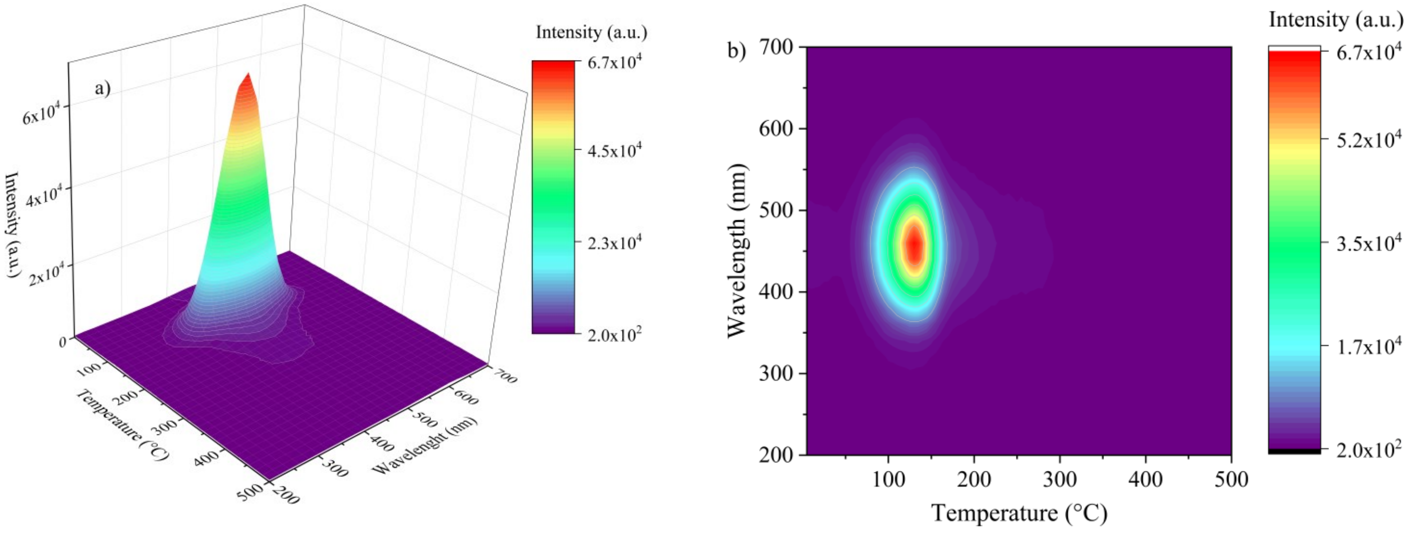

Figure 5.17 - TL spectrum for HfO_2 powder sample calcined at 1200 °C after a dose of 24.3 Gy, considering (a) 3D plot and (b) the contour map.

The TL spectrum for HfO_2 calcined at 1400 °C is shown in Figure 5.18a, in which the main peak and shallower one has a broad emission band, that spans from 350 up to 600 nm. This characteristic is easily visualised in the respective contour plot (Fig. 5.18b). Although the emission is centred at 450 nm (which is the same result as found for the samples calcined at 1000 and 1200 °C) but in this case the band is slightly wider. In addition, here the deeper peaks at temperatures of 250 and nearly 400 °C are more intense and can be better distinguished.

Another aspect that is worth drawing attention to is the peak shape. As shown in Figure 5.19b, the first peak is not symmetrical (regarding the temperature), and therefore, does not follow a second-order kinetic. The CGCD study has estimated a *b* value of 1.001. Peaks of first-order kinetic are meant to have a first-half wider than the second one, because once the electrons are released, they recombine, not going through a retrapping process.

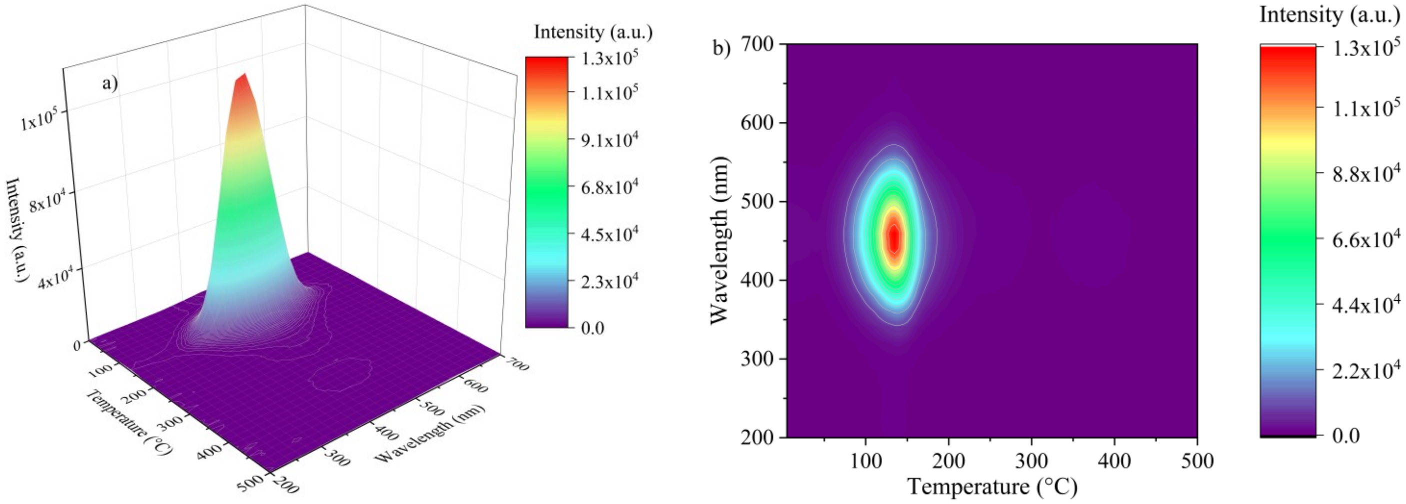

Figure 5.18 - TL spectrum for HfO_2 powder sample calcined at 1400 °C after a dose of 24.3 Gy, considering the (a) 3D plot and (b) the contour map.

Following a similar pattern, the TL spectrum of HfO_2 calcined at 1600 °C shows an intense peak at 125 °C which is centred at about 450 nm (Fig. 5.19a.). However, different from the previous results for the other samples, here it is possible to notice the effect of the heat treatment in creating deep peaks in the TL glow curve. The deep peak at about 400 °C has its emission in the same region as the other peaks though (Fig. 5.19b).

Those results may indicate that despite the electron traps having different energy levels when considering the luminescent centre, it seems to be the same set responsible for the common emission centred at 450 nm. Furthermore, the deepest peak is much more symmetrical than the first one, indicating a kinetic order closer to 2 (CGCD study has found a value of 1.98).

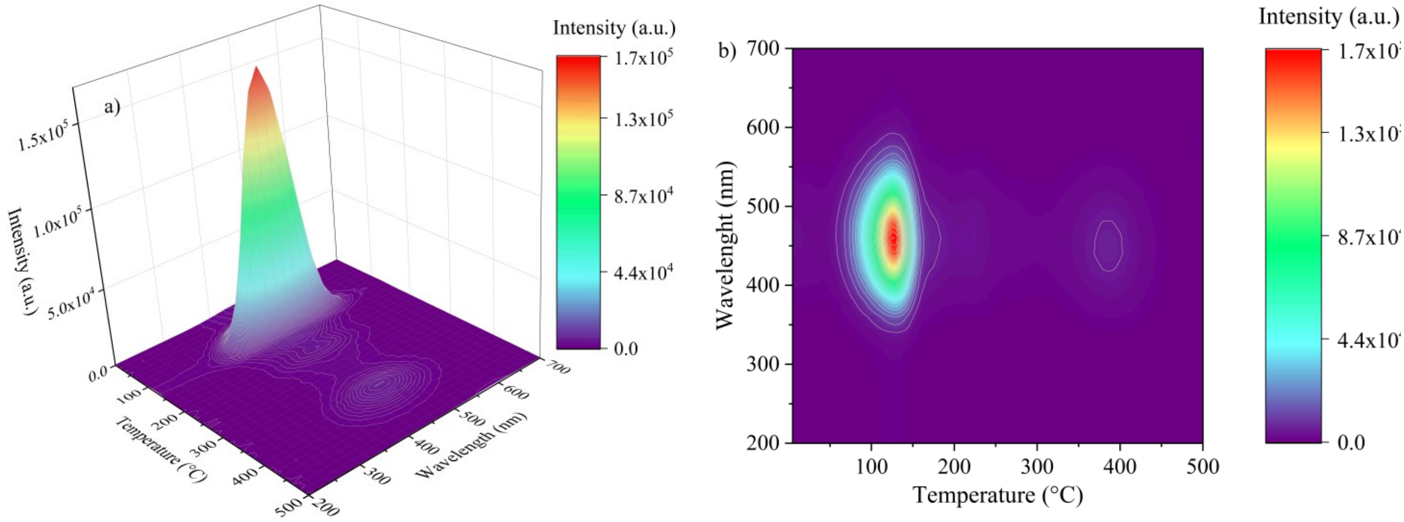

Figure 5.19 - TL spectrum for HfO_2 powder sample calcined at 1600 °C after a dose of 24.3 Gy, considering (a) 3D plot and (b) the contour map.

Although it is possible to identify the deeper peaks in the TL spectra for the samples calcined at 1400 and 1600 °C, because the first peak is much more intense, in scale, they are not that clear. Therefore, a new measurement was performed for both samples, adding a pre-heating step after the irradiation at 180 °C, to remove the contribution of the first peak, with a heating rate of 5°C/s, and a duration of 10 s (when reaching the temperature). A higher dose (243 Gy) was used as the deeper peaks are less intense. Figures 5.20a and 5.20b show the TL spectra of HfO_2 calcined at 1400 and 1600 °C, respectively, including the additional step and higher dose. In both cases, it is clear that there is a peak above 350 °C. The emission is narrower than the other peaks for the same sample but still centred at about 450 nm.

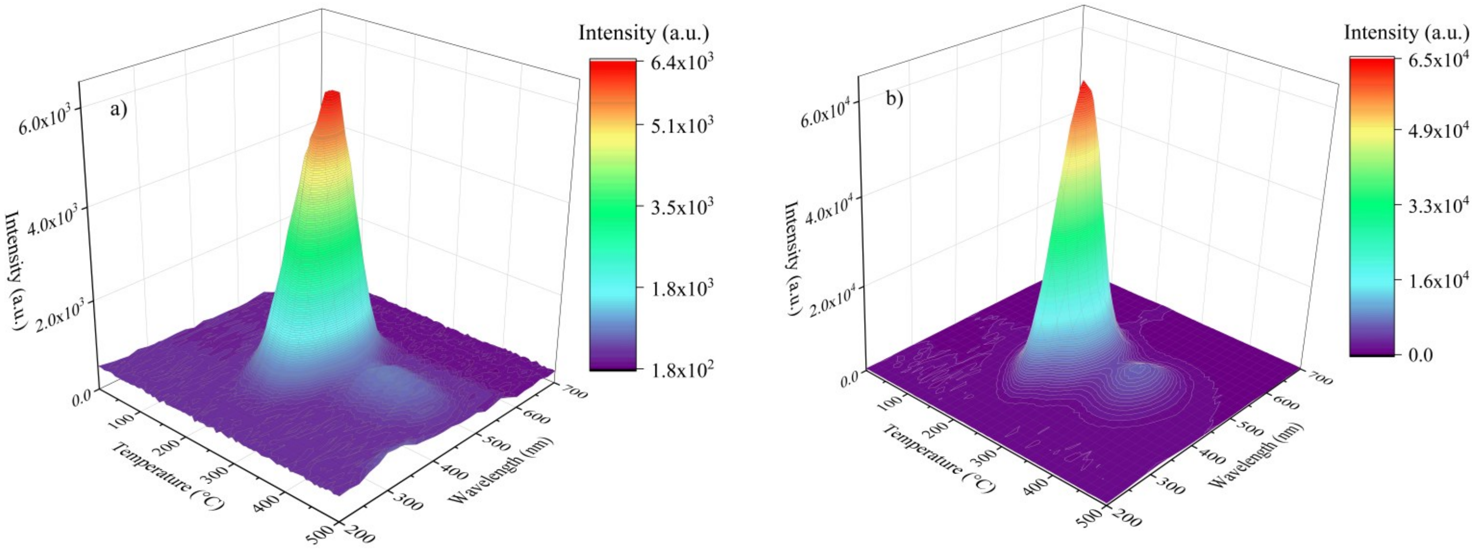

Figure 5.20 - TL spectra for HfO_2 powder samples calcined at (a) 1400 and (b) 1600 °C after a dose of 243 Gy, and considering a preheat up to 180 °C after the irradiation and before the TL measurement.

TL spectral results showed that nanocrystals of HfO_2 synthesised by the precipitation method supply an intense emission TL in the blue region centred at approximately 450 nm, which agrees with the emission band observed in the fluorescence analyses (near 480 nm). Therefore, it is expected that the same type of defects may be responsible for both fluorescence and TL emissions.

A high temperature of calcination showed again to improve the signal, probably by increasing the concentration of defects in the material. This broad blue emission of HfO_2 is usually associated with the presence of oxygen vacancies, as briefly commented before. More attention is given to the defects in Section 5.3.

5.2.5.2 OSL spectra

In Section 5.2.5.1, it was possible to observe that the TL emission, independent of the heat treatment temperature or the peak temperature, is centred at a wavelength of about 450 nm. This result matches the findings from the fluorescence measurements shown before. It is a strong indicator that the same types of defects (recombination centres) are responsible for the luminescence of HfO_2.

Similar to the protocol performed for TL spectra, the measurements of OSL spectra were carried out using the Lexsyg Research reader, which has the CCD camera coupled with a spectrometer. Because the signal is divided by wavelength (in the conventional OSL measurement it is a sum), the intensity is much less significant. Thus, the samples were irradiated with a dose of 800 Gy, using the Xstrahl chamber (details in Section 4.4). In addition, as in OSL measurements, light stimulation was used, and the detection window was limited to not detect the stimulation light.

Figure 5.21a shows the green OSL spectra for all the samples, that is, the OSL spectra when the stimulation is done with green light (centred at 525 nm). It is observed that all the samples show a noticeable signal, apart from HfO_2 calcined at 1000 °C, which, in that scale, does not have a defined band. Higher temperatures of heat treatment led to the improvement of the emission, in which the sample calcined at 1600 °C supplied an intensity of 10^3 counts of magnitude. The OSL spectra were fitted by Gaussians, and the emission was found to be centred at 2.61, 2.71, 2.69 and 2.67 eV for the samples calcined at 1000, 1200, 1400 and 1600 °C, respectively.

The emission is in the same range that was observed for TL spectra, as well as for fluorescence. It is also possible to notice that at the beginning of each curve, there is noise (for energy < 2.6 eV). This is due to the correction done with the experimental data plus the proximity to the light stimulation wavelength. This effect was not observed for the sample calcined at 1600 °C, which may be explained by its higher intensity that overlaps the background.

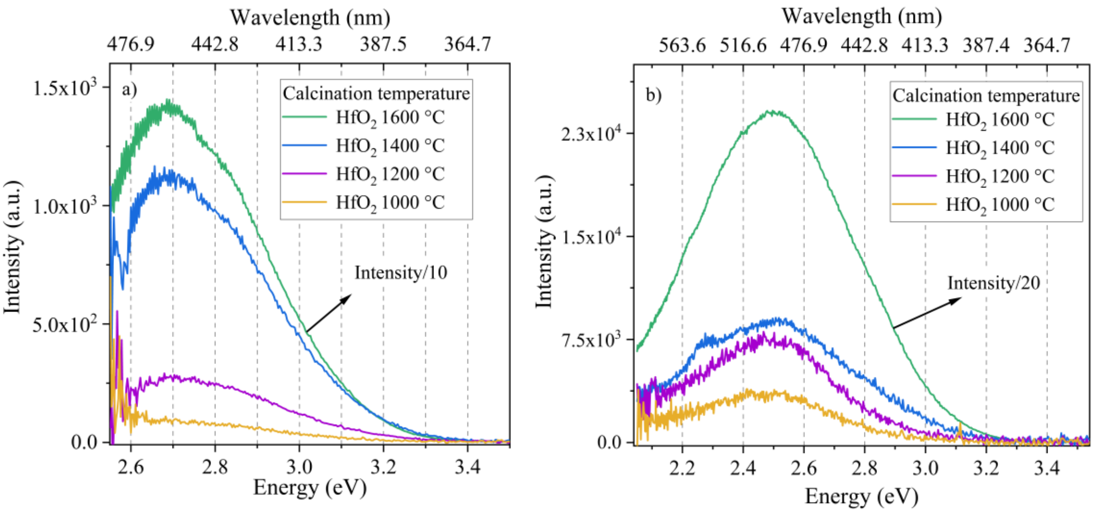

Figure 5.21 - (a) Green OSL and (b) IR OSL (or IRSL) spectra for HfO_2 powder samples calcined at different temperatures of 1000, 1200, 1400 and 1600 °C. Samples were irradiated with a dose of 800 Gy of X-rays.

When stimulating the sample with infrared at 850 nm instead of green, the OSL spectra have the appearance shown in Figure 5.21b. The emission is centred at about 480 nm for all the samples, which falls into the blue region, corroborating with the results reported before. Once again, HfO_2 – 1600 °C showed to be the most intense, by an order of magnitude.

Comparing the infrared and green OSL spectra, it is noticed that the band is better defined and wider. The infrared OSL spectral curves are wider because the wavelength of stimulation is further from the emission band than the green. As for being more intense, two hypotheses may explain why, one would be the higher photoionisation cross-section for the infrared, and the other the stimulation power (power density), which is higher for the infrared case.

The emission band of the infrared spectra were fitted using Gaussians and the emission was found to be centred at 2.44, 2.46, 2.48 and 4.49 eV, for HfO_2 calcined at 1000, 1200, 1400 and 1600 °C (Table 5.5).

Table 5.5 - Calculated emission bands (eV) for HfO_2 powder calcined at different temperatures, according to the technique. The fittings were obtained with Gaussians.

	HfO_2 sample			
Technique	**1000 °C – 2h**	**1200 °C – 2h**	**1400 °C – 2h**	**1600 °C – 2h**
Fluorescence (λ_{exc} = 300 nm)	2.56	2.58	2.58	2.59
Green OSL	2.61	2.71	2.69	2.67
Infrared OSL	2.44	2.46	2.48	2.49

By comparing the emission band for the samples using different techniques, it is possible to note a shift to higher energies due to the heat treatment temperature, in the fluorescence measurements (from 2.56 to 2.59 eV), and for the infrared OSL (from 2.44 to 2.49 eV). Although it represents a slight increase, it might indicate that the defects associated with those emissions are from different energy levels. This result was not obtained for the green OSL spectral analyses. In this case, it might be attributed to the lower signal-to-noise ratio obtained.

5.2.5.3 Radiofluorescence

Another type of spectral measurement can be obtained by exciting the sample with radiation and measuring the emission simultaneously, so-called radiofluorescence (or radioluminescence). The measurement was carried out using the Lexsyg Research reader which has an in-built β source. As the irradiation rate of the source is 0.02 Gy/s, the signal emitted for the samples calcined at 1000, 1200 and 1400 °C would not be distinguishable. Therefore, the analysis was made for the most intense sample, that is, HfO_2 - 1600 °C.

Figure 5.22a gives the radiofluorescence spectrum for HfO_2 calcined at 1600 °C measured at RT (black circles) and its respective fitting using Gaussian (red line). The table has the values of the parameters calculated for the fitting. The emission is in the blue region, at about 2.52 eV, evidencing that this blueish emission is a feature of HfO_2.

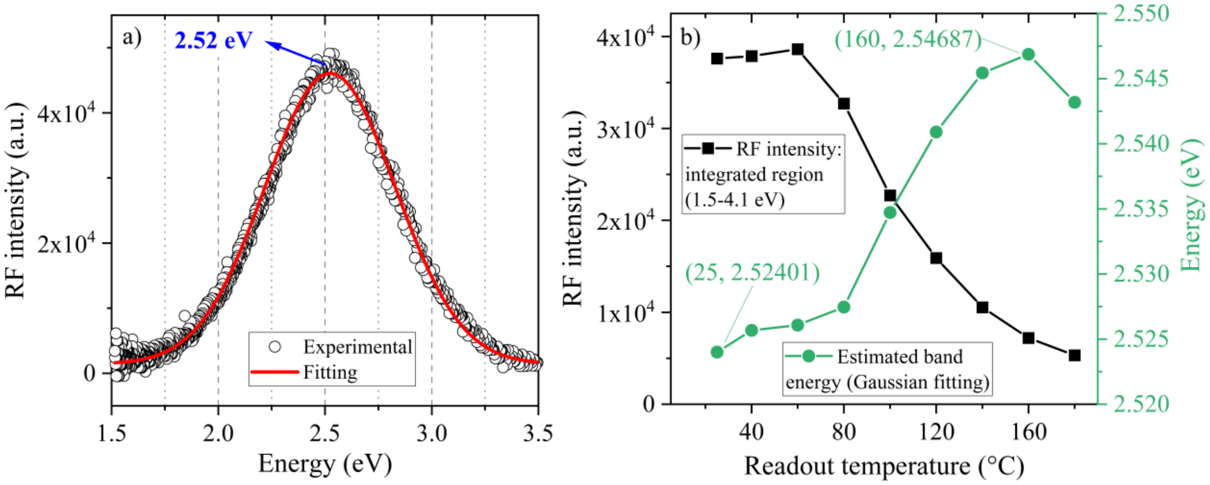

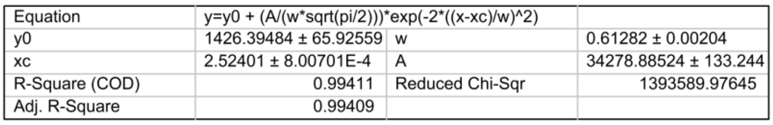

Equation	y=y0 + (A/(w*sqrt(pi/2)))*exp(-2*((x-xc)/w)^2)		
y0	1426.39484 ± 65.92559	w	0.61282 ± 0.00204
xc	2.52401 ± 8.00701E-4	A	34278.88524 ± 133.244
R-Square (COD)	0.99411	Reduced Chi-Sqr	1393589.97645
Adj. R-Square	0.99409		

Figure 5.22 - (a) Radiofluorescence spectrum for HfO_2 powder sample calcined at 1600 °C for 2 h. The circles indicate the experimental data and the red line the fitting using a Gaussian. The parameters of the fitting are described in the table below the image. And (b) analysis of the dependence of the radiofluorescence signal on the readout temperature. The black line with squares curve shows the intensity as a function of the readout temperature, considering the area over an integrated region between 1.5 and 4.1 eV. Whilst the green line with circles represents the estimated band energy value according to the Gaussian fitting as a function of the readout temperature.

The radiofluorescence signal was also evaluated regarding the readout temperature, to try to verify thermal quenching or some other effect. Figure 5.22b shows the result for it, considering the intensity over the integrated area between 1.5 to 4.1 eV (black line with squares), and the band emission energy by Gaussian fitting (green line with circles).

The intensity of the radiofluorescence signal remains nearly constant for readout temperatures below 60 °C. For temperatures above 60 °C, it induces a reduction of the signal, that decreases sharply. It may indicate the thermal quenching effect occurring, which is the reduction of the luminescent efficiency due to the temperature.

Analysing the curve of band energy with readout temperature, the curve has a kind of opposite behaviour in comparison with the intensity versus readout temperature. This result may be associated with thermal assistance. However, as the difference is low, at about 0.03 eV, this statement needs to be pondered. Another possibility would be a non-radiative transition due to the temperature, as observed by the work of Laganovska *et al*. (2023).

5.2.5.4 Comments on the Spectral Measurements

The spectral measurements for the samples of HfO_2 presented in Sections 5.2.2 and 5.2.5 demonstrated that the material has a feature emission in the blue region between 2.44-2.71 eV depending on the technique used, and on the heat treatment performed. In the case of fluorescence, the wavelength of excitation was more energetic than the emission one, therefore, this mechanism might follow a more conventional process of fluorescence.

However, when the OSL spectra were analysed, the creation of electron-hole pairs is due to the ionising radiation, and it is the light stimulation which is responsible for releasing the trapped electrons, which may recombine in a centre. The wavelength of stimulation used was less energetic than the emission one of about 1.46 and 2.36 eV, for green and infrared OSL, respectively. Therefore, what would be the likely explanations for this?

A first hypothesis relies on the idea that the electrons trapped due to the ionising radiation are in traps with energies lower than the stimulation one. Thus, the energy supplied by the stimulation would be enough for releasing them.

Another hypothesis would be related to a non-linear optical process. Gavartin *et al.* (2006) estimated the optical excitation energy (E_{opt}) to be 3.33 eV for oxygen vacancies (type V^{+}) in m-HfO_2, by using density functional theory (DFT). Considering that oxygen vacancy is the kind of defect most likely responsible for the luminescence, the stimulation light in the OSL might not be enough for directly releasing the trapped electron.

One processes of non-linearity in optics explains the emission of light at a shorter wavelength/less energetic than that necessary for an electron to go directly from the ground sate to the excited state. The common case considers the absorption of one photon (Fig. 23a) which supplies enough energy for this transition to happen. By non-linear optics, virtual states might allow the electron to undergo a two-photon (Fig. 23b), three photon (Fig. 23c) or n-photon (Fig. 23d) absorption (Boyd, 2008).

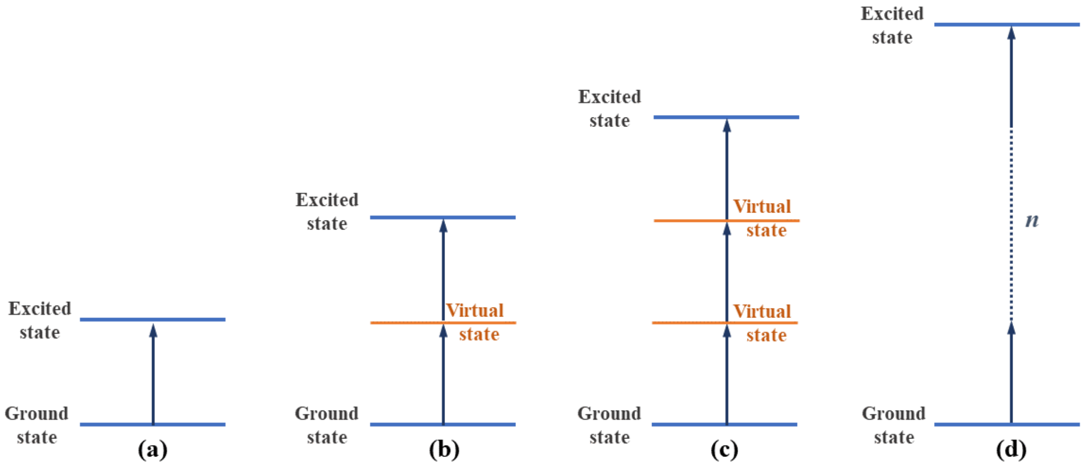

Figure 5.23 - Examples of multiphoton absorption processes: (a) one photon, (b) two-photon, (c) three-photon and (d) n-photon.

The studies regarding non-linear effects in wide bandgaps oxides (especially thin films) have been increasing in number with the development of laser technologies (Chen, M. *et al.*, 2022), including observations of them in HfO_2 (Zuber *et al.*, 2023). Chen M. *et al.* (2022) showed a two-photon absorption at 343 nm, and a three-photon absorption at 515 nm for HfO_2 thin film, considering a bandgap energy between 5.4-5.8 eV. Therefore, if we consider the ground state in OSL to be the metastable one in which the electron is trapped, a three-photon absorption might explain the infrared wavelength being responsible for releasing trapped electrons, as well as a two or three-photon absorption for the green wavelength case.

There are few studies that evaluated the non-linearities properties of HfO_2, and they were made for thin films. Hence, a direct correlation cannot be done to the results in here, and this is not the intention. However, it is worth to raising this possibility. Further analyses, for example, Z-scan, which is a standard technique for studying non-linear optical properties, would be necessary (Singla; Pandey; Sharma, 2019).

5.3 Defects in Hafnium Oxide and Their Influence on the Luminescence Properties

The results of previous sections showed that HfO_2 powder synthesised by the precipitation method supplies an intense blue emission in the range between 2.44-2.71 eV, which depends on the technique and the heat treatment performed.

Ito *et al.* (2005) studied the PL emission from HfO_2 samples obtained by pulsed laser and plasma-enhanced chemical vapour depositions, and a peak was observed around 2.8 eV for all the samples when exciting the sample with UV photons. The study reported that the PL signal did not have a dependence on the oxygen vacancy, crystallinity, deposition method or the substrate used. Therefore, the emission would not be related to either oxygen vacancies or defects in the interface between the sample and substrate, but to an intrinsic mechanism in the material, for example, radiative recombination between the localised states at the band tails. Although the emission is in a similar region to that reported here, the samples in that study were amorphous and synthesised via a different route.

Other studies have reported that the presence of oxygen vacancies might be associated with luminescent properties. Kiisk *et al.* (2010) obtained samples of crystalline HfO_2 by the sol-gel method followed by a thermal treatment up to 1000 °C. They found two emission bands at about 2.4 and 4.0 eV, the first one being the most prominent. The band at 2.4 eV was associated mainly with an excitation band at 4.2 eV. Those results have similarities with the ones found here, however, the band has a different shape. Considering that oxygen vacancies are the most common kind of defects in metal oxides, and theoretical studies reported before, the authors ascribe the excitation band at 4.2 eV to charge transfer transition from VB to ionised oxygen vacancies. Laganovska *et al.* (2023) identified the oxygen vacancies of types V_{O3}^{+}, V_{O3}^{+2}, V_{O4}^{+} and V_{O4}^{+2} as the potential defects based on PL and TL measurements, and similarly, Méndez-Castillo *et al.* (2023) found by using cathodoluminescence.

Chuang, Lin and Chen (2012) also obtained the material by using the sol-gel method followed by either microwave or conventional heat treatment. Increasing the temperature of heat treatment led to an increase in the PL intensity. Moreover, the results from energy dispersive spectroscopy (EDS) showed a decrease in the O/Hf ratio with temperature. Hence, the improvement in luminescence was attributed to existing oxygen vacancies within the material. Pejaković (2010) analysed polycrystalline HfO_2 after different sintering temperatures. The study also raised the possibility that the oxygen vacancies are associated with both luminescence activation and charge trapping.

Theoretical studies have also gone into the direction of oxygen vacancies playing an important role in the charge carrier traps (Islamov *et al*., 2014; Gritsenko; Perevalov; Islamov, 2016). Foster *et al*. (2002), for example, used DFT to investigate the atomic structure with singly and doubly positively charged oxygen vacancies, as well as charged interstitial oxygen atoms (singly and doubly). DFT was also adopted by Gavartin *et al*. (2006) in which the findings indicated oxygen vacancies to be likely responsible for the intrinsic electron traps.

Based on those studies, and considering the results from the spectral measurements above-mentioned, it is reasonable to infer that the emission reported here might be associated with the presence of oxygen vacancies, which benefit from high temperatures of heat treatment. To investigate this hypothesis, measurements of ESR were carried out, and the results are presented in the next subsection.

5.3.1 Defects According to ESR Findings

Samples of HfO_2 calcined at different temperatures were irradiated with X-rays with a dose of 100 Gy, and the ESR signal was measured. Before the irradiation, the samples were thermally cleaned at 500 °C for 10 minutes, to erase any residual signal. However, at first, the parameters used for carrying out the measurements were defined by evaluating the signal over a range (of the parameter itself), as shown in Figure 5.24. The sample used was the one calcined at 1600 °C, as it was shown to have the highest luminescent signal.

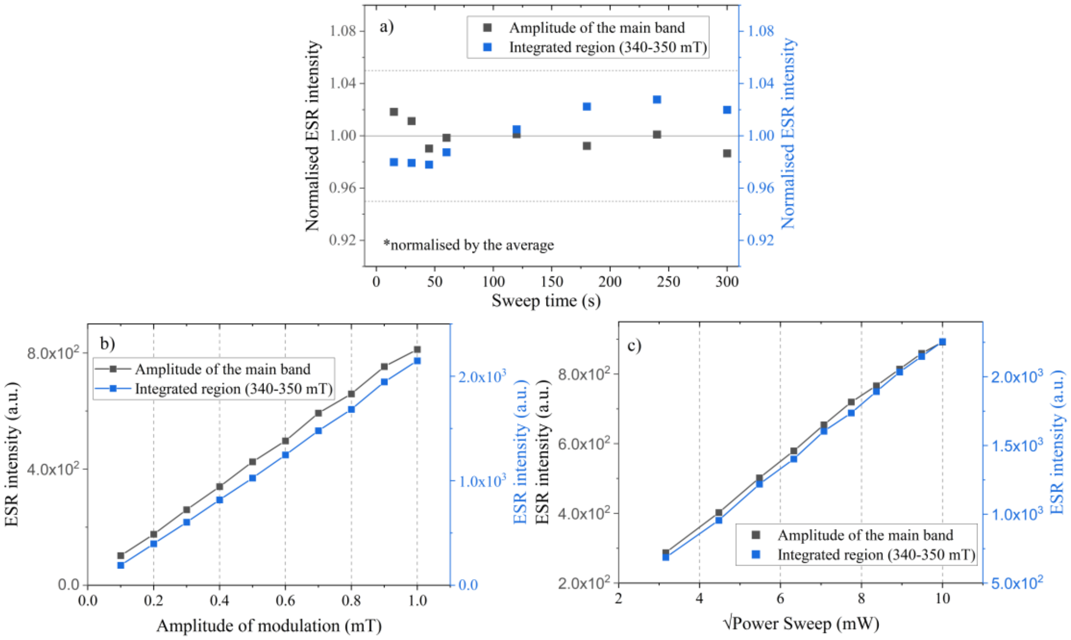

Figure 5.24 - ESR intensity for HfO_2 calcined at 1600 °C for 2 h, as a function of the (a) sweep time (intensity normalised by the average), (b) amplitude of modulation and (c) the square root of the power sweep. The sample was irradiated with X-rays with a dose of 100 Gy before the measurement was carried out.

Figure 5.24a shows the normalised (by the average of 5 measurements of the same sample) intensity of the ESR signal as a function of the sweep time, considering either the integrated area between 340-350 mT or the amplitude of the main signal (at about 345 mT). As is shown, the increase in the sweep time does not induce any significant change in the intensity, thus a sweep time of 60 s was adopted. By evaluating the amplitude of modulation, an amplitude of 1 mT showed to be the best as it supplies the highest signal (Fig. 5.24b). The power sweep (microwave power) used was 80 mW because, at this value, the curve is not following a saturation trend yet (Fig. 5.24c).

Once the parameters were defined, the ESR signal was evaluated for all the samples and the results are shown in Figure 5.25, in the range between 330-350 mT. It can be noticed that HfO_2 calcined at 1000 °C displays two main signals with *g* values of about 2.011 and 1.997 - for estimating the *g* position (that is, the *g* value).

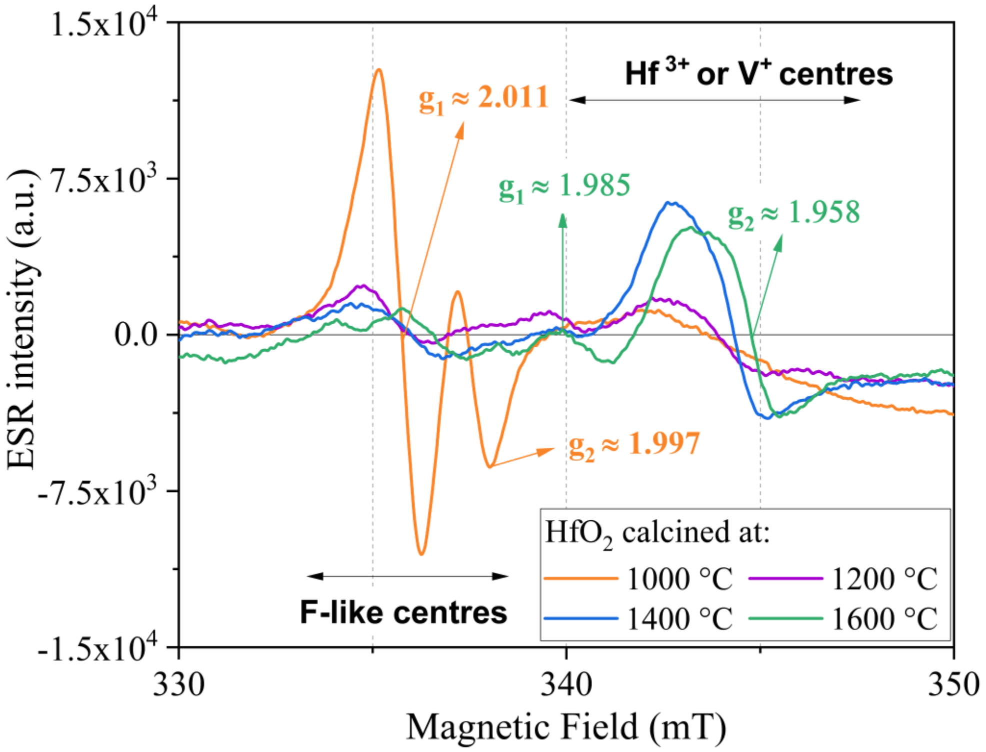

Figure 5.25 - ESR signal for HfO_2 calcined at different temperatures of calcination of 1000, 1200, 1400 and 1600 °C for 2 h, after a dose of 100 Gy of X-rays irradiation. The *g* values were estimated assuming orthorhombic symmetry.

When the same analysis is performed for the sample calcined at 1200 °C, the signals in the region around 335 mT are still possible to identify, however, they are less intense; conversely, signals between 340-350 mT appear. This finding is important because it shows a change in the defects in the material due to the heat treatment temperature.

The ESR signals for the samples calcined at 1400 and 1600 °C have a behaviour similar to the one calcined at 1200 °C, however, the signal is more intense. It leads us to consider that a higher temperature of heat treatment is indeed promoting this change. The *g* values are estimated to be 1.985 and 1.958 - it was assumed an orthorhombic symmetry, which is common for polycrystalline samples such as the ones studied here (Rowlands; Murphy, 2017). Note that the third signal is not shown due to the range analysed as the interest was to do a comparison, but it is properly presented in Figure 5.26a.

As the *g* values are different amongst the samples, they represent different kinds of defects. So, which kinds of defects benefitted from heat treatment at higher temperatures? Few studies have been dedicated to studying the ESR signal of HfO_2 samples. Kang, Lenahan and Conley Jr. (2003) evaluated the defects in thin films of HfO_2 on silicon by using the same technique, and their results showed two signals which would be related to O_2^- and Hf^{3+} defects. The O_2^- was associated with a g_{yy} value of 2.01, which is similar to the one found here. While the *g* value at zero-crossing at 1.96 was attributed to an Hf^{3+} ion defect, which may play an important role in electron trapping.

Several samples of commercial HfO_2 were analysed regarding their ESR signals and correlation with the annealing treatment after γ irradiation doses in the work of Wright and Barklie (2009). It also covers results previously reported by the same authors (Wright; Feeney; Barklie, 2007), with a wider and more extensive approach. Moreover, the study considered samples of ZrO_2 as they share structural similarities with HfO_2. The study reported four paramagnetic centres, and the identification of their respective defects, by comparing the results with the literature. For the signal with a *g* value close to the free electron one (g_e), that is, close to 2.0023, it was found that the signal very likely belongs to an oxygen hole centre, probably involving O^-. This was also pointed out in another report where it stated that it might be associated with an F^+-like centre, as an electron trapped at an O^{2-} vacancy (Wright; Barklie, 2006). As regards the signals in the region at lower *g* values, they might be related to Hf^{3+} centres.

Ramo *et al.* (2007) performed an *ab initio* study about defects in the monoclinic HfO_2 and calculated the principal *g* values of a V^+ 4C (an oxygen vacancy in a charge state +1 and in a four-coordinated arrangement) to be 1.945, 1.963 and 1.984.

Based on these cited studies, it is reasonable to infer that the signals shown in Figure 5.26 are likely related to F-like centres, and either Hf^{3+} centres or V^+ four-coordinated ones. The F-like centres are more prominent in the sample calcined at 1000 °C, whilst the higher heat treatment temperatures lead to the predominance of Hf^{3+} or V^+ centres.

It is important to mention that the ESR signal was measured after a dose of X-ray radiation. In the absence of irradiation previous to the measurement, no signal was detected in this range, which indicates that the signals' precursors are trapping charges generated due to the radiation.

As the sample calcined at 1600 °C supplied the most intense luminescent signal (see Figure 5.25), it was decided to do a more detailed analysis of the ESR signal, regarding the dose-response curve and the thermal stability of the signal.

Figure 5.26a depicts the ESR signal for HfO_2 calcined at 1600 °C after an irradiation dose of 100 Gy of X-rays. The signal was evaluated after different preheat temperatures of thermal cleaning after the irradiation. The main signal and their respective g values are indicated in the figure. Note that the values of g_1 and g_2 are quite similar to the ones found in the *ab initio* study by Ramo *et al.* (2007), hence, it might reinforce the hypothesis of V^+ four-coordinated centres being responsible for these signals.

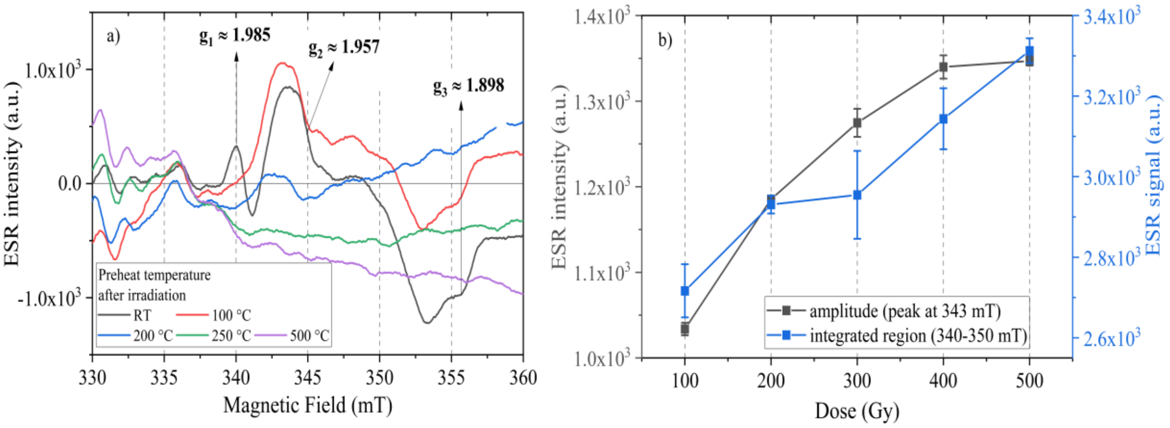

Figure 5.26 - ESR signal for HfO_2 calcined at 1600 °C for 2 h (a) after an X-rays irradiation dose of 100 Gy as a function of the preheat temperature and (b) its dose-response curve for doses from 100 up to 500 Gy of X-rays. The error bars in part (b) refer to the standard deviation of the average of five measurements for the same aliquot. The dose-response was analysed regarding both the amplitude of the peak at 343 mT and an integrated region between 340 and 350 mT (for the integrated region, it was used the absolute area without correcting the inclination of the signal as it was not observed in the analysed range).

This analysis also shows that increasing the temperature of thermal cleaning leads to a reduction of the signal intensity. With a preheat temperature of 250 °C, the centres are already depleted. By comparing this result with the TL emission, it may be inferred that this kind of defect is associated with the TL peaks observed.

Figure 5.26b shows the dose-response curve, considering either the amplitude of the signal or an integrated region. The curve shows an exponential increase followed by a saturation trend for doses above 400 Gy. This result indicates that the material also has the potential to be used for ESR dosimetry, this is to be studied. Moreover, the dependence of the ESR intensity (hence, of the centres) on the irradiation, confirms the role as a charge trap. Wright, Feeney and Barklie (2007) evaluated the dose-response curve of some centres in HfO_2 and observed saturation of the signal for doses above 250 Gy.

The samples with highest luminescent signal, that is, HfO_2 calcined at 1400 and 1600 °C, have a more important contribution of Hf^{3+} or V^{+} centres as observed from the ESR results. As those centres are induced by ionising irradiation, it is reasonable to infer that they are related to the TL and OSL emission. The analysis of thermal dependence indicated that those centres are depleted after a preheating at 250 °C, hence, it might be inferred that they are related with the shallower peaks in TL, as well as with the OSL signal, as the CW-OSL signal was shown to be reduced due to the thermal bleaching.

But which sort of defects might be associated with the deeper peaks observed in the TL glow curves, that is, in temperatures higher than 300 °C? These peaks are less intense when compared with the shallow ones, which may lead to a less intense ESR signal, thus, not observed here. However, it is noticeable that the oxygen vacancies are the main kind of defects in oxides-based materials, as HfO_2. Therefore, another type of oxygen vacancy (different charge and/or coordination) might reasonably be responsible for those peaks.

5.4 Application of Hafnium Oxide as a Luminescent Dosimeter

Previous sections of this study demonstrated that HfO_2 synthesised by the precipitation method supplies an intense luminescence when considering either its TL or its OSL signal. As the luminescence response has an increasing intensity with the absorbed dose over a certain range, it makes it suitable to investigate its application as a luminescent dosimeter.

Despite the material having this interesting property, not many studies have been dedicated to evaluating its dosimetric characteristics. Sekar *et al.* (2020) synthesised nanoparticles of HfO_2 (size of about 58 nm) by the precipitation method and investigated the TL response after a ^{60}Co beam irradiation. Pellets of HfO_2 were analysed regarding the TL dose-response for doses between 5 to 100 cGy, and the resulting curve was fitted with a linear function. The signal reproducibility was found to be within 95 %. Batch homogeneity and the thermal quenching effect were also investigated. The material has a high crystallographic density, which is useful for absorbing incident gamma or X-rays, and its high cross-section is interesting for neutron detection, therefore, the authors stated that HfO_2 is an excellent material for use in radiation dosimetry.

Other studies which evaluated the luminescent response after irradiation were also interested in the doping effect in the morphological and luminescent properties. Montes *et al.* (2014), for example, used the hydrothermal route for obtaining nanoparticles of undoped HfO_2 and Tb^{3+} doped up to 20 at%. By analysing the TL emission after UV irradiation at 200 nm, the doping at 7 at% proved to be the best one for increasing the TL intensity. The curve for this sample is constituted of a main and broad peak at about 125 °C. Although no further analyses concerning dosimetry are reported in the paper, the finding indicates the potential of using the material for UV dosimetry. This application as a UV dosimeter was also mentioned by the study of Manríquez *et al.* (2014), in which $HfO_2:Dy^{3+}$ films deposited by ultrasonic spray pyrolysis were irradiated with UV light, and the TL was measured. A shallow and prominent peak at about 120 °C was found plus smaller and overlapped ones at higher temperatures.

Fiaczyk *et al.* (2016) used the Pechini method to produce Ti-doped HfO_2 up to a concentration of 2 mol% of Ti, and evaluated the TL response between 0-300 K, after X-ray radiation. Several peaks were found in this range, and the best response was obtained for a doping concentration of 0.25 mol%, however, no other dosimetric properties were analysed.

Gd^{3+} doped HfO_2 was studied by Sekar *et al.* (2021) regarding its TL response after irradiation with gamma and X-rays in the range of 5 to 100 cGy of doses. The dose-response curve was estimated to be linear in this range, and the peaks' characteristics were investigated by deconvolution.

Therefore, considering that the sample studied here has an intense TL and OSL luminescence which increases with the absorbed irradiation dose, and the lack of reports on the dosimetric properties of HfO_2, this section is dedicated to the potential application of HfO_2 as an ionising radiation dosimeter (section 3.2.3.1 shows some aspects to take into account when analysing the dosimetric properties).

It is important to highlight that the Z_{eff} of HfO_2 is higher than that of human tissue, which might be a complicating factor for its use in medical dosimetry (in this case, corrections might be needed). However, using the material in retrospective or accidental dosimetry would be a more straightforward application.

5.4.1 Infrared-Stimulated Luminescence Properties of Hafnium Oxide

In Section 5.2, it was demonstrated that HfO_2 synthesised by the precipitation method has intense TL and OSL signals after irradiation doses of β particles. In addition, the best heat treatment temperature in terms of luminescent intensity was found to be 1600 °C for 2 hours.

As the TL measurement requires heating the sample to high temperatures to obtain the signal, the most prominent peak of the HfO_2 studied here is at a low temperature (lower than 200 °C, which is considered to be a good temperature for a dosimetric peak), and the presence of overlapped peaks, it is more reasonable to study the application of the material as an OSL dosimeter.

But which wavelength of stimulation would be the most sensible to use? In order to compare the OSL response using different stimulations, a sample of HfO_2 was irradiated with beta particles and the CW-OSL was measured. Figure 5.27a shows the OSL shine-down curves measured at RT, after a dose of 0.6 Gy. All curves were obtained with the same equipment (Lexsyg Research).

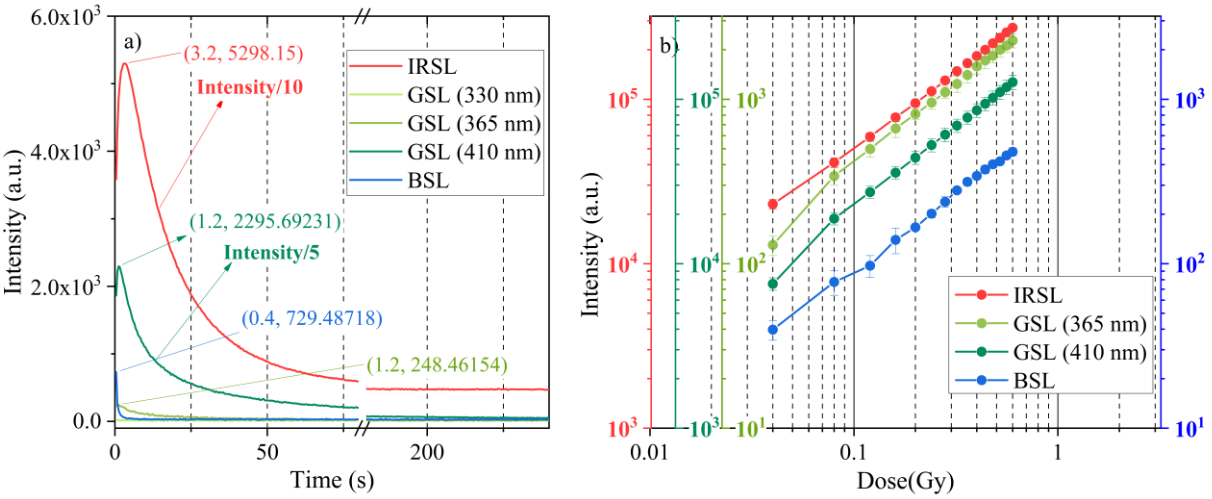

Figure 5.27 - (a) OSL shine-down curves for HfO_2 powder calcined at 1600 °C for 2 h, for an irradiation dose of 0.6 Gy of beta particles, using different wavelengths of stimulation centred at 850 nm for IRSL, 525 nm for GSL, and 458 nm for BSL. In the case of GSL, different filter arrangements are used to narrow the detection window around 330, 365 and 410 nm. And (b) the OSL dose-response curves for IRSL, GSL and BSL for beta doses up to 0.6 Gy. The intensity in the dose-response curve was taken by an integrated region between 0 and 20 s.

The most intense OSL was obtained with IR stimulation at 850 nm (then, here named IR stimulated luminescence or IRSL). The signal with blue stimulation at 458 nm (BSL) also supplies an intense signal. For green stimulation at 525 nm (GSL), in addition to the Schott BG39 (3 mm thick) and the Edmund Shortpass OD4 (also 3 mm thick) filters, to block the green detection, an interference filter was also used, to narrow the detection window. By reducing the detection window, the luminescent intensity detected is reduced, and it may allow the use of higher doses of radiation without reaching the threshold of intensity to keep the photomultiplier safe. The wavelength mentioned in the inset refers in Figure 5.27 to the main transmission band of the filter. Only with the GSL (330 nm), there was no significant OSL signal, which can be explained due to the emission band in the OSL spectrum – the band is centred at higher wavelengths, hence, not detected here.

It is noticeable that the IRSL signal is more intense than the BSL. Although the stimulation power used for IRSL was ten times higher than in the GSL, of 300 mW/cm^2, the photons are less energetic. A hypothesis for this finding might rely on the difference in the photoionisation cross-section, which would favour the IRSL. Note also that the curve has a sharp decay for the BSL, however, for the other cases, there is a built-up trend forming a peak. This peak, at the beginning of the curve, is an indicator of the phototransfer phenomenon, hence the signal is delayed. Moreover, the traps showed to be light-sensitive beyond being thermal sensitive.

Figure 5.27b depicts the dose-response curve of the OSL signal for the different wavelengths of stimulation, apart from the GSL centred at 330 nm which has quite a low intensity. It shows that for doses above 0.1 Gy, the dose-response curve follows a linear trend. The linear behaviour starts even at lower doses in the case of IRSL. This type of growth of intensity with dose is useful for use in dosimetry.

To the best of our knowledge, our study is the first report of IRSL for HfO_2. Not only the novelty, but the IRSL also showed to supply the most intense signal. Based on these features, it was decided to investigate the dosimetric properties of the OSL with IR stimulation.

5.4.2 Dosimetry Characterisation for IRSL

To evaluate the dosimetric features of the IRSL, some analyses were considered and are discussed in the next sections, which include, the thermal stability (that can infer about trap's depth involved in the process); the deconvolution (to verify the components existent in the curve); the minimum dose estimated to be detected; reproducibility and repeatability of the signal; fading, and the response for different photon energies. A brief discussion about bleaching and the defects associated with this luminescence is also made. Note that all the measurements of IRSL of Section 5.4.2 were carried out using the Risø DA15 equipment, with stimulation light at 850 nm (more details in Section 4.2.1.3).

5.4.2.1 Thermal Stability and Deconvolution Analysis

When analysing a material to be used as an OSL dosimeter, it is worth verifying how the signal changes due to the temperature as it may be exposed to different environmental conditions. In addition, depending on the traps of electrons in the material, even temperatures near RT may be enough for releasing electrons and decreasing the signal. In order to evaluate thermal stability, the sample of HfO_2 calcined at 1600 °C was irradiated with β particles (dose of 0.2

Gy), followed by an IRSL measurement. Two variations were adopted: one configuration varying the readout temperature from 30 up to 250 °C, with steps of 10 °C per cycle, and another, similar, in which a preheat was performed in between the irradiation and the IRSL measurement (in this case, measured at RT). In the latter case, the preheat temperature varied from 30 to 400 °C, also with steps of 10 °C.

Figure 5.28a shows the results of this analysis. The purple line with squares indicates the IRSL intensity for a dose of 0.2 Gy in different conditions of readout temperature. The intensity has a first sharp drop with the increasing temperature up to 80 °C. This trend may be associated with the shallow traps in the material, which are light-sensitive. By considering the TL emission curve, one might easily correlate this to the low-temperature peaks. This decay is followed by a short plateau region, and then, another dropping until a temperature of about 140 °C. This second drop is likely associated with the main TL peak at about 120 °C. Therefore, most of the trapped electrons released by the IR stimulation are in the temperature range below 150 °C.

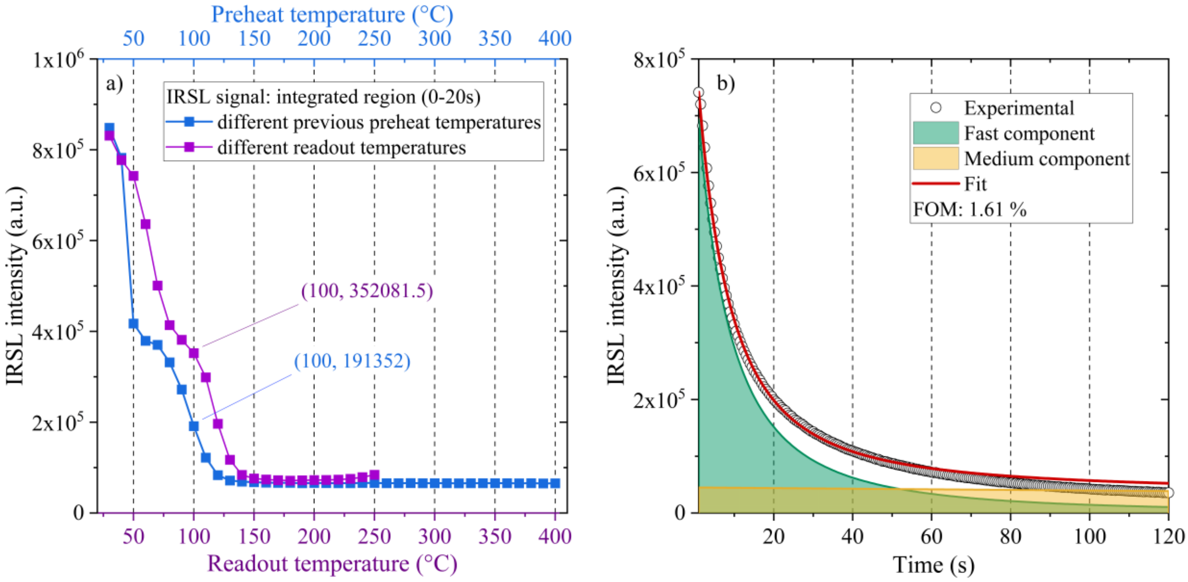

Figure 5.28 - (a) IRSL intensity for HfO_2 powder calcined at 1600 °C for 2 h, after a beta dose of 0.2 Gy, as a function of the readout temperature (purple line with squares), and the different preheat temperatures (blue line with squares). The intensity was taken from an integrated region between 0 and 20 s. And (b) CGCD study for IRSL measured at 100 °C, after a beta dose of 2 Gy, and using the GOK model.

What if instead of using a readout temperature a preheating is used? The behaviour is quite similar as can be seen in Figure 5.28a (blue line with squares). There is a first abrupt decay, followed by a short plateau region, and a second decay. Again, most of the signal is associated with traps at temperatures below 150 °C. However, by comparing both curves, a shift to lower temperatures is observed in this case. This difference might be explained by the occurrence of a transfer of charges. In the case of using a preheat temperature, when the preheat is finished, the sample is cooled again to RT, and then the IRSL is measured. Hence, there will be empty shallow traps, which may trap electrons in this interval until the stimulation starts, these electrons come from deeper traps and are released quicker. While using a high readout temperature, the electrons would not be trapped at traps located at temperatures below the one used during the measurement.

Based on this analysis of thermal stability, it was decided that further measurements would be performed at a readout temperature of 100 °C (unless differently stated), which is a good compromise between removing the influence of the shallowest traps and getting an intense signal.

The IRSL measured at 100 °C after a dose of 2 Gy is shown in Figure 5.28b, together with the respective CGCD study. It is worth noticing that in this curve, because of the high readout temperature, there is an exponential decay shape, not forming a peak at the beginning of the curve as shown in Figure 5.27a (measured at RT). Therefore, the effect of photo transfer is significantly removed.

The parameters for the IRSL CGCD study are described in Table 5.6. According to this analysis, the IRSL is composed of two components, a fast and a medium one, with respective kinetic order values of 2 and 1. The faster component which decays at about 15.7 seconds, is the most intense, therefore, this one would contribute more to the overall signal. The background was estimated by taking the average of the five final points in the curve. The FOM value of 1.61 % indicates a good fitting.

Table 5.6 - Parameters used in the CGCD study of LM-OSL curves of IRSL for HfO_2 calcined at 1600 °C for 2 h and a beta irradiation dose of 2 Gy.

Parameters	Component 1 – fast	Component 2 - medium
I_0 (a.u.)	785000	45000
b	2	1.000001
τ (s)	15.7	800
σ (cm^2)	1.19697×10^{-19}	2.34904×10^{-21}
Background (a.u.)	3022	

The photoionisation cross-section for the fast component is quite a bit bigger than the medium one (as expected), hence the trapped electrons related to the fast component are more easily released. The decay time of this fast component is much longer than the fast and medium ones for the OSL stimulated with blue light, which has values of 0.22 and 1.76 seconds, and which we have reported before (Soares; Tatumi; Rocca, 2021). It is reasonably explained by the blue photons being more energetic, and so more easily releasing the trapped electrons. Moreover, this comparison is not straightforward because the readout temperatures are different.

5.4.2.2 Dose-Response Curve and Minimum Detectable Dose

As the investigation is about the dosimetric properties, it is necessary to evaluate how the OSL intensity behaves with the absorbed dose. As has already been briefly discussed, the dose-response curve has a linear behaviour. Figure 5.29 shows the dose-response curve of HfO_2 calcined at 1600 °C for doses from 0.02 up to 2 Gy of beta particles. Considering either the signal at 1 second (blue curve) or an integrated region in the range of 0-20 seconds (red curve), the curve obtained is similar in shape. The linearity is observed over the region analysed, but it is even more noticeable for doses above 0.3 Gy.

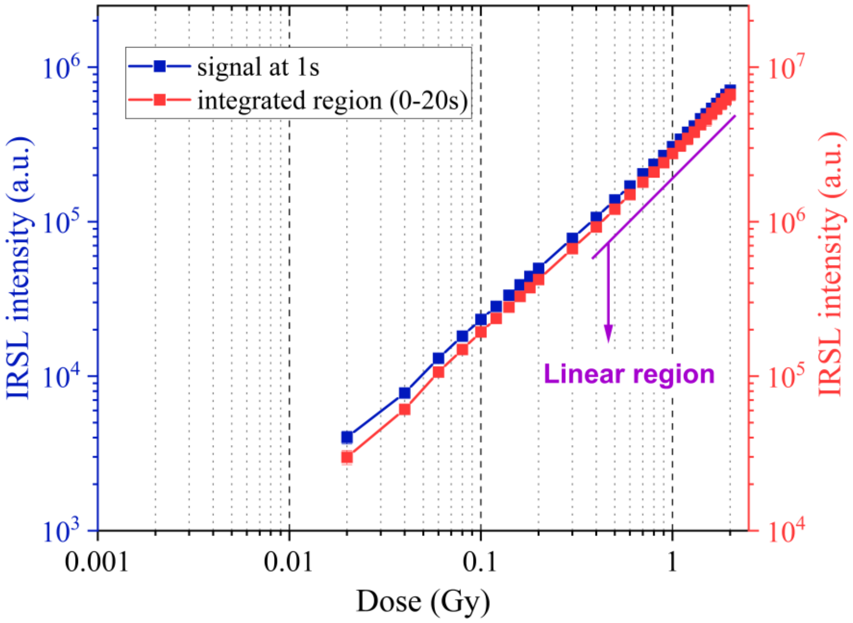

Figure 5.29 - IRSL dose-response curve for HfO_2 powder calcined at 1600 °C for 2h, for beta irradiation varying from 0.02 to 2 Gy. The blue line with squares refers to the signal at 1 s, and the red one for an integrated region between 0 and 20 s. The error bars refer to the standard deviation for the average of three aliquots with the same mass. The purple line indicates the area with the most prominent linear trend.

The linear aspect of the curve is a desired feature for a dosimeter because it facilitates the estimation of the absorbed dose. In this case, the material seems to be suitable to be used in low dose (less than 1 Gy) cases. But what would be the minimum detectable dose? To calculate the minimum detectable dose (MDD), it was associated with the detection threshold (D_{MDD}), with D_{MDD} being three times the standard deviation of the signal of an unirradiated sample (Harvey; Kearfott; Rafique, 2015):

$$D_{MDD} = 3 \times s_{\bar{E}} \tag{5.2}$$

Where $s_{\bar{E}}$ is the standard deviation of the signal of an unirradiated sample. Based on this, the average MDD of three samples of HfO_2 was calculated to be 18.9 ± 3.3 mGy and 25.3 ± 3.3 mGy (average ± σ), considering the signal at 1 s and an integrated area, respectively.

5.4.2.3 Reproducibility and Repeatability

For being used in dosimetry, it is important that the material (as well as the dosimetry) supplies a reproducible signal. Therefore, to investigate if the HfO_2 calcined at 1600 °C meets this requisite two aspects were evaluated, reproducibility and repeatability. For the first case, three aliquots (here named Al_1, Al_2 and Al_3) were irradiated with the same dose (0.02 Gy of beta particles), and the coefficient of variation (CV) was calculated. For reproducibility, the signal of the same aliquot was analysed over 30 cycles of the same irradiation and IRSL measurement, and the CV was also calculated. The CV is given by:

$$CV = \frac{\sigma}{\bar{x}} \times 100\ \% \tag{5.3}$$

Where σ is the standard deviation and $\bar{x}$ is the average signal.

Figure 5.30 summarises the result. The average of the normalised IRSL intensity for the three aliquots as a function of the measuring cycle is given, either considering the intensity at 1 s (blue squares) or the integrated region (red squares). The error bar shows the standard deviation for the average of the three aliquots, which is an indirect measure of reproducibility. And the variation over the number of cycles is associated with repeatability. After 3 cycles, the variation is lower than 10%, which falls qualifies as a reproducible signal. The build-up trend at the beginning of the curve might be explained by a sensitisation of the sample, which gets stabilised after the fifth cycle.

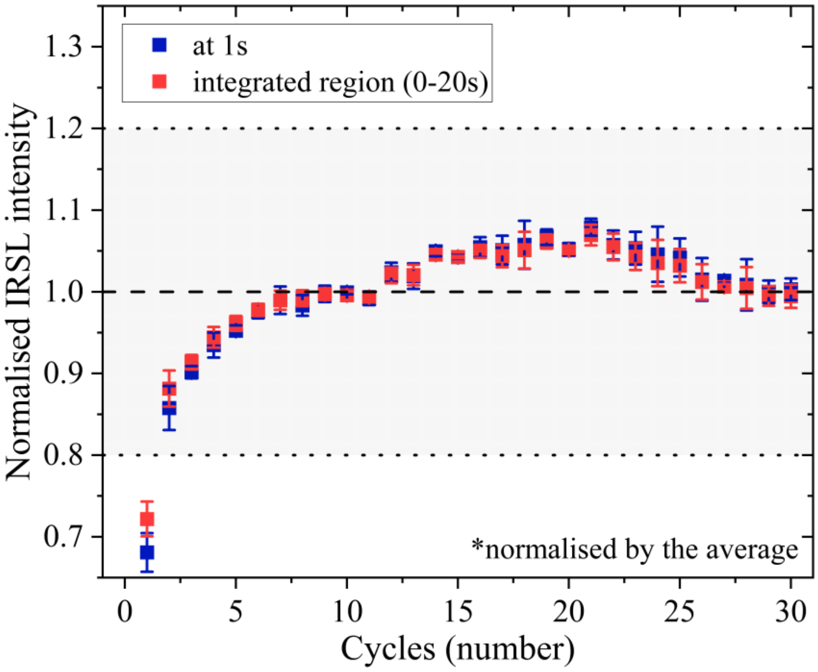

Figure 5.30 - IRSL signal reproducibility for HfO_2 powder calcined at 1600 °C for 2 h after a beta irradiation dose of 0.2 Gy. The values represent the average of a normalised intensity for three aliquots, and the error bars represent the respective standard deviation values. The blue squares refer to the signal at 1 s, and the red ones to an integrated region between 0 and 20 s.

This experimental protocol also allows us to calculate the CV associated with both reproducibility and repeatability. Considering the signal at 1 second of measurement, the CV for a sample measured at the same conditions over 30 cycles (repeatability) was 7.03, 8.03 and 8.71 %, which were lower when analysing the integrated region, being 6.09, 6.95 and 7.61 %, for Al_1, Al_2 and Al_3, respectively.

The CV for a 3-aliquot batch measured under the same conditions (reproducibility) was found to be 2.39 and 2.77 %, for the signal at 1 second and over an integrated region. In both cases, for the first cycle of measurement. Those results of CV indicate that the variation is low, therefore, the material is feasibly reproducible.

5.4.2.4 Photon Energy Response

The dosimeter material is meant to be used for estimating the absorbed dose in a determined medium of interest. However, the materials used in TL and OSL dosimetry might have a different chemical composition than the medium of interest, for example, different from tissue or water. A consequence of it is the dependence of the response on the photon energy (Yukihara; Mckeever, 2011).

In order to verify this dependence, the IRSL signal of HfO_2 powder energy response was evaluated regarding the photon energy, varying from 24 to 250 keV of X-rays sources (see more detail in Section 4.4), and normalised by the response after gamma irradiation with energy of 662 keV (^{137}Cs source). Note that the same elapsed time was used between the irradiation and the IRSL measurement for all cases, to ensure better reproducibility. IRSL was measured at RT as the signal was measured not long after the irradiation.

Figure 5.31a shows the average IRSL energy response for three aliquots considering both the signal at 8 s (blue curve) and an integrated region (red curve). It is shown that there is a noticeable overresponse for photon energies of 48 and 65 keV, which is followed by a sharp decline until reaching a steadier region for photo energies above 200 keV.

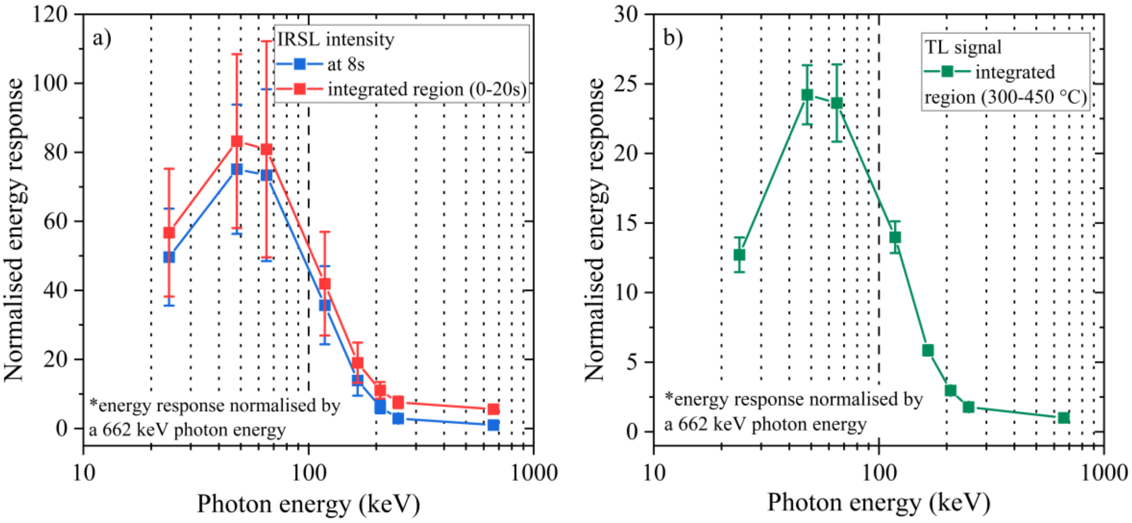

Figure 5.31 - (a) IRSL and (b) TL photon energy response for HfO_2 powder calcined at 1600 °C for 2 h and irradiated with a dose of 0.2 Gy of X-rays. Photon energies ranged between 24 to 250 keV, and the signal was normalised by the response for the same dose of irradiation, using a gamma source with a photon energy of 662 keV. The error bars refer to the standard deviation for an average of the signal of three aliquots with the same mass. The IRSL intensity was evaluated regarding both the intensity at 8 s (blue curve) and an integrated region between 0 and 20 s (red curve), whilst for TL, an integrated region between 300 and 450 °C was taken.

To do a comparison, the same analysis was made by considering the TL signal (using a Schott BG39 filter). Figure 5.31b shows the average TL energy response for three aliquots considering an integrated region between 300-450 °C. A similar shape is obtained as in the IRSL case, when a peak of overresponse is observed at a photon energy of 65 keV, with a decay trend seen afterwards.

HfO_2 has a high effective atomic number ($Z_{eff} \approx 67.2$) in comparison with human tissue (Wiatrowska; Zych, 2012). In addition, it has a high density (9.6 g/cm^3) and a significant stopping power (Sekar *et al.*, 2021). This overresponse might be associated with these characteristics, and hence, the high efficiency in absorbing ionising radiation. For use in dosimetry, the result is not interesting as corrections would be necessary for interpreting the signal and estimating the absorbed dose, an example would be to use filter to attenuate this effect.

5.4.2.5 Fading

An important aspect to be investigated when dealing with TL and OSL materials is fading, which is the unintentional loss of the signal, even at RT. Therefore, the existence of fading may lead to the underestimation of the absorbed dose. To evaluate this loss, the sample is irradiated with a determined dose (sufficient to obtain a detectable output signal), and the luminescence is measured. The same procedure is repeated several times, including a storage time between the irradiation and the measurement. Therefore, one might obtain the signal over a period of storage.

Figure 5.32 shows the normalised IRSL intensity (by the intensity of the signal measured just after the irradiation, without a storage time) after a dose of 1 Gy of β irradiation. It is noticed that during the first hour of storage, the IRSL signal keeps quite constant, indicating there is no significant loss of signal.

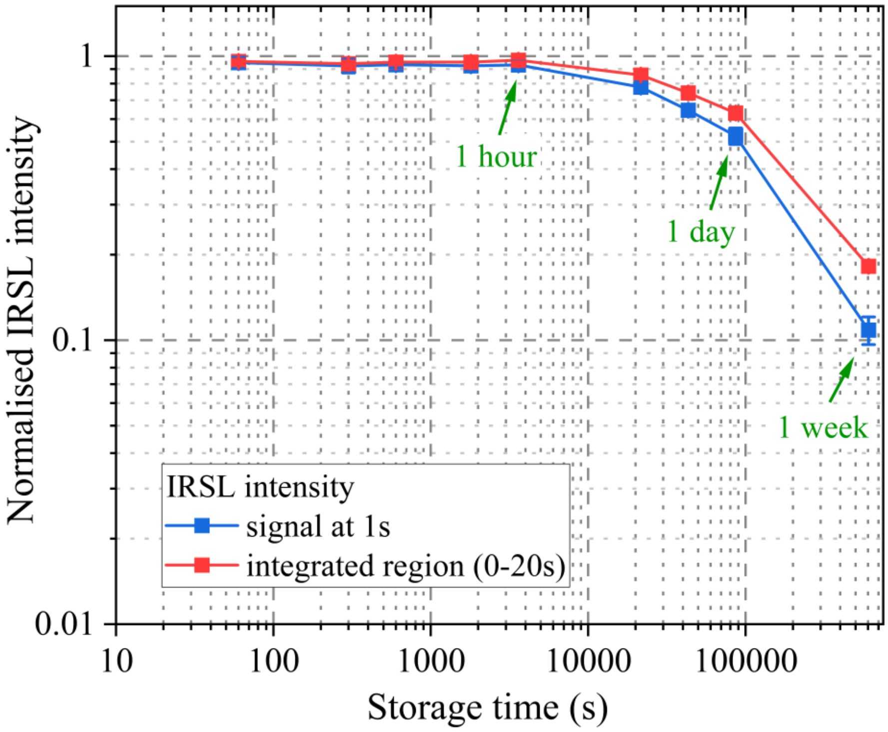

Figure 5.32 - Fading of the IRSL signal for HfO_2 powder calcined at 1600 °C, for a beta irradiation dose of 1 Gy, and for storage times up to a week. The intensity was normalised by the intensity of the curve with no storage time (measured just after irradiation). The fading was estimated considering the signal at 1 s (blue curve) and the integrated region between 0 and 20 s (red curve). The error bars refer to the standard deviation from an average of three aliquots with the same mass.

At the beginning of the curve, the absence of fading might be attributed to the temperature in which the measurement was carried out (100 °C), which effectively removes the contribution of the shallowest traps. After one day of storage, there is a noticeable decrease, and the signal is reduced to about 53 and 63 % of the initial value (without storage), considering the intensity at 1 second and over an integrated region, respectively. Further in time, after a week of storage, the signal drops to less than 20 % of the initial one, which is more remarkable in the curve that uses the signal at 1 second.

Which mechanisms would be involved in the fading for HfO_2? This is a not straightforward answer. However, some hypotheses might be raised to explain this elevated fading. In the case of IRSL, the photons are less energetic than those used in the most common OSL dosimetric systems, that use blue and green stimulation. Hence, the OSL signal measured in IRSL arises from charges trapped in shallower traps. Because the de-trapping energy is low, the loss of the signal at RT would be facilitated.

Some materials present the phenomenon of tunnelling between closely related defects. This carrier of charges in the proximity of the defects might be associated with fading. Tunnelling is a well-known reason for fading in feldspar (Huntley; Lian, 2006). In addition, different from the TL measurements, in which trapped electrons of different levels are released more progressively, in OSL measurements, several trapping centres are stimulated at once (Yukihara; Mckeever, 2011).

5.4.2.6 Bleaching

TL and OSL may share the same electron traps, as well as recombination centres. The spectral analyses so far presented indicate that the sample has a featured emission in the blue region. Therefore, it is worthwhile carrying out measurements to evaluate the effect of bleaching with IR in the TL peaks. For this, an aliquot of HfO_2 was irradiated with a dose of 2 Gy, bleached with IR for a certain period (IRSL measurement at 100 °C), followed by a residual TL recording.

As shown in Figure 5.33a, the IRSL signal comes from the same charge traps as the ones associated with TL as the residual TL is reduced when the stimulation time is increased. The IRSL empties the traps associated with all the peaks in the range between 100 and 300 °C. Note that there is no contribution of the shallow peaks above 100 °C, which is due to the readout temperature used.

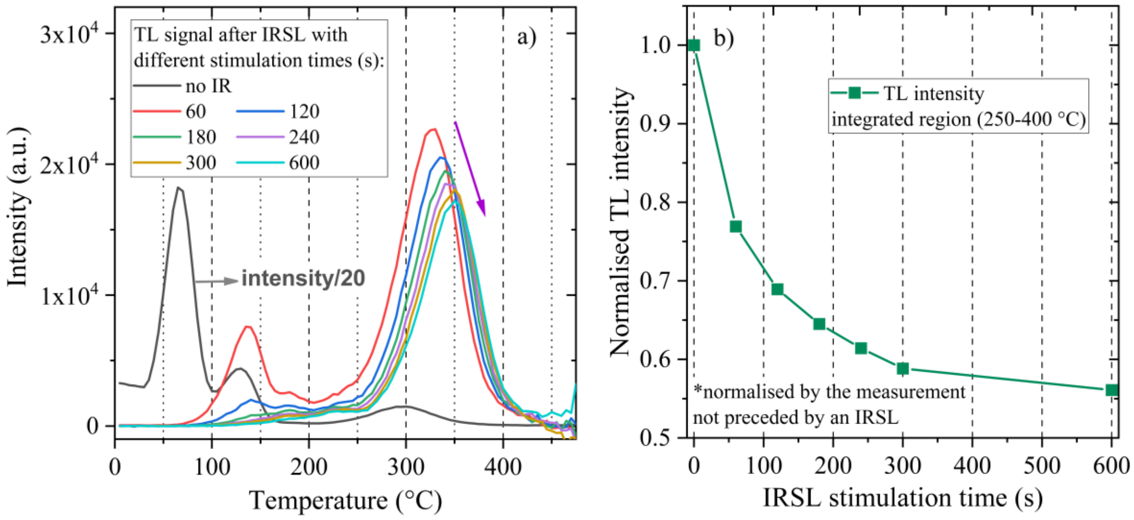

Figure 5.33 - TL glow curves for HfO_2 powder calcined at 1600 °C for 2 h, for a beta irradiation dose of 2 Gy. The TL was bleached with different IRSL measurement durations up to 600 s. And (b) the normalised integrated region of the TL glow curve between 250 and 400 °C. TL was detected using a Hoya U-340 filter and IRSL was measured at a readout temperature of 100 °C.

Figure 5.33b shows the normalised residual TL intensity over an integrated region between 250 and 400 °C. It shows that the deeper peak above 300 °C contributes significantly to the IRSL signal. By using longer stimulation times, more trapped electrons related to that peak are released. After an IRSL with 120 s of stimulation time, there is a reduction of about 30 % of the signal in comparison to a non-bleached one.

It is also interesting to notice the curves' characteristics in the range between 250 and 300 °C. If the deep peak above 300 °C progressively decreases with the stimulation time, why does the intensity in that range seem to be steadier? A hypothesis for this is the occurrence of a transfer of charges from deeper trap levels associated with the peaks in that region. Once those charges are trapped in an "intermediate" energetic level, they would be released again, and then, recombine in a recombination centre and emitting photons. This retrapping feature was considered when doing the CGCD analysis, and the fast component was found to have a second-order kinetic, therefore, it agrees.

5.4.2.7 IRSL Signal and Associated Defects

The IRSL signal is interesting by itself as we are reporting this emission for HfO_2 for the first time. In addition, the emission occurs in the blue region (at about 2.49 eV, for the sample calcined at 1600 °C), which is at a shorter wavelength than the stimulation one. Naturally one might wonder what defects and mechanisms are responsible for it.

As mentioned before, HfO_2 has a large bandgap which can vary between 5.5-6.0 eV (Choi; Mao; Chang, 2011), and the studies so far have reported the emission band in the blue region as a feature of this material. This emission has been mainly associated with the presence of oxygen vacancies in the material, which would act as traps (Gritsenko; Perevalov; Islamov, 2016). However, comparison with the results here is not straightforward because previous studies have used more energetic photons to stimulate the sample, for example, within the UV region of the spectrum (Pejaković, 2010). That said, some questions remain: what are the defects associated with the IRSL emission here reported? And what processes would be occurring in it?

A way of trying to correlate the defects with the IRSL might be done by analysing the results of the bleaching using IR stimulation, and the dependence of the ESR signal with the preheat temperature. As discussed in the previous section, the IRSL measurement with a readout temperature of 100 °C bleaches all TL peaks in the range of 100-400 °C, which changes, depending on the peak position (shallower peaks are more easily bleached). Moreover, a possible transfer mechanism was found to exist. Therefore, if the ESR signal appears due to the irradiation, and is affected by temperatures below 300 °C, then it can give us an idea of the TL peaks associated with it.

The ESR results for HfO_2 synthesised by the precipitation method and calcined at 1600 °C show the presence of three signals, for which the calculated *g* values similar to the ones estimated by Ramo *et al.* (2007) in their *ab initio* study and are likely related to V^+ four-coordinated centres. As those signals are radiation-induced and are completely depleted at a temperature of 250 °C, it is reasonable to infer that V^+ type centres play a role in the IRSL. Hence, this study reinforces that oxygen vacancies are responsible for the blue emission of HfO_2.

A recent study by Laganovska *et al.* (2023) tried to correlate the TL peaks with different types of oxygen vacancies in HfO_2 and obtained activation energies between 1.20 and 1.24 eV for the TL peak at about 172 °C and related it to V^+ defects. Therefore, it also agrees with the findings obtained here, and it might reaffirm they play a role in the IRSL.

According to the study of Gavartin *et al.* (2006), which used a non-local density functional theory approach, the optical excitation energy (E_{opt}) and the thermal activation energy (E_{the}) for oxygen vacancies of type V^+ in m-HfO_2 are 3.33 and 2.32 eV, respectively. Méndez-Castillo *et al.* (2023) by measurements of cathodoluminescence analysed this energy according to the coordination (three or four-coordinated oxygen vacancy), and for a four-coordinated vacancy, it was estimated to vary between 2.37-2.78 eV (523-446 nm). Those values of E_{opt} are much higher than the IR, however, it is within the UV region. Therefore, it might at least explain the PL emission observed, when an excitation at 300 nm was used, as reported here and in Soares *et al.* (2022).

But what could explain the IRSL (as well as the green OSL)? Non-linear effects have been demonstrated for wide bandgaps oxides. In a recent work, Chen M. *et al.* (2022) showed that HfO_2 undergoes a process of two-photon absorption at 343 nm, and a three-photon absorption at 515 nm, for a bandgap energy between 5.4-5.8 eV in the material. Therefore, if we consider the E_{opt} of 3.33 eV, which is higher than 1.46 and 2.36 eV (for IR and green stimulations used in OSL, respectively), a two or three-photon absorption would be a feasible mechanism.

Only for illustration, a three-photon absorption in the IRSL case would result in a total energy absorption of about 4.38 eV, whilst a two-photon absorption for the green OSL would result in an absorption of about 4.72 eV, values which are higher than the E_{opt}. Even considering the bottom limit of 2.37 eV found by Méndez-Castillo *et al.* (2023) for oxygen vacancy four-coordinated, green and IR would not give energy to the transition to happen.

In any case, more effort is still necessary to elucidate the defects existing in HfO_2 and their relationship with luminescence. However, this work has given a further step along this path by first reporting the IRSL emission, as well as demonstrating that this feature is likely associated with oxygen vacancies (V^+) in a four-coordinated arrangement and might also rely on the presence of non-linear optics processes of two or three-photon absorption.

5.5 First Results on POSL of HfO_2

This section aims to present some initial analyses regarding the POSL signal for HfO_2, considering the sample calcined at 1600 °C, and therefore, with the best signal. When analysing the CW-OSL of the material, because the light stimulation is constant and the emission is detected whilst the sample is stimulated, one may estimate the decay lifetime which is related to the electron trapping centres (process in blue in Figure 5.34).

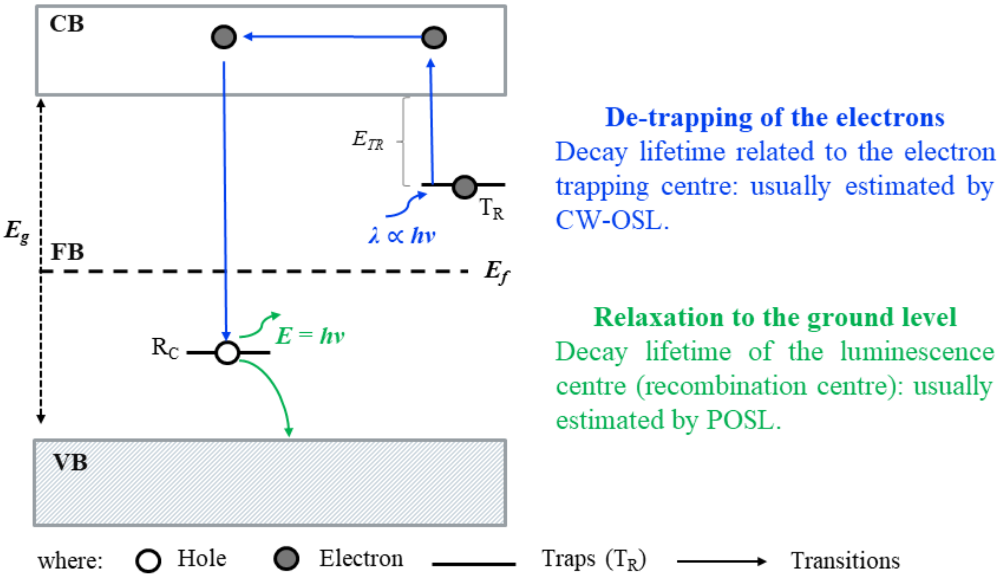

Figure 5.34 - Illustrative scheme of the de-trapping of electrons process (blue arrows) and the relaxation one (green arrows), when measuring the OSL signal.

By using pulses shorter than the relaxation time, it is possible to estimate the relaxation time. The relaxation is the process in which the excited centre goes to the ground state level after the recombination process (process in green colour in Figure 5.34). Therefore, it may allow us to discriminate the lifetime of the recombination centres and have a more detailed understanding of the underlying mechanisms involved in the OSL emission (Yukihara; Mckeever, 2011).

At first, there was an attempt to identify the decay times of the centres of fast decays. The sample of HfO_2 was stimulated with 500 ns pulses, with wavelength in the blue region at 458 nm and considering the recording on the rising edge. The choice of using blue stimulation was adopted as it allowed us to use the shortest pulses available in the equipment.

Figure 5.35a depicts the pulsed blue OSL (here also called BSL) for HfO_2 calcined at 1600 °C, after an irradiation dose of 10 Gy. Notice that firstly there is no signal, which is associated with the triggered delay of about 115 ns whilst the light turns on. After, there is a build-up behaviour which is due to the turning on and off process of the light, which takes about 30 ns. Finally, there is the decay trend, which is related to the period when the stimulation is off, and one can relate it to the relaxation process to the ground state. The three different curves analyse the influence of the number of repetitions of the pulses. Therefore, increasing the number of repetitions implies increasing the total stimulation time. If there are still trapped electrons, a longer stimulation time will induce more recombination, and hence, increase the signal.

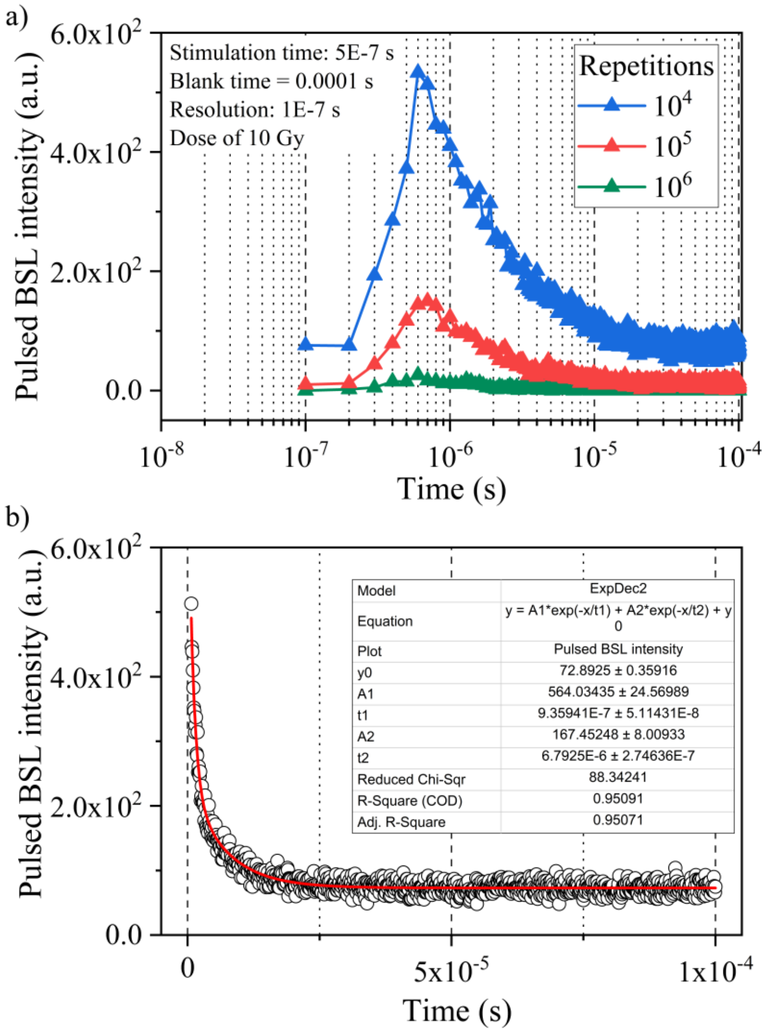

Model	ExpDec2
Equation	y = A1*exp(-x/t1) + A2*exp(-x/t2) + y0
Plot	Pulsed BSL intensity
y0	72.8925 ± 0.35916
A1	564.03435 ± 24.56989
t1	9.35941E-7 ± 5.11431E-8
A2	167.45248 ± 8.00933
t2	6.7925E-6 ± 2.74636E-7
Reduced Chi-Sqr	88.34241
R-Square (COD)	0.95091
Adj. R-Square	0.95071

Figure 5.35 - (a) Pulse BSL curves for HfO_2 powder calcined at 1600 °C for 2 h, for a beta irradiation dose of 10 Gy, as a function of the number of pulse repetitions. The pulse width was 500 ns, blank time of 0.0001 s, and resolution of 1×10^{-7} s (resolution is given by the blank time divided by the number of channels. The maximum number of channels in the equipment used is 1000). And (b) the fitting of the curve with 10^6 repetitions using a double exponential equation. The signal was recorded on the rising edge.

Figure 5.35b takes the curve of 10^6 repetitions from part a, and using the decay trend (after the build-up region), it shows the fitting done by using a double exponential decay function, in order to calculate the decay times of the centres (Bulur; Kartal; Saraç, 2014):

$$I(t) = I_1 e^{-\frac{t}{\tau_1}} + I_2 e^{-\frac{t}{\tau_2}} + B_G \tag{5.4}$$

Where the intensity of the signal I is as a function of the time t is dependent on the intensity of each component I_1 and I_2, the lifetimes τ_1 and τ_2, and the background B_G.

Based on the fitting using Equation 5.4, the lifetimes of those two shortest components (related to two relaxation decay centres) were calculated to be 0.89 ± 0.09 μs and 6.72 ± 0.37 μs (average ± σ), respectively. The average was taken from three measurements of three aliquots with the same mass and experimental conditions. As a means of comparison, Bulur, Kartal and Saraç (2014) reported decay times of 17 and 109 µs for zircon, which they referred to as “fast” and “slow” lifetimes, respectively. Those short lifetimes of the centre relaxation found here might be interesting for applications as a scintillator, for example.

However, considering the results of CW-OSL with blue and IR stimulations reported here, it is expected that longer components, that is, longer lifetime centres might exist. Therefore, a similar analysis was made, but using a much longer pulse, of 500 µs.

Figure 5.36 depicts the results for the pulsed BSL of HfO_2 calcined at 1600 °C, after a dose of 10 Gy and a pulse width of 500 µs. In this case, it was varied the resolution. Resolution is given by blank time divided by the number of channels (which was kept constant at 1000, this value was the maximum available on the equipment).

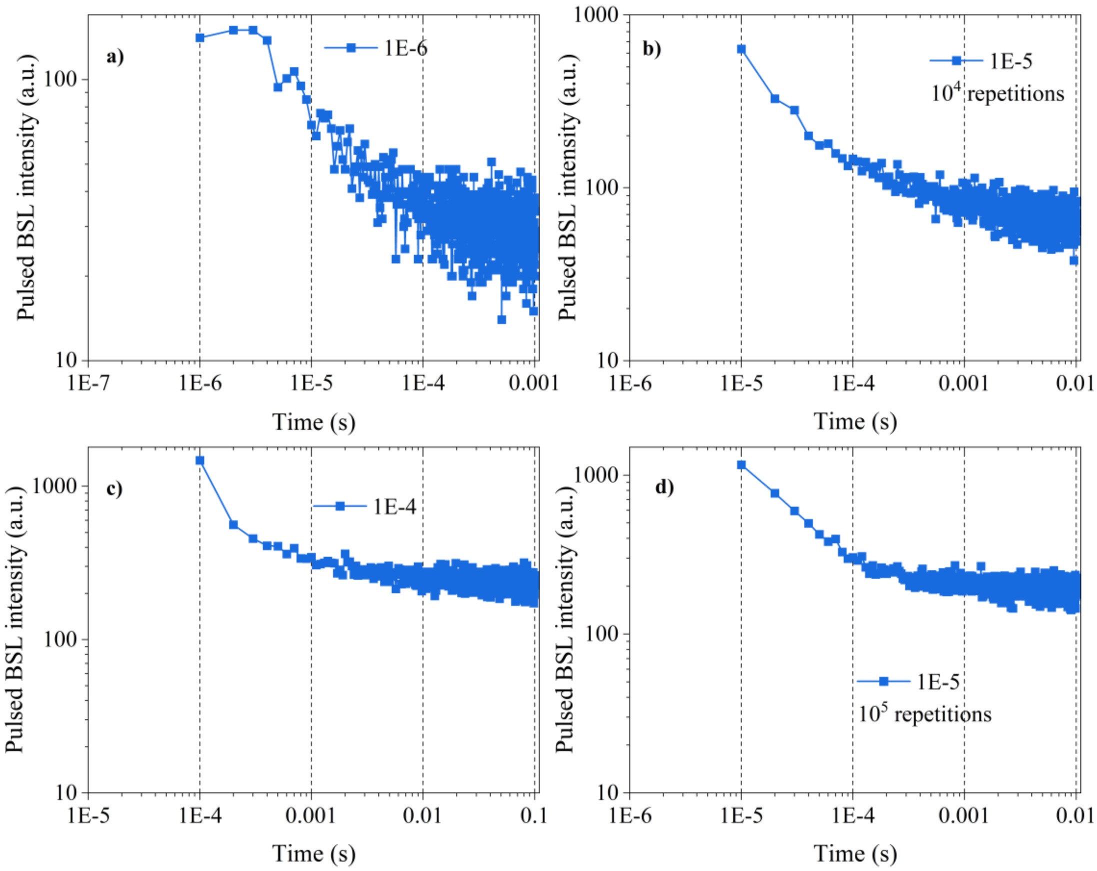

*Dose of 10 Gy, pulse width of 500 µs, recorded in the falling edge.

Figure 5.36 - Pulse BSL curves for HfO_2 powder calcined at 1600 °C for 2 h, for a beta irradiation dose of 10 Gy, as a function of the resolution (blank time/number of channels) of (a) 1×10^{-6} s, (b) 1×10^{-5} s, (c) 1×10^{-4} s (for 10^4 repetitions), and (d) 1×10^{-5} s (for 10^5 repetitions). The pulse width was of 500 µs and the signal was recorded in the falling edge. Cases a, b and c have the same number of repetitions for comparison of the resolution.

It is observed that a blank time of 0.01 seconds proved to be the best one, as the decay curves are clearer (Fig. 5.36b and 5.36d) in comparison with blank times of 0.001 and 0.1

seconds, shown in Figures 5.36a and 5.36c, respectively. Furthermore, by increasing the number of repetitions from 10^4 to 10^5, and keeping the resolution, the curve has a better-defined shape. The curves were measured on the falling edge because of the interest in the longer lifetimes.

The experimental curve from Figure 5.36d was used for fitting the data with a double exponential function, as done previously for the shorter components. The result is shown in Figure 5.37. Based on this, the lifetimes of the other two centres were estimated to be 20 ± 8.1 µs and 0.81 ± 0.17 ms (average ± σ). The average stands for the average of three aliquots of the same mass and measured under the same conditions. Although the fitting was successful, with an R^2 of about 0.96, the high values of standard deviation might indicate that further in-depth analyses on these longer components are necessary.

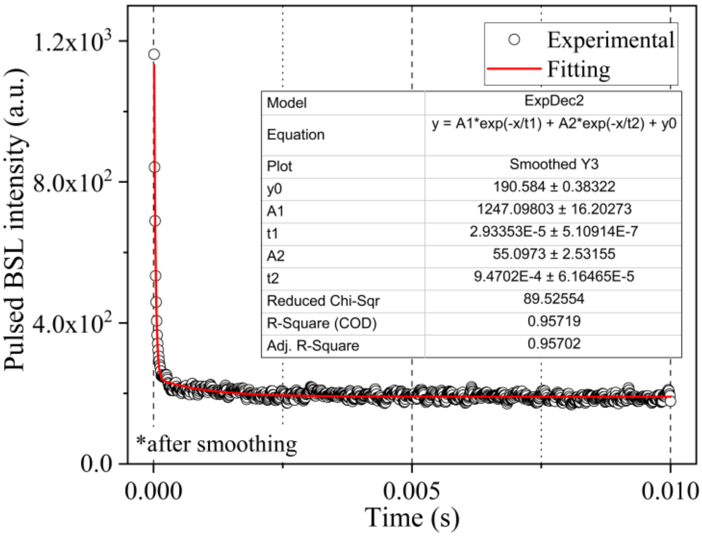

Model	ExpDec2
Equation	y = A1*exp(-x/t1) + A2*exp(-x/t2) + y0
Plot	Smoothed Y3
y0	190.584 ± 0.38322
A1	1247.09803 ± 16.20273
t1	2.93353E-5 ± 5.10914E-7
A2	55.0973 ± 2.53155
t2	9.4702E-4 ± 6.16465E-5
Reduced Chi-Sqr	89.52554
R-Square (COD)	0.95719
Adj. R-Square	0.95702

Figure 5.37 - Pulsed BSL for HfO_2 powder calcined at 1600 °C for 2h, for a beta irradiation dose of 10 Gy. Parameters of the measurement: resolution of 1×10^{-5} s, 10^5 repetitions and pulse width of 500 µs. The signal was recorded on the falling. Circles represent the experimental data after smoothing and the red line the fitting of the curve using a double exponential equation.

The results of POSL are important for starting a "time-resolved OSL" study for HfO_2. The presence of multiple and different values of lifetimes of the centres sheds light that the mechanisms underlying the OSL emission might involve different relaxation transition pathways. Furthermore, it opens the door to additional studies on it.

Chapter 6

6 Conclusions

This study had as its main objectives to synthesise samples of HfO_2 by the precipitation method and evaluate its luminescent properties. Also, the influence of the heat treatment on those properties, the potential application in ionising radiation dosimetry, and to try and identifying which defects that play a role in luminescence. Therefore, this section is divided into four sections which correspond to each of the objectives.

6.1 On the Synthesis and Crystalline Structure

The method of precipitation showed to be successful in synthesising HfO_2 samples with monoclinic crystalline structure. The monoclinic arrangement was expected as it is the phase usually obtained in normal conditions of pressure and temperature. Moreover, the XRD patterns showed a high crystallinity level in the samples, and considering that large bands were not observed, which might indicate an amorphous region.

Although the heat treatment (which was performed at four different conditions at 1000, 1200, 1400 and 1600 °C for 2 hours) did not change the crystalline phase, the calculation of the crystallite size showed that a higher temperature led to an increase in the average size. Moreover, the findings confirmed that the sample is arranged in nanoscale crystals. For the sample calcined at 1000 °C, for example, it was estimated to be about 23 nm, whilst the one calcined at 1600 °C has an average crystallite size of about 42 nm. This increase showed that more energy added to the system induced rearrangements in the crystal lattice, may have created more defects (as oxygen vacancies) and making the interatomic distances longer.

6.2 On the Luminescence and the Heat Treatment Influence

Luminescent measurements performed here showed that HfO_2 has an impressive emission in the blue region, which is observed in different techniques and is enhanced by the heat treatment.

The TL emission of HfO_2 nanocrystals is composed of several peaks, indicating that different trap levels are involved in the trapping of electrons. Independent of the heat treatment, all the samples showed to have an intensity which is proportional to the absorbed dose, and no saturation tendency was observed for doses up to 30 Gy. Although the response was proportional to the absorbed dose, it varied according to the heat treatment. The sample calcined at 1000 °C has a linear dose-response curve over the entire range of doses studied (from 0.32 to 30 Gy), whilst the others have non-linear tendencies for doses higher than 5 Gy. This non-linearity might be associated with the presence of deep trapping centres. Considering that the heat treatment improved the signal of peaks at higher temperatures, it seems to be a feasible hypothesis.

Using the methods of T_M-T_{stop} and CGCD was demonstrated to be a powerful way to deepen the understanding of TL emission. In addition, the results from both methods showed excellent agreement. Whilst the sample calcined at 1000 °C has a curve composed of eight peaks between 0 and 500 °C, with energy activation values from 0.68 to 1.4 eV, the samples calcined at 1400 and 1600 °C have a TL curve with six peaks, with slightly higher activation energy values of up to 1.6 eV. In all the cases, the most prominent peak was at about 130 °C and follows a kinetic order close to 1. However, more remarkable is that the heat treatment at high temperatures proved to be beneficial for creating deep traps: in the case of the sample calcined at 1600 °C, the second most intense peak is also the deepest one.

And how has the heat treatment influenced the OSL emission? As was observed for TL, HfO_2 has an important OSL emission, indicating that the traps are not only thermal-sensitive but light-sensitive as well. The high temperature of the heat treatment led to a more intense OSL signal. However, the dose-response curve with more clear linear tendency was obtained for the sample calcined at 1600 °C.

Again, the deconvolution of the curves proved to be an effective method to analyse the signal. Either the CW or LM-OSL curves are composed of two components (or peaks for LM). In the case of CW-OSL, the heat treatment enhanced the medium component, which became more intense and with a longer decay: whilst it is 0.81 and 0.85 s for the samples calcined at 1000 and 1200 °C, for the ones calcined at 1400 and 1600 °C, the values are of 1.84 and 1.76 s, respectively.

The analysis of the CW-OSL signal as a function of the readout temperature showed the existence of competition of shallow traps, which is likely related to the main peak in TL being at a low temperature.

The trapping centres were evaluated by the TL measurement when the activation energy and kinetic order were also estimated. To study the recombination centre side, spectral measurements were performed.

Heat treatment did not change the main emission band of HfO_2, which is in the blue region, centred between 2.44-2.71 eV, according to the technique, as given by Gaussian fittings. However, it led to a more intense signal, which is feasibly associated with the creation of defects.

For the case of fluorescence, as the sample was excited with UV photons, the emission in the visible region follows a conventional pathway. It is different from the OSL spectra results because in OSL the stimulation energy was lower than the emission: 1.46 eV for IR and 2.36 eV for green. Based on the previous report in the literature, it was demonstrated here that the HfO_2 might undergo a non-linear optics process, possibly of two or three-photon absorption, which would explain the underlying mechanism in OSL.

6.3 On the Defects and Luminescence

Several studies have already pointed out that oxygen vacancies are the most common type of defects found in oxide materials, as well as in HfO_2. Despite this knowledge, the type of oxygen vacancy is still in discussion, only a few studies have tried to elucidate it, and it remains a topic of interest.

The HfO_2 sample synthesised by the precipitation method and calcined at 1000 °C has as the main defect the F-like centres, as verified by the ESR signals with *g* values of 1.997 and 2.011. By increasing the heat treatment temperature, the F-like centres' contribution is reduced, and the main defect turns out to be oxygen vacancies in charge state +1 (V^+) in a four-coordinated arrangement, which was identified by the *g* values of 1.898, 1.957, and 1.985.

The evaluation of the ESR signal related to the V^+ defect showed it is radiation-dependent and temperature-dependent as well. Since it is completely depleted when heated above 250 °C, V^+ centres may be associated with both the TL and OSL emission (bleaching measurements showed that all peaks here analysed are affected by light stimulation). This result also supports the necessity of a non-linear optics process to explain the emission in OSL, as the optical excitation energy of a V^+ centred was reported to be 3.33 eV.

6.4 On the Application in Ionising Radiation Dosimetry

The sample with the highest signal, that is, calcined at 1600 °C, was evaluated regarding its dosimetric properties. The emission chosen was the IRSL as it supplies a noticeable intensity.

Because of the contribution of shallow traps, which are more unstable, it was found that a readout temperature of 100 °C might be a good compromise of signal intensity and stability. The IRSL is reproducible, with a variation lower than 9 % when considering repeatability, and below 3 % for reproducibility. In addition, MDD was calculated to be of about 19 mGy, when considering the signal at the first point of the IRSL decay curve.

IRSL has a considerable fading after a one-day storage period though, which can reduce the signal to about half of the initial intensity (it might be useful to study a potential application where the time of a passage of a radioactive source would be associated with the signal decay). A photon energy overresponse was also observed, which is expected for a high Z_{eff} material.

Based on those results, HfO_2 synthesised by the precipitation method and calcined at 1600 °C has a limited potential use in ionising radiation dosimetry once the intermediate peaks (which are related to the IRSL signal measured at 100 °C) do not follow a first-order kinetic, meaning the peak changes position with doses; the photon energy overresponse occurs in a range which is widely used in medicine; and there is a high fading. Hence, proper corrections would be necessary to obtain a good accuracy. Considering the high Z_{eff} of hafnia, instead of medical dosimetry, the material might be more adequate for retrospective/accidental. But even for these latter applications, it would not be straightforward, for example, due to strong fading effect.

Although the results indicated that the use of hafnia for dosimetry seems to be hampered by the aspects mentioned, the material has an intense response to ionising radiation, characterising it as a proper detector, and not only that, but its emission in the blue region also falls into the best efficiency range of the most widely used PMT tubes. For a matter of exemplification, hafnia has a potential to be studies for image plate applications, once it has a strong response to IR stimulation and emits in the blue region.

6.5 Some Remarks

This work presented the luminescent characterisation of HfO_2 nanocrystals obtained by the precipitation method and the influence of heat treatment on it, which was by itself an achievement. Before the publications derived from this thesis (see Appendix C), the OSL emission had not yet been reported for HfO_2.

Defects in the material were identified here by ESR signal and V^+ centres associated with the blue emission observed in the fluorescence, TL and OSL emissions. Moreover, different luminescent mechanisms were experimentally attested, such as competition of shallow traps, transfer of charges and non-linear optics process.

The results widened the perspective of the application of HfO_2 which has already been proved to be promising in electronics, showing it has remarkable luminescence, that it can be used in radiation detection and lightning, among other areas (the strong fading might be advantageous for scintillation purposes, for example). In addition, to the best of the author's knowledge, it is the first report of IRSL for HfO_2.

Chapter 7

7 Outlook

HfO_2 is a promising material for use in the luminescence area, and the recent reports have pointed in this direction. Although most of the studies had first approached applications in the electronics area, even in electronics the results keep being surprising.

This study shed light in the luminescent emission by using techniques that were not reported previously for this material and pointed out the defects and mechanisms involved. The results not only contributed to reaching the objectives here established but may be a useful source for other researchers that are investigating the same material.

Despite all the effort used and findings reported here, the results only showed that there is a lot to be explored regarding the luminescence of hafnia. Therefore, as suggestions for future works, one might consider:

- Analysing the TL and OSL emissions using lower irradiation doses and different sources, for example, gamma and UV radiation.
- Studying changes in the synthesis, seeking to improve the dosimetric properties of fading and MDD, for example by doping or using different synthesis routes.
- Performing an in-depth analysis on the POSL, to better elucidate the decay time of the relaxation process.
- Investigating the non-linear optics processes by using appropriate techniques, such as Z-scan.

References

AFOUXENIDIS, D. *et al*. Computerised curve deconvolution of TL/OSL curves using a popular spreadsheet program. **Radiation Protection Dosimetry**, v. 149, p. 363–370, 2012.

AHMED, S. N. **Physics & engineering of radiation detection**. London: Elsevier, 2007.

AITKEN, M. J. Thermoluminescence dating: past future trends. **Nuclear Tracks**, v. 10, p. 3-6, 1985.

AITKEN, M. J. **An introduction to optical dating:** the dating of Quaternary sediments by the use of photo-stimulated luminescence. Oxford: Oxford University Press, 1998.

AKSELROD, M. S. *et al*. Highly sensitive thermoluminescent anion-defective α-$Al_2O_{3:C}$ single crystal detectors. **Radiation Protection Dosimetry**, v. 32, p. 15-20, 1990.

AKSELROD, M. S.; BØTTER-JENSEN, L.; MCKEEVER, S. W. S. Optically stimulated luminescence and its use in medical dosimetry. **Radiation Measurements**, v. 41, p. S78-S99, 2007.

ALEKSIEVA, K. I.; YORDANOV, N. D. Various approaches in EPR identification of gamma-irradiated plant foodstuffs: A review. **Food Research International**, v. 105, p. 1019-1028, 2018.

ALPER, A. M. **High temperature oxides.** Part II: Oxides of rare earths, titanium, zirconium, hafnium, niobium and tantalum. New York: Academic Press, Inc., 1970.

ALTUNAL, *et al*. A calcination study on BeO ceramics for radiation dosimetry. **Materials Research Bulletin**, v. 130, p. 1-15, article nº 110921, 2020.

ALTUNAL, V.; GUCKAN, V.; YEGINGIL, Z. Effects of oxygen vacancies on luminescence characteristics of BeO ceramics. **Journal of Alloys and Compounds**, v. 938, p. 1-14, article nº 168670, 2023.

ANDREO, P. *et al*. **Fundamentals of ionizing radiation dosimetry**. Weinheim: Wiley, 2017.

ANKJÆRGAARD, C.; JAIN, M.; WALLINGA, J. Towards dating Quaternary sediments using the quartz Violet Stimulated Luminescence (VSL) signal. **Quaternary Geochronology**, v. 18, p. 99-109, 2013.

ATAŞ, H. *et al*. Serum levels of homocysteine, folate and vitamin B12 in patients with vitiligo before and after treatment with narrow band ultraviolet B phototherapy and in a group of controls. **Journal of Photochemistry and Photobiology B: Biology**, v. 148, p. 174-180, 2015.

ATTIX, F. H. **Introduction to radiological physics and radiation dosimetry**. Weinheim: Wiley, 1986.

BAILEY, D. L. *et al*. **Nuclear medicine physics:** a handbook for teachers and students. Vienna: International Atomic Energy Agency, 2014.

BAILIFF, I. K.; SHOLOM, S.; MCKEEVER, S. W. S. Retrospective and emergency dosimetry in response to radiological incidents and nuclear mass-casualty events: a review. **Radiation Measurements**, v. 94, p. 83-139, 2016.

BALIAN, H. G.; EDDY, N. W. Figure-of-merit (FOM), an improved criterion over the normalized chi-squared test for assessing goodness-of-fit of gamma-ray spectral peaks. **Nuclear Instruments and Methods**, v. 145, p. 389–395, 1977.

BANERJEE, W.; KASHIR, A.; KAMBA, S. Hafnium Oxide (HfO_2) – a multifunctional oxide: a review on prospect and challenges of hafnium oxide in resistive switching and ferroelectric memories. **Small**, v. 18, article nº 2107575, 2022.

BHAGYARAJ, S. M. *et al*. **Synthesis of inorganic nanomaterials**: advances and keys technologies. Duxford: Elsevier, 2018.

BIASIN, M. *et al*. UV-C irradiation is highly effective in inactivating SARS-CoV-2 replication. **Scientific Reports**, v. 11, p. 1-7, article nº 6260, 2021.

BISWAS, R. H. *et al*. Thermoluminescence of the meteorite interior: a possible tool for the estimation of cosmic ray exposure ages. **Earth and Planetary Science Letters**, v. 304, p. 36-44, 2011.

BORGES, F. H. *et al*. Highly red luminescent stabilized tetragonal rare earth-doped HfO_2 crystalline ceramics prepared by sol-gel. **Optical Materials: X**, v.16, p. 1-10, article nº 100206, 2022.

BOS, A. J. J. High sensitivity thermoluminescence dosimetry. **Nuclear Instruments and Methods in Physics Research B**, v. 184, p. 3-28, 2001.

BOS, A. J. J. Theory of thermoluminescence. **Radiation Measurements**, v. 41, p. S45-S56, 2007.

BOSSIN, L. *et al*. Thermoluminescence characteristics of a chondrite (Holbrook) and an aubrite achondrite (Norton County) meteorites. **Applied Radiation and Isotopes**, v. 127, p. 26-34, 2017.

BOYD, R. W. **Nonlinear optics**. 3rd ed. Academic Press, 2008.

BØTTER-JENSEN, L.; MCKEEVER; S. W. S.; WINTLE, A. G. **Optically stimulated luminescence dosimetry**. The Netherlands: Elsevier Science B.V., 2003.

BROWN, N. D.; RHODES, E. J.; HARRISON, T. M. Using thermoluminescence signals from feldspars for low-temperature thermochronology. **Quaternary Geochronology**, v. 42, p. 31-41, 2017.

BRUNDLE, C. R.; EVANS, C. A.; WILSON, S. **Encyclopedia of materials characterization**. 1st ed. Stoneham: Butterworth-Heinemann, a division of Reed Publishing (USA) Inc., 1992.

BRUSTOLON, M.; GIAMELLO, E. **Electron paramagnetic resonance**: a practitioner's toolkit. Hoboken: John Wiley & Sons, Inc., 2009.

BULL, R. K. Thermoluminescence and its applications: an introduction. **Nuclear Tracks and Radiation Measurements**, v. 11, p. 105-113, 1986.

BULUR, E. An alternative technique for Optically Stimulated Luminescence (OSL) experiment. **Radiation Measurements**, v. 26, p. 701-709, 1996.

BULUR, E. A simple transformation for converting CW-OSL curves to LM-OSL curves. **Radiation Measurements**, v. 32, p. 141-145, 2000.

BULUR, E.; SARAÇ, B. E. Time-resolved OSL studies on BeO ceramics. **Radiation Measurements**, v. 59, p. 129-138, 2013.

BULUR, E.; KARTAL, E.; SARAÇ, B. E. Time-resolved OSL of natural zircon: a preliminary study. **Radiation Measurements**, v. 60, p. 46-52, 2014.

CAÑEZ-MORALES, M. *et al*. Beta particle excited thermoluminescence of new ZnO:Ce phosphors. **Optical Materials**, v. 141, 113963, 2023.

CARAVACA, M.A.; CASALI, R. A. Ab initio localized basis set study of structural parameters and elastic properties of HfO_2 polymorphs. **Journal of Physics: Condensed Matter**, v. 17, p. 5795-5811, 2005.

CHATTOPADHYAY, A.; NAYAK, J. Hafnium oxide nanoparticles synthesized via sol-gel route for an efficient detection of volatile organic compounds at room temperature. **Materials Science in Semiconductor Processing**, v. 139, p. 1-12, article nº 106336, 2022.

CHEN, R.; KIRSH, Y. **Analysis of thermally stimulated processes**. Oxford: Pergamon Press Ltd, 1981.

CHEN, R.; PAGONIS, V. **Thermally and Optically Stimulated Luminescence**: a simulation approach. United Kingdom: John Wiley & Sons Ltd, 2011.

CHEN, R.; PAGONIS, V. **Advances in physics and applications of optically and thermally stimulated luminescence**. Singapore: World Scientific Publishing Europe Ltd, 2019.

CHEN, M. *et al*. High-sensitivity measurements of the nonlinear absorption coefficient of wide bandgap oxide thin films with the Z-scan method. **Optical Materials Express**, v. 12, p. 533-544, 2022.

CHEN, Y. *et al*. NIR-II light-assisted radiotherapy based on ultrasmall HfO_2-embedded porous carbon nanooctahedra for overcoming tumor radioresistance. **Materials Today Nano**, v. 20, p. 1-10, article nº 100253, 2022.

CHITHAMBO, M. L. The analysis of time-resolved optically stimulated luminescence: I. Theoretical considerations. **Journal of Physics D: Applied Physics**, v. 40, p. 1874-1879, 2007a.

CHITHAMBO, M. L. The analysis of time-resolved optically stimulated luminescence: II. Computer simulations and experimental results. **Journal of Physics D: Applied Physics**, v. 40, p. 1880-1889, 2007b.

CHOI, J. H.; MAO, Y.; CHANG, J. P. Development of hafnium based high-k materials – A review. **Materials Science and Engineering R**, v. 72, p. 97-136, 2011.

CHUANG, S-H.; LIN, H-C.; CHEN, C-H. Oxygen vacancy relationship to photoluminescence and heat treatment methods in hafnium oxide powders. **Journal of Alloys and Compounds**, v. 534, p. 42-46, 2012.

ĆIRIĆ, A.; STOJADINOVIĆ, S.; DRAMIĆANIN, M. D. Judd-Ofelt and chromaticity analysis of hafnia doped with trivalent europium as a potential white LED phosphor. **Optical Materials**, v. 88, p. 392-395, 2019.

COLAROSSI, D. *et al*. Testing single aliquot regenerative dose (SAR) protocols for violet stimulated luminescence. **Radiation Measurements**, v. 120, p. 104-109, 2018.

CULLITY, B. D.; STOCK, S. R. **Elements of X-Ray Diffraction**. 3rd ed. Harlow: Pearson Education Limited, 2014.

DANIELS, F.; BOYD, C. A.; SAUNDERS, D. F. Thermoluminescence as a research tool. **Science**, v. 117, p. 343-349, 1953.

DAS, K. C. *et al*. Role of Gd dopants on electrical properties of RF co-sputtered HfO_2 thin films for resistive switching applications. **Materials Science & Engineering B**, v. 265, p. 1-6, article nº 114997, 2021.

DISCHER, M.; BASSINET, C.; WODA, C. A TL study of protective glasses of mobile phones for retrospective dosimetry. **Optical Materials: X**, v. 18, p. 1-7, article nº 100233, 2023.

DTU Nutech. Radiation Instruments. **Product Catalogue**. 42 pages. Available on https://www.fysik.dtu.dk/english/research/radphys/research/radiation-instruments/tl_osl_reader, and accessed on 12.05.23.

DUNN, L. *et al*. Commissioning of optically stimulated luminescence dosimeters for use in radiotherapy. **Radiation Measurements**, v. 51-52, p. 31-39, 2013.

DURAGKAR, A. *et al*. Versatility of thermoluminescence materials and radiation dosimetry – A review. **Luminescence**, v. 34, p. 1-10, 2019.

ET ENTERPRISES. 51 mm (2”) photomultiplier. 9235B series. **Data sheet**. 2 pages, 2010.

FATTIBENE, P.; CALLENS, F. EPR dosimetry with tooth enamel: a review. **Applied Radiation and Isotopes**, v. 68, p. 2033-2116, 2010.

FIACZYK, K. *et al*. Thermoluminescent properties of HfO_2:Ti after exposure to X-rays. **Radiation Measurements**, v. 90, p. 140–144, 2016.

FOSTER, A. S. *et al*. Vacancy and interstitial defects in hafnia. **Physical Review B**, v. 65, p. 1-13, article nº 174117, 2002.

FURASOVA, A. D. *et al*. Synthesis of a rare-earth doped hafnia hydrosol: Towards injectable luminescent nanocolloids. **Colloids and Surfaces B: Biointerface**, v. 154, p. 21-26, 2017.

FURETTA, C. **Handbook of thermoluminescence**. Singapore: World Scientific Publishing Co. Pte. Ltd., 2003.

GALBRAITH, R. F.; ROBERTS, R. G. Statistical aspects of equivalent dose and error calculation and display in OSL dating: an overview and some recommendations. **Quaternary Geochronology**, v. 11, p. 1-27, 2012.

GALLAGHER, R. P.; LEE, T. K. Adverse effects of ultraviolet radiation: a brief review. **Biophysics and Molecular Biology**, v. 92, p. 119-131, 2006.

GARCÍA, H. *et al*. Study of the set and reset transitions in HfO_2-based ReRAM devices using a capacitor discharge. **Solid State Electronics**, v. 183, p. 1-5, article nº 108113, 2021.

GARLICK, G. F. J.; GIBSON, A. F. The electron trap mechanism of luminescence in sulphide and silicate phosphors. **Proceedings of the Physical Society**, v. 60, n. 6, p. 574-590, 1948.

GAVARTIN, J. L. *et al*. Negative oxygen vacancies in HfO_2 as charge traps in high-k stacks. **Applied Physics Letters**, v. 89, p. 1-3, article nº 082908, 2006.

GÖKSU-ÖGELMAN, H. Y.; REGULLA, D. F. Detection of irradiated food. **Nature**, v. 340, 1989.

GREITER, M. B.; DENK, J.; HOEDLMOSER, H. Secondary standard calibration, measurement and irradiation capabilities of the individual monitoring service at the Helmholtz Zentrum München: aspects of uncertainty and automation. **Radiation Protection Dosimetry**, v. 170, p. 1-4, 2016.

GRITSENKO, V. A.; PEREVALOV, T. V.; ISLAMOV, D. R. Electronic properties of hafnium oxide: a contribution from defects and traps. **Physics Reports**, v. 613, p. 1–20, 2016.

HAMAMATSU. Photomultiplier tube modules, **Catalog**. 40 pages, 2019.

HARVEY, E. N. **A history of luminescence**: from the earliest times until 1900. United States of America: The American Philosophical Society, 1957.

HARVEY, J. A.; KEARFOTT, K. J.; RAFIQUE, M. Dose response linearity and practical factors influencing minimum detectable dose for various thermoluminescent detector types. **Journal of Radioanalytical and Nuclear Chemistry**, v. 303, p. 1711-1718, 2015.

HECKELSBERG, L. F. Thermoluminescent Dosimetry (LiF). **Health Physics**, v. 39, p. 391-393, 1980.

HORIBA. Fluorolog®-3 Spectrofluorometer. **Operation Manual**. Part number 81014, version 3.2, 320 pages, 2008.

HUNTLEY, D. J.; GODFREY-SMITH, D. I.; THEWALT, M. L. W. Optical dating of sediments. **Nature**, v. 313, p. 105-107, 1985.

HUNTLEY, D. J.; LIAN, O. B. Some observations on tunnelling of trapped electrons in feldspars and their implications for optical dating. **Quaternary Science Review**, v. 25, p. 2503-2512, 2006.

ICRP. ICRP Publication 60: Recommendation of the International Commission on Radiological Protection. **Annals of the ICRP**, 1st ed., v. 21 (1-3), 1991.

ICRP. ICRP Publication 92: Relative Biological Effectiveness (RBE), Quality Factor (Q), and Radiation Weighting Factor (w_R). **Annals of the ICRP**, v. 33 (4), 2003.

ICRP. ICRP Publication 116: Conversion Coefficients for Radiological Protection Quantities for External Radiation Exposure. **Annals of the ICRP**, v. 40 (2-5), 2010.

ICRU. Fundamental Quantities and Units for Ionizing Radiation (Revised). ICRU Report 85. **Journal of the ICRU**, v. 11, 2011.

ISLAMOV, D. R. *et al*. Origin of traps and charge transport mechanism in hafnia. **Applied Physics Letters**, v. 105, p. 1-4, article nº 222901, 2014.

ITO, T. *et al*. Similarities in photoluminescence in hafnia and zirconia induced by ultraviolet photons. **Journal of Applied Physics**, v. 97, 054104, 2005.

JAIN, M.; GURALNIK, B.; ANDERSEN, M. T. Stimulated luminescence emission from localized recombination in randomly distributed defects. **Journal of Physics: Condensed Matter**, v. 24, p. 1-12, article nº 385402, 2012.

JENKINS, R.; SNYDER, R. L. **Introduction to X-ray powder diffractometry**. New York: John Wiley & Sons, Inc., 1996.

JOHNS, H. E.; CUNNINGHAM, J. R. **The physics of radiology**. 4th ed. Illinois: Charles C Thomas Publisher, 1983.

KALITA, J. M.; WARY, G. Estimation of band gap of muscovite mineral using thermoluminescence (TL) analysis. **Physica B**, v. 485, p. 53-59, 2016.

KANG, A. Y.; LENAHAN, P. M.; CONLEY JR, J. F. Electron spin resonance observation of trapped electron centers in atomic-layer-deposited hafnium oxide on Si. **Applied Physics Letters**, v. 83, p. 1-2, article nº 3407, 2003.

KARA, E.; WODA, C. Further characterization of BeO detectors for applications in external and medical dosimetry. **Radiation Measurements**, v. 165, p. 1-8, article nº 106950, 2023.

KARAMPIPERI, M.; THEOLOGITIS, S.; KAZAKIS, N. A. Thermoluminescence characterization of minerals extracted from dried oregano for retrospective and/or sterilization dosimetry. **Radiation Measurements**, v. 158, p. 1-9, article nº 106850, 2022.

KASZEWSKI, J. *et al*. HfO_2:Eu nanoparticles excited by X-rays and UV-visible radiation used in biological imaging. **Journal of Rare Earths**, v. 37, p. 1176-1182, 2019.

KIISK, V. *et al*. Photoluminescence of sol–gel-prepared hafnia. **Physica B**, v. 405, p. 758-762, 2010.

KIM, J. H. *et al*. Possible effects of radiofrequency electromagnetic field exposure on central nerve system. **Biomolecules & Therapeutics**, v. 27, n.3, p. 265-375, 2019.

KIM. M. J.; CHOI, J. H.; HONG, D. G. Dose and dose rate dependence of time-resolved OSL from Korean paleosol quartz. **Radiation Measurements**, v. 46, p. 1518-1521, 2011.

KITIS, G.; GOMEZ-ROS, J. M.; TUYN, J. W. N. Thermoluminescence glow-curve deconvolution functions for first, second and general orders of kinetics. **Journal of Physics D: Applied Physics**, v. 31, p. 2636–2641, 1998.

KITIS, G.; PAGONIS, V. computerized curve deconvolution analysis for LM-OSL. **Radiation Measurements**, v. 43, p. 737-741, 2008.

KITIS, G.; POLYMERIS, G. S.; PAGONIS, V. Stimulated luminescence emission: from phenomenological models to master analytical equations. **Applied Radiation and Isotopes**, v. 153, p. 1-26, article nº 108797, 2019.

KITTEL, C. **Introduction to solid state physics**. 8th ed. United States of America: John Wiley & Sons, 2005.

KIYAK, N. Application of thermoluminescence technique to identify radiation processed foods. **Radiation Physics and Chemistry**, v. 46, p. 721-723, 1995

KNOLL, G. F. **Radiation detection and measurement**. 4th ed. United States of America: John Wiley & Sons, 2010.

KONG, S. *et al*. Advance on monitoring of radioactivity in food in China and Japan after Fukushima nuclear accident. **Radiation Medicine and Protection**, v. 3, p. 37-42, 2022.

KRAKOWIAN, D. *et al*. Application of EPR spectroscopy to the examination of pro-oxidant activity of coffee. **Food Chemistry**, v. 151, p. 110-119, 2014.

KRBETSCHEK, M. R.; TRAUTMANN, T. A spectral radioluminescence study for dating and dosimetry. **Radiation Measurements**, v. 32, p. 853-857, 2000.

LADD, M.; PALMER, R. **Structure determination by X-ray crystallography**. 4th ed. New York: Springer Science+Business Media, 2003.

LAGANOVSKA, K. *et al*. Thermostimulated luminescence analysis of oxygen vacancies in HfO_2 nanoparticles. **Materials Research Bulletin**, v. 167, p. 1-9, article nº 112409, 2023.

LANGFORD, J. I.; WILSON, A. J. C. Scherrer after sixty years: a survey and some new results in the determination of the crystallite size. **Journal of Applied Crystallography**, v. 11, p. 102-113, 1978.

LATA, L. K. *et al*. Resistive switching characteristics of HfO_2 based bipolar nonvolatile RRAM cell. **Materials Today: Proceedings**, v. 30, p. 217-220, 2020.

LEE, D. *et al*. Ultra-low operation current and abnormal bipolar switching phenomena of hydrogen-passivated HfO_2 memristive devices for low power artificial neural network applications. **Ceramics International**, v. 49, p. 17497-17505, 2023.

LIAO, J. *et al*. HfO_2-based ferroelectric thin film and memory device applications in the post-Moore era: A review. **Fundamental Research**, v. 3, p. 332-345, 2023.

LUKONG, V. T.; UKOBA, K. O.; JEN, T. C. Heat-assisted sol-gel synthesis of TiO_2 nanoparticles structural, morphological and optical analysis for self-cleaning application. **Journal of King Saud University – Science**, v. 34, p. 1-8, article nº 101746, 2022.

MAHMOOD, M. M. *et al*. Thermoluminescence (TL), kinetic parameters and dosimetric features of Pakistani limestone. **Applied Radiation and Isotopes**, v. 188, p. 1-11, article nº 110357, 2022.

MANIKANTAN, J. *et al*. Physical and optical properties of HfO_2 NPs – synthesis and characterization in finding its feasibility in opto-electronic devices. **Advanced Powder Technology**, v. 28, p. 1636-1646, 2017.

MANRÍQUEZ, R. R. *et al*. Photo-, cathodo- and thermoluminescent properties of dysprosium-doped HfO_2 films deposited by ultrasonic spray pyrolysis. **Applied Radiation and Isotopes**, v. 92, p. 91-95, 2014.

MARKEY, B. G.; COLYOTT. L. E.; MCKEEVER, S. W. S. Time-resolved optically stimulated luminescence from α-$A1_2O_3$:C. **Radiation Measurements**, v. 24, p. 457-463, 1995.

MARTIN, J. E. **Physics for radiation protection:** a handbook. 2nd ed. Weinheim: Wiley, 2006.

MATTHEWS, J.N.A. Semiconductor industry switches to hafnium-based transistors. **Physics Today**, v. 61, n. 2, p. 25–26, 2008.

MAY, C. E.; PARTRIDGE, J. A. Thermoluminescence kinetics of alpha-irradiated alkali halides. **The Journal of Chemical Society**, v. 40, p. 1401-1409, 1964.

MCKEEVER, S. W. S. On the analysis of complex thermoluminescence glow-curves: resolution into individual peaks. **Physica Status Solidi (a)**, v. 62, p. 331-340, 1980.

MCKEEVER, S. W. S. **Thermoluminescence of solids**. Cambridge: Cambridge University Press, 1985.

MCKEEVER, S. W. S.; AKSELROD, M. S.; MARKEY, B. G. Pulsed optically stimulated dosimetry using α-$A1_2O_3$:C. **Radiation Protection Dosimetry**, v. 65, p. 267-272, 1996.

MCKEEVER, S. W. S.; CHEN, R. Luminescence models. **Radiation Measurements**, v. 27, p. 625-661, 1997.

MCKEEVER, S. W. S. Optically stimulated luminescence dosimetry. **Nuclear Instruments and Methods in Physics Research B**, v. 184, p. 29-54, 2001.

MENDOZA, J. G. *et a*l. Synthesis and characterization of hafnium oxide films for thermo and photoluminescence applications. **Applied Radiation and Isotopes**, v. 68, p. 696-699, 2010.

MÉNDEZ-CASTILLO, M. D. *et al*. Structural, morphological and luminescence properties of hafnia nanoparticles obtained by hydrothermal synthesis. **Ceramics International**, *ahead of print*, 2023. DOI: https://doi.org/10.1016/j.ceramint.2023.08.169. Accessed on: 22/08/2023.

MONACA, S. R.; FATTIBENE, P.; BORTOLIN, E. A thermoluminescence study of mineral silicates extracted from herbs in the dose range 0.5-5 Gy. **Radiation Measurements**, v. 53-54, p. 74-79, 2013.

MONTES, E. *et al*. Thermoluminescent characterization of $HfO_2:Tb^{3+}$ synthesized by hydrothermal route. **Applied Radiation and Isotopes**, v. 83, p. 196–199, 2014.

MÜLLER, J. *et al*. Ferroelectric hafnium oxide based materials and devices: assessment of current status and future prospects. **ECS Journal of Solid State Science and Technology**, v. 4(5), p. N30-N35, 2015.

MURRAY, A. S.; OLLEY, J. M. Precision and accuracy in the optically stimulated luminescence dating of sedimentary quartz: a status review. **Journal on Methods and Applications of Absolute Chronology**, v. 21, p. 1-16, 2002.

MURRAY-WALLACE, C. V. *et al*. Aminostratigraphy and thermoluminescence dating of coastal aeolianites and the later Quaternary history of a failed delta: The River Murray mouth region, South Australia. **Quaternary Geochronology**, v. 5, p. 28-49, 2010.

OBODOVSKIY, I. **Radiation:** fundamentals, applications, risks, and safety. Oxford: Elsevier, 2019.

OGUNDARE, F. O. *et al*. Thermoluminescence of kunzite: a study of kinetic processes and dosimetry characteristics. **Nuclear Instruments and Methods in Physics Research B**, v. 373, p. 44-51, 2016.

OKS, H. *et al*. Assessment of thermoluminescence peaks in porcelain for use in retrospective dosimetry. **Radiation Measurements**, v. 46, p. 1873-1877, 2011.

OLKO, P. Advantages and disadvantages of luminescence dosimetry. **Radiation Measurements**, v. 45, p. 506-511, 2010.

OZDEMIR, A. *et al*. Luminescence characteristics of newly-developed $MgB_4O_7:Ce^{3+}$, Na^+ phosphor as an OSL dosimeter. **Journal of Alloys and Compounds**, v. 865, p. 1-9, article nº 158498, 2021.

PAGONIS, V.; KITIS, G. Prevalence of first-order kinetics in thermoluminescence materials: An explanation based on multiple competition processes**. Physica Status Solidi B**, v. 249, p. 1590-1601, 2012.

PAGONIS, V.; KITIS, G.; FURETTA, C. **Numerical and practical exercises in thermoluminescence**. New York: Springer Science+Business Media, Inc., 2006.

PAN, L. *et al*. Magnesium aluminate spinel for optically stimulated luminescence dosimetry. **Journal of Alloys and Compounds**, v. 880, p. 1-9, article nº 160503, 2021.

PEJAKOVIĆ, D. A. Studies of the phosphorescence of polycrystalline hafnia. **Journal of Luminescence**, v. 130, n. 6, p. 1048–1054, 2010.

PENG, J. *et al*. Thermoluminescence glow-curve deconvolution using analytical expressions: A unified presentation. **Applied Radiation and Isotopes**, v. 168, p. 1-13, article nº 109440, 2021.

PERKOWITZ, S. **Optical characterization of semiconductors**: infrared, Raman, and photoluminescence spectroscopy. London: Academic Press Limited, 1993.

PODGORŠAK, E. B. **Radiation oncology physics**: a handbook for teachers and students. 3rd ed. Vienna: International Atomic Energy Agency, 2005.

PODGORŠAK, E. B. **Radiation physics for medical physicists**. 3rd ed. Switzerland: Springer Nature, 2016.

POLIKRETI, K.; MICHAEL, C. T.; MANIATIS, Y. Thermoluminescence characteristics of marble and dating of freshly excavated marble objects. **Radiation Measurements**, v. 37, p. 87-94, 2003.

POLYMERIS, G. S. *et al*. Dose response features of quenched and reconstructed, TL and deconvolved OSL signals in BeO. **Results in Physics**, v. 25, p. 1-11, article nº 104222, 2021.

QIU, Z. *et al*. Carbonate thermoluminescence and its implication for marine productivity change during the Permian-Triassic transition. **Palaeogeography, Palaeoclimatology, Palaeoecology**, v. 526, p. 72-79, 2019.

RAMADOSS, A.; KIM, S. J. Synthesis and characterization of HfO_2 nanoparticles by sonochemical approach. **Journal of Alloys and Compounds**, v. 544, p. 115-119, 2012.

RAMADOSS, A.; KRISHNAMOORTHY, K.; KIM, S. J. Novel synthesis of hafnium oxide nanoparticles by precipitation method and its characterization. **Materials Research Bulletin**, v. 47, p. 2680–2684, 2012.

RAMO, D. M. *et al*. Intrinsic and defect-assisted trapping of electrons and holes in HfO_2: an ab initio study. **Microelectronic Engineering**, v. 84, p. 2362-2365, 2007.

RANDALL, J. T.; WILKINS, M. H. F. Phosphorescence and electron traps I – the study of traps distributions. **Proceedings of the Royal Society A**, v. 184, p. 365-389, 1945a.

RANDALL, J. T.; WILKINS, M. H. F. Phosphorescence and electron traps II – the interpretation of long-period phosphorescence. **Proceedings of the Royal Society A**, v. 184, p. 390-407, 1945b.

RAUWEL, P. *et al*. Selective photocurrent generation in HfO_2 and carbon nanotube hybrid nanocomposites under ultra-violet and visible photoexcitations. **Materials Letters**, v. 246, p. 45-48, 2019.

RICHTER, D. *et al*. A novel beta source design for uniform irradiation in dosimetric applications. **Ancient TL**, v. 30, p. 57-64, 2012.

RICHTER, D.; RICHTER, A.; DORNICH, K. Lexsyg – A new system for luminescence research. **Geochronometria**, v. 40, n.4, p. 220-228, 2013.

RIEGER, P. H. **Electron Spin Resonance**: analysis and interpretation. Cambridge: Royal Society of Chemistry, 2007.

RODRIGUES, K.; HUOT, S.; KEEN-ZEBERT, A. Exploring the application of blue and red thermoluminescence for dating volcanic glasses. **Radiation Measurements**, v. 153, p. 1-11, article nº 106731, 2022.

ROWLANDS, C. C.; MURPHY, D. M. EPR Spectroscopy, theory. In: LINDON, J. C.; TRANTER, G. E.; KOPPENALL, D. **Encyclopedia of spectroscopy and spectrometry**. 3rd ed. London: Elsevier, 2017.

RÜHM, W. *et al*. The European radiation dosimetry group – Review of recent scientific achievements. **Radiation Physics and Chemistry**, v. 168, p. 1-18, article nº 108514, 2020.

SABTU, S. N. *et al*. Thermoluminescence dating analysis at the site of an ancient brick structure at Pengkalan Bujang, Malaysia. **Applied Radiation and Isotopes**, v. 105, p. 182-187, 2015.

SAWAKUCHI, A. O.; DEWITT, R.; FALEIROS, F. M. Correlation between thermoluminescence sensitivity and crystallization temperatures of quartz: potential application in geothermometry. **Radiation Measurements**, v. 46, p. 51-58, 2011.

SCHMIDT, C. *et al*. Radiofluorescence of quartz: a review. **Quaternary Geochronology**, v. 27, p. 66-77, 2015.

SCHROEDER, U.; HWANG, C. S.; FUNAKUBO, H. F. **Ferroelectricity in doped hafnium oxide**: materials, properties and devices. Duxford: Elsevier, 2019.

SCHWEIGER, A.; JESCHKE, G. **Principles of pulse electron paramagnetic resonance**. Oxford: Oxford University Press, 2001.

SEKAR, N. *et al*. Analysis of structural, morphological and dosimetric parameters of HfO_2 NPs in clinical ^{60}Co beam. **Radiation Physics and Chemistry**, v. 172, p. 1-7, article nº 108833, 2020.

SEKAR, N. *et al*. Characterizing and comparing the kinetic parameters of Gd^{3+} doped hafnium oxide nanoparticles in clinical photon and neutron beam. **Radiation Measurements**, v. 148, p. 1-10, article nº 106647, 2021.

SHIN, C.; KIM, H-O.; LIM, Y. A preliminary approach to identify irradiated foods by thermoluminescence measurements. **Journal of Luminescence**, v. 132, p. 1619-1622, 2012.

SHURYAK, I. Analysis of causal effects of ^{137}Cs deposition on ^{137}Cs concentrations in trees after the Fukushima accident using machine learning. **Journal of Environmental Radioactivity**, v. 264, p. 1-9, article nº 107205, 2023.

SILVA, A. *et al*. Unraveling the ferroelectric switching mechanisms in ferroelectric pure and La doped HfO_2 epitaxial thin films. **Materials Today Physics**, v. 34, p. 1-6, article nº 101064, 2023.

SINCLAIR, S. A.; PECH-CANUL, M. I. Development feasibility of TLD phosphors and thermoluminescent composite materials for potential applications in dosimetry: A review. **Chemical Engineering Journal**, v. 443, p. 1-14, article nº 136522, 2022.

SINGLA, S.; PANDEY, O. P.; SHARMA, G. Z-scan study of nonlinear absorption in gold doped borosilicate glass: Effect of Dy^{3+}. **Journal of Non-Crystalline Solids**, v. 521, p. 1-6, article nº 119481, 2019.

SOARES, A. F. *et al*. Study of morphological and luminescent properties (TL and OSL) of ZnO nanocrystals synthetized by coprecipitation method. **Journal of Luminescence**, v. 186, p. 135-143, 2017.

SOARES, A. F. *et al*. Morphological and luminescent properties of HfO_2 nanoparticles synthesized by precipitation method. **Journal of Luminescence**, v. 219, p. 1-8, article nº 116866, 2020.

SOARES, A. F.; TATUMI, S. H.; ROCCA, R. R. Influence of heat treatment on luminescent properties of the HfO_2, synthesized by precipitation method. **Radiation Physics and Chemistry**, v. 180, p. 1-13, article nº 109292, 2021.

SOARES, A. F. *et al*. The role of heat treatment in improving photoluminescence and optically stimulated luminescence of HfO_2. **EPJ Web of Conferences**, v. 266, p. 1-2, article nº 06010, 2022.

SONI, A. *et al*. OSL and thermally assisted OSL response in dental enamel for its possible application in retrospective dosimetry. **Radiation and Environmental Biophysics**, v. 53, p. 763–774, 2014.

SPOONER, N. A. Luminescence from NaCl for application to retrospective dosimetry. **Radiation Measurements**, v. 47, p. 883-889, 2012.

SUNTA, C. M. **Unraveling Thermoluminescence**. Springer Series in Materials Science Volume 202. India: Springer, 2015.

TATUMI, S. H. *et al*. Sol-gel synthesis of strontium aluminate phosphor and its TL and OSL properties. **Radiation Physics and Chemistry**, v. 157, p. 15-21, 2019.

TATUMI, S. H.; ROSSETTI, D. F.; SOARES, E. A. A. **Optically Stimulated Luminescence (OSL) dating in the Amazonian wetlands**. Cambridge: Cambridge Scholars Publishing, 2020.

TRICOT, R. The metallurgy and functional properties of hafnium. **Journal of Nuclear Materials**, v. 189, p. 277-288, 1992.

TSODOULOS, I. M. *et al*. Middle–Late Holocene earthquake history of the Gyrtoni Fault, Central Greece: Insight from optically stimulated luminescence (OSL) dating and paleoseismology. **Tectonophysics**, v. 687, p. 14-27, 2016.

TSOULFANIDIS, N.; LANDSBERGER, S. **Measurement & detection of radiation**. 4th ed. Boca Raton: Taylor & Francis Group, 2015.

TURNER, J. E. **Atoms, radiation, and radiation protection**. 3rd ed. Weinheim: Wiley, 2007.

VICHAIDID, T.; SAEINGJAEW, P. Thermoluminescence and electron spin resonance dating of freshwater fossil shells from Pa Toh Roh Shelter archaeological site in southern Thailand. **Heliyon**, v. 8, p. 1-9, article nº e10555, 2022.

WANG, J.; LI, H. P.; STEVENS, R. Hafnia and hafnia-toughened ceramics. **Journal of Materials Science**, v. 27, p. 5397-5430, 1992.

WASEDA, Y.; MATSUBARA, E.; SHINODA, K. **X-Ray diffraction crystallography**: introduction, examples and solved Problems. Heidelberg: Springer-Verlag Berlin Heidelberg, 2011.

WIATROWSKA, A.; ZYCH, E. Modeling luminescent properties of HfO_2:Eu powders with Li, Ta, Nb, and V codopants. **The Journal of Physical Chemistry C**, v. 116, p. 6409-6419, 2012.

WINTLE, A. G. Thermoluminescence dating of late Devensian loesses in southern England. **Nature**, v. 289, p. 479-480, 1981.

WINTLE, A. G. Luminescence dating: laboratory procedures and protocols. **Radiation Measurements**, v. 27, p. 769-817, 1997.

WINTLE, A. G.; ADAMIEC, G. Optically stimulated luminescence signals from quartz: a review. **Radiation Measurements**, v. 98, p. 10-33, 2017.

WOOLFSON, M. M. **An introduction to X-ray crystallography**. 2nd ed. Cambridge: Cambridge University Press, 1997.

WRIGHT, S.; BARKLIE, R. C. EPR characterization of defects in monoclinic powders of ZrO2 and HfO_2. **Materials Science in Semiconductor Processing**, v. 9, p. 892-896, 2006.

WRIGHT, S.; FEENEY, S.; BARKLIE, R. C. EPR study of defects in as-received, γ-irradiated and annealed monoclinic HfO_2 powder. **Microelectronic Engineering**, v. 84, p. 2378-2381, 2007.

WRIGHT, S.; BARKLIE, R. C. Electron paramagnetic resonance characterization of defects in monoclinic HfO_2 and ZrO_2 powders. **Journal of Applied Physics**, v. 106, p. 1-15, article nº 103917, 2009.

YANAGIDA, T. *et al.* A review and future of RPL dosimetry. **Radiation Measurements**, v. 158, p. 1-9, article nº 106847, 2022.

YASMIN, S. *et al.* The effectiveness of ornamental building materials (tiles) for retrospective thermoluminescence dosimetry. **Applied Radiation and Isotopes**, v. 184, p. 1-11, article nº 110218, 2022.

YEE, K. P.; MO, R. H. Thermoluminescence dating of stalactitic calcite from the early Palaeolithic occupation at Tongamdong site. **Journal of Archaeological Science: Reports**, v. 19, p. 405-410, 2018.

YUKIHARA, E. G.; MCKEEVER, S. W. S. **Optically stimulated luminescence – fundamentals and applications**. United Kingdom: John Wiley & Sons Ltd, 2011.

YUKIHARA, E. G.; MCKEEVER, S. W. S.; AKSELROD, M. S. State of art: optically stimulated luminescence dosimetry – frontiers of future research. **Radiation Measurements**, v. 71, p. 15-24, 2014.

YUKIHARA, E. G. A review on the OSL of BeO in light of recent discoveries: the missing piece of the puzzle? **Radiation Measurements**, v. 134, p. 1-7, article nº 106291, 2020.

YUKIHARA, E. G. TL and OSL as research tools in luminescence: possibilities and limitations. **Ceramics International**, v. 49, p. 24356-24369, 2022.

YUKIHARA, E. G. *et al*. The quest for new thermoluminescence and optically stimulated luminescence materials: Needs, strategies and pitfalls. **Radiation Measurements**, v. 158, p. 1-19, article nº 106846, 2022a.

YUKIHARA, E. G. *et al*. Luminescence dosimetry. **Nature Reviews - Methods Primer**, v. 2, p. 1-21, article nº 27, 2022b.

ZHOU, J. *et al*. Defect engineering in lanthanide doped luminescent materials. **Coordination Chemistry Reviews**, v. 448, p. 1-26, article nº 214178, 2021.

ZHYDACHEVSKII, Ya. *et al*. Time-resolved OSL studies of $YAlO_3:Mn^{2+}$ crystals. **Radiation Measurements**, v. 94, p. 18-22, 2016.

ZOLOTOYABKO, E. **Basic concepts of X-ray diffraction**. Weinheim: Wiley, 2014.

ZUBER, D. *et al*. Third and fifth order nonlinear susceptibilities in thin HfO_2 layers. **Optics Express**, v. 31, n.12, p. 1-10, article nº 19309, 2023.

ZÚÑIGA-RIVERA *et al*. Persistent luminescence, TL and OSL characterization of beta irradiated $SrAl_2O_4:Eu^{2+}$, Dy^{3+} combustion synthesized phosphor. **Nuclear Instruments and Methods in Physics Research B**, v. 326, p. 99-102, 2014.

APPENDIX A – Fitting by Gaussian of the experimental fluorescence and OSL spectra data

The spectral curves for fluorescence and OSL with blue and IR stimulations were fitted with Gaussians, in order to estimate the position (energy) of the main emission band for each of those measurements. Figure A1 depicts the fitted curves of the fluorescence emission spectra, Figure A2 depicts the same analysis for the OSL spectra with green stimulation, and Figure A3 for IRSL. In all the cases, the value of the R squared (R^2) is indicated.

In most of the cases, the R^2 values was higher than 0.98, which indicates a good adjust. The sample calcined at 1000 °C for 2 h has a lower signal, hence, the noise is more representative, and lower are the R^2 values, as noticed for fluorescence and IRSL spectra.

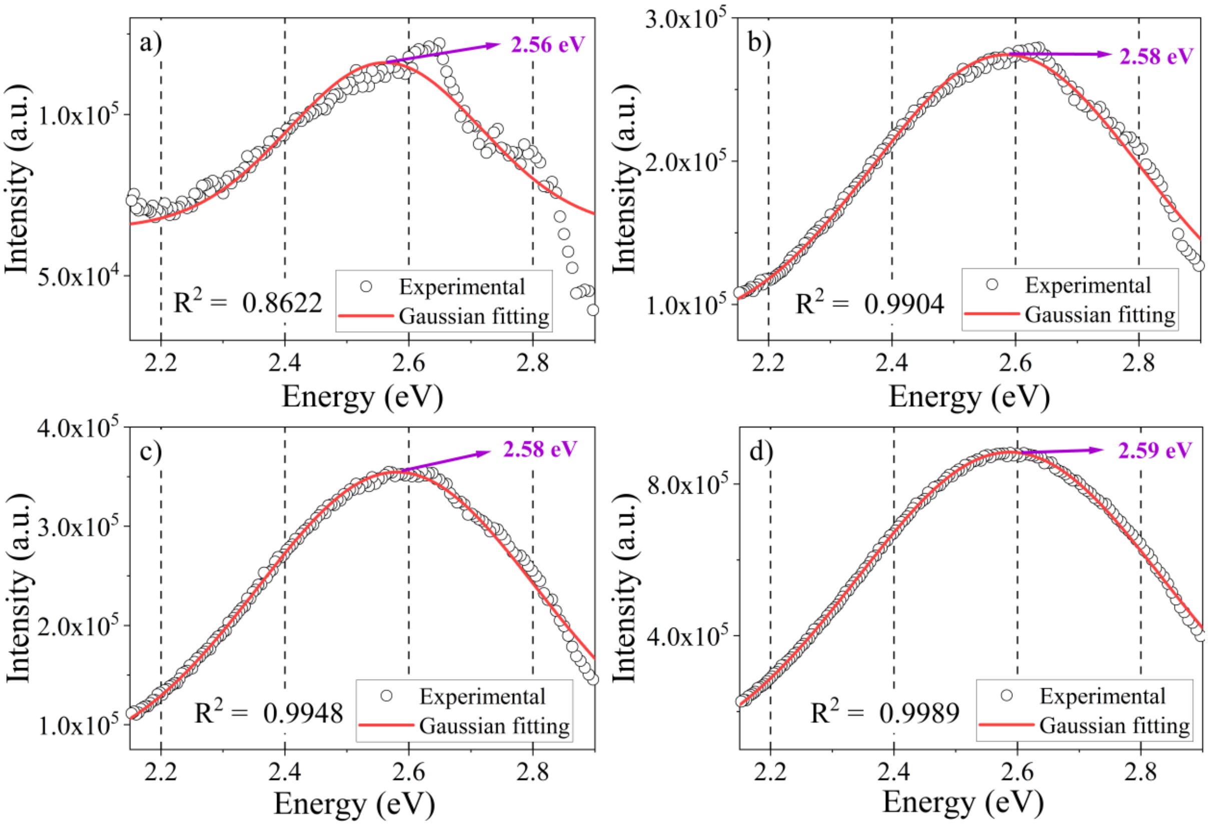

Figure A1 – Fluorescence emission (λ_{exc} =300 nm) spectra for HfO_2 calcined at (a) 1000, (b) 1200, (c) 1400 and (d) 1600 °C for 2h. Squares curves stand for the experimental data, whilst red lines stand for the Guassian fitting.

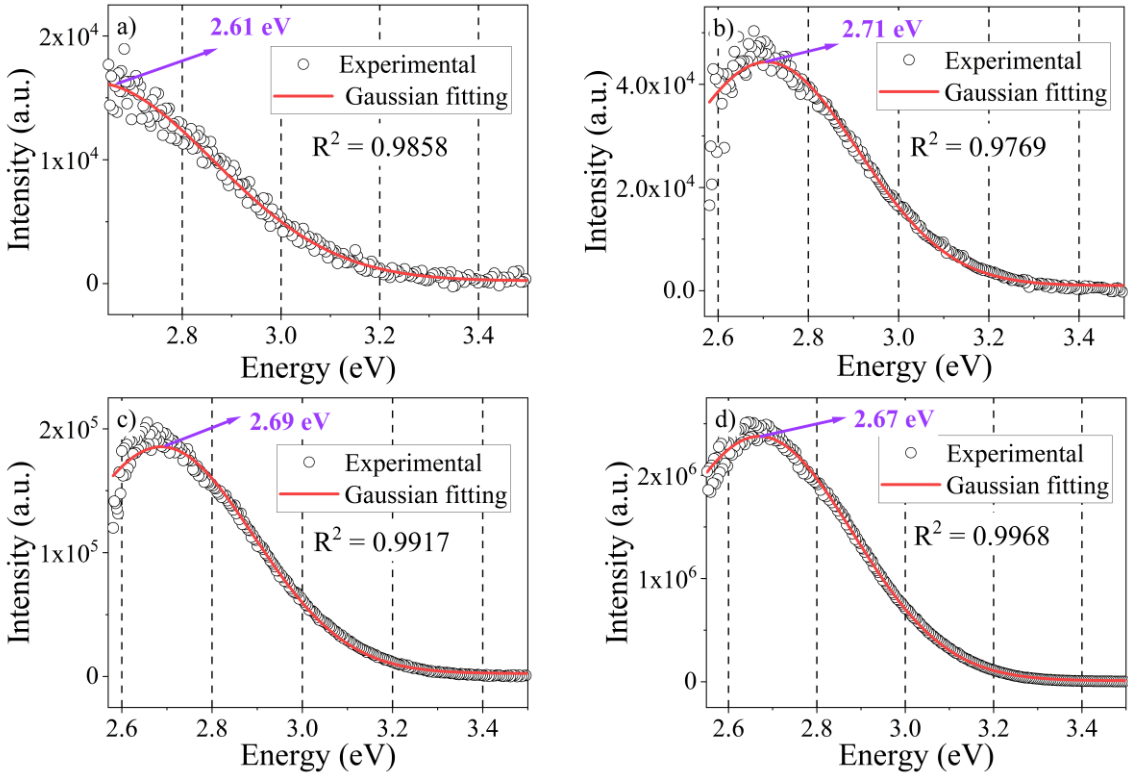

Figure A2 - OSL with green stimulation spectra for HfO_2 calcined at (a) 1000, (b) 1200, (c) 1400 and (d) 1600 °C for 2h, after a dose of 800 Gy of X-rays irradiation. Squares curves stand for the experimental data, whilst red lines stand for the Gaussian fitting.

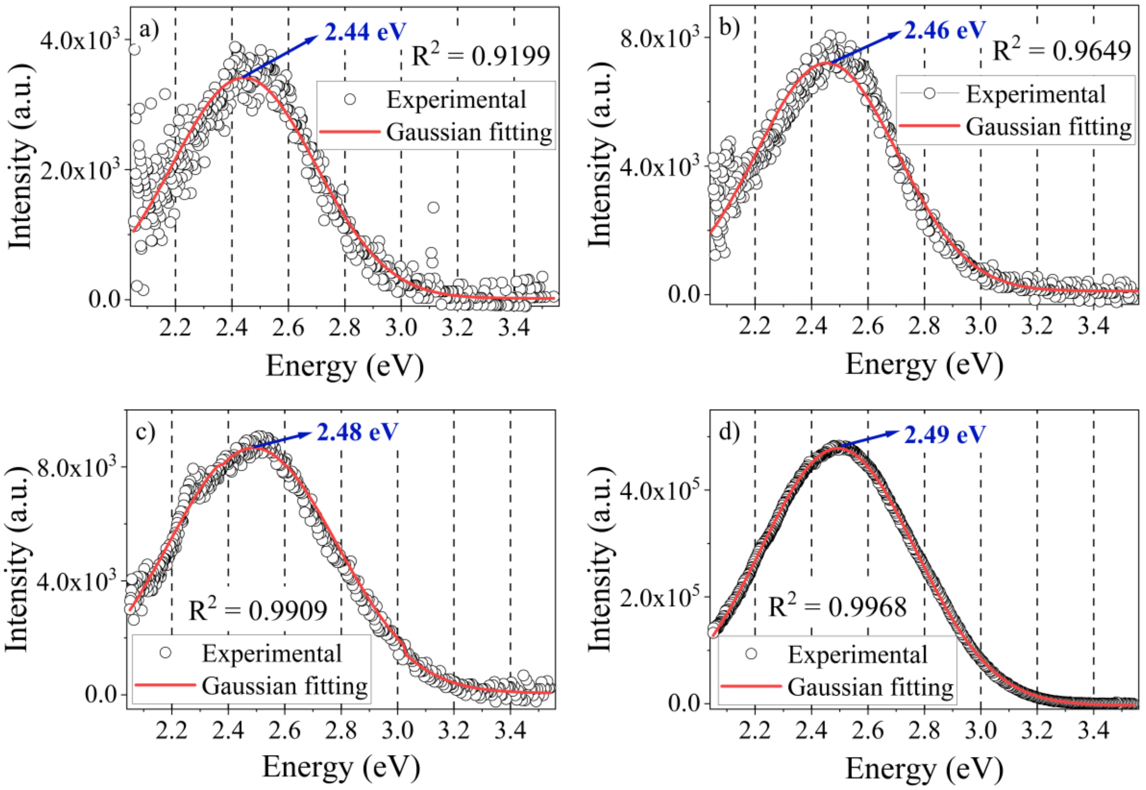

Figure A3 - IRSL spectra for HfO_2 calcined at (a) 1000, (b) 1200, (c) 1400 and (d) 1600 °C for 2h, after a dose of 800 Gy of X-rays irradiation. Squares curves stand for the experimental data, whilst red lines stand for the Gaussian fitting.

APPENDIX B – CGCD parameters for TL glow curves (doses of 5 and 30 Gy) using GOK model

Parameters used in the CGCD study of TL glow curves of HfO_2 samples calcined at different temperatures, for beta irradiation doses of 5 and 30 Gy, additionally to the results presented in section 5.2.3.1.

a) HfO_2 calcined at 1000 °C for 2 hours.

Table A1 - Parameters used in the CGCD study of TL glow curves of HfO_2 samples calcined at 1000 °C for 2 hours, for beta irradiation doses of 5 and 30 Gy.

Peak number	**Parameter**				
	I (a.u.)	**T_m (°C)**	**E (eV)**	**b**	**s (s^{-1})**
Dose of 5 Gy - FOM: 5.58 %					
1	5450	100	0.68	1.15	8.16×10^8
2	7590	128	0.7	1.34	1.53×10^8
3	900	140	1.05	1.7	2.25×10^{12}
4	1170	188	1.11	1.52	3.99×10^{11}
5	870	228	1.2	1.34	3.19×10^{11}
6	770	269	1.3	1.57	3.02×10^{11}
7	510	331	1.35	2	3.67×10^{10}
8	720	411	1.4	2	4.32×10^9
Dose of 30 Gy - FOM: 3.14 %					
1	6800	99	0.68	1.15	4.59×10^8
2	47200	129	0.7	1.34	1.45×10^8
3	7650	140	1.05	1.7	2.25×10^{12}
4	7800	188	1.11	1.52	3.99×10^{11}
5	5200	228	1.2	1.34	3.19×10^{11}
6	4600	269	1.3	1.57	3.02×10^{11}
7	2100	331	1.35	2	3.67×10^{10}
8	2300	412	1.4	2	3.19×10^9

b) HfO_2 calcined at 1200 °C for 2 hours.

Table A2 - Parameters used in the CGCD study of TL glow curves of HfO_2 samples calcined at 1200 °C for 2 hours, for beta irradiation doses of 5 and 30 Gy.

Peak number	**Parameter**				
	I (a.u.)	**T_m (°C)**	**E (eV)**	**b**	**s (s^{-1})**
Dose of 5 Gy - FOM: 5.83 %					
1	5450	130	0.68	1.4	7.45×10^7
2	7590	194	1	1.7	1.56×10^{10}
3	900	268	1.15	1.4	1.09×10^{10}
4	1170	346	1.5	2	3.46×10^{11}
5	870	403	1.51	2	4.22×10^{10}
Dose of 30 Gy - FOM: 4.41 %					
1	1610000	132	0.68	1.4	6.7×10^7
2	77000	194	1	1.7	1.6×10^{10}
3	31000	268	1.15	1.4	1.09×10^{10}
4	4700	345	1.5	2	3.64×10^{11}
5	5500	403	1.51	2	3.22×10^{10}

c) HfO_2 calcined at 1400 °C for 2 hours.

Table A3 - Parameters used in the CGCD study of TL glow curves of HfO_2 samples calcined at 1400 °C for 2 hours, for beta irradiation doses of 5 and 30 Gy.

Peak number	**Parameter**				
	I (a.u.)	**T_m (°C)**	**E (eV)**	**b**	**s (s^{-1})**
		Dose of 5 Gy - FOM: 3.72 %			
1	185000	126	0.69	1.001	1.31×10^{8}
2	27000	163	0.97	1.8	4.55×10^{10}
3	2900	203	1	1.4	9.53×10^{9}
4	2800	240	1.15	1.5	4.85×10^{10}
5	2500	281	1.3	1.6	1.58×10^{11}
6	5600	399	1.5	2	3.18×10^{10}
		Dose of 30 Gy - FOM: 5.26 %			
1	6467000	134	0.69	1.001	8.47×10^{7}
2	1450000	164	0.97	1.8	4.40×10^{10}
3	3900	203	1	1.4	9.61×10^{9}
4	15500	240	1.15	1.5	4.85×10^{10}
5	33500	281	1.3	1.6	1.58×10^{11}
6	33000	399	1.5	2	3.18×10^{10}

d) HfO_2 calcined at 1600 °C for 2 hours.

Table A4 - Parameters used in the CGCD study of TL glow curves of HfO_2 samples calcined at 1600 °C for 2 hours, for beta irradiation doses of 5 and 30 Gy.

Peak number	**Parameter**				
	I (a.u.)	**T_m (°C)**	**E (eV)**	**b**	**s (s^{-1})**
		Dose of 5 Gy - FOM: 5.63 %			
1	382000	123	0.76	1.001	1.32×10^{9}
2	8300	167	0.97	1.9	3.51×10^{10}
3	10500	221	1	1.4	3.66×10^{10}
4	900	237	1.14	1.6	4.48×10^{10}
5	3300	284	1.2	2	1.50×10^{10}
6	39000	411	1.6	1.8	1.15×10^{11}
		Dose of 30 Gy - FOM: 3.80 %			
1	5320000	128	0.76	1.001	9.78×10^{8}
2	150000	167	0.97	1.9	3.64×10^{10}
3	150000	221	1	1.4	3.66×10^{10}
4	7000	237	1.14	1.6	4.48×10^{10}
5	30000	284	1.2	2	1.50×10^{10}
6	199000	397	1.6	1.8	2.12×10^{11}

APPENDIX C - Derived Scientific Contributions

Throughout the doctorate and the development of this study, the results contributed to international peer-reviewed publications and participation in conferences. Contributions related only to the studies on the HfO_2 (not considering other reports or co-authored publications) are listed below.

- **Publications/papers:**

  SOARES, A. de F. *et al*. Morphological and luminescent properties of HfO_2 nanoparticles synthesized by precipitation method. **Journal of Luminescence**, v. 219, 116866, 2020. DOI: https://doi.org/10.1016/j.jlumin.2019.116866

  SOARES, A. de F. *et al*. Influence of heat treatment on luminescent properties of the HfO_2, synthesized by precipitation method. **Radiation Physics and Chemistry**, v. 180, 109292, 2021. DOI: https://doi.org/10.1016/j.radphyschem.2020.109292

  SOARES, A. de F. *et al*. The role of heat treatment in improving photoluminescence and optically stimulated luminescence of HfO_2. **EPJ Web of Conferences,** v. 266, 06010, 2022. DOI: https://doi.org/10.1051/epjconf/202226606010

- **Participation in conferences:**

  September/2022. Oral presentation in: European Optical Society Annual Meeting (EOSAM) 2022.Title: The role of heat treatment in improving photoluminescence and optically stimulated luminescence of HfO_2.

  September/2023. Oral presentation in: 20th International Conference on Solid State Dosimetry. Title: Investigating the luminescence properties of hafnia using IRSL, TL, RF emissions and correlations to ESR centres.
  Successful application for getting a fully waived conference registration fee to attend the conference and the Marko Moscovitch School.